Forschungsbericht 2026-13

About Helmholtz Resonators with Flexible Walls for Acoustic Damping

Fleming Kohlenberg

Deutsches Zentrum für Luft- und Raumfahrt
Institut für Antriebstechnik
Berlin

DLR Deutsches Zentrum für Luft- und Raumfahrt

Forschungsbericht 2026-13

About Helmholtz Resonators with flexible Walls for Acoustic Damping

Fleming Kohlenberg

Deutsches Zentrum für Luft- und Raumfahrt
Institut für Antriebstechnik
Berlin

188 Seiten
198 Bilder
9 Tabellen
321 Literaturstellen

DLR Deutsches Zentrum für Luft- und Raumfahrt

Herausgeber:

Deutsches Zentrum
für Luft- und Raumfahrt e. V.
Wissenschaftliche Information
Linder Höhe
D-51147 Köln

ISSN 1434-8454
ISRN DLR-FB-2026-13
Erscheinungsjahr 2026
DOI: 10.57676/0t9m-m873

Fluglärm, Lärmreduzierung, Schalldämpfer, Resonanz, akustische Impedanz

Fleming KOHLENBERG
DLR, Institut für Antriebstechnik, Berlin

Über Helmholtz-Resonatoren mit flexiblen Wänden zur Schalldämpfung
Technische Universität Berlin (Dissertation)

Flugzeugtriebwerke sind eine Hauptquelle für Lärm, der Gesundheit und Lebensqualität von Anwohner in der Nähe von Flughäfen beeinträchtigt. Zukünftige Triebwerke werden aus Effizienzgründen größer und der Lärm daher tieffrequenter werden, welchen konventionelle Dämpfungsstrukturen (Liner) nicht effektiv dämpfen können. In dieser Arbeit wird ein neues Linerkonzept untersucht: ein Helmholtz-Resonator mit flexibler Wand, der durch strukturdämpfende Schwingungen zusätzliche Dämpfung erzeugt und das Resonanzverhalten verändert.
Zur Vorhersage der akustischen Eigenschaften wurde ein analytisches und ein numerisches Modell entwickelt. Das analytische Modell ermöglicht ein besseres Verständnis der physikalischen Mechanismen während das numerische Finite-Elemente-Modell die Kopplung zwischen Resonator und Wand detaillierter auflöst und eine Visualisierung der Schallfelder und Schwingungen ermöglicht. Zur Validierung wurde ein modularer Prototyp designt und im Impedanzrohr untersucht, wobei Perforat, Wandmaterial, Form und Kavitätstiefe variiert wurden. Mit Laservibrometrie und internen Mikrophonen wurden Wandschwingungen und Schallfelder erfasst. Auch eine zusätzlich designte mehrzellige Probe zeigte unter realistischen Bedingungen (hohe Schalldruckpegel, Überströmung) zusätzliche Dämpfung beim streifenden Schalleinfall.
Die Ergebnisse bestätigen, dass das Konzept sowohl bei direktem als auch bei streifendem Schalleinfall mit und ohne Strömung wirkt. Die validierten Modelle bilden die Grundlage für die Optimierung und zukünftige Anwendung zur effizienten Reduktion von Fluglärm.

Aircraft noise, acoustic liner, noise reduction, resonance, acoustic impedance
(Published in English)

Fleming KOHLENBERG
German Aerospace Center (DLR), Institute of Propulsion, Berlin

About Helmholtz Resonators with Flexible Walls for Acoustic Damping

Technische Universität Berlin (dissertation)

Aircraft engines are a major source of noise, affecting health and quality of life near airports. To reduce fuel consumption, future engines are expected to be larger and produce more low-frequency, broadband noise—challenging conventional liners. This thesis investigates a new liner concept combining a Helmholtz resonator with flexible walls to enhance damping via structural losses and modify resonance behaviour. An analytical and numerical model were developed to predict the acoustic performance of the coupled system, consisting of a perforated face sheet and a cavity divided by a flexible wall. The analytical model enables physical insight into the damping mechanisms, whereas the finite element model resolves detailed coupling effects and visualises sound fields and vibrations.

A modular Helmholtz resonator with a flexible wall was designed and tested in a normal incidence tube, enabling a systematic study of face sheet, wall material, shape, and cavity depth to validate the models. In-situ measurements used a laser vibrometer and cavity microphones. An additional multi-cell liner tested under grazing flow with high sound pressure levels confirmed additional dissipation in realistic conditions.

Results show the concept effectively enhances damping under both normal and grazing incidence, with and without flow. The validated models provide a foundation for future optimisation to efficiently reduce aircraft noise.

About Helmholtz Resonators with Flexible Walls for Acoustic Damping

vorgelegt von

Hans-Fleming Kohlenberg, M. Sc.

ORCID: 0000-0002-6983-1545

an der Fakultät V – Verkehrs- und Maschinensysteme
der Technischen Universität Berlin
zur Erlangung des akademischen Grades

Doktor der Ingenieurwissenschaften
– Dr.-Ing. –

genehmigte Dissertation

Promotionsausschuss:

Vorsitzender:	Prof. Dr.-Ing. Dieter Peitsch
Gutachter:	Prof. Dr.-Ing. Ennes Sarradj
Gutachter:	Dr.-Ing. Christoph Richter

Tag der wissenschaftlichen Aussprache: 16. Februar 2026

Berlin 2026

Zusammenfassung

Flugzeugtriebwerke sind eine maßgebliche Lärmquelle die ein Gesundheitsrisiko und eine Belästigung für die Anwohner in Flughafennähe darstellt und deshalb reduziert werden sollte. Um den Treibstoffverbrauch zu senken werden zukünftige Triebwerke vorraussichtlich größer und deren Lärm demnach tieffrequenter und breitbandiger. Konventionelle Dämpfungsstrukturen (Liner) in Flugzeugtriebwerken können diesen Lärm nicht wirksam dämpfen. Daher müssen neuartige Liner entwickelt werden, die eine höhere und breitbandigere Schalldämpfung bei niedrigeren Frequenzen bei gleichzeitig kleinerem Bauraum erreichen.
In dieser Arbeit wird ein neuartiges Linerkonzept untersucht, bei dem ein herkömmlicher Helmholtz-Resonator-Liner mit flexiblen Wänden kombiniert wird, um durch gedämpfte Strukturschwingungen für zusätzliche Dämpfung zu sorgen und das Gesamtresonanzverhalten zu verändern. Für einen erfolgreichen zukünftigen Einsatz muss dieses Linerkonzept vorhersagbare akustische Vorteile bieten. Daher wird in dieser Arbeit untersucht, ob die flexiblen Wände für zusätzliche Dämpfung sorgen und wie das Verhalten des Gesamtsystems mit mehreren Freiheitsgraden verstanden und modelliert werden kann.
Im Rahmen dieser Arbeit wurde ein analytisches und ein numerisches Modell des Linerkonzepts entwickelt, um die akustischen Eigenschaften des gekoppelten Resonatorsystems vorherzusagen. Dieses besteht aus einem Perforat und einer Kavität, die durch eine flexible Wand unterteilt ist. Das analytische Modell kombiniert die Effekte der einzelnen Elemente mithilfe der Wellenleitertheorie. Die Effekte des Perforats werden durch semi-analytische Modelle aus der Literatur berücksichtigt. Die flexible Wand wird als äquivalente Impedanz einer dünnen eingespannten rechteckigen oder kreisförmigen Platte modelliert, bei der höhere Plattenmoden mitberücksichtigt werden. Die mechanischen Verluste innerhalb des Materials werden dabei durch einen komplexen Elastizitätsmodul abgebildet. Das analytische Modell trägt zum Verständnis der zugrundeliegenden physikalischen Mechanismen des Konzepts bei und ermöglicht eine schnelle Vorhersagemöglichkeit. Zusätzlich wurde ein numerisches Finite-Elemente-Modell erstellt, um die Kopplungseffekte zwischen dem Helmholtz-Resonator und den flexiblen Platten detaillierter aufzulösen. Die Visualisierung der räumlichen Schallfelder und der strukturellen Schwingungen helfen bei der Erklärung der Wirkmechanismen. Außerdem ermöglichen die numerischen Simulationen auch eine Quantifizierung des Dämpfungsbeitrags der flexiblen Wand zur gesamten Schallabsorption.
Im Rahmen dieser Arbeit wurde ein modularer Helmholtz-Resonator mit einer flexiblen Wand entworfen und in einem Kundt'schen Rohr untersucht. Die Modularität ermöglicht eine Untersuchung von Einzelelementen wie dem Perforat, dem Material, der Form und Größe der flexiblen Wand sowie der hinteren Kavitätstiefe. Diese experimentellen Ergebnisse bieten eine Validierungsgrundlage für die analytischen und numerischen Modelle. Zusätzlich wurde die Wandschwingungen in-situ mit einem Laservibrometer und zusätzlichen Mikrophonen innerhalb der Resonatorzelle untersucht.
Eine mehrzellige Linerprobe, die in einem Strömungsprüfstand mit streifendem Schalleinfall getestet wurde, zeigte zusätzliche Dissipation auch unter realistischeren Bedingungen mit hohen Schalldruckpegeln und Überströmung.
Die experimentellen Ergebnissen zeigen, dass das neuartige Linerkonzept sowohl bei direkten als auch bei streifendem Einfall für zusätzliche Dissipation sorgt. Die validierten analytischen und numerischen Modelle bieten eine Grundlage für die zukünftige Optimierung und Auslegung des neuartigen Linerkonzepts, um Fluglärm in Zukunft effizient zu reduzieren.

Abstract

Aircraft engines are a dominant contributor to aircraft noise, which needs to be reduced because it impacts the health and quality of life of dwellers in the vicinity of airports. To reduce fuel consumption, aircraft engines are expected to become larger with a more low-frequency and broadband noise signature. Conventional damping structures (liners) in aircraft engines cannot effectively attenuate such noise. Therefore, novel liners need to be developed that achieve higher and broader peak noise attenuation at lower frequencies.
This thesis investigates a novel liner concept in which a conventional Helmholtz resonator is combined with flexible walls. These flexible walls are expected to alter the resonance behaviour and provide additional damping through mechanical losses. For a successful future application, this liner concept needs to be acoustically beneficial and predictable. Therefore, it is investigated whether the flexible walls provide additional damping and how the behaviour of this multi-degree-of-freedom damping system can be understood and modelled.
To answer these questions, an analytical and numerical model of the liner concept was developed to predict the acoustic properties of the coupled resonator system. The coupled resonator system consists of a face sheet and a cavity, which is subdivided by a flexible wall. The analytical model combines the effects of individual elements using waveguide theory. Face sheet effects are accounted for by semi-analytical models from the literature. The flexible wall is modelled as an equivalent impedance of a thin clamped rectangular or circular plate that takes into account higher-order plate modes. Mechanical losses are represented by a complex Young's modulus. The analytical model offers a physical understanding of the concept and a fast approach to investigate the individual contributions towards the overall damping capabilities. A numerical finite element model was created to resolve the coupling effects between the Helmholtz resonator and the flexible plates in greater detail. Additionally, resolving the spatial sound fields and structural vibrations can be used to gain a deeper understanding of the underlying physics. The numerical simulations also allow the quantification of the contribution of the flexible wall to the overall noise absorption.
A modular Helmholtz resonator with a flexible wall was designed and evaluated in a normal incidence tube. The modular approach allowed for an investigation of the sub-elements of the liner structure like the face sheet, flexible wall material, shape, and back cavity size. These experimental results provide a validation basis for the analytical and numerical models. Additionally, the plate behaviour was investigated in-situ using a laser vibrometer and cavity microphones.
A multi-cell liner sample tested in a grazing flow test rig showed that additional dissipation is also achieved in more realistic conditions with high sound pressure levels and grazing flow.
The experimental results demonstrate that the novel liner concept provides additional dissipation, both in an acoustic normal and grazing incidence setting with and without grazing flow. The validated analytical and numerical models provide a basis for future optimisation of the proposed concept to efficiently reduce future aircraft noise.

Danksagung

Auch wenn am Ende nur ein Verfasser auf der Doktorarbeit steht – No man is an Iland, intire of it selfe. Diese Arbeit entstand im Rahmen meiner Tätigkeit als wissenschaftlicher Mitarbeiter bei der Abteilung Triebwerksakustik des Instituts für Antriebstechnik am Deutschen Zentrum für Luft- und Raumfahrt. Ich schätze mich unglaublich glücklich, dass ich in so einem unterstützenden Umfeld meine Flügel ausbreiten konnte.

Ich möchte mich bei meinem universitären Doktorvater Prof. Ennes Sarradj bedanken, dessen Fachexpertise und der klare Fokus auf das Wesentliche insbesondere in der letzten Phase wichtige Leitplanken der Promotion waren. Dr. Christoph Richter danke ich vielmals für die unkomplizierte Bereitschaft als Gutachter für diese Arbeit aufzutreten und Prof. Peitsch für die Übernahme des Vorsitz des Prüfungsausschusses.

Mein größter Dank geht an meinen Gruppenleiter und DLR-Doktorvater Dr. Karsten Knobloch, dessen fachliche, organisatorische und auch menschliche Leitung, diese Arbeit überhaupt erst ermöglicht hat.

Auch möchte ich mich bei Prof. Lars Enghardt dafür bedanken, mich mit der Linerforschung in Kontakt gebracht zu haben. Außerdem gilt mein Dank Dr. Friedrich Bake für seine Fürsorge und Anleitung in den ersten Jahren und Prof. Anita Schulz dafür, dass sie mich stets ermutigt hat einen wachen Geist zu behalten und jedes Ergebnis kritisch zu hinterfragen.

Ich verneige mich vor Sebastian Kruck aus der Metallwerkstatt für dessen Talent, aus ungenauen Zeichungen präzise Produkte zu fertigen. Mein Dank gilt auch Julia Genßler, Moritz Neubauer und dem gesamten Flexis Konsortium für die wunderbare Zusammenarbeit sowie der Deutschen Forschungsgemeinschaft für dessen Finanzierung.

Jede Promotion ist immer auch ein Lebensabschnitt, der Ablenkung und Abwechslung braucht um nicht zu verkümmern. Ich danke allen Freunden und Weggefährten in meinem Leben dafür, dass ich nicht die Blumen am Rande während meiner Reise übersehen habe. Wahre Freunde erkennt man in schweren Zeiten – und auch eine Promotion liegt gelegentlich schwer auf dem Herzen. Ohne die Unterstützung von Vincent und Lukas ‘Kollegen, keine Freunde’ und Daniels Bodenständigkeit wäre diese Arbeit ebenfalls nie wirklich geworden. Danke dir, Lihua, für die Zukunft die noch vor uns liegt. Es gibt mir viel Halt, dass ich mich im Zweifelsfall immer auf meine Eltern verlassen kann. Dafür bin ich unendlich dankbar.

»Ich musste mich vergleichen einem Bergsteiger, der, ohne den Weg zu kennen, langsam und mühselig hinaufklimmt, oft umkehren muss, weil er nicht weiter kann, der bald durch Überlegung, bald durch Zufall neue Wegspuren entdeckt, die ihn wieder ein Stück vorwärts leiten, und endlich, wenn er sein Ziel erreicht, zu seiner Beschämung einen königlichen Weg findet, auf dem er hätte herauffahren können, wenn er gescheidt genug gewesen wäre, den richtigen Anfang zu finden. In meinen Abhandlungen habe ich natürlich den Leser dann nicht von meinen Irrfahrten unterhalten, sondern ihm nur den gebahnten Weg beschrieben, auf dem er jetzt ohne Mühe die Höhe erreichen mag.«

Hermann von Helmholtz [1891]

Contents

Nomenclature

Latin symbols

a	Plate length	m
A_{cav}	Cavity cross section	m^2
a_{cav}	Distance between hole centre and cavity wall	m
A_{D}	Duct cross section	m^2
A_{h}	Hole cross section	m^2
A_{p}	Plate area	m^2
A_{ref}	Reference area around each orifice	m^2
b	Plate width	m
c	Mean speed of sound	$\mathrm{m\,s}^{-1}$
C_{d}	Discharge coefficient	–
D	Flexural rigidity	$\mathrm{Pa\,m}^3$
d	Diameter	m
D^+, D^-	Energy dissipation coefficient downstream and upstream	–
d_{cav}	Cavity diameter	m
E	Young's modulus	Pa
f	Frequency	Hz
f_{BPF}	Blade passing frequency	Hz
f_{c}	Cut on frequency of first higher order duct mode	Hz
f_{HR}	Helmholtz resonance frequency	Hz
$f_{\mathrm{m,n}}$	Plate eigenfrequency for mode m, n	Hz
h'_{fs}	Face sheet thickness with end corrections	m
h_{fs}	Face sheet thickness	m
h_{p}	Plate thickness	m
I	Area moment of inertia	m^4
I_m	Modified Bessel function of the first kind of m^{th} order	–
$I_{\{1-6\}}$	Abbreviations in plate impedance derivation	

i	Imaginary number	–
J_n	Bessel function of the first kind of n^{th} order	–
k_0	Free field acoustic wavenumber	m^{-1}
k_b	Free bending wave number	m^{-1}
k_{cav}	Wavenumber inside cavity	m^{-1}
k_{ph}	Wavenumber inside plate holder	m^{-1}
k_{th}	Thermal diffusion wave number	m^{-1}
k_ν	Viscous diffusion wave number	m^{-1}
$k_{\{x,y,z\}}$	Spatial acoustic wavenumber	m^{-1}
L	Liner length	m
l_{cav_1}	Main cavity depth	m
l_{cav_2}	Back cavity depth	m
l_{cav}	Cavity depth	m
l_{ph}	Plate holder thickness	m
$l_{xy,p}$	Plate square length	m
l_x	Duct length	m
l_y	Duct width	m
l_z	Duct height	m
M	Mach number	–
M_{gf}	Mean grazing flow Mach number	–
m_{HR}	Equivalent mass of a Helmholtz resonator	kg
n, m	Axial and lateral mode number	–
n_b	Number of blades	–
n_{fs}	Number of orifices per unit area	–
$\hat{p}$	Complex acoustic pressure amplitude	Pa
$\hat{p}^+, \hat{p}^-$	Complex plane wave pressure amplitude downstream and upstream	Pa
p'	Acoustic pressure	Pa
p'_{in}	Incident sound pressure level	m
P^+, P^-	Acoustic energy flux downstream and upstream	W
p_0	Ambient static pressure	Pa
Pr	Prandtl number	–
q	Acoustic volume velocity	$m^3\,s^{-1}$
d_h	Hole diameter	m
r	Amplitude reflection coefficient	–

R^+, R^-	Energy reflection coefficient downstream and upstream	–
r^+, r^-	Amplitude reflection coefficient downstream and upstream	–
r_D	Duct radius	m
r_h	Hole radius	m
r_port	Reflection coefficient at port boundary in numerical simulations	–
R_p	Outer radius of circular plate	m
r_p	Circular plate radius	m
R_s	Specific gas constant	$\mathrm{J\,kg^{-1}\,K^{-1}}$
$r_\mathrm{y}, r_\mathrm{z}$	Reflection coefficient at the duct walls	–
$\boldsymbol{S}$	Scattering matrix	–
s_HR	Equivalent stiffness of a Helmholtz resonator	$\mathrm{kg/s^2}$
Sh	Shear wave number	–
St	Strouhal number	–
T	Ambient temperature	K
t	Time	s
T^+, T^-	Energy transmission coefficient downstream and upstream	–
t^+, t^-	Amplitude transmission coefficient downstream and upstream	–
U	Perimeter	m
u^*	Skin friction velocity	$\mathrm{m\,s^{-1}}$
u_0	Bulk velocity	$\mathrm{m\,s^{-1}}$
u_cl	Centre line flow velocity	$\mathrm{ms^{-1}}$
u_gf	Grazing flow velocity	$\mathrm{m\,s^{-1}}$
u_h	Flow velocity in face sheet hole	$\mathrm{m\,s^{-1}}$
v'	Acoustic particle velocity	$\mathrm{m\,s^{-1}}$
v'_h	Acoustic particle velocity in the face sheet hole	$\mathrm{m\,s^{-1}}$
V_cav	Cavity volume	$\mathrm{m^3}$
v_p	Plate velocity	$\mathrm{m\,s^{-1}}$
v_sh	Shaft rotation speed	rpm
$\hat{w}_\mathrm{p}$	Plate displacement amplitude	m
w_cav	Normalised wave impedance inside cavity	–
w_ph	Normalised wave impedance inside plate holder	–
w_p	Plate displacement	m
w_{mn}	Modal deflection amplitude	m
x, y, z	Spatial coordinates	m

X_m	Beam mode shape of order m	–
x_n	Axial position of n^{th} microphone	m
Y_n	Beam mode shape of order n	–
$Z_{\mathrm{p,c}}$	Transfer impedance of a circular plate	$\mathrm{Pa\,s\,m^{-1}}$
$Z_{\mathrm{p,r}}$	Transfer impedance of a rectangular plate	$\mathrm{Pa\,s\,m^{-1}}$
Z_{pq}	Acoustic impedance	$\mathrm{Pa\,s\,m^{-3}}$
Z_{pv}	Specific acoustic impedance	$\mathrm{Pa\,s\,m^{-1}}$
Z_{p}	Plate transfer impedance	$\mathrm{Pa\,s\,m^{-1}}$

Greek symbols

α	Normal incidence sound absorption coefficient	–
α_∞	Geometrical tortuosity	–
α_{th}	Thermal diffusivity	$\mathrm{m^2\,s^{-1}}$
χ	Normalised specific acoustic reactance	–
χ_{cav}	Normalised specific acoustic cavity reactance	–
χ_{fs}	Normalised specific acoustic face sheet reactance	–
χ_{HR}	Normalised specific acoustic reactance of a simplified Helmholtz resonator	–
Δp	Sound pressure difference	Pa
δ^*	Boundary layer displacement thickness	m
$\delta_{\mathrm{add,gf}}$	End correction for grazing flow	–
δ_{add}	End correction length	m
Δ_{SPL}	Sound pressure difference between main and back cavity	dB
δ_{th}	Thermal boundary layer thickness	m
δ_ν	Viscous boundary layer thickness	m
$\delta_{\{\mathrm{in,out}\}}$	One sided end correction length	m
η	Mechanical loss coefficient	–
η_{jk}	Mode coupling factor	–
Γ	Propagation constant	–
γ	Isentropic exponent	–
Γ_{p}	Plate edge	–
κ	Empirical constant	–
κ_{gf}	Empirical constant to account for grazing flow	–
κ_{nl}	Empirical constant to account for high sound pressure levels	–
λ	Acoustic wavelength	m

$\lambda_{m,n}$	Modal frequency parameter	–
μ	Dynamic viscosity	$\mathrm{kg\,m^{-1}\,s^{-1}}$
ν	Kinematic viscosity	$\mathrm{m^2\,s^{-1}}$
ν_p	Poisson's ratio	–
ω	Angular frequency	Hz
ω_{mn}	Modal angular resonance frequency	Hz
ψ	Hole and wall interaction factor	–
ψ_Fock	Hole and wall interaction factor by Fock	–
ψ_nl	Reactance correction due to high sound pressure levels and grazing flow	–
$\psi_{m,n}$	Plate mode shape function of m,n$^\mathrm{th}$ mode	–
ρ_0	Mean density of air	$\mathrm{kg\,m^{-3}}$
ρ_p	Plate density	$\mathrm{kg\,m^{-3}}$
σ	Face sheet porosity or open area ratio	–
σ_t	Fluid resistivity	$\mathrm{kg\,m^{-3}\,s^{-2}}$
θ	Normalised specific acoustic resistance	–
θ_gf	Normalised specific acoustic resistance due to grazing flow	–
$\theta_\mathrm{nl+gf}$	Normalised specific acoustic resistance due to high sound pressure levels and grazing flow	–
θ_nl	Normalised specific acoustic resistance due to high sound pressure levels	–
$\tilde{\rho}_\mathrm{e}$	Effective density	$\mathrm{kg\,m^{-3}}$
φ	Azimuthal angle	$^\circ$
ξ	Hole to wall fraction	–
ξ'	Acoustic particle deflection	m
ζ	Normalised specific acoustic impedance	–
$\zeta_\mathrm{bl,th}$	Normalised specific acoustic impedance of the thermal boundary layer	–
ζ_cav	Normalised specific acoustic cavity impedance	–
ζ_fs	Normalised specific acoustic face sheet impedance	–
ζ_h	Normalised specific impedance of one face sheet hole	–
ζ_opt	Optimal normalised specific impedance	–
$\zeta_{\{1-6\}}$	Intermediate impedances in analytical model	–

Abbreviations

AAC	Adaptive Noise Absorption Control
ANC	Active Noise Control

avg Average

cav Cavity

D-NIT DLR-AT-TRA – Normal Incidence Tube

DDOF Double-degree of freedom

DUCT-NIT DUct aCoustic Test rig – Normal Incidence Tube configuration

DUCT-R DUct aCoustic Test rig – Rectangular configuration

EBA Ethylene butyl acrylate

FEM Finite Element Method

FS Face sheet

FXW Flexible wall

gf Grazing flow

HR Helmholtz resonator

MDOF Multi-degree of freedom

nl Nonlinear

OTR Over-the-rotor

ph Plate holder

RMS Root mean square

SDOF Single-degree of freedom

SPL Sound pressure level

TPU Thermopolastic polyurethan

UHBR Ultra High Bypass Ratio

1. Introduction

'Humanity has always dreamt of flying – but the dream is cursed.'[1] Modern aeroplanes turn that dream into reality. Civil aeroplanes connect civilisations, yet they are a significant contributor to human-caused climate change, with $\approx 3\,\%$ of total global CO_2 emissions. These emissions are projected to reach 2.6 times 2021 values in 2050[1]. Additionally, noise from aircraft negatively affects the crew, staff, and passengers on the aircraft and airport, as well as residents in surrounding communities in the vicinity of airports[2]. Aircraft noise is associated with the risk of hypertension, incidence of Ischaemic Heart Disease, and obesity, albeit with a low quality of evidence so far[3]. In 2019, approximately 1.7 million people in the European Union suffered from aircraft-induced high sleep disturbance, which is 31 % more than 2005[4, p. 29]. In the future, a reduction in average noise exposure is expected, but only if manufacturers develop quieter aircraft types to offset the anticipated growth in traffic, i.e., the benefits from introducing noise reduction technologies need to overcompensate the increased noise emissions due to an increased number of flights. To reduce the environmental impact of civil aviation, the European Commission has set ambitious goals for 2050: 'Increase the fleet fuel efficiency (30-50 % relative to 2018 levels) and reduce the perceived noise emission of flying aircraft (65 % per operation relative to the 2000 baseline)'[5].

In the following chapter, a general introduction of aircraft noise and possible noise reduction means is presented to set the frame for the novel liner concept investigated in this thesis.

Aircraft noise can be classified into airframe and propulsion noise. Airframe noise is mainly due to the interaction of turbulence and wakes with structures at the fuselage, the wings, the lift systems and the landing gear[6]. Propulsion noise is the sound radiated by the fan, compressor, combustion chamber, turbine, and the jet outside the engine. The relative contribution of the individual components differs from the type of aircraft and engine as well as the specific flight condition, such as takeoff or landing. As a rule of thumb, propulsion noise is dominant for takeoff condition, and is similar in magnitude to airframe noise for approach condition during landing[7],[8]. Therefore, putting emphasis on propulsion noise is beneficial for overall aircraft noise reduction.

Nowadays, state-of-the-art aircraft are 75 % quieter compared to the first civilian jets in operation 50 years ago[9, pp. 36–41]. This evolution is largely due to the transition from turbojet to turbofan engines. In a turbofan engine, a portion of the air flowing through the fan is diverted into the bypass duct, whereas the rest is mixed with fuel and the mixture is burned in the engine core. Turbofan engines have a bypass ratio greater than one, which is defined as the ratio between the bypass stream's mass flow rate and the mass flow rate entering the core. Higher bypass ratios imply a reduction of exhaust airflow velocity, which makes it possible to employ a lower fan pressure ratio with improvements in the propulsive and overall efficiency[10]. The reduced airflow velocity leads to less jet noise and is the main

[1] From: 風立ちぬ (The Wind Rises) by 宮崎駿. The original quote was referring to military aviation.

reason why current aircraft are quieter[9, pp. 36–41]. Modern turbofan aircraft engines have a very high bypass ratio of up to 12, and engine manufacturers are developing engines with even larger fans. For example, the state-of-the-art aircraft Airbus A320neo is powered by CFM International LEAP turbofan engines with a bypass ratio of 11[11] or P&W 1100G geared turbofan engines with an even higher bypass ratio of 12.1[12]. Currently, Rolls-Royce is developing an aero-engine with a 15+ bypass-ratio called 'Ultrafan'. They also filed a patent for an Ultra High Bypass Ratio (UHBR) turbofan engine with a bypass ratio up to 40[13].

The development towards higher bypass ratios was possible due to advancements in material technology, allowing turbine blades to withstand higher temperatures, which enables higher core efficiency; advanced aerodynamic design, such as wide chord fans with lightweight materials and structures, leading to overall weight reduction[10],[14]. However, the benefits of increasing the bypass ratio are limited because larger fans have increased drag and a larger nacelle is heavier. At a certain high bypass ratio, this leads to a loss of fuel efficiency compared with the gain from propulsive efficiency. Furthermore, the nacelle size is limited by the amount of ground clearance[15].

For modern aero-engines with high bypass ratios, the turbofan provides the majority of thrust and radiates sound through the inlet duct in a forward and through the bypass duct in a backward arc. Turbofan noise is expected to become the main noise source of future aircraft, at least in the forward arc and under almost all flight conditions[16],[17].

1.1. Turbofan noise

A typical sound power spectrum of noise generated by a generic turbofan is depicted in Fig. 1.1. The sound power spectrum has broadband components and harmonic tones that correspond to the blade passing frequency $f_{\mathrm{BPF}} = n_{\mathrm{B}} v_{\mathrm{sh}}$, which is the product of the number of blades n_{B} and the shaft rotation speed v_{sh} in Hz. For example, the aforementioned PW1100G engine with twenty fan blades has a first blade passing frequency of $f_{\mathrm{BPF}} = 20 \cdot 54.7\,\mathrm{Hz} = 1094\,\mathrm{Hz}$ at maximum speed during takeoff[18], which corresponds to 656 Hz for the approach condition with 60 % engine speed. This also excites tonal noise at higher harmonics, e.g. at 1312 Hz as the second and 1968 Hz as the third blade passing frequencies, respectively. A reduction of the rotation velocity for modern engine, consequently, leads to tonal noise at lower frequencies.

The noise of a fan stage, which consists of a rotor and a stator, can be classified into self-noise and interaction noise. Self-noise is emitted by the fan blades alone, whereas interaction noise is due to inflow disturbances at the inlet or rotor-stator interactions. The unsteady aerodynamics of the rotor–stator interaction is often recognised as the dominant contribution to both tonal and broadband noise in modern aircraft engines[20]. Tonal noise is generated by the cyclic pressure field induced by the fan and the wake interactions between blades and stators, but may also arise due to ingested upstream distortion. Broadband noise results from the propagation of sound produced near the blade surface and stems from pressure fluctuations associated with turbulent flow. Important sources for turbulence in the fan system are the boundary layers at the outer wall of the inlet duct and spinner, and the wakes shed from the blades[6].

The tonal interaction noise at the source can be significantly reduced by modifying the fan

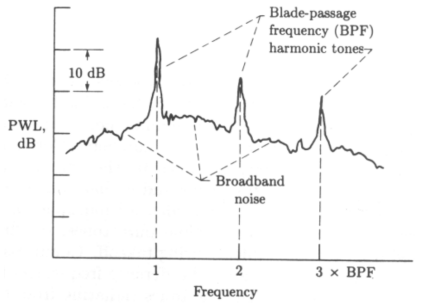

Figure 1.1.: Typical subsonic turbofan sound power spectrum, reprinted from[19, p. 154]

geometry. The number of blades and vanes can be chosen in a 'cut-off design' such that a large proportion of sound energy decays within the duct, and hence, does not propagate to a far-field observer[6]. Modern engines are usually designed in such a way, that noise at the first blade passing frequency cannot propagate. Another measure is for example increasing rotor-stator spacing to enable additional viscous wake decay. However, a large rotor-spacing may diminish the aerodynamic effectiveness of the fan stage. Additionally, rotor-stator-spacing is limited by the available space in the engine and the recent development tends rather towards shorter and more lightweight engines[21]. Additionally, the tonal fan noise can be reduced by leaning and sweeping the fan blades, which enables additional variation in the phase of the incident wake along the vane span[22]. Geared turbofans allow for a lower rotation frequency, which significantly reduces buzz-saw noise due to nonuniform shock waves when the rotor tip reaches supersonic speeds. Trailing edge noise and the fan wake can be reduced by blade geometry optimisation or porous trailing edges. Other technologies, such as fan trailing edge blowing, trailing edge serrations, and active blades, have been investigated with no recent developments[15]. Alternative noise control strategies to reduce fan noise include scarfed inlets, forward swept fans, swept and leaned stators, and soft vanes[23]. However, these acoustic measures may lead to decreased aerodynamic performance and consequently conflicting goals between noise reduction and performance, reliability, maintenance, and costs. Therefore, not all noise sources can be eliminated by design, and additional damping structures, i.e., liners, are required to attenuate inevitable propulsion noise of turbofans.

1.2. Acoustic liners in aero engines

Typically, noise attenuation is most effective near the source. Hence, an effective means of suppressing propulsion noise is the acoustic treatment of the inner walls of the nacelle, called acoustic liners, on its propagation way out through the engine's inlet and outlet. Liners convert acoustic energy to flow turbulence or thermal energy. The effect on the perceived noise level is depicted in Fig. 1.2, as taken from a system noise prediction for an aero-engine with a bypass ratio of six. The acoustic treatment is expected to reduce fan noise by $\approx 10\,\mathrm{dB}$, whereas for example, the jet noise remains unaffected. This is due to their location upstream and downstream of the fan in the nacelle, as depicted in Fig. 1.3. A

different type of liner, a bias flow liner, is installed in the combustion chamber to enhance wall cooling and suppress combustion instabilities. The overall acoustic liner absorption depends on the covered area. Since the aft duct is longer, more fan exhaust noise than fan inlet noise is damped, which is visible in Fig. 1.2.

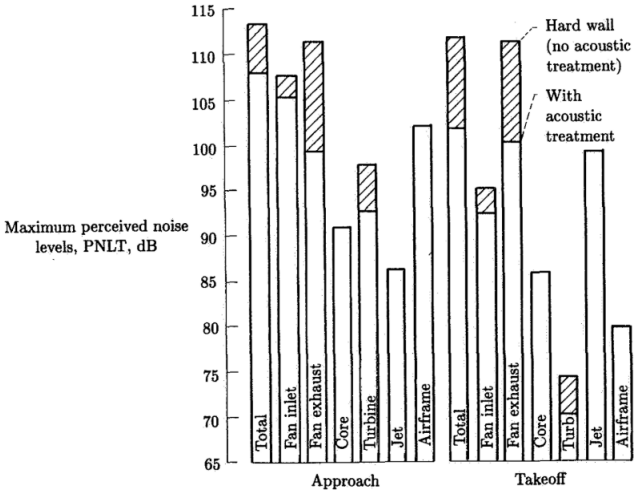

Figure 1.2.: Effect of acoustic liners on the perceived noise levels of an turbofan engine, reprinted from[19], original data from[24]

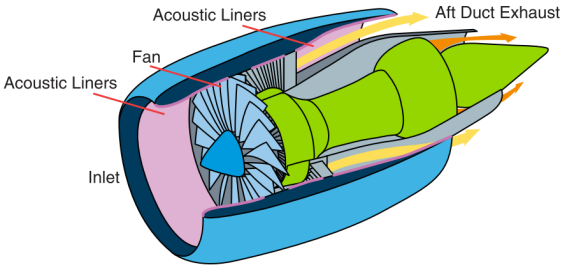

(a) Liner positions in an aircraft engine nacelle. This image is protected by copyright; reprinted with permission from[25]

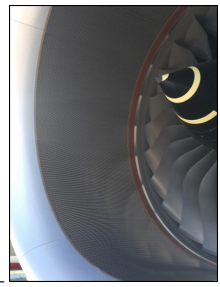

(b) Acoustic inlet liner

Figure 1.3.: Liner position and example of inlet liner in use

However, acoustic liners also have disadvantages. A typical acoustic liner produces about 70 % higher aerodynamic drag per plane area than a hydraulically smooth wall[26]. However, in the case of acoustic liners, the acoustical benefit outweighs the drawback of additional fuel consumption. Liner drag can be reduced by using smaller perforation holes, tapered holes, or perpendicular slots instead of a conventional round-hole perforate to reduce

the interaction of the flow above and below the surface of the face sheet[27],[28]. Under unfavourable flow conditions, an acoustic liner may even generate noise by itself when self-sustained resonance occurs and the air flow inside the cavity forces the shear layer that develops over the orifice[29],[30],[31],[32].

An optimal liner reduces the engine's radiated sound power with minimal required space in the nacelle. The liner effect can be evaluated as the difference between a hard-walled and lined configuration in the radiated sound power of the whole engine or the reduction of the effective perceived noise level, which is a critical measure in the certification process. Alternatively, the in-duct sound power transmission loss can be maximised, which is easier to calculate. Depending on the goal, optimisation routines can be used to determine the optimal liner impedance, which depends on the sound field in the duct where the liner is deployed. Once the liner's optimal impedance is found, the corresponding liner geometry can be selected by an appropriate liner model, if available[33],[34]. Therefore, the majority of liner research deals with the development of liner impedance prediction and determination.

1.2.1. Conventional liners

Conventional liners are usually modelled as an array of independent Helmholtz resonators. A Helmholtz resonator is a cavity connected to the surrounding environment by small holes in its surface, where all three dimensions are very small compared to the relevant acoustic wavelength[35]. A conventional acoustic liner comprises a perforated face sheet bonded to impervious honeycomb cells terminated by a rigid backing. In this case, the cavity formed by the honeycomb structure can be regarded as a spring, and the holes in the perforated face sheet can be considered as a mass[36]. In a Helmholtz resonator, sound energy is dissipated by the viscous boundary layer near the openings of the perforated plates. At the resonance frequency of the liner, the movement of the fluid through the openings is maximised and, consequently, the transformation of kinetic energy into thermal energy – i.e. sound absorption– as well. Conventional liners are called single-degree of freedom (SDOF)[2] liner, because the main damping occurs in a narrow band near the Helmholtz resonance frequency. SDOF liners are inexpensive, simple, lightweight, and maintenance-free structures that can withstand harsh conditions (e.g., high grazing flow, fluids such as water and fuel, sand, ice, heat, vibrations, and bird strikes) for at least 20 years ('fit-and-forget') in an aero-engine[37].

The design parameters for a perforated-plate SDOF treatment panel are the perforate porosity (open area ratio), orifice hole diameter, face sheet thickness, and cavity depth. Additionally, the attenuation due to the liner is affected by the mean flow Mach number, boundary layer thickness, and incident sound pressure[38],[39]. To obtain a low resonance frequency, a deep cavity is needed, which is limited by the available nacelle space. The perforated face sheet serves two purposes. First, it reduces drag compared to an open cavity and, second, allows a resonance frequency lower than that of a resonator that only consists of a cavity (quarter-wave-resonator). This, however, comes at the cost of a smaller sound-absorption bandwidth. A face sheet can be combined with a wire mesh to reduce the formation of turbulent structures near the face sheet holes due to a grazing flow or high

[2]The term SDOF is slightly misleading, as a perforate-over-honeycomb has infinite non-harmonic resonance frequencies. However, the main attenuation occurs at a single resonance frequency, the lowest, so-called Helmholtz resonance frequency. The term most likely originates from modelling a Helmholtz resonator as a simple mass-spring-system with one degree-of-freedom.

sound pressure amplitude[40].

To broaden the noise absorption bandwidth, a second perforate or septum may be implemented to subdivide the honeycomb cell into two parts. This adds a resonance to the resonator system and thus forms a double-degree of freedom (DDOF) liner. This improves the noise absorption bandwidth at higher frequencies but increases the manufacturing complexity. DDOF liners have been in use by Boeing since at least 1992, and they are believed to give approximately 20 % 'better'[3] noise attenuation for a fan duct application in a Boeing 767 than an optimised single layer wire mesh liner[41],[42]. An example of a SDOF and a DDOF liner with highlighted different components is depicted in Fig. 1.4.

Intake acoustic liners were initially manufactured as several segments separated by thin hardwall stripes, called liner splices. However, these splices have been found to scatter energy and reduce attenuation[43]. Therefore, thanks to advancements in manufacturing capabilities state-of-the-art aircraft such as the Boeing 787, Airbus A350, or the Airbus 320neo family use aero engines with zero-splice-liners, as depicted in Fig. 1.3b.

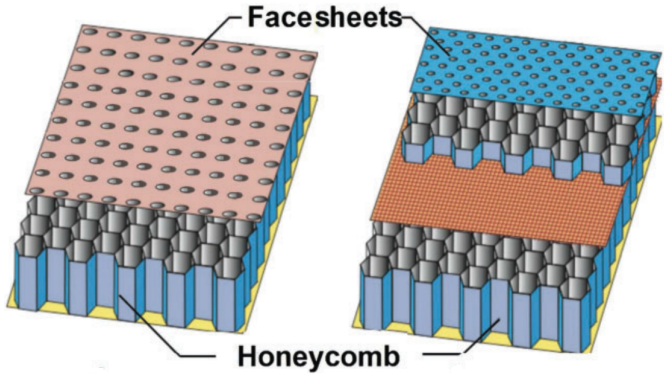

Figure 1.4.: Schematic SDOF and DDOF liner. This image is protected by copyright; reprinted with permission from[25]

1.2.2. Future liner requirements

The trend towards UHBR aero engines yields several challenging aspects for future acoustic liners:

- A slower rotation frequency leads to a lower blade passing frequency and consequently to fan noise with tonal components at lower frequencies.
- The relative importance of broadband noise will increase, e.g., due to less buzz-saw noise.
- To reduce weight and drag, the nacelle is thinned and shortened with less available liner depth and acoustic treatment area, especially in the inlet.

[3] 'Better' always depends on the optimisation goal, e.g. more broadband or higher damping at a target frequency.

- The simultaneous increase in fan diameter and decrease in nacelle length may reduce the overall effectiveness of existing acoustic liners.

Therefore, future acoustic liners should achieve higher and broader peak noise attenuation at lower frequencies, e.g. down to approximately 500 Hz[25], than conventional liner structures. Conventional liners require deeper cavities to reduce low-frequency noise. The installation space in the nacelle is limited due to drag and weight restrictions and finite ground clearance. Therefore, deeper cavities are usually not an option. Consequently, new advanced liner technologies are needed to tackle this low-frequency and broadband noise with limited installation space. An overview of current novel liner technologies is presented in the following.

1.2.3. Novel liner developments

Many liner concepts revolve around the Helmholtz resonance principle and seek to improve either the perforated face sheet or the cavity structure underneath. One drawback of SDOF liners is the limited bandwidth around the single Helmholtz resonance frequency. A DDOF liner extends the damping bandwidth to higher frequencies with an additional degree of freedom. The natural choice then is to add more degrees of freedom towards multi-degree of freedom (MDOF) liner. Therefore, a straightforward approach to increase the absorption bandwidth is to combine multiple different resonators[44]. This can be achieved for example by designing a liner with multiple variable cavity depths[7],[45],[46],[47],[48]. Variable-depth liners with alternative channel designs (e.g. curved or bent) provide an opportunity to minimise the overall liner thickness in limited space[49]. The proposed method can also be used to maximise space usage in curved nacelle sections, such as the inlet lip. Alternatively, liners with different orifice diameter distributions can be used for broadband damping[50],[51],[52]. However, connecting multiple resonators reduces the damping effectiveness for each absorption peak. Therefore, there is always a trade-off between achieving a wide bandwidth and maximum absorption in equally sized multi-resonator array panels.

Additional degrees of freedom can also be obtained by further subdividing the cavity. In a 'mesh-cap liner', with the help of new manufacturing techniques, each cell can be individualised in the number, resistance, and position of each mesh cap for each honeycomb cavity to increase the broadband damping[7],[53],[54],[55],[56],[57]. A mesh-cap liner extends the broadband damping of the conventional DDOF liner, i.e., a liner with one mesh cap at the same position for every cell, by adding more septa inside the cavities and individually tuning each cell.

New manufacturing methods, such as additive manufacturing, allow the realisation of complex cavities for future liner concepts. A relatively simple approach consists of a perforated diagonal septum core to increase the acoustic propagation path[58]. More sophisticated folded-cavity liners, realise broadband low-frequency damping characteristics by combining bent chambers with multiple porous plates subdividing the cavity[32],[58],[59],[60],[61],[62]. The additional benefits of different novel liner compared to conventional SDOF and DDOF liners were recently verified on a full-scale test rig[62],[63].

One approach to enhance the attenuation capabilities of conventional liners for low-frequency damping is to extend the holes in the perforated face sheet. The acoustic effect of a hole

extension is a prolongation of the air column length in the orifice, similar to a very thick perforate without additional weight. This extension can be achieved with a bent perforation[64] or by inserting a tube into the perforate hole called 'Helmholtz resonator with extended neck'[65],[66]. This extended neck can be either straight or prolonged by a spiral pattern. With additive manufacturing, the neck can have an arbitrary shape and can be roughened for additional viscothermal losses[67],[68],[69]. Additionally, a resonator with a prolonged neck length is less sensitive to changes in the incident acoustic pressure and grazing flow as the relative contribution of the viscothermal damping increases. However, the low-frequency damping is accompanied by a smaller resonance bandwidth. Individualised cells can be used to regain broadband damping[25].

The liner types presented so far are locally reacting absorbers, as they only admit wave propagation in the direction normal to the wall by partitioning the cavity behind the facing sheet, e.g., by a honeycomb structure. In contrast, non-locally reacting absorbers do not constrict the propagation direction. They are usually either homogeneous bulk absorbers (e.g., foams or glass fibres) or consist of a porous layer positioned at a certain distance from an acoustically hard wall.[4] If the cavity cells are specifically made porous, the perforated liner is effectively transformed into a bulk absorber, which allows for more design options[71]. However, this complicates the liner design as the impedance boundary condition loses its usefulness for non-local liners since a duct propagation model must couple the resolved acoustic propagation inside the liner with the air passage through the duct.

Bulk absorbers filled with porous material are commonly used in silencer design in heating, ventilation, and air conditioning systems. However, most porous materials cannot be used in aero-engines due to harsh environmental conditions. Metallic foam is one exception, which can withstand harsh conditions but is also more expensive and heavier than conventional liners[25],[37]. Thus, their usage is only investigated in extraordinary areas, such as over-the-rotor (OTR) treatments, at or very near the fan rotor plane. Due to the small liner over-the-rotor area, the attenuation is mostly attributed to source modification[72],[73],[74]. The main drawback is the significant aerodynamic penalty, which can be reduced by circumferential grooves[73].

Liners can also make use of non-locally reacting behaviour by deconstructive interference, such as a Herschel-Quincke tube[75],[76],[77]. This approach involves installing circumferential arrays of hollow side-tubes in the turbofan engine's inlet. Since the sound in the tubes travels a larger distance, frequencies exist where the sound in the tube exit is in anti-phase with the sound in the main-duct cancelling each other out at those frequencies. The concept has been applied to a turbofan engine to reduce tonal noise[78]. The Herschel-Quincke tube is predominantly used to reduce low-frequency noise, but it can be combined with other liner types for better broadband damping[79],[80],[81]. A similar non-locally reacting liner concept is the spiral liner, which consists of helical waveguides covered by a perforate plate and optionally filled with a porous material to suppress tonal rotor noise[82]. However, the lower the target frequency, the longer the additional tube needs to be, making the concept difficult for future UHBR engines.

The noise suppression characteristics of a liner are a function of the ambient conditions and its geometries. A passive liner has a fixed performance because its design is fixed by

[4]However, in practice, conventional liner with a rigid honeycomb structure are also partially non-locally reacting. This is because of drainage holes on the cell bottom to allow for leakage of unwanted fluids, which also leads to sound propagation between cells[70].

its dimensions and material properties. However, different flight phases have different flow and source conditions. Ideally, the liner impedance should be tunable to achieve good suppression over all flight phases. One can differentiate between 'Adaptive Noise Absorption Control' (AAC), which seeks to adjust the geometrical properties in operation, and 'Active Noise Control' (ANC), which introduces a feedback control with a second sound source into the system. AAC can be realised in the context of aero-engine liners by changing the cavity volume using a piston[83] or a movable wall[84],[85] to alter the resonance frequency.[5] Alternatively, the face sheet porosity can be made adaptive by changing the face sheet porosity using an iris valve[86] or by misaligning multiple face sheets to tune the effective hole length and, consequently, the resonance[87],[88],[89],[90],[91],[92],[93]. This system can also be used to close the liner, thereby reducing drag. This effectively deactivates the liner, which is acceptable mid flight when the aircraft is far away from communities, where sound attenuation is expendable to improve fuel efficiency.

A different approach is to change the acoustical properties of the fluid near the face sheet by additional vortex generation by AAC[94] or ANC[95],[96]. Active systems always suffer from the drawback of additional instrumentation and power supply which at one point must be certified to be used in-flight. This has hindered the implementation of active liners in aero-engines so far.

Acoustic absorbers are sometimes modelled as acoustic metamaterials, which are artificial structures that are typically periodic and consist of small elementary cells. In bulk, these structures behave like continuous materials with unconventional properties. Metamaterials are characterised by local resonators that are subwavelength in scale. Therefore, porous absorbers, Helmholtz resonators, and quarterwave resonators are often part of acoustic metamaterials. In this context, quarter-wave resonators are sometimes called Fabry-Perot-resonators[97].
Acoustic metamaterials can be used for wave manipulation by tailoring the arrangement of phase delays introduced in the acoustic field. These phase-gradient metasurfaces involve repetitions of elementary cells, such as an array of differently tuned Helmholtz resonators or quarter wave tubes[98]. A possible usage to reduce aero-engine noise is to use sound refraction at the nacelle tip region to form a 'virtual scarf inlet' with a nonuniform liner and, therefore, without the aerodynamic and weight penalties of a real scarfed inlet[99],[100],[101]. The concept has proven to be effective in a purely acoustic domain, but a turbulent grazing flow near the inlet may introduce severe complications in the wave manipulation for future applications.

Another approach to broaden the absorption spectrum of Helmholtz resonators is to combine them with mechanical elements such as beams, membranes or flexible plates, which eigenfrequencies have the benefit of being tunable independent of the Helmholtz resonance. With this approach, low-frequency noise can be potentially damped without increasing the overall resonator volume. This includes the usage of flexible walls to couple multiple resonator chambers, which is the focus of this thesis. The modelling of these concepts is analysed in-depth in the next chapter in Section 2.6.

In summary, the fan stage of an aero engine contributes significantly to aircraft noise. Acoustic liners are required to reduce this fan noise. Future aircraft engines are expected to become larger, which is a challenge for existing acoustic liners. Many novel liner concepts

[5] A movable piston is also commonly used in normal-incidence tubes to adapt the rigid end to different sample sizes.

revolve around the extension of the Helmholtz resonance principle with the help of advanced manufacturing techniques. This thesis investigates the possible benefits of combining flexible walls with structural resonances with a Helmholtz resonator liner to reduce future aircraft noise.

1.3. Thesis objectives

This thesis investigates a Helmholtz resonator with a flexible intermediate wall. The liner concept combines the Helmholtz resonance in the air domain with the flexible wall's structural resonances to achieve low-frequency and broadband sound attenuation. An additional damping mechanism is introduced if materials with mechanical losses, such as polymers, are used.

The objective of this thesis is to investigate the interactions between a flexible wall and a Helmholtz resonator as an acoustic liner by subdividing the cavity using a flexible material. The following research questions are addressed:

1. Is this liner concept suitable as a silencer on a fundamental level?
2. How can the coupled resonator system be modelled?

The first research question is addressed by designing and experimentally investigating a modular Helmholtz resonator with a flexible wall, as sketched in Fig. 1.5, in a normal incidence tube. In addition, a multi-cell resonator array liner is tested in a grazing flow test rig under high sound pressure and grazing flow conditions. This includes a comparison of the dissipation of the novel liner with a conventional Helmholtz resonator liner to evaluate the possible benefits of flexible structures. Additionally, the response of the flexible wall due to acoustic excitation is investigated using a vibrometer setup and cavity microphones to separate the contributions.

The second research question is addressed by deriving and validating an analytical model using waveguide theory to predict the acoustic impedance of a Helmholtz resonator with an intermediate flexible wall of different shapes. The analytical model is compared to the experimental data and used to evaluate the damping contributions of the main parameters, such as the material stiffness and cavity size. Additionally, a finite element model is developed using commercial software to spatially resolve the sound field inside the resonator and plate vibrations. The numerical results are compared with the analytical and experimental data to investigate the need for higher-fidelity prediction methods.

The contributions of this thesis include:

- *Design and evaluation of a modular Helmholtz resonator with a flexible wall*
- *Development and implementation of an analytical and a numerical model to predict the acoustic properties of the coupled resonator*
- *Insight into the contribution of flexible walls to the overall noise absorption mechanisms of an acoustic liner*
- *Comparison of a liner with flexible walls with a conventional liner under high sound pressure levels and grazing flow*

This thesis is structured as follows: This chapter serves as an introduction to aircraft

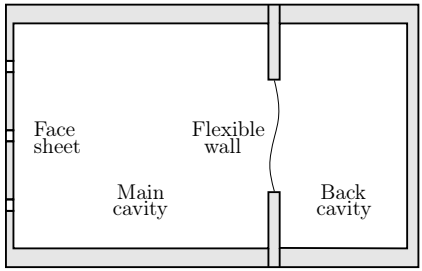

Figure 1.5.: Sketch of a Helmholtz resonator with a flexible wall and a back cavity

noise sources and current liner developments as a remedy. The theoretical background to understand the modelling and results of the investigated Helmholtz resonator with a flexible wall as a liner concept is presented in Chapter 2. This includes the modelling of a Helmholtz resonator and the vibration of flexible plates, as well as their interactions. The chapter concludes with a literature review that focuses on different modelling approaches for similar systems and gives context for the proposed analytical model, which is presented in Chapter 3. The proposed analytical model combines the models presented in the previous chapter for the face sheet, cavities, and flexible plate.
The concept is experimentally investigated in a normal incidence setup using a modular Helmholtz resonator that enables testing of different face sheets and flexible walls. Additionally, a resonator array is manufactured and tested to investigate the effect of high sound pressure levels and grazing flow in a grazing incidence setup. The sample specifications, the corresponding experimental test rigs and measurement procedures are presented in Chapter 4. Numerical models of the resonator systems are analysed to assess the benefits of using higher-fidelity prediction methods. Their properties and underlying models are stated in Chapter 5. The experimental, analytical, and numerical results of these studies are presented in Chapter 6. Finally, a conclusion is drawn with respect to the research questions and an outlook for future research is given in Chapter 7.

2. Theoretical Background and Literature Review

This chapter presents the theoretical background to understand the modelling and results of the investigated Helmholtz resonator with a flexible wall. The idea is to subsequently introduce relevant effects which are then finally combined to model the whole system in Chapter 3. As liners are deployed in ducts, the acoustic wave propagation in such with relevant effects is briefly introduced. The acoustic wave propagation, including the viscothermal effects, is relevant for the experimental test procedures and the modelling of the resonator system. The second and third parts of this chapter deal with modelling the relevant physical phenomena of the Helmholtz resonator, which can be dissected into a face sheet and a cavity, whereas the main dissipation occurs in the face sheet. Numerous contributing phenomena of the face sheet need to be modelled such as the viscothermal boundary layers, hole-to-hole interaction, high sound pressure levels, and grazing flow. Several models for these effects are presented and compared to select the most appropriate one for the analytical model. Next, the underlying theory of plate vibration is introduced to model the flexible wall. A brief introduction of the vibration of circular and rectangular plates is given to understand the behaviour of the flexible wall. Eigenforms are presented to compare them later with predicted operating deflection shapes, and a transfer impedance for the plate is derived from models from the literature. This transfer impedance is thought to capture the vibroacoustic plate effects within the analytical model. This also includes a section dealing with plate-cavity-interactions to better understand the interplay between plate and Helmholtz resonances. The literature review at the end of this chapter provides context on how similar acoustic systems are modelled.

2.1. Acoustic wave propagation

In fluids, sound propagates as a compression wave. Sound propagation in an incompressible constant mean flow of a homogeneous, lossless fluid can be described by the acoustic wave equation

$$\nabla^2 p' - \frac{1}{c^2}\left(\frac{\partial}{\partial t} + u_0 \nabla\right)^2 p' = 0 \tag{2.1}$$

with ∇ denoting the gradient, p' the acoustic pressure, c the speed of sound, and u_0 the bulk velocity of the medium[102]. Equation (2.1) can be derived from the conservation of mass, conservation of momentum, and an equation of state that links pressure with density fluctuations. The derivation is omitted here for the sake of brevity but can be found in textbooks such as by Morse and Ingård[102], Kinsler[36], Pierce[103] or Rienstra and Hirschberg[104].

The acoustic wave equation is valid for small acoustic perturbations $p' << p$, where all

thermodynamic processes are assumed to be isentropic, i.e., adiabatic and reversible, with no sources present in the domain, and the mean density ρ_0 and speed of sound c constant in space. The speed of sound in a gas $c = \sqrt{\gamma R_\mathrm{s} T}$ depends on the fluid's isentropic exponent γ, its specific gas constant R_s and the ambient temperature T, which was first shown by Laplace[105].

The Fourier transform of Eq. (2.1) is referred to the convective Helmholtz equation. For a stationary fluid, it can be expressed as

$$\Delta p' + k_0^2 p' = 0 \tag{2.2}$$

with $k_0 = \frac{\omega}{c}$ denoting the free field wavenumber, which increases linearly with the angular frequency $\omega = 2\pi f$[103, p. 28].

The propagation of an unhindered sound pressure wave in three-dimensional space can be expressed as

$$p'(x, y, z, t) = \mathrm{Re}\left(p_0 \, \mathrm{e}^{-\mathrm{i}k_\mathrm{x} x} \, \mathrm{e}^{-\mathrm{i}k_\mathrm{y} y} \, \mathrm{e}^{-\mathrm{i}k_\mathrm{z} z} \, \mathrm{e}^{+\mathrm{i}\omega t}\right), \tag{2.3}$$

where p_0 denotes the acoustic pressure amplitude[106, pp. 54–56]. The time dependence and denotation of the real part is dropped in the following for ease of notation.

Inserting Eq. (2.3) into Eq. (2.2) yields the dispersion relation[106, pp. 54–56]

$$k_0 = \sqrt{k_x^2 + k_y^2 + k_z^2}, \tag{2.4}$$

which connects the free field wavenumber k_0 with the spatial wavenumbers $k_\mathrm{x}, k_\mathrm{y}, k_\mathrm{z}$.

2.1.1. Propagation in rectangular ducts

The acoustic propagation in ducts is constrained by the duct walls. Given the case of an infinite rectangular duct of width l_y and height l_z without flow, the acoustic pressure field as a solution of Eq. (2.1) can be described as

$$p'(x, y, z, t) = \hat{p} \, \mathrm{e}^{-\mathrm{i}k_\mathrm{x} x} \left(\mathrm{e}^{-\mathrm{i}k_\mathrm{y} y} + r_\mathrm{y} \, \mathrm{e}^{\mathrm{i}k_\mathrm{y} y}\right) \left(\mathrm{e}^{-\mathrm{i}k_\mathrm{z} z} + r_\mathrm{z} \, \mathrm{e}^{\mathrm{i}k_\mathrm{z} z}\right) \tag{2.5}$$

with $\hat{p}$ denoting the complex acoustic pressure amplitude, x, y, z denoting the propagation directions and $r_\mathrm{y}, r_\mathrm{z}$ denoting the reflection coefficients at the duct walls[106, pp. 56–59]. The sound field is the superposition of a forth travelling wave in axial direction, which is not reflected because of its infinite length, and backward and forward travelling waves perpendicular to the duct main axis.

In the case of sound hard walls ($r_\mathrm{y} = r_\mathrm{z} = 1$), Eq. (2.5) can be expressed as

$$p'(x, y, z, t) = \hat{p} \, \mathrm{e}^{-\mathrm{i}k_\mathrm{x} x} \cos\left(k_\mathrm{y} y\right) \cos\left(k_\mathrm{z} z\right) \tag{2.6}$$

with the help of the identity $\cos(\square) = \frac{\mathrm{e}^{\mathrm{i}\square} + \mathrm{e}^{-\mathrm{i}\square}}{2}$ with $\square$ denoting a placeholder for either x, y or z. The sound hard walls require the sound particle velocity to become zero at the walls, which translates to maximum sound pressure. $|\cos(k_\mathrm{y} y = 0)| = |\cos(k_\mathrm{y} y = k_\mathrm{y} l_\mathrm{y})| = 1$ is fulfilled for $k_\mathrm{y} = \frac{n\pi}{l_\mathrm{y}}$ and accordingly in z-direction $k_\mathrm{z} = \frac{m\pi}{l_\mathrm{z}}$ with $n, m \in \mathbb{N}_0$. Using

Eq. (2.4), the axial wave number can be expressed as

$$k_\mathrm{x} = \sqrt{k_0^2 - \left(\frac{n\pi}{l_\mathrm{y}}\right)^2 - \left(\frac{m\pi}{l_\mathrm{z}}\right)^2}. \tag{2.7}$$

Sound waves with $k_0^2 < \left(\frac{n\pi}{l_\mathrm{y}}\right)^2 + \left(\frac{m\pi}{l_\mathrm{z}}\right)^2$ have a purely imaginary wavenumber k_x and decay exponentially instead of propagating. Frequencies, where higher order modes $m, n > 1$ start to be able to propagate are called 'cut-on-frequencies', and can be calculated with

$$f_c = \frac{c}{2\pi}\sqrt{\left(\frac{n\pi}{l_\mathrm{y}}\right)^2 + \left(\frac{m\pi}{l_\mathrm{z}}\right)^2}. \tag{2.8}$$

They depend on the channel dimensions $l_\mathrm{y}, l_\mathrm{z}$ and the ambient temperature as $c(T)$. Spatially decaying modes are also called evanescent or cut-off modes and form the near field of the sound source or a channel inhomogeneity. Evanescent modes cannot transport any acoustic power in the channel because their complex power is purely imaginary (reactive power)[106, pp. 153–154].

For frequencies below the first cut-on frequency, only plane waves ($m, n = 0$) are able to propagate. All fluid properties are uniformly distributed over a duct cross-section for plane waves. They can always propagate in a duct with sound hard walls but may become evanescent in a duct with sound soft boundary conditions $r = 0$[107, p. 109]. For plane waves, Eq. (2.1) becomes

$$\frac{\partial p'}{\partial x} - \frac{1}{c^2}\left(\frac{\partial}{\partial t} + u_0\frac{\partial}{\partial x}\right)^2 p' = 0, \tag{2.9}$$

which describes one dimensional wave propagation. Plane waves are of particular importance in the characterisation of the acoustic properties of sound absorbers since they yield several simplifications. Many methods for determining the acoustic properties of absorbers are restricted to the plane wave regime, such as the methods used in this work, later introduced in Chapter 4.

2.1.2. Viscothermal damping

In reality, purely sound hard walls do not exist. Instead, a viscous and thermal boundary layer forms near the wall. The concept of an acoustic boundary layer similar to a fluid dynamic boundary layer was introduced by Cremer[108]. The idea is to consider dissipative effects only in the vicinity of the wall, whereas the acoustic wave is not affected in the remaining fluid. In contrast to an ordinary boundary layer, the acoustic boundary layer cannot develop much, because the fluid never flows in one direction for more than half of an acoustic period[109, pp. 322–325]. Viscothermal damping is important to account for losses in a duct, cavity, or face sheet holes as part of a Helmholtz resonator.

Because of viscosity, the wall surface exerts a frictional shear force on the overlying fluid. A transition region exists near the wall where the sound particle oscillation amplitude decreases from its nominal value in the mean flow to zero at the wall. This transition region is referred to as the viscous boundary layer or Stokes layer. The wavenumber of the viscous

diffusion wave is[106, p. 69][109, pp. 322–327]

$$k_\nu = \sqrt{\frac{\mathrm{i}\omega}{\nu}} = \frac{1+\mathrm{i}}{\delta_\nu}. \tag{2.10}$$

$\delta_\nu = \sqrt{2\frac{\nu}{\omega}}$ is the viscous boundary layer thickness, i.e., the distance required for the particle velocity amplitude to increase from zero at the wall to $1/\mathrm{e}$ of its undisturbed value in the mean flow, with e denoting Euler's number. $\nu = \frac{\mu}{\rho_0}$ denotes the kinematic viscosity, which is linked to the dynamic viscosity μ via the mean density ρ_0.

The thermal boundary layer is formed when the thermal conductivity of the wall is much greater than that of the fluid. Consequently, heat conduction at the wall levels out all temperature fluctuations over time. This changes the acoustic process from being adiabatic far away from the wall to being isothermal near the wall. The layer with a significant temperature gradient is called the thermal or heat-conduction boundary layer. The wavenumber of the thermal diffusion wave is[106, p. 69][109, pp. 322–327]

$$k_\mathrm{th} = \sqrt{\frac{\mathrm{i}\omega}{\alpha_\mathrm{th}}} = \frac{1+\mathrm{i}}{\delta_\mathrm{th}}. \tag{2.11}$$

Its characteristic thickness is $\delta_\mathrm{th} = \sqrt{2\frac{\alpha_\mathrm{th}}{\omega}}$, where α_th denotes the thermal diffusivity.

The viscous and thermal boundary layer thicknesses are related via the Prandtl number $\sqrt{Pr} = \delta_\mathrm{th}/\delta_\nu$ and are of the same order of magnitude, e.g., for air: $Pr = 0.71$. The effect of the viscous and thermal boundary layers largely depends on the shear wave number $Sh = \frac{d}{2}\sqrt{\frac{\omega}{\nu}}$. Small shear numbers refer to narrow ducts with a small diameter d at low frequencies, whereas high shear numbers refer to wide ducts at high frequencies.

Multiple analytical solutions exist to describe the effect of the acoustic boundary layer, which are summarised by Tijdeman[110] and Kampigna[111]. The solutions assume plane wave propagation, a constant cross-section and the geometry length in the propagation direction larger than the boundary layer thickness to neglect inlet effects. Three commonly used approximate solutions are presented below.

Kirchhoff[112] investigated the effect of sound propagation through a uniform circular tube without flow with a viscothermal boundary layer. He gave a 'wide-tube' approximation for high shear wave numbers $Sh > 120$, i.e., when the viscothermal boundary layer is much smaller than the duct cross-section. This leads to an effective wave number for the plane wave

$$k_x = k_0 \frac{\Gamma}{\mathrm{i}} = k_0 \left[1 + \frac{1-\mathrm{i}}{\sqrt{2}} \left(\frac{\gamma - 1 + \sqrt{Pr}}{\sqrt{Pr}\, Sh} \right) \right] \tag{2.12}$$

$$= k_0 \left[1 + \frac{1-\mathrm{i}}{4} \left(1 + \frac{\gamma - 1}{\sqrt{Pr}} \right) \frac{U \delta_\nu}{A_\mathrm{D}} \right] \tag{2.13}$$

with U the duct perimeter and A_D the duct cross-section area.

Zwikker and Kosten[113],[110] developed an analytical solution that covers the range from very low frequencies or very narrow tubes with isothermal conditions to very high frequencies or

wide ducts:

$$k_\mathrm{x} = k_0 \frac{\Gamma}{\mathrm{i}} = \frac{k_0}{\mathrm{i}} \sqrt{\frac{J_0(\mathrm{i}^{3/2} Sh)}{J_2(\mathrm{i}^{3/2} Sh)}} \sqrt{\frac{\gamma}{n_\mathrm{ZK}}} \quad \text{, with} \quad n_\mathrm{ZK} = \left(1 + \frac{\gamma - 1}{\gamma} \frac{J_0(\mathrm{i}^{3/2}\sqrt{Pr}\, Sh)}{J_2(\mathrm{i}^{3/2}\sqrt{Pr}\, Sh)}\right)^{-1}. \tag{2.14}$$

J_0 and J_2 denote the Bessel functions of the first kind of zeroth and second order, respectively.

Dokumacı[114] modelled the thermoviscous wall losses with the wide-tube approximation Eq. (2.13) while taking into account the convective effect of a mean flow as[1]

$$k_\mathrm{x}^{\pm} = k_0 \frac{\Gamma}{1 \pm \Gamma M}, \text{ with } \Gamma = 1 + \frac{1 - \mathrm{i}}{\sqrt{2} Sh} \left(1 + \frac{\gamma - 1}{\sqrt{Pr}}\right), \tag{2.15}$$

where $M = {}^{u_0}/_{c}$ refers to the Mach number of the mean flow.

2.1.3. Acoustic impedance

A common entity to describe acoustic absorbers is the acoustic impedance. The idea stems from electro-acoustic analogies, i.e., representing systems by electrical circuits in which the motion of the analogous mechanical fluid is equivalent to the electrical current. The electrical analogy of the pressure difference across an acoustic element is the voltage across the corresponding part of the electric circuit. The specific acoustic impedance[2] is defined as the ratio of the complex acoustic pressure p' and the acoustic particle velocity v':

$$Z_\mathrm{pv} = \frac{p'}{v'} \tag{2.16}$$

The specific acoustic impedance can be normalised by the characteristic impedance of air $\rho_0 c$. The normalised specific acoustic impedance

$$\zeta = \frac{Z_\mathrm{pv}}{\rho_0 c} = \theta + \mathrm{i}\chi \tag{2.17}$$

is a complex number consisting of the real part θ, which refers to the specific normalised acoustic resistance, and the imaginary part χ, which refers to the normalised specific reactance. Physically speaking, the real part describes the extent of energy loss in the system, whereas the imaginary part represents energy storage and determines the frequency at which resonances occur[116],[117]. Reactance can also be understood as an indicator of the phase delay between the acoustic pressure and velocity at the sample surface. Therefore, a reactance equal to zero implies a specific superposition between the incident and reflected acoustic particle velocity wave. Taking the Helmholtz resonator as an example: In the additive *resonance* case, the particle velocity at the perforated plate increases, leading to greater dissipation. Conversely, in the subtractive *antiresonance* case, a low particle velocity in the face sheet and consequently little dissipation is observed. The resonance case is associated with a positive slope of the reactance at the zero-crossing and a high absorption, whereas the antiresonance is associated with a negative slope and a sharp local maximum of the resistance leading to a low absorption.

[1] Note, that Dokumacı uses a different definition of the propagation constant Γ, see the discussion in Lahiri[115, pp. 114–130].

[2] An alternative definition of the (non-specific) acoustic impedance Z is the quotient of the complex acoustic pressure p divided by the complex volume velocity q at the acting surface A as $Z_\mathrm{pq} = \frac{p}{q} = \frac{p}{v \cdot A}$ [36].

Additionally, there exists the acoustic transfer impedance[118, p. 74] that is defined as the average sound pressure drop Δp over a partition plane, such as a face sheet or flexible plate, divided by the average acoustic particle or plate velocity v'_{avg} as

$$Z_{\Delta \mathrm{p}} = \frac{\Delta p}{v'_{\mathrm{avg}}} = \frac{p'_{\mathrm{avg,front}} - p'_{\mathrm{avg,back}}}{v'_{\mathrm{avg}}}. \tag{2.18}$$

The impedance of a sample can be directly determined using a standing wave tube[119], in situ cavity microphones[120], or indirectly by impedance eduction methods[106]. The latter can be combined with laser Doppler anemometry techniques to measure the acoustic velocity fields in the vicinity of the liner[121]. For indirect methods, the liner is placed in a realistic installation situation in a flow channel. The impedance is inversely determined by adapting a sound-field model to experimentally determined sound-field parameters. A comparison between impedance methods can be found in[122],[37],[48],[123]. The precise determination of liner impedances remains a large research topic, especially regarding flow direction effects[124],[125]. A complicating fact is that the impedance modelling in shear grazing flow and the impedance inference using eduction techniques are interrelated.

The normal incidence absorption of a sample is connected to its impedance and can be determined by

$$\alpha = 1 - |r|^2 = \frac{4\theta}{(\theta+1)^2 + \chi^2}, \tag{2.19}$$

with the normal incidence reflection coefficient defined by

$$r = \frac{\rho_0 c - Z_{\mathrm{pv}}}{\rho_0 c + Z_{\mathrm{pv}}} = \frac{\zeta - 1}{\zeta + 1}. \tag{2.20}$$

The highest absorption under normal incidence is achieved at the purely real impedance $\zeta = 1 + \mathrm{i}\,0$ when the wall impedance matches that of the surrounding medium. High reflection and, consequently, low absorption occur at high wall resistance or high reactance.[3]

An optimal impedance in the grazing incidence case depends on the duct geometry, liner length, flow conditions, mode order, and the optimisation goal (absorption, transmission loss, radiated sound out of the nacelle,...)[126],[34]. The optimal impedance for maximising the attenuation of the least attenuated modes for a liner of infinite length in a rectangular duct of well cut-on modes with uniform flow can be expressed as[127],[128],[129]

$$\zeta_{\mathrm{opt}} = (0.929 - \mathrm{i}0.744)\frac{k_0 l_{\mathrm{z}}}{\pi}\frac{1}{(1+M)^2} \tag{2.21}$$

with M denoting the bulk flow Mach number. This impedance leads to the greatest possible sound attenuation in a rectangular one-sided lined duct. This is because there is no sound-carrying mode in the duct whose attenuation is greater at any frequency, i.e., the maximum attenuation of the least attenuated modes is achieved[130, pp. 79–88]. The optimal impedance for the flow duct used in this work (introduced in Chapter 4) with a height of $l_{\mathrm{z}} = 60\,\mathrm{mm}$ with and without uniform flow is plotted in Fig. 2.1.

Note that the optimal impedance is frequency-dependent, which differs from the optimal

[3] An acoustic hard wall ($\frac{\partial p'}{\partial x}|_{\mathrm{wall}} = 0$) with $\zeta = \infty \rightarrow r = 1$ in Eq. (2.20) is totally reflective with no absorption. An acoustic soft wall ($p'|_{\mathrm{wall}} = 0$) with $\zeta = 0 \rightarrow r = -1$ is also totally reflective with no absorption.

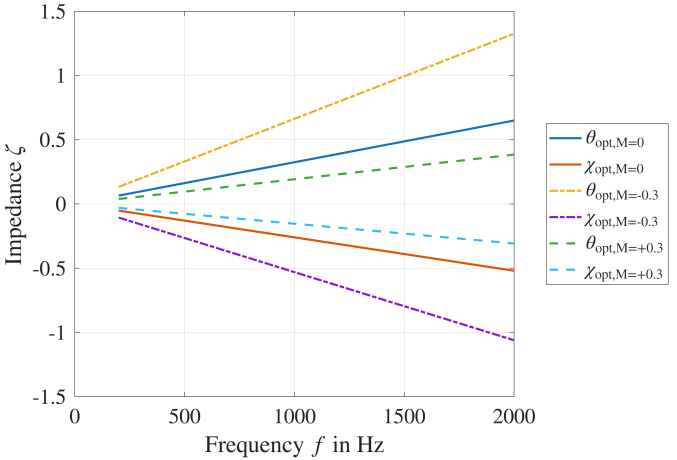

Figure 2.1.: Optimal impedance for a rectangular duct with a height of 60 mm with and without uniform flow of $M = 0.3$, upstream (-) and downstream (+)

impedance in the normal incidence case. The optimal resistance increases with frequency, whereas the reactance has a negative slope. An optimal liner impedance should have the same slope for optimal damping across all frequencies.[4]. In addition, the slope of the optimal impedance changes with the flow strength and direction. Thus, a liner placed at the inlet (upstream of the source) needs to be optimised differently than that in the aft section (downstream of the source). Note that this is only a rough estimate, and a rigorous liner optimisation requires much more effort, as it needs to be adapted to the noise environment where the liner is deployed. Therefore, no general-purpose optimal liner exists.

Terminology

In the context of acoustics, 'absorption', 'damping' and 'dissipation' are sometimes used synonymously. This short paragraph clarifies the use of certain terms in this work. The definition of these terms is adapted from Morfey[117].

Attenuation refers to the reduction in the amplitude of an acoustic field variable, such as acoustic pressure fluctuations. *Absorption* at a boundary is defined as the loss (or escape) of acoustic energy from a sound field, i.e., the loss of acoustic energy between an incoming and reflected wave, relative to the incoming wave's acoustic energy. In this work, absorption refers to the attenuation of acoustic energy in the normal incidence case. *Damping* is defined as the absorption of energy in a propagating wave or the loss of energy from an oscillation system via dissipation or radiation. In this work, damping is used to describe the dissipation of acoustic energy. *Dissipation* is defined more generally as the irreversible conversion of acoustic energy into thermal energy. In this work, dissipation is used to describe this physical mechanism, as well as an abbreviation for 'dissipation coefficient', which is based on scattering coefficients and introduced in Chapter 4. *Silencer*

[4]This is most likely impossible to fully realise as the reactance of liners generally have a positive slope, as depicted later in Fig. 2.3.

and *(acoustic) liner* are used synonymously in this work to describe passive devices intended to reduce noise emissions. Another common entity to describe silencers, although not used in this work, is the *transmission loss*, which is defined as the reduction in sound power level between an incident-wave power arriving at, and the transmitted-wave power leaving the silencer, when the silencer is anechoically terminated. A high transmission loss can be due to high reflection, dissipation of energy, or both, whereas a high dissipation coefficient is only due to dissipation, given that there is no sound leakage or mode scattering.

2.2. Helmholtz resonator

In essence, a Helmholtz resonator is a rigid walled enclosure with an aperture that links it to its surroundings. The lowest resonance, known as the Helmholtz resonance, is primarily volume-dependent rather than being affected by the cavity's specific dimensions. This is in contrast to standing waves, e.g., in pipes, where a fraction of the corresponding acoustic wavelength in the resonance case matches the system's dimensions. Consequently, no higher harmonics of Helmholtz resonance frequencies exist. The Helmholtz resonator is named after Hermann von Helmholtz, who applied potential theory to describe open organ pipes[131]. He also used spherical Helmholtz resonators[5] as selective Fourier analysers of sound[132]. Helmholtz's work on organ pipes and resonators, later named after him, was largely extended by Rayleigh[35] and Ingård[133]. Helmholtz resonators are mainly used to damp sound as sound absorbers for low frequencies in silencer design[134]. Apart from liners, they can also be found as absorbers in room acoustics[116], such as the prism-shaped resonators[6] which also act as diffusors in the Berliner Philharmonie[135, pp. 181–182]. According to Roman architect and siege-engineer Vitruvius, vessels, i.e., Helmholtz resonators, were placed in ancient Greek and Roman theatres in the audience area. Whether the purpose of these vessels was to absorb or amplify sound remains unclear. In any case, their impact on most metrics is negligible, which could be the reason for their abandonment in subsequent theatres[136]. In contrast to attenuation, Helmholtz resonators are also used as amplifiers in musical instruments such as ocarinas or resonant bodies of string instruments[137], enhancers of deep bass tones of organs[138] or bass reflex loudspeakers[139]. Recently, even the sound of hand-clapping was found to be similar to that of a flow-excited elastic Helmholtz resonator[140].

The system can be treated as acoustically compact for frequencies with wavelengths much smaller than the dimensions of the resonator. In this case, the Helmholtz resonator can be modelled as an equivalent mechanical mass-spring system. A sketch of a Helmholtz resonator and its equivalent mechanical system is depicted in Fig. 2.2.

In the mechanical analogy, the air inside the perforate with a single hole of diameter d_h moves as one piston with a mass $m_\mathrm{HR} = \rho_0 A_\mathrm{h} h'_\mathrm{fs}$ and the air in the cavity is adiabatically compressed with an equivalent stiffness $s_\mathrm{HR} = \rho_0 c^2 A_\mathrm{h}^2 / V_\mathrm{cav}$, which leads to the resonance

[5] The resonators used by Helmholtz had a second opening at the back, which was terminated by a flexible wall - the ear drum. However, the latter was assumed to be sufficiently rigid.

[6] However, predicting the absorption of these resonators was found to be too difficult and instead the absorption spectrum was determined experimentally in a reverberation chamber.

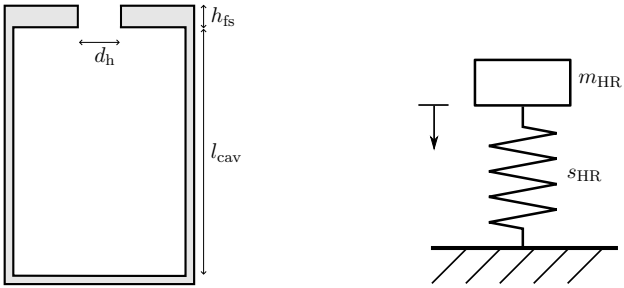

(a) Physical sketch (b) Mechanical model

Figure 2.2.: Sketch and simple mechanical model of a Helmholtz resonator

frequency of a simple harmonic oscillator[36]

$$f_{\mathrm{HR}} = \frac{1}{2\pi}\sqrt{\frac{s_{\mathrm{HR}}}{m_{\mathrm{HR}}}} = \frac{c}{2\pi}\sqrt{\frac{A_{\mathrm{h}}}{V_{\mathrm{cav}} h'_{\mathrm{fs}}}}. \tag{2.22}$$

A_{h} denotes the hole surface area, h'_{fs} the perforate thickness with additional end corrections that are introduced in Section 2.3 and V_{cav} the cavity volume. Therefore, the Helmholtz resonance frequency is lower for larger cavities with thick perforates.[7] A mass-spring-damper model of a Helmholtz resonator with an additional damping term can be used as a time-domain impedance boundary condition for numerical liner simulations[141].

Alternatively, the simple Helmholtz resonator can be modelled as a series connection between a short open tube and short closed cavity[109, p. 154]

$$\chi_{\mathrm{HR}} = \chi_{\mathrm{fs}} \frac{A_{\mathrm{h}}}{A_{\mathrm{cav}}} + \chi_{\mathrm{cav}} \tag{2.23}$$

with χ_{cav} and χ_{fs} denoting the reactance of the air in the cavity and the face sheet respectively, as

$$\chi_{\mathrm{cav}} = -\cot\left(k_0 l_{\mathrm{cav}}\right) \approx -\frac{1}{k_0 l_{\mathrm{cav}}}, \qquad \text{for } k_0 l_{\mathrm{cav}} \ll 1 \tag{2.24}$$

$$\chi_{\mathrm{fs}} = \tan\left(k_0 h'_{\mathrm{fs}}\right) \approx k_0\, h'_{\mathrm{fs}}, \qquad \text{for } k_0 h'_{\mathrm{fs}} \ll 1, \tag{2.25}$$

where l_{cav} denotes the cavity depth. The factor $\frac{A_{\mathrm{h}}}{A_{\mathrm{cav}}}$ ensures the continuity of the acoustic flux since the face sheet hole and the cavity have different cross-sections. Resonance occurs

[7] Unintuitively, the resonance frequency *increases* with a wider orifice area, which one would assume increases the resonator's equivalent mass and consequently lowers the resonance frequency. This result stems from the fact that whereas the equivalent mass of the air in the orifice is indeed proportional to A_{h}, the equivalent mechanical spring stiffness of the air in the cavity is proportional to A_{h}^2.

at $\chi = 0$ and therefore

$$0 = \frac{2\pi f_{\mathrm{HR}} h'_{\mathrm{fs}}}{c} \frac{A_{\mathrm{h}}}{A_{\mathrm{cav}}} - \frac{1}{2\pi f_{\mathrm{HR}}} \frac{c}{l_{\mathrm{cav}}} \tag{2.26}$$

$$f_{\mathrm{HR}} = \frac{c}{2\pi} \sqrt{\frac{A_{\mathrm{h}}}{A_{\mathrm{cav}} l_{\mathrm{cav}} h'_{\mathrm{fs}}}}, \tag{2.27}$$

which is the same result as Eq. (2.22).

The normalised reactance of the simplified Helmholtz resonator model for a generic geometry is plotted in Fig. 2.3. The Helmholtz resonance, which is a zero-crossing of the reactance

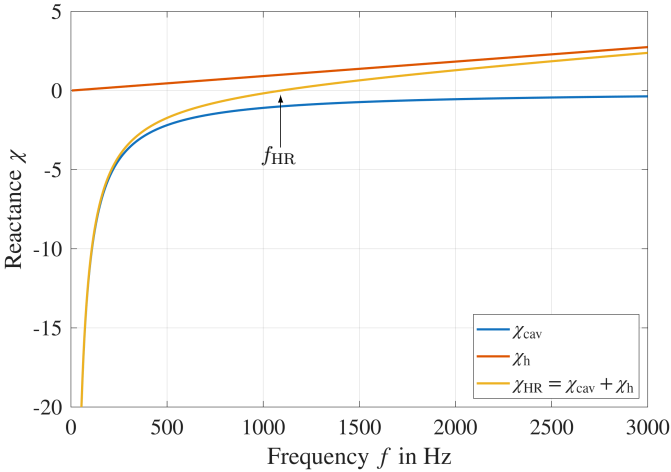

Figure 2.3.: Normalised reactance of a generic simplified Helmholtz resonator

with a positive slope is marked with f_{HR}. The overall reactance at low frequencies is dominated by the cavity $\chi_{\mathrm{cav}} \propto -1/f$. In contrast, because the inertial impedance of the perforate increases linearly with frequency $\chi_{\mathrm{h}} \propto f$, it dominates the impedance above the resonance. For higher frequencies, the inertia of the air in the holes acts as an acoustic barrier to incident sound waves, which is expressed as a high reactance.

A more realistic impedance model of a Helmholtz resonator liner must incorporate additional effects. The face sheet impedance consists of the impedance of the air in the face sheet itself, exterior end corrections, nonlinear effects due to high sound pressure levels and grazing flow. All these contributors are introduced in the next section.

2.3. Modelling of Helmholtz resonator impedance

This section provides a brief overview of important aspects when trying to model the impedance of the perforate face sheet ζ_{fs} and the cavity, which together constitute a Helmholtz resonator. The face sheet impedance needs to incorporate multiple phenomena,

such as viscous losses at the viscothermal boundary layer in the orifices, the effect of orifice interaction and exterior boundaries, high sound pressure levels, and the effect of grazing flow.

2.3.1. Viscous impedance of an orifice

An opening can be understood as a very short duct with the same physics as in Section 2.1.2. The viscous boundary layers on the walls inside the opening contribute to the resistance and, for long openings with a small cross-section, also to the reactance. The influence of the thermal boundary is layer is negligible due to the short duct length since there is no build-up of pressure in a short tube[133]. Most current perforated face sheet impedance prediction models are based on Crandall's derivations for circular ducts[142],[143]. Crandall's theoretical model of an aperture's impedance considers the air in an infinite duct and the shear forces due to the viscous boundary layer at the wall. In an infinite duct, the velocity profile has only a radial dependency, and any end effects are absent. The mean velocity can be calculated by integrating over the tube under the appropriate boundary conditions, and the transfer impedance can be derived from the pressure gradient over the tube. By treating the orifice as a duct of finite length h_{fs} the impedance of the duct can be expressed as[144]

$$\zeta_{\mathrm{h}} = \mathrm{i}k_0 h_{\mathrm{fs}} \left[1 - \frac{2}{k_{\mathrm{s}} r_{\mathrm{h}}} \frac{J_1(k_{\mathrm{s}} r_{\mathrm{h}})}{J_0(k_{\mathrm{s}} r_{\mathrm{h}})}\right]^{-1} \tag{2.28}$$

with $J_{\{0,1\}}$ the Bessel function of the first kind of zeroth and first order respectively, r_{h} the hole radius, and $k_{\mathrm{s}} = \sqrt{-\mathrm{i}\omega/\nu}$.[8] Before the introduction of modern computer technology, the evaluation of these Bessel functions used to be challenging and several approximations of Eq. (2.28) have been derived and used in several impedance models:

- For low frequencies and *very* narrow orifices (e.g. $d_{\mathrm{h}} < 0.1\,\mathrm{mm}$ at $1000\,\mathrm{Hz}$) Eq. (2.28) can be approximated by

  $$\zeta_{\mathrm{h,lf}} = \frac{8\mu h_{\mathrm{fs}}}{\rho_0 c r_{\mathrm{h}}^2} + \mathrm{i}\frac{4}{3} k_0 h_{\mathrm{fs}}, \qquad \text{for } Sh < 1. \tag{2.29}$$

  Equation (2.29) is only relevant for porous materials and is associated with Poiseuille flow[113],[145].

- For macro-perforated plates (e.g. $d_{\mathrm{h}} > 1\,\mathrm{mm}$ at $1000\,\mathrm{Hz}$) Crandall gave an approximation of Eq. (2.28) as

  $$\zeta_{\mathrm{h,hf}} = \frac{h_{\mathrm{fs}}}{r_{\mathrm{h}}} \frac{\sqrt{2\mu\rho_0\omega}}{\rho_0 c}(1 + \mathrm{i}) + \mathrm{i}k_0 h_{\mathrm{fs}}, \qquad \text{for } Sh > 10, \tag{2.30}$$

  which was used for example by Guess[146]. Note that both the resistance and reactance depend on the orifice length-to-width ratio $\frac{h_{\mathrm{fs}}}{r_{\mathrm{h}}}$ and are frequency dependent.

- Maa[145] investigated micro-perforated plates (e.g., $0.1\,\mathrm{mm} < d_{\mathrm{h}} < 1\,\mathrm{mm}$ at $1000\,\mathrm{Hz}$)

[8] Note that $|k_\nu r_{\mathrm{h}}| = |Sh|$ and that by neglecting any viscous effect, the imaginary part of Eq. (2.28) reduces to Eq. (2.25).

and gave an approximation of Eq. (2.28) for intermediate shear wave numbers

$$\zeta_{\mathrm{h,mf}} = \frac{8\nu h_{\mathrm{fs}}}{r_{\mathrm{h}}^2}\sqrt{1+\frac{r_{\mathrm{h}}^2\omega}{32\nu}} + \mathrm{i}k_0 h_{\mathrm{fs}}\left(1+\frac{1}{\sqrt{9+\frac{r_{\mathrm{h}}^2\omega}{2\nu}}}\right), \qquad \text{for } 1 < Sh < 10. \quad (2.31)$$

Atalla and Sgard[147] proposed to model the impedance of an orifice, including viscothermal losses, as an equivalent fluid. Equivalent fluid models are generally used to describe the impedance of porous materials. The idea is to describe the porous material as a fluid whose properties are approximated by an equivalent or effective density and an equivalent compression modulus. There are several approaches for describing the equivalent parameters, which differ in terms of complexity and area of application[148].[9] Atalla and Sgard showed that a perforated plate can be modelled as an equivalent fluid following the Johnson–Allard approach[150],[151] with an equivalent tortuosity. Modelling the perforated plates as an equivalent fluid offers the advantage of being able to represent both macro- and micro-perforated plates. They also showed that their impedance model can be converted into the classical equations based on Crandall's work for describing the impedance of openings and perforated plates in the high and low frequency limit[147]. The impedance of one hole is given as

$$\zeta_{\mathrm{eqf}} = \mathrm{i}k_0 h_{\mathrm{fs}}\frac{\tilde{\rho}_{\mathrm{e}}}{\rho_0} \quad (2.32)$$

All viscothermal effects are captured in the effective density $\tilde{\rho}_{\mathrm{e}}$, which for circular holes can be expressed as

$$\tilde{\rho}_{\mathrm{e}} = \alpha_\infty \rho_0 \left(1+\frac{\sigma\sigma_{\mathrm{t}}}{\mathrm{i}\omega\alpha_\infty\rho_0}\sqrt{1+\frac{\mathrm{i}4\rho_0\omega\mu\alpha_\infty^2}{\sigma^2\sigma_{\mathrm{t}}^2 r_{\mathrm{h}}^2}}\right). \quad (2.33)$$

Neglecting end corrections and hole interactions yields $\alpha_\infty = \sigma = 1$, with α_∞ denoting the geometrical tortuosity. $\sigma_{\mathrm{t}} = \frac{8\mu}{\sigma r_{\mathrm{h}}^2}$ denotes the flow resistivity, which non-normalised corresponds to the resistance in the low frequency approximation Eq. (2.29).

A comparison between these approximations and the original formulation by Crandall is presented in Fig. 2.4. If viscothermal losses are neglected, the resistance is zero (black dashed). Except for the high-frequency approximation (green), all models coincide with the low-frequency approximation (yellow, dashed) for small shear wave numbers. For $Sh > 5$, the original formulation (red, solid) shows the highest resistance, whereas the mid-frequency approximation (purple, dashed) and the equivalent fluid formulation (light blue, dashed) predict similar but slightly smaller resistances. The high-frequency approximation predicts lower resistances.

The reactance is predicted almost identically by all models. The only exceptions is the low-frequency approximation (yellow), which overpredicts the reactance for higher shear wave numbers, and the neglection of viscothermal effects (black), which leads to a lower reactance prediction.

The impact of different viscothermal models for a generic orifice ($d_{\mathrm{h}} = h_{\mathrm{fs}} = 1\,\mathrm{mm}$) in a typical low-frequency range up to 2000 Hz is depicted in Fig. 2.5. The low-frequency

[9] A similar approach is commonly used in the context of acoustic metamaterials where an dynamic effective mass and effective bulk modulus is used that may even become negative at local resonances[149].

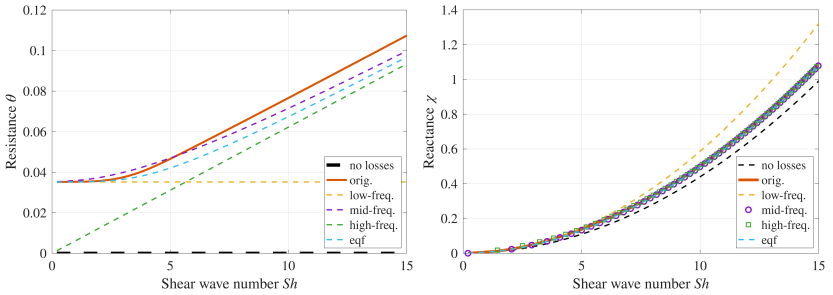

(a) Resistance (b) Reactance

Figure 2.4.: Different approximations of specific normalised orifice impedance as a function of shear wave number Sh. 'no losses' refers to Eq. (2.25). 'orig.', refers to the original formulation by Crandall Eq. (2.28), and 'low-freq.', 'mid-freq.', and 'high-freq.' refer to Eq. (2.29), Eq. (2.31) and Eq. (2.30), respectively. 'eqf' refers to Eq. (2.32).

approximation and neglection of viscothermal losses significantly deviate from the other models with respect to the resistance. However, there is not much difference between Crandall's original formulation, its mid-frequency approximation and the equivalent fluid model. All models except the low-frequency approximation are aligned for the reactance. Moreover, viscothermal effects do not significantly affect the reactance inside the orifice for the exemplary orifice, as all models also align with the 'no losses' case.

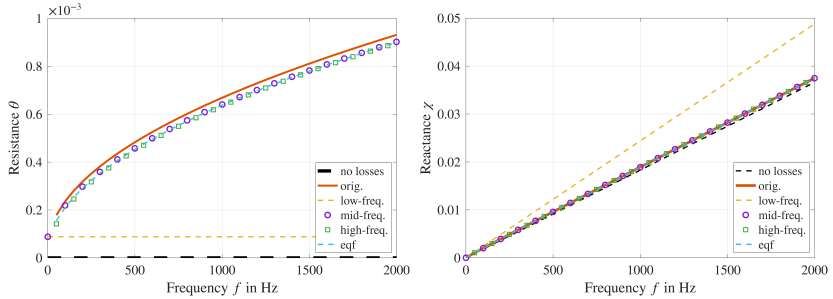

(a) Resistance (b) Reactance

Figure 2.5.: Different approximations of specific normalised orifice impedance for a generic orifice ($d_\mathrm{h} = h_\mathrm{fs} = 1\,\mathrm{mm}$) versus frequency. 'no losses' refers to Eq. (2.25). 'orig.', refers to the original formulation by Crandall Eq. (2.28), and 'low-freq.', 'mid-freq.', and 'high-freq.' refer to Eq. (2.29), Eq. (2.31) and Eq. (2.30), respectively. 'eqf' refers to Eq. (2.32).

2.3.2. End corrections

The airflow through the orifice affects the surrounding air in a close proximity. The air outside yet in the vicinity of the orifice increases the face sheet impedance. The additional

mass of fluid beyond the orifice participates in the oscillatory motion and must be considered to accurately predict the resonance frequency of a Helmholtz resonator in Eq. (2.27). This is usually incorporated by modifying the orifice length h_{fs} with an added length $h'_{\mathrm{fs}} = h_{\mathrm{fs}} + \delta_{\mathrm{add}}$, with $\delta_{\mathrm{add}} = \delta_{\mathrm{in}} + \delta_{\mathrm{out}}$[133],[144]. The situation is depicted schematically in Fig. 2.6, where a finite element simulation was conducted to calculate the velocity field in the vicinity of a generic orifice.

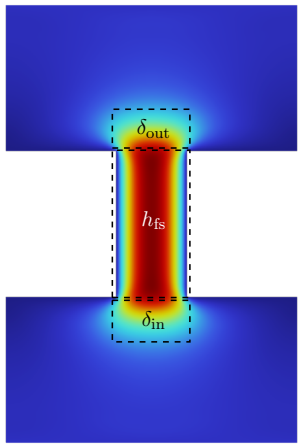

Figure 2.6.: Exemplary acoustic velocity field at a generic orifice ($h_{\mathrm{fs}}/r_{\mathrm{h}} = 3, f = 400\,\mathrm{Hz}$) generated with the commercial finite element software Comsol Multiphysics with visible extension of acoustic velocity outside the orifice

Rayleigh[152, p. 151] investigated the vibration of a circular plate in an infinite baffle. Assuming that the air mass behaves similarly as a vibrating piston in an infinite baffle, he showed analytically that the one-sided end correction for a round opening is

$$\delta_{\mathrm{in}} = \delta_{\mathrm{out}} = \frac{8}{3\pi} r_{\mathrm{h}}. \tag{2.34}$$

The radiation resistance and reactance are the real and imaginary parts of the fluid loading on the driving piston[153, p. 92]. The end correction can be seen as the reactive part of the radiation impedance[102, pp. 383–387]. An in-depth discussion of the radiation impedance for various geometries was given by Mechel[154, pp. 281–356]. Note that Eq. (2.34) is independent of the frequency since it is the limit case for $k_0 r_{\mathrm{h}} \to 0$, i.e., wavelengths larger than the hole radius, and only depends on the orifice width.
The end correction's relative contribution depends on the orifice length. It can be neglected for $h_{\mathrm{fs}} \gg r_{\mathrm{h}}$; but in the case of an infinitely thin plate, the orifice reactance only consists of its end correction term. Dickey found a good agreement between the correction obtained by Rayleigh and measured values at low sound pressure levels[155]. Ingård[133] generalised the solution for other aperture geometries by considering higher order modes at the cross-section at the orifice's edge and found that the end corrections for square and round apertures do

not show any significant differences.[10] This was later confirmed experimentally for various aperture geometries (circular, square, triangular, star-shaped, stepped oval) at a constant porosity[91].

Looking closer at Fig. 2.6, the added length is not simply a virtual extension of the cylindrical shape of the orifice mass. In reality, air is also drawn in from the radial direction. Two sources of friction losses in the vicinity of the aperture opening exist. Friction losses on the wall surrounding the orifice were accounted for by an additional resistive term by Ingård[133] as the real part of the radiation impedance for $k_0 r_\mathrm{h} \to 0$ as $0.5(k_0 r_\mathrm{h})^2$. Sivian[157] argued that the radiation resistance is negligible and proposes an additional resistance by extending the orifice length similar to the mass-end correction. This may appear as a mixture of different effects, e.g., modelling the friction losses on the surrounding wall and outside the hole by friction effects inside the orifice. There is no consensus yet on how to incorporate these effects[144],[146],[158] which might be due to the fact that their contribution in practice is rather low, where flow effects dominate the resistance.

Wall effects

The end correction in Eq. (2.34) was derived from a piston in an *infinite* baffle and assumes no constrictions of the air mass outside the orifice due to nearby walls. For a single hole in a large cavity equivalently $\delta_\mathrm{in} = \delta_\mathrm{out}$, and therefore $\delta_\mathrm{add} = \frac{16}{3\pi} r_\mathrm{h}$. However, this is invalid when the holes are close to the cavity walls, e.g., for a Helmholtz resonator with a narrow cavity. In this case, the additional air mass is reduced, and the end correction is scaled by an 'end-correction-correction' $h'_\mathrm{fs} = h_\mathrm{fs} + \delta_\mathrm{add}\psi$. There exist several solutions for ψ in the literature.

Ingård[133], by means of an inviscid theory, analytically derived the end correction for a circular perforation in a circular duct, a circular perforation in a rectangular duct, and a rectangular perforation in a rectangular duct by taking into account the effect of higher modes around the cross-section change near the orifice borders. For a circular aperture in a circular tube, he provided an approximate solution

$$\psi_\mathrm{c,c} = 1 - 1.25\xi_\mathrm{c,c} \qquad \text{with } \xi_\mathrm{c,c} = \frac{r_\mathrm{h}}{r_\mathrm{cav}}, \tag{2.35}$$

which is valid for low $\xi_\mathrm{c,c} < 0.4$. He did not provide an explicit approximate correction term for a circular aperture in a square tube. However, this value can be derived graphically as the curvature for low porosities[159], which is based on a plot from his more rigorous solution and is given here as

$$\psi_\mathrm{c,s} = 1 - 1.14\xi_\mathrm{c,s} \qquad \text{with } \xi_\mathrm{c,s} = \frac{r_\mathrm{h}}{a_\mathrm{cav}}, \tag{2.36}$$

which is also valid for $\xi_\mathrm{c,s} < 0.4$ with a_cav the distance between the aperture centre and the wall.

[10] In contrast, the sound hole shape of a violin is important, as the face sheet, i.e., top-plate, itself acts as a vibrating source, which is excited by the bowed string through the bridge. The evolution of the sound hole shape of a violin from O-shaped to C-shaped to f-shaped is due to the maximisation of radiated sound power near the outer perimeter[156].

Alternatively, the effect of cavity walls can be accounted for by the Fock[160] function[11]. Fock investigated the end correction for an infinitely thin circular perforation in a circular duct at low frequencies. The Fock function is a Taylor series expansion of the underlying Bessel function and reads

$$\psi_{\text{Fock}} = \sum_{n=0}^{12} a_n (\xi_{\text{c,c}})^n \tag{2.37}$$

with

$$\begin{aligned}
&a_0 = 1 \\
&a_1 = -1.40925 \qquad a_2 = 0 \qquad a_3 = 0.33818 \qquad a_4 = 0 \\
&a_5 = 0.06793 \qquad a_6 = -0.02287 \qquad a_7 = 0.03015 \qquad a_8 = -0.01641 \\
&a_9 = 0.01729 \qquad a_{10} = -0.01248 \qquad a_{11} = 0.01205 \qquad a_{12} = -0.00985.
\end{aligned}$$

2.3.3. Impedance of multiple orifices

The impedance of an orifice can be used to determine the impedance of the whole face sheet by considering the continuity of pressure and acoustic flux. If there is no interaction between the holes, then the impedance of the face sheet as a collection of holes is given as[29, p. 29]

$$\zeta_{\text{fs}} = \frac{\zeta_{\text{h}}}{\sigma}. \tag{2.38}$$

The porosity or open-area-ratio σ is defined as the ratio of the open-area of one orifice to its unit area $\sigma = A/(A_{\text{ref}})$. For a circular orifice in a regular square perforation pattern $\sigma = \frac{\pi r_{\text{h}}^2}{n_{\text{fs}}^2}$ where n_{fs} denotes the number of orifices per cavity and A_{cav} the cavity's cross-section. If the hole distance is approximately twice the distance from the outer holes to the cavity walls, $\sigma \approx n_{\text{fs}} \frac{\pi r_{\text{h}}^2}{A_{\text{cav}}}$. Porosities for different perforation patterns can be found in Lahiri[161, p. 24]. Neglecting interaction effects in Equation (2.38) is only valid for low porosities $\sigma < 4\,\%$, when the apertures are far apart. In this case, the holes can be treated as independent. This assumption is invalid at higher porosities because the acoustic flow through one opening affects the acoustic flow through the adjacent orifices.

The interaction effects between apertures and walls can be used to describe the interaction effect between multiple apertures in one face sheet because the effect of multiple openings above one cavity can be expressed by mirror sources that act like virtual cavity walls at the rims of each opening. Thus, the approximate solutions to model the constricting effect of the cavity walls can also be used to model the hole interaction effects. Equation (2.36) is used for example in Atalla and Sgard[147]. Based on experimental data, Nesterov[162] gave an approximate of Eq. (2.37)

$$\psi_{\text{Nesterov}} = 1 - 1.47\xi_{\text{c,c}} + 0.47\xi_{\text{c,c}}^3, \tag{2.39}$$

which is used for example to model the influence of the porosity in Ver and Beranek[163, p. 270] or Elnady[164].

Many common impedance models[146],[165],[166],[167],[168] use the correction term $\psi_{\text{Guess}} =$

[11] Note that Fock[160] introduced a correction term for the *conductance* of a hole, which is inversely proportional to its impedance. Consequently, the original function was defined as the inverse of ψ_{Fock} used here. ψ_{Fock}, as defined in Eq. (2.37) shortens the additional length.

$1 - 0.7\sqrt{\sigma}$, with Guess being the first, citing Ingård[133] as his source.[12] Special care must be taken when the apertures are not distributed homogeneously, i.e., when the distance between the holes is not equal and the distance from the holes close to the wall is not spaced away from half the distance to other holes. In this case, the interaction factor may differ for each hole and for δ_{in} and δ_{out}. A more in-depth discussion of inhomogeneous hole interactions can be found in Tayong[169], Schiller and Jones[170], or Javareshkian et al.[171].

The aforementioned hole interaction factors with $\xi = \sqrt{\sigma}$ are displayed in Fig. 2.7. Liners usually have a porosity lower than 30 %, as perforates with $\sigma > 30\,\%$ can be treated as acoustically transparent up to high frequencies[172, p. 254]. Most models show similar values in this region, except $\psi_{\text{Guess}} = 1 - 0.7\sqrt{\sigma}$. ψ_{Fock} (purple) and ψ_{Nesterov} (green) predict the strongest reduction. Note that Ingård's approximations (red and yellow) do not approach zero for a porosity of 100 % as they are only valid for porosities up to 16 %, marked with a dashed line. However, the rigorous, but not the approximate solution, of the interaction

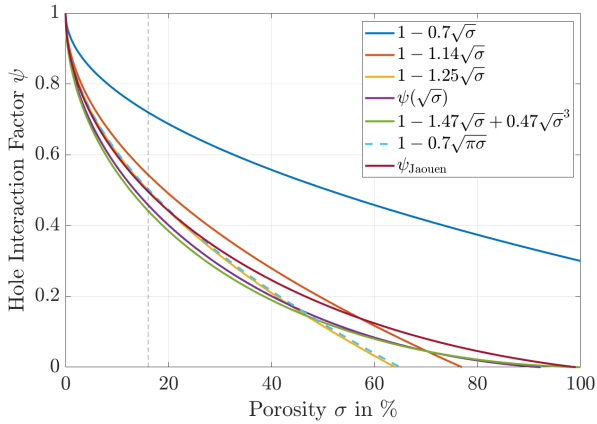

Figure 2.7.: Comparison between different hole interaction functions

effect correction by Ingård gives very similar results to the end correction as obtained by Fock[173, p. 15]. Jaouen and Bécot[174] gave a fit to Ingård's rigorous solution for a circular orifice in a square duct that is valid for the whole porosity range

$$\psi_{\text{Jaouen}} = 1 - 1.13\xi - 0.09\xi^2 + 0.27\xi^3, \text{ with } \xi = 2\sqrt{\frac{\sigma}{\pi}}. \tag{2.40}$$

2.3.4. Influence of high sound pressure level

At sufficiently large incident sound pressures, the impedance of an orifice depends on the amplitude of the acoustic particle velocity in the vicinity of the orifices, making it

[12] However, this correction term is not explicitly stated in Ingårds original paper. One possible derivation might be from the identity of the porosity given a square pattern $\sigma = \frac{\pi r_{\text{h}}^2}{s^2} = \pi\xi_{\text{c,s}}^2$ with the end correction for a circular aperture in a circular tube $\psi_{\text{Guess}} \stackrel{?}{=} \psi_{\text{c,c}}(\xi_{\text{c,s}}) = 1 - 1.25\xi_{\text{c,s}} = 1 - 1.25\sqrt{\frac{\sigma}{\pi}} \approx 1 - \sqrt{\frac{\sigma}{2}} \approx 1 - 0.7\sqrt{\sigma}$ (dashed light blue in Fig. 2.7).

nonlinear[175]. In this case, the assumptions of the linear wave equation do not hold because acoustic energy is converted into turbulent energy and heat. The sound particle velocity in the vicinity of the orifice is maximised near the Helmholtz resonance. Therefore, nonlinear effects in a Helmholtz resonator can occur at lower sound pressure levels than in a free field situation.

The nonlinear behaviour of orifices was analysed first by Sivian[157]. He interpreted the behaviour as the conversion of acoustic energy to turbulent energy. He modelled the additional nonlinear resistance by assuming an isentropic stationary flow and found acceptable agreement with his experimental data when adding this term to the linear impedance. Ingård and Labate[176] carried out Schlieren experiments to visualise the acoustic flow through openings and showed that acoustic excitation with large amplitudes leads to jets and the generation of vortex rings that detach from the openings at the frequency of the acoustic excitation. This was later confirmed by numerical simulations by Tam et al.[177]. Additionally, they confirmed that the vortex-shedding mechanism is the dominant sound dissipation mechanism at high sound pressure levels. Ingård and Labate demonstrated the existence of several possible flow regimes for given particle velocities. They also found that the reactance was reduced in addition to an increase in resistance. This was explained in a later study by Ingård[133] where he showed that the acoustically induced flow separation pushes away some of the external oscillating fluid mass. The corresponding kinetic energy is transferred into turbulent motion and finally dissipated at a certain distance from the hole. Consequently, this effect can be considered by a decrease in the face sheet reactance and an increase in the face sheet resistance. Ingård and Ising[178] used hot-wire measurement of the oscillatory flow in the orifice and derived an analytical expression of the nonlinear face sheet resistance assuming quasi-stationary flow using Bernoulli's principle $p' \simeq \rho_0 v_\mathrm{h}'^2$, where v_h' denotes the root mean square acoustic particle velocity in the orifice. Zinn[179] proposed a nonlinear resistance of Helmholtz resonators as a function of the discharge coefficient C_d. The discharge coefficient is defined as the ratio of the actual flow rate to the theoretical flow rate through the orifice. The discharge coefficient considers the jet contraction and friction losses and depends on the flow conditions as well as the orifice geometry. Typical values for sharp-edged orifices range from 0.6 to 0.8[115, p. 38]. Most models for additional nonlinear resistance are of the following type:

$$\theta_\mathrm{nl} = \kappa_\mathrm{SPL} \frac{1-\sigma^2}{\sigma C_\mathrm{d}^2} \frac{v_\mathrm{h}'}{c} \tag{2.41}$$

with Melling giving $\kappa_\mathrm{SPL} = 0.6$[144]. Elnady uses $\kappa_\mathrm{SPL} = 0.5$[164], Laly et al. use $\kappa_\mathrm{SPL} = 4/3\pi \approx 0.42$[180] whereas Motsinger and Kraft use $\kappa_\mathrm{SPL} = \frac{\kappa_i + \kappa_e}{2}$, with $\kappa_i + \kappa_e \approx 1$ for simple perforates[165]. Murray uses Eq. (2.41) with an unpublished constant κ_SPL[168]. Guess uses no empirical constants, i.e. $\kappa_\mathrm{SPL} = C_\mathrm{d} = 1$[146]. Note, that Eq. (2.41) is purely real and, therefore, neglects any nonlinear effects on the reactance. Furthermore, it depends on the face sheet porosity σ and linearly on the root-mean-square acoustic particle velocity in the vicinity of the orifice v_h'. Because the acoustic particle velocity is a function of the surface impedance $\left|v_\mathrm{h}'\right| = p'/|\zeta(v_\mathrm{h}')|$, the particle velocity and impedance must be determined via an iterative process. Using an electro-acoustical analogy and Bernoulli's principle, Park[181] gives an estimation of the root-mean-square velocity in the orifice:

$$v_\mathrm{rms}' \approx \frac{c}{\sqrt{2}} \frac{\sigma}{1-\sigma^2} \left(\sqrt{0.25 + \frac{2\sqrt{2} p_\mathrm{in}'}{\rho_0 c^2} \frac{1-\sigma}{\sigma^2}} - 0.5 \right), \tag{2.42}$$

which can be used as a starting point for the iterative procedure. p'_{in} denotes the root-mean-square incident pressure in Pascal, which in air can be calculated from the incident sound pressure level p_{dB} as $p'_{\mathrm{in}} = 2 \times 10^{-5}\,\mathrm{Pa}\; 10^{p_{\mathrm{dB}}/20}$.

Temiz et al.[182] investigated the transition from the linear to the nonlinear regime, where there are nonlinear effects, but the assumption of a stationary flow does not hold. They showed that the resistance in the transition region is proportional to the square of the amplitude of the sound velocity in the holes. This is different for regimes with strong nonlinearities where there is a linear dependency, see Eq. (2.41). They also found a dependence on the shear number Sh, which, however, rapidly disappears with increasing hole diameter. Furthermore, the effect of the sound velocity can be neglected, when $1/St_{\mathrm{d_h}} < 0.2$. This threshold is expressed by the Strouhal number on the basis of the hole diameter $St_{\mathrm{d_h}} = \frac{d_{\mathrm{h}}}{|\xi'|} = \frac{2\pi f d_{\mathrm{h}}}{|v'|}$ with $\xi' = v'/\omega$ denoting the acoustic particle deflection of a plane wave.

The sound pressure level alone is insufficient to characterise the nonlinear behaviour of orifices and, consequently, liners when excited by complex sound sources. Rice[183] found that vortices at the edges of an opening can detach if the acoustic particle deflection exceeds the orifice diameter. He observed a strong interaction of the amplitude at one frequency upon the resistance at the other frequency with a two-frequency excitation. Bodén and Fritzell found that the excitation type affects the overall acoustic behaviour[184]. Kreitzman and Jones[185] investigated the influence of various source types, such as broadband noise, multitones, and swept sine waves. They found that the relative phases and velocity ratios between different frequencies need to be considered. Roncen[186] recently revised the nonlinear impedance of acoustic liners and showed that a frequency-isolated liner impedance is insufficient in broadband excitation contexts with high sound pressure levels. He proposed a time-domain representation instead. The link between acoustic impedance and source type is a current research topic under investigation by the International Forum for Aviation Research[187],[188].

2.3.5. Influence of grazing flow

The main applications of acoustic liners are flow channels. A grazing flow changes the liner impedance – the resistance is increased, whereas the reactance decreases[189],[190],[191]. The underlying physics is still not fully understood[13] and still a great topic of debate within the acoustic liner community, especially regarding flow direction[125].

Feder and Dean[189], as well as Ingård[175] hypothesised that the grazing flow leads to the formation of a turbulent boundary layer above the opening and to velocity fluctuations in the boundary layer, which are superimposed onto the acoustic flow. Assuming that the characteristic frequency of the turbulent flow is considerably smaller than the acoustic frequency, the influence of the turbulent velocity fluctuations on the acoustic impedance is similar to that of a steady velocity through the orifices. In this case, the behaviour can be approximated with Bernoulli's law with quasi-stationary behaviour similar to the high sound pressure level case. Rodgers and Hersh[193] illustrate the overflow of openings by considering the shear layer detaching at the leading edge of the openings as a lid fixed at

[13] E.g. Hersh[192]: 'Although it is clear that a correlation exists between the resistance peaks and the local "flattening" out of the reactance, we do not understand the physical mechanism(s) causing this behaviour. The model empirical parameters need to be calibrated by a large database of impedance data.'

the leading edge that moves at the frequency of the acoustic flow. As the flow velocity increases, the mobility of the lid decreases, which impedes the acoustic volume flow through the openings. Guess[146] gives an estimation of the additional face sheet resistance due to grazing flow

$$\theta_{\mathrm{gf}} = \frac{1-\sigma^2}{\sigma}\frac{u_{\mathrm{h}}}{c} \approx \kappa_{\mathrm{gf}}\frac{1-\sigma^2}{\sigma}M_{\mathrm{gf}}, \tag{2.43}$$

where $u_{\mathrm{h}} \approx \kappa_{\mathrm{gf}} u_{\mathrm{gf}}$. $\kappa_{\mathrm{gf}} = 0.3$ is an empirical constant that links the grazing flow velocity u_{gf} with the flow velocity in the orifices u_{h}. It was determined from acoustic resistance measurements with flow by Rice et al.[183]. Kabral et al.[194] use the same expression, but with $\kappa_{\mathrm{gf}} = 0.5$.

Later, Heidelberg et al.[195] realised that the effect of the turbulent boundary layer cannot be ignored and based on new resistance measurements, proposed

$$\theta_{\mathrm{gf}} = \frac{M_{\mathrm{gf}}}{\sigma\left(2 + 1.256\ {}^{\delta^*}\!/_{d_{\mathrm{h}}}\right)} \tag{2.44}$$

with δ^* denoting the boundary layer displacement thickness. For a uniform grazing flow with no boundary layers and small porosities, Eq. (2.44) reduces to Eq. (2.43) with $\kappa_{\mathrm{gf}} = 0.5$.

Jones et al.[143] used an optimiser and their large experimental database of liner impedances at their Grazing Flow Impedance Tube and proposed to replace 1.256 with 3.32 in Eq. (2.44). Other published models usually take a modified form of Eq. (2.44) with empirically determined constants[166],[196],[197]. Using these empirical constants has the drawback that they lack physical insight, may suffer from over-fitting and are most likely dependent on the testrig and flow conditions.

Kooi and Sarin[167] investigated the effect of different boundary layer profiles by injecting air and based on in-situ measurements proposed:

$$\theta_{\mathrm{gf}} = \frac{5 - {}^{h_{\mathrm{fs}}}\!/_{d_{\mathrm{h}}}}{4}\left(9.9\frac{u^*}{f d_{\mathrm{h}}} - 3.3\right), \qquad \text{if} \begin{cases} (1) & 0.4 < {}^{h_{\mathrm{fs}}}\!/_{d_{\mathrm{h}}} < 1.6 \\ (2) & \frac{u^*}{f d_{\mathrm{h}}} > 0.2 \\ (3) & {}^{v'}\!/_{u^*} < 4. \end{cases} \tag{2.45}$$

u^* denotes the skin friction velocity that was determined by measuring the flow velocity in the vicinity of the wall using hot-wires and fitting the data to the velocity distribution in the 'law of the wall' region. The first limitation in Eq. (2.45) stems from the geometries of their liner samples, the second limitation ensures that the flow induces resistance is significant, and the third limitation restricts the applicability to cases where the grazing influence dominates over high sound pressure level effects. The drawback of Eq. (2.45) is that it involves the experimental determination of u^* which requires significantly more effort than the mean grazing flow Mach number M_{gf}.

Zhang et al.[198] numerically studied a single Helmholtz resonator with grazing flow. They confirmed that the flow in the orifice was asymmetric due to the grazing mean flow. They also found that the inflow and outflow profiles differ and depend on the turbulent boundary layer. The external boundary layer of the grazing flow creates background vorticity analogous to a lid-driven cavity and imposes a velocity scale proportional to the boundary layer friction velocity, further justifying the approach of Eq. (2.45). They identified multiple velocity scales due to turbulent boundary layer velocity fluctuations and the incident sound pressure

that is modulated by the background vorticity.

The reactance effect of the grazing flow is usually either ignored or modelled by an empirical 'end correction correction' in absence of an analytical model[167],[199],[146] such as $\delta_{\mathrm{add,gf}} = \frac{\delta_{\mathrm{add}}}{1+305M_{\mathrm{gf}}^3}$ as proposed by Rice[199]. In contrast, Kabral et al.[194] use $\chi_{\mathrm{gf}} = -0.3\,M_{\mathrm{gf}}/\sigma$.

Most impedance models rely on empirical constants to model the influence of grazing flow on the liner impedance. In addition, the overall resistance is often dominated by flow effects even under moderate grazing flow. Jones et al. evaluated the accuracy of multiple impedance models. Although the impedance without flow agreed well with the experimental data, the error was significantly higher in the grazing flow case[200]. However, these errors may also stem from imperfect liner eduction techniques, as the overall liner impedance cannot be directly measured in a grazing incidence setting. This highlights the need for better analytical modelling of the underlying physics, both, in impedance eduction and liner impedance modelling and may indicate that certain key parameters are missing in the analysis so far.

The momentum transfer from the flow to the wall may be such a key parameter that was neglected but may be a central physical mechanism that alters the liner impedance. Aurégan and Renou[201],[202] define a wall friction coefficient to consider the transfer of momentum into the lined wall induced by molecular and turbulent viscosities. Schulz et al.[124] argue that additional viscous forces arise when a flow grazes over an opening that strongly decelerates the acoustic flow through the opening, depending on the flow profile in the duct. Modelling the influence of the wall shear stress by a so-called impulse transfer impedance is still an ongoing research.

Combination of high sound pressure levels and grazing flow

Liners in aircraft engines are subject to both grazing flow and high sound pressure levels. Ingård assumes a linear additive superimposition of both effects as a first order approximation

$$\theta_{\mathrm{nl+gf}} = \frac{(1-\sigma)^2}{\sigma}\frac{|v'| + u_{\mathrm{h}}}{c}. \tag{2.46}$$

Goldman and Panton[191] showed experimentally that high sound pressure levels only affect the acoustic behaviour if $|v'|/u_* > 3$, with u_* denoting the skin friction velocity, which is linked to the turbulent wall boundary layer. Therefore, the additive superimposition is valid only above a certain threshold. Kooi and Sarin[167] found the threshold to be $|v'|/u_* > 4$, see Eq. (2.45), whereas Burgmayer[158] also gave $|v'|/u_* \approx 2-3$. Thus, flow separation occurs only when the sound particle velocity exceeds twice the wall shear stress, resulting in a change in impedance due to the periodic flow. However, this value refers to a region and is not meant as a singular threshold point. A more comprehensive overview that includes bias flow effects, was given recently by Burgmayer[158].

2.3.6. Cavity losses

Most impedance models neglect the viscothermal losses inside the cavity and use Eq. (2.24) to determine the cavity reactance. A notable exception is the model proposed by Parrott and Jones[45], who used a transfer matrix approach with an effective wavenumber based on

the Zwikker-Kosten approximation, see Eq. (2.14), to account for the viscothermal losses at the sidewalls. Kohlenberg et al.[203] consider the thermal boundary layer at the backplate and the face sheet, as well as the viscothermal losses at the wall, using the wide tube approximation Eq. (2.13).
Losses within the cavity *fluid*, i.e., excluding wall effects, can be neglected under ambient conditions because they are two orders of magnitude smaller than the losses at the walls[161, p. 130]. They become significant only at elevated pressures and temperatures.

The cavity can be viewed as a waveguide with viscothermal losses at the cavity walls with an intermediate cross-section between face sheet holes and a large duct. The predicted impedance for a generic cavity (cavity diameter $d_{\mathrm{cav}} = 5\,\mathrm{mm}$, $l_{\mathrm{cav}} = 50\,\mathrm{mm}$, $f \in [200, 2000]$ Hz) for the different approximations Eq. (2.13), Eq. (2.14) and without losses Eq. (2.24) is depicted in Fig. 2.8. The main difference is visible in the normalised resistance in Fig. 2.8a. The cavity resistance is zero if the viscothermal effects in the cavity are neglected (blue). The 'Wide Tube' (yellow) and 'Zwikker-Kosten' (purple) approximations coincide for larger shear wave numbers but differ for shear numbers below $Sh = \frac{d}{2}\sqrt{\frac{\omega}{\nu}} = 50$ with the 'Zwikker-Kosten' approximation predicting a higher resistance. Considering the viscothermal effects leads to a slightly higher reactance, barely visible in Fig. 2.8b. Note that a smaller cavity leads to smaller shear wave numbers and a larger viscothermal contribution, whereas the relative effect decreases for larger cavities. The contribution of the thermal acoustic boundary layer alone at the back wall is insignificant, except for very low shear wave numbers. A square cavity with a cross-section of $35\,\mathrm{mm} \times 35\,\mathrm{mm}$ corresponds to shear wave numbers higher than 300 for frequencies over 200 Hz. In this case, the wide tube solution yields the same results as the Zwikker-Kosten approximation.

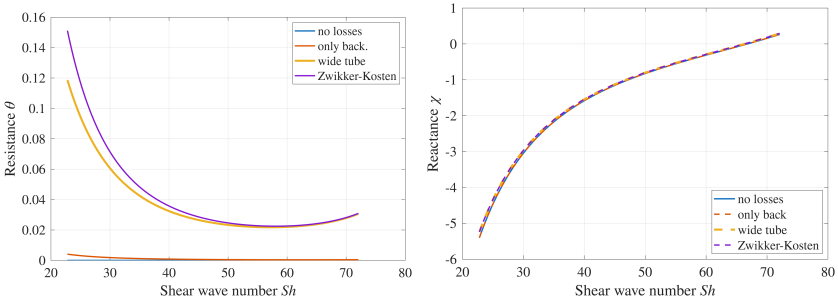

(a) Resistance (b) Reactance

Figure 2.8.: Different approximations of cavity losses for a generic cavity ($d_{\mathrm{cav}} = 5\,\mathrm{mm}$, $l_{\mathrm{cav}} = 50\,\mathrm{mm}$, $f \in [200, 2000]$ Hz)

Summed up, the face sheet and the cavity form the central elements of a Helmholtz resonator. The acoustic wave is dampened due to a viscothermal boundary layer near rigid boundaries, such as cavity walls or face sheet holes. Viscothermal effects in the cavity can be considered by incorporating the boundary layers effects in the fluid to obtain an equivalent impedance. The wide tube approximation is justified for typical cavity sizes and frequency ranges found in acoustic aircraft liners. Except for very narrow cavities, the resistive effects are small compared to that of the face sheet. Most common face sheet impedance models are based on a formulation by Crandall. Alternatively, the impedance can be described by an equivalent fluid approach that yields similar results.

Additional damping occurs when high sound pressure levels or grazing flow is present. High sound pressure levels lead to jet formation in which acoustic energy is converted to turbulent energy when the acoustic particle deflection exceeds the face sheet thickness. Most impedance models consider this behaviour based on Bernoulli's principle and differ in empirical constants. Recent research suggests that solely relying on the sound pressure level alone is insufficient, and the phase information of complex sound sources must be taken into account. Even more empiricism is involved when attempting to model the effect of grazing flow. Many impedance models treat grazing flow effects similar to high sound pressure level effects with different empirical constants that link the grazing flow velocity in the duct with the flow velocity in the face sheet hole. Other models include boundary layer effects, which are difficult to measure in the vicinity of the face sheet holes.

While viscothermal effects can be modelled accurately analytically, flow effects are much more complex and are presently only approximated with empirical coefficients, which are specific to the flow and test rig. A complicating fact is that these flow effects usually dominate over viscothermal effects when a grazing flow and high sound pressure levels are present. The development of a generally accepted face sheet model that correctly predicts these flow effects remains a major research topic in liner research; however, not the focus of this work.

2.4. Vibration of plates

Plates are thin, flat, elastic sheets with mass and bending stiffness that can vibrate. Membranes, on the other hand, are thin idealised vibrating elements with mass that support tension but inhibit no bending stiffness. The mean tension provides the linear restoring force for a membrane during out-of-plane vibration[204]. The term 'membrane' is often used imprecisely in literature[14]. Mechel[210, pp. 767–882] distinguishes between limp foils, membranes, and elastic plates. Limp foils only oppose the pressure difference between the front and back sides with their mass restraint like a piston, i.e., neglecting tension or flexural rigidity. A limp foil can still form a resonant system with a support structure, e.g., air in a back cavity.

Plates and membranes are idealised representations of reality, and hybrid forms exist in which the restoring force is due to both bending stiffness and tension, such as a prestressed plate or a thick membrane. Tensile in-plane edge loads increase the natural frequency of 'pure' plates; a strongly prestressed plate can be approximated by a tensioned membrane.[15] In this work, the flexible wall is treated as a thin isotropic plate with uniform thickness without any pretension.

A general plate behaviour of a finite plate is depicted in Fig. 2.9. The mass and coincidence region are important in building acoustics in the context of sound transmission between rooms. Owing to the small sizes of the liners compared with the walls found in buildings, only region I is relevant for this work. A low sound transmission loss indicates good excitability of a plate, which is lowest in the resonance frequency region. Therefore, the flexible wall is expected to be effective close to structural resonances.

2.4.1. Thin plate theory

The flexible wall is modelled in this thesis according to the classical thin plate theory, which is based on the Kirchhoff hypothesis[212, pp. 95–115] that states:

- transverse normals before deformation remain straight after deformation;
- transverse normals rotate such that they remain perpendicular to the mid-surface after deformation;
- transverse normals are not elongated during deformation.

Consequently, transverse strains are zero and transverse stresses are omitted. The bending stresses and strains are proportional to the distance from the mid-surface. The maximum stress is on the surface of the plate.

Given these assumptions, the governing equation of motion of a thin vibrating plate due to an external pressure difference Δp between the two faces of the plate can be expressed as[213, pp. 139–215]:

$$D\nabla^4 w_\mathrm{p} + \rho_\mathrm{p} h_\mathrm{p} \frac{\partial^2 w_\mathrm{p}}{\partial t^2} = \Delta p \tag{2.47}$$

[14] Foils or plates are sometimes called membranes, even though they are not prestressed[205],[206],[207],[208],[209]. In the case of 'membrane absorbers', the 'membrane' is being treated as a single mass and, therefore, as a piston[116, p. 246]. Other ambiguous expressions for either membranes or plates are 'films' or 'panels', which confuscate establishing a comprehensive literature.

[15] Contrary, sufficient compressive edge loads buckle the plate[204, p. 208].

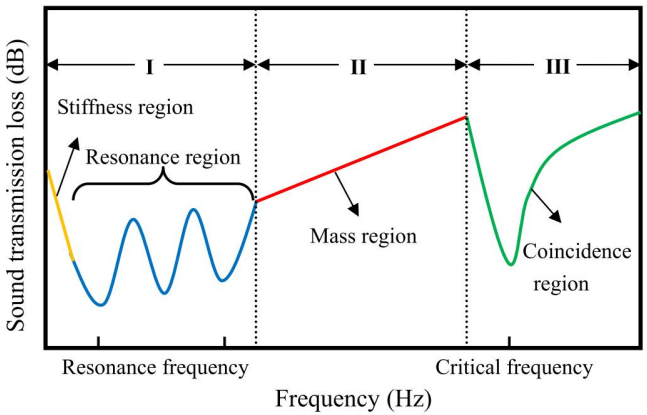

Figure 2.9.: General plate behaviour. This image is protected by copyright; reprinted with permission of Elsevier Ltd. from[211]

with D denoting the flexural rigidity, ∇ the gradient, w_p the plate displacement, and ρ_p and h_p the plate density and thickness, respectively. A detailed derivation of Eq. (2.47) is omitted here for the sake of brevity but can be found in textbooks by Timoshenko[214], Szilard[215] or Reddy[212]. The flexural rigidity or bending stiffness D for a thin plate including mechanical losses expressed in the mechancal loss coefficient η is given by

$$D = (1 + \mathrm{i}\eta)EI = (1 + \mathrm{i}\eta)\frac{Eh_\mathrm{p}^3}{12(1 - \nu_\mathrm{p}^2)}, \tag{2.48}$$

where E denotes Young's modulus, I denotes the area moment of inertia and ν_p denotes Poisson's ratio, which links transverse strain with axial strain[216, p. 153]. The mechanical loss coefficient or mechanical damping measures the degree to which a material dissipates kinetic energy.

Assuming a harmonic excitation $\Delta p = \Delta\hat{p}\,\mathrm{e}^{\mathrm{i}\omega t}$ and a harmonic response $w_\mathrm{p} = \hat{w}_\mathrm{p}\,\mathrm{e}^{\mathrm{i}\omega t}$, Eq. (2.47) can be expressed as

$$D\nabla^4\hat{w}_\mathrm{p} - \mathrm{i}\omega^2\rho_\mathrm{p}h_\mathrm{p}\hat{w}_\mathrm{p} = \Delta\hat{p} \tag{2.49}$$

$$\nabla^4\hat{w}_\mathrm{p} - k_\mathrm{b}^4\hat{w}_\mathrm{p} = \frac{\Delta\hat{p}}{D} \tag{2.50}$$

with

$$k_\mathrm{b} = \sqrt{\omega}\sqrt[4]{\frac{\rho_\mathrm{p}h_\mathrm{p}}{D}} \tag{2.51}$$

denoting the free bending wave number[216, p. 55].[16] For free vibrations, Eq. (2.49) reduces to

$$\nabla^4\hat{w}_\mathrm{p} - k_\mathrm{b}^4\hat{w}_\mathrm{p} = 0. \tag{2.52}$$

[16]Note, that unlike the phase speed in air c, $c_\mathrm{b} = \omega/k_\mathrm{b} \propto \sqrt{\omega}$ is dispersive. The propagating waveforms are distorted because the high-frequency components propagate faster than the low-frequency components.

The plate displacement amplitude $\hat{w}$ can be expressed as the infinite sum of mode shapes ψ_{mn} and their corresponding modal amplitudes w_{mn}[204, pp. 200–234]

$$\hat{w}_\mathrm{p}(x,y) = \sum_m^\infty \sum_n^\infty w_{mn}\psi_{mn}. \tag{2.53}$$

A finite plate's motion is bounded by its edges. The boundary condition at the edge Γ_p is commonly idealised either as:

- Free, no loads
- Simply supported, no moment or displacement ($w_\mathrm{p}|_{\Gamma_\mathrm{p}} = \frac{\partial^2 w_\mathrm{p}}{\partial r^2}|_{\Gamma_\mathrm{p}} = 0$)
- Clamped, no edge rotation or displacement ($w_\mathrm{p}|_{\Gamma_\mathrm{p}} = \frac{\partial w_\mathrm{p}}{\partial r}|_{\Gamma_\mathrm{p}} = 0$)

The boundaries of many plates in engineering practice are intermediate between clamped and simply supported. The boundary conditions have a stronger impact for lower eigenmodes and smaller plates, because a larger portion of the free plate area is in the vicinity of the edges. The boundary conditions between clamped and simply supported at one edge can be represented by spring or load considerations. However, in these cases, analytical solutions are rarely, if ever, available.

In the following subsections, the complex transfer impedances of the circular and rectangular plates are derived, which form a central part of the analytical model of the resonator system. The plate impedance can be derived by assuming a harmonic plate response to the incoming plane wave acoustic excitation. To calculate the one-dimensional complex plate transfer impedance, see Eq. (2.18), the mean plate velocity v_avg due a incoming plane wave pressure difference Δp needs to be determined. This includes a modal decomposition of the plate deflection in the appropriate coordinate system. The corresponding eigenfrequencies are important as a first estimate where the plate is easily excitable. The analytically determined eigenmodes can be compared with the numerically determined operating deflection shapes to better understand the plate's vibration inside the resonator system.

2.4.2. Circular plates

The mode shapes of a circular plate simply supported or clamped at its edge at the outer radius R_p can be obtained from Eq. (2.52) in polar coordinates with

$$\nabla^4 = \nabla^2\nabla^2 = \left(\frac{\partial^2}{\partial r^2} + \frac{1}{r}\frac{\partial}{\partial r} + \frac{1}{r^2}\frac{\partial^2}{\partial \varphi^2}\right)\left(\frac{\partial^2}{\partial r^2} + \frac{1}{r}\frac{\partial}{\partial r} + \frac{1}{r^2}\frac{\partial^2}{\partial \varphi^2}\right) \tag{2.54}$$

as

$$\psi(r,\varphi,m,n) = \left[J_m\left(\frac{\lambda_{m,n} r}{R_\mathrm{p}}\right) - \frac{J_m(\lambda_{m,n})}{I_m(\lambda_{m,n})} I_m\left(\frac{\lambda_{m,n} r}{R_\mathrm{p}}\right)\right]\cos(m\varphi) \tag{2.55}$$

with J_m denoting the Bessel function of the first kind of order m and I_m the modified Bessel function of the first kind of order m[204, pp. 209–210]. m is an azimuthal modal index that denotes the number of nodal diameters. n is a radial modal index that denotes the number of nodal circles. $\lambda_{m,n}$ is a frequency parameter distinct for each mode, and the angle is denoted by φ.

The frequency parameter $\lambda_{m,n}$ differs for each modal index and boundary condition. According to Leissa[217, pp. 7–10], the frequency parameter for a simply supported plate $\lambda_{m,n,\mathrm{s}}$ can be calculated using the transcendental equation

$$\frac{J_{m+1}(\lambda_{m,n,\mathrm{s}})}{J_m(\lambda_{m,n,\mathrm{s}})} + \frac{I_{m+1}(\lambda_{m,n,\mathrm{s}})}{I_m(\lambda_{m,n,\mathrm{s}})} = \frac{2\lambda_{m,n,\mathrm{s}}}{1-\nu_\mathrm{p}}, \tag{2.56}$$

whereas for a clamped plate the frequency parameter $\lambda_{m,n,\mathrm{c}}$ is defined as

$$J_m(\lambda_{m,n,\mathrm{c}})I_{m+1}(\lambda_{m,n,\mathrm{c}}) + I_m(\lambda_{m,n,\mathrm{c}})J_{m+1}(\lambda_{m,n,\mathrm{c}}) = 0. \tag{2.57}$$

The corresponding eigenfrequencies can be calculated by linking the frequency parameter with the bending wave number as $\lambda_{m,n} = k_\mathrm{b} R_\mathrm{p}$, as[217, pp. 7–10]

$$f_{m,n} = \frac{\lambda_{m,n}}{2\pi R_\mathrm{p}^2}\sqrt{\frac{D}{\rho_\mathrm{p}}} = \frac{\lambda_{m,n}^2}{2\pi R_\mathrm{p}^2}\sqrt{\frac{E h_\mathrm{p}^2}{12\rho_\mathrm{p}(1-\nu_\mathrm{p})}}. \tag{2.58}$$

The first four radial solutions for λ, for simply supported and clamped edges are presented in Table 2.1. The first radial eigenfrequency of a simply supported plate $f_{m,\mathrm{s}}$ is approximately half of the first radial eigenfrequency of a clamped plate $f_{m,\mathrm{c}}$. This factor rapidly decreases for higher order modes. Consequently, the edge condition affects the eigenfrequencies more strongly for lower radial modes. For illustration purpose, the first nine mode shapes of a

Table 2.1.: First four radial solutions of Eq. (2.56) and Eq. (2.57)

m	1	2	3	4
$\lambda_{m,\mathrm{s}}$	2.221	5.455	8.612	11.760
$\lambda_{m,\mathrm{c}}$	3.197	6.306	9.439	12.577
$f_{m,\mathrm{s}}/f_{m,\mathrm{c}}$	0.48	0.75	0.83	0.88

circular clamped plate are displayed in Fig. 2.10. Plate modes with a higher azimuthal mode order ($m > 1, n$) have a mean displacement averaged over the whole plate close to zero because of equally strong displacements in both out-of-plane directions. The mean displacement is not exactly zero due to edge effects at the boundaries and is highest for the plate mode (1,1), followed by (3,1) and (2,1).

Following Škvor[218, p. 60], Bongard et al.[219] and Jimenez et al.[220, p. 133] the displacement of a clamped plate for forced oscillations and only considering axially symmetrical modes can be written from Eq. (2.49) as

$$\hat{w}_\mathrm{p} = -\frac{\Delta\hat{p}}{k^4 D} + AJ_0(k_\mathrm{b} r) + BI_0(k_\mathrm{b} r). \tag{2.59}$$

The two constants A and B can be determined by the clamped boundary conditions

$$\hat{w}_\mathrm{p}|_{r=R_\mathrm{p}} = 0 \qquad \longrightarrow \qquad \frac{\Delta\hat{p}}{k_\mathrm{b}^4 D} = AJ_0(k_\mathrm{b}R_\mathrm{p}) + BI_0(k_\mathrm{b}R_\mathrm{p}) \tag{2.60}$$

$$\frac{\partial\hat{w}_\mathrm{p}}{\partial r}|_{r=R_\mathrm{p}} = 0 \qquad \longrightarrow \qquad 0 = -AJ_1(k_\mathrm{b}R_\mathrm{p}) + BI_1(k_\mathrm{b}R_\mathrm{p}) \tag{2.61}$$

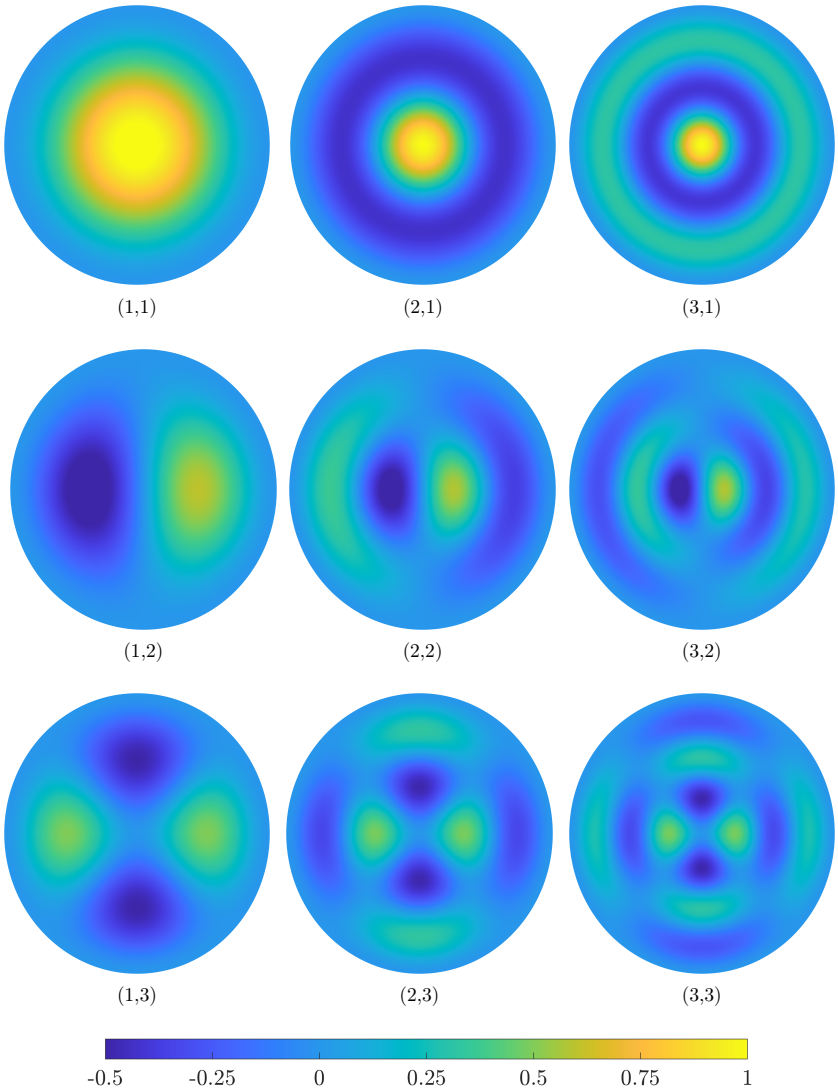

Figure 2.10.: First three radial and azimuthal mode shapes of a clamped circular plate

as

$$A = \frac{\Delta\hat{p}}{k_\mathrm{b}^4 D} \frac{I_1(k_\mathrm{b}R_\mathrm{p})}{J_0(k_\mathrm{b}R_\mathrm{p})I_1(k_\mathrm{b}R_\mathrm{p}) + J_1(k_\mathrm{b}R_\mathrm{p})I_0(k_\mathrm{b}R_\mathrm{p})} \tag{2.62}$$

$$B = \frac{\Delta\hat{p}}{k_\mathrm{b}^4 D} \frac{J_1(k_\mathrm{b}R_\mathrm{p})}{J_0(k_\mathrm{b}R_\mathrm{p})I_1(k_\mathrm{b}R_\mathrm{p}) + J_1(k_\mathrm{b}R_\mathrm{p})I_0(k_\mathrm{b}R_\mathrm{p})}. \tag{2.63}$$

The mean displacement $\hat{w}_{\mathrm{avg,p}}$ can be calculated as

$$\begin{aligned}\hat{w}_{\mathrm{avg,p}} &= \frac{1}{\pi R_{\mathrm{p}}^2}\iint_S \hat{w}_{\mathrm{p}}(r)\mathrm{d}A_{\mathrm{p}} \\ &= \frac{\pi R_{\mathrm{p}}^2 \Delta\hat{p}}{k_{\mathrm{b}}^4 D}\frac{J_2(k_{\mathrm{p}}R_{\mathrm{p}})I_1(k_{\mathrm{p}}R_{\mathrm{p}}) - J_1(k_{\mathrm{p}}R_{\mathrm{p}})I_2(k_{\mathrm{p}}R_{\mathrm{p}})}{J_0(k_{\mathrm{p}}R_{\mathrm{p}})I_1(k_{\mathrm{p}}R_{\mathrm{p}}) + J_1(k_{\mathrm{p}}R_{\mathrm{p}})I_0(k_{\mathrm{p}}R_{\mathrm{p}})}\end{aligned} \tag{2.64}$$

with A_{p} denoting the plate surface area. A detailed derivation of Eq. (2.64) can be found in the Appendix in Section A.1. Assuming a plane wave excitation of the plate

$$\Delta\hat{p}_{\mathrm{avg}} = \frac{1}{\pi R_{\mathrm{p}}^2}\iint_{A_{\mathrm{p}}} \Delta\hat{p}\,\mathrm{d}A_{\mathrm{p}} = \Delta\hat{p}, \tag{2.65}$$

the equivalent impedance of a circular clamped plate can be calculated as

$$\begin{aligned}Z_{p,c} &= \frac{\Delta\hat{p}}{\hat{v}_{\mathrm{avg,p}}} = \frac{\Delta\hat{p}}{\mathrm{i}\omega\hat{w}_{\mathrm{avg,p}}} \\ &= -\frac{\mathrm{i}\omega\rho_{\mathrm{p}}h_{\mathrm{p}}}{\pi R_p^2}\frac{J_0(k_{\mathrm{p}}R_{\mathrm{p}})I_1(k_{\mathrm{p}}R_{\mathrm{p}}) + J_1(k_{\mathrm{p}}R_{\mathrm{p}})I_0(k_{\mathrm{p}}R_{\mathrm{p}})}{J_2(k_{\mathrm{p}}R_{\mathrm{p}})I_1(k_{\mathrm{p}}R_{\mathrm{p}}) - J_1(k_{\mathrm{p}}R_{\mathrm{p}})I_2(k_{\mathrm{p}}R_{\mathrm{p}})}.\end{aligned} \tag{2.66}$$

Note, that the plate vibration velocity v_{p} is the time derivative of the deflection w_{p} and for harmonic signals it yields $v_{\mathrm{p}} = \frac{\partial w_{\mathrm{p}}}{\partial t} = \mathrm{i}\omega w_{\mathrm{p}}$. The complex impedance of a clamped circular plate with multiple resonances in the low-frequency range ($E = 16\,\mathrm{MPa},\ \rho_{\mathrm{p}} = 1080\,\mathrm{kg/m^3},\ \nu = 0.48, \eta = 0.1,\ h_{\mathrm{p}} = 0.3\,\mathrm{mm},\ R_{\mathrm{p}} = 30\,\mathrm{mm}$) is plotted in Fig. 2.11. The corresponding specific mass reactance $\omega\rho_{\mathrm{p}}h_{\mathrm{p}}$ is displayed as a dashed line for reference. Note that the resistance and reactance increase non-monotonous with frequency, even

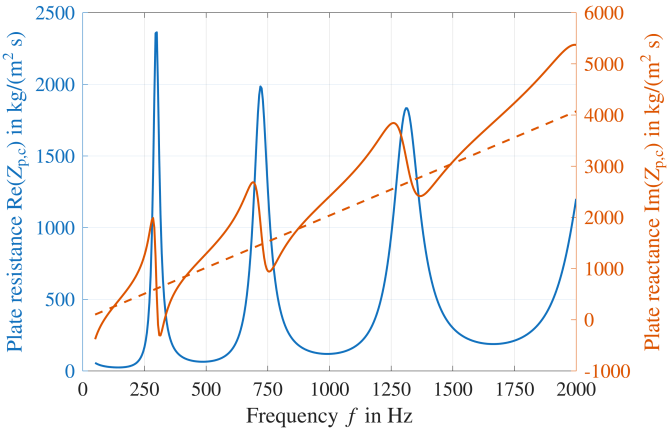

Figure 2.11.: Impedance of a clamped circular plate showing multiple higher order modes, dashed: specific mass reactance $\omega\rho_{\mathrm{p}}h_{\mathrm{p}}$

though the overall behaviour is dominated by resonances. Because the impedance is a measure of the complex resistance to an external acoustic pressure, the plate is excitable

more easily at low frequencies where the impedance is small.

The frequencies where the plate reactance (solid) intersects with the specific mass reactance alone near 150 Hz, 400 Hz, 850 Hz and 1500 Hz are also the minima of the second derivative of the reactance and can be thought of resonance frequencies because the overall impedance is low and the plate is expected to vibrate the strongest. The frequencies of the local resistance minima are slightly higher. Antiresonances between the resonances are visible as local resistance maxima with a negative slope of the reactance e.g. at 290 Hz, 730 Hz or 1350 Hz. The plate is expected to be very stiff at these frequencies because the absolute impedance is very high.

2.4.3. Rectangular plates

The harmonic displacement w_p of a rectangular plate in Cartesian coordinates can be obtained from Eq. (2.52) with

$$\nabla^4 = \left(\frac{\partial^4}{\partial x^4} + 2\frac{\partial^4}{\partial x^2 \partial y^2} + \frac{\partial^4}{\partial y^4} \right). \tag{2.67}$$

Using the separation of variables and assuming a harmonic response yields

$$w_\mathrm{p}(x,y,t) = X(x)Y(y)T(t) \tag{2.68}$$

$$= \sum_m^\infty \sum_n^\infty w_{mn}\psi_{mn}\,\mathrm{e}^{\mathrm{i}\omega t}. \tag{2.69}$$

The treatment of rectangular plate vibration requires more effort than the circular case, because there are twenty-one possible combinations of free, simply supported, and clamped edge conditions[204, pp. 219–221]. In most cases, eigenfrequencies are determined only approximately by numerical means such as the Ritz-Rayleigh method or the finite element method. Leissa[217] summarised solutions for all 21 cases. By using the hamiltonian symplectic dual method, Xing and Liu[221] were able to obtain the exact vibration solutions for rectangular plates with any combination of clamped and simply supported edges (including all four edges clamped). This thesis is restricted to plates that are either clamped or simply supported on all four sides.

Warburton[222] presented the first comprehensive collection of solutions for rectangular plates. He used the Ritz-Rayleigh method with deflection functions as the product of beam functions using a separation of variables $\psi_{mn}(x,y) = X_m(x)Y_n(y)$, where $X_m(x)$ and $Y_n(y)$ are chosen as the fundamental beam mode shapes with the same boundary conditions. Thus, the waveforms of vibrating plates and beams are assumed to be similar, so that they are the product of the characteristic functions for two beams with the same boundary condition.

The modal solution of a rectangular plate simply supported on all edges with length a and width b has a sinusoidal mode shape:

$$\psi_{mn,\mathrm{s}}(x,y) = X_{m,\mathrm{s}}(x)Y_{n,\mathrm{s}}(y) = \sin\left(\frac{m\pi x}{a}\right)\sin\left(\frac{n\pi y}{b}\right) \tag{2.70}$$

The corresponding eigenfrequencies are[204, p. 215]

$$f_{m,n} = \frac{\lambda_{mn}^2}{2\pi a^2}\sqrt{\frac{D}{\rho_\mathrm{p} h_\mathrm{p}}} \tag{2.71}$$

with the frequency parameter for a rectangular simply supported plate being

$$\lambda_{mn} = \pi\sqrt{m^2 + n^2\left(\frac{a}{b}\right)^2}. \tag{2.72}$$

The modal solution of a rectangular plate with clamped edges on all sides can be written as[223]

$$\psi_{mn}(x,y) = X_m(x)Y_n(y) \tag{2.73}$$

with

$$X_m(x) = \left[\cosh\left(\frac{\lambda_m}{a}x\right) - \cos\left(\frac{\lambda_m}{a}x\right)\right] - \frac{\cosh(\lambda_m) - \cosh(\lambda_m)}{\sinh(\lambda_m) - \sin(\lambda_m)}\left[\sinh\left(\frac{\lambda_m}{a}x\right) - \sin\left(\frac{\lambda_m}{a}x\right)\right] \tag{2.74}$$

$$Y_n(y) = \left[\cosh\left(\frac{\lambda_n}{b}y\right) - \cos\left(\frac{\lambda_n}{b}y\right)\right] - \frac{\cosh(\lambda_n) - \cosh(\lambda_n)}{\sinh(\lambda_n) - \sin(\lambda_n)}\left[\sinh\left(\frac{\lambda_n}{b}y\right) - \sin\left(\frac{\lambda_n}{b}y\right)\right], \tag{2.75}$$

where λ_m and λ_n satisfy

$$\cosh(\lambda_\square)\cos(\lambda_\square) = 1 \tag{2.76}$$

with $\square$ as a placeholder for m, n, which can be solved numerically. The first five values are given in Table 2.2. Approximate solutions of the corresponding eigenfrequencies for

Table 2.2.: First five solutions of Eq. (2.76)

i	1	2	3	4	5
λ_i	4.7300	7.8532	10.9956	14.1372	17.2788

clamped plates are given by Warburton, Leissa and Blevins[222],[217],[204]. The first three modal solutions of a generic rectangular plate clamped on all edges are plotted in Fig. 2.12. The mean displacement is close to zero if one mode order is even, e.g., (1,2) or (2,3). Following Sung and Jan[223] the equivalent transfer impedance of a rectangular plate to a plane incident wave can be obtained in the following way: Inserting the modal sum of the plate displacement in Eq. (2.69) into the plate differential equation Eq. (2.47) with the gradient in Cartesian coordinates in Eq. (2.67) yields

$$D\sum_{m,n=1}^{\infty} w_{mn}\nabla^4\psi_{mn}\,\mathrm{e}^{\mathrm{i}\omega t} - \rho_\mathrm{p} h_\mathrm{p}\omega^2\sum_{m,n=1}^{\infty} w_{mn}\psi_{mn}\,\mathrm{e}^{\mathrm{i}\omega t} = \Delta\hat{p}\,\mathrm{e}^{\mathrm{i}\omega t}. \tag{2.77}$$

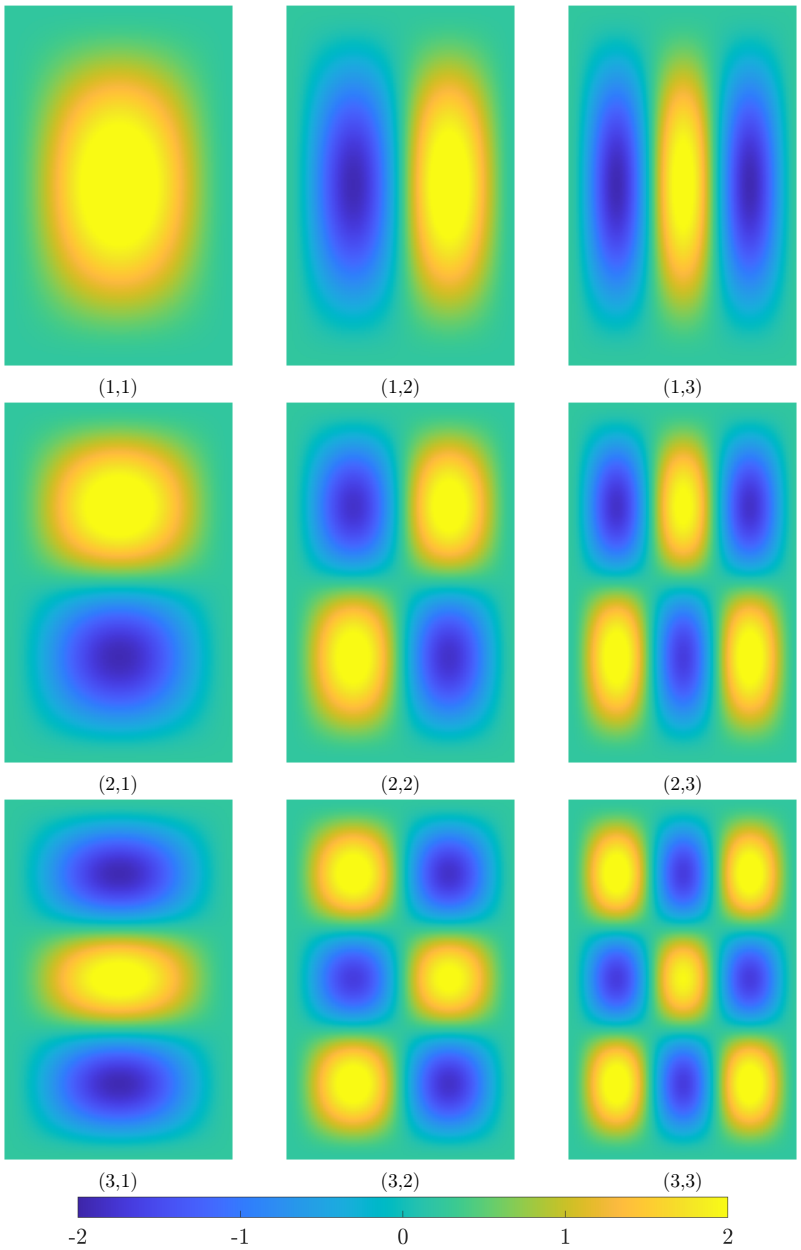

Figure 2.12.: First three vertical and lateral mode shapes of a generic rectangular plate ($a/b = 15/26$)

The time dependence can be cancelled out, since the differential equation must be true for all times t. Next, Eq. (2.77) is multiplied by arbitrary mode functions ψ_{ij} and integrated over the plate surface to yield

$$D \sum_{m,n=1}^{\infty} \sum_{i,j=1}^{\infty} w_{mn} \iint_A \psi_{ij} \nabla^4 \psi_{mn} \mathrm{d}A - \rho_\mathrm{p} h_\mathrm{p} \omega^2 \sum_{m,n=1}^{\infty} \sum_{i,j=1}^{\infty} w_{mn} \iint_A \psi_{ij} \psi_{mn} \, \mathrm{d}A = \sum_{m,n=1}^{\infty} \iint_A \Delta\hat{p} \, \psi_{ij} \, \mathrm{d}A, \quad (2.78)$$

exploiting the fact that the mode amplitudes w_{mn} are constant over the plate surface. By choosing the shape functions as defined in Eq. (2.70) as $\psi_{mn} = X_m(x)Y_n(y)$ and $\psi_{ij} = X_i(x)Y_j(y)$ one obtains:

$$D \sum_{m,n=1}^{\infty} \sum_{i,j=1}^{\infty} w_{mn} \left[\int_0^a \int_0^b \frac{\partial X_m^4}{\partial x^4} Y_n X_i Y_j + 2 \frac{\partial X_m^2}{\partial x^2} \frac{\partial Y_n^2}{\partial y^2} X_i Y_j + \frac{\partial Y_n^4}{\partial y^4} X_m X_i Y_j \right] \mathrm{d}x \, \mathrm{d}y - \rho_\mathrm{p} h_\mathrm{p} \omega^2 \sum_{m,n=1}^{\infty} \sum_{i,j=1}^{\infty} w_{mn} \int_0^a \int_0^b X_m Y_n X_i Y_j \mathrm{d}x \, \mathrm{d}y = \sum_{i,j=1}^{\infty} \int_0^a \int_0^b \Delta\hat{p} X_i Y_j \mathrm{d}x \, \mathrm{d}y. \quad (2.79)$$

The eigenfunctions $X_m(x), Y_n(y), X_i(x), Y_j(y)$ are orthogonal to each other[223] in a sense that for arbitrary chosen indices p, q

$$\left. \begin{array}{l} \int_0^a X_p X_q \, \mathrm{d}x = \int_0^a \frac{\partial X_p^2}{\partial x^2} \frac{\partial X_q^2}{\partial x^2} \, \mathrm{d}x = 0 \\ \int_0^b Y_p Y_q \, \mathrm{d}y = \int_0^b \frac{\partial Y_p^2}{\partial y^2} \frac{\partial Y_q^2}{\partial y^2} \, \mathrm{d}y = 0 \end{array} \right\} \text{, if } p \neq q. \quad (2.80)$$

Therefore, Eq. (2.79) can be written as:

$$D \sum_{m,n=1}^{\infty} w_{mn} \int_0^a \int_0^b \left[\frac{\partial X_m^4}{\partial x^4} X_m Y_n^2 + 2 \frac{\partial X_m^2}{\partial x^2} X_m \frac{\partial Y_n^2}{\partial y^2} Y_n + X_m^2 \frac{\partial Y_n^4}{\partial y^4} Y_n \right] \mathrm{d}x \, \mathrm{d}y - \rho_\mathrm{p} h_\mathrm{p} \omega^2 \sum_{m,n=1}^{\infty} w_{mn} \int_0^a \int_0^b X_m^2 Y_n^2 \, \mathrm{d}x \, \mathrm{d}y = \sum_{m,n=1}^{\infty} \int_0^a \int_0^b \Delta\hat{p} X_m Y_n \, \mathrm{d}x \, \mathrm{d}y. \quad (2.81)$$

Assuming a plane wave excitation, i.e. $\Delta\hat{p}$ independent of x, y, Eq. (2.81) can be expressed as

$$D \sum_{m,n=1}^{\infty} w_{mn} \left[I_1 I_2 + 2 I_3 I_4 + I_5 I_6 \right] - \rho_\mathrm{p} h_\mathrm{p} \omega^2 \sum_{m,n=1}^{\infty} w_{mn} I_2 I_6 = \Delta p \sum_{m,n=1}^{\infty} I_7 I_8 \quad (2.82)$$

with the abbreviations I_i:

$$I_1 = \int_0^a X_m \frac{\partial^4 X_m}{\partial x^4} \mathrm{d}x \qquad I_2 = \int_0^b Y_n^2 \mathrm{d}y \tag{2.83}$$

$$I_3 = \int_0^a X_m \frac{\partial^2 X_m}{\partial x^2} \mathrm{d}x \qquad I_4 = \int_0^b Y_n \frac{\partial^2 Y_n}{\partial y^2} \mathrm{d}y \tag{2.84}$$

$$I_5 = \int_0^b Y_n \frac{\partial^4 Y_n}{\partial y^4} \mathrm{d}y \qquad I_6 = \int_0^a X_m^2 \mathrm{d}x \tag{2.85}$$

$$I_7 = \int_0^a X_m \mathrm{d}x \qquad I_8 = \int_0^b Y_n \mathrm{d}y. \tag{2.86}$$

Eq. (2.82) can be rearranged to determine the modal amplitudes

$$w_{mn} = \frac{\Delta\hat{p} I_7 I_8}{D(I_1 I_2 + 2I_3 I_4 + I_5 I_6) - \rho_\mathrm{p} h_\mathrm{p} \omega^2 I_2 I_6}. \tag{2.87}$$

The resonance frequencies ω_{mn} can be determined from Eq. (2.87) when w_{mn} reaches infinity in the absence of damping ($D \in \mathbb{R}$), i.e., by setting the denominator to zero, which leads to:

$$\omega_{mn} = \sqrt{\frac{D(I_1 I_2 + 2I_3 I_4 + I_5 I_6)}{\rho_\mathrm{p} h_\mathrm{p} I_2 I_6}} \tag{2.88}$$

The resonance frequencies obtained from Eq. (2.88) agree closely with eigenfrequencies obtained with the Ritz-Rayleigh method[223].

The mean plate velocity can be determined by inserting Eq. (2.87) into Eq. (2.69)

$$\hat{v}_\mathrm{avg,p} = \frac{1}{A_\mathrm{p}} \int_0^a \int_0^b \frac{\partial w_\mathrm{p}}{\partial t} \,\mathrm{d}x\,\mathrm{d}y \tag{2.89}$$

$$= \frac{\mathrm{i}\omega}{A_\mathrm{p}} \int_0^a \int_0^b \sum_{m=1}^{\infty} \sum_{n=1}^{\infty} w_{mn} X_m(x) Y_n(y) \,\mathrm{d}x\,\mathrm{d}y \tag{2.90}$$

$$= \mathrm{i}\omega \Delta\hat{p} \sum_{m=1}^{\infty} \sum_{n=1}^{\infty} \frac{(I_7 I_8)^2}{\rho_\mathrm{p} h_\mathrm{p} (\omega_{mn}^2 - \omega^2) I_2 I_6} \tag{2.91}$$

and using Eq. (2.88) as a substitution.

Knowing that $Z_\mathrm{p} = {}^{\Delta p}/_{\hat{v}_\mathrm{avg,p}}$, see Eq. (2.18), one finally obtains the mean plate impedance of a clamped rectangular plate excited by a plane wave as

$$Z_\mathrm{p,r} = \left[\mathrm{i}\omega \sum_{m=1}^{\infty} \sum_{n=1}^{\infty} \frac{(I_7 I_8)^2}{\rho_\mathrm{p} h_\mathrm{p} (\omega_{mn}^2 - \omega^2) I_2 I_6} \right]^{-1}. \tag{2.92}$$

Huang et al.[224] obtained the same plate impedance[17] of a clamped rectangular plate,

[17] Note, that the resulting impedance from Huang et al. Eq. (2.93) has to be multiplied with the plate area $A_\mathrm{p} = ab$ to obtain a specific acoustic impedance (Unit: $\frac{\mathrm{kg}}{\mathrm{m^2 s}}$).

however expressed in a different way:

$$Z_{\mathrm{p,r}} = \left[\mathrm{i}\omega ab \int_0^a \int_0^b \left(\sum_{m=1}^{\infty} \sum_{n=1}^{\infty} \frac{\int_0^a \int_0^b X_m Y_n \,\mathrm{d}x \,\mathrm{d}y}{D(I_1 I_2 + 2I_3 I_4 + I_5 I_6 - \rho_{\mathrm{p}} h_{\mathrm{p}} \omega^2 I_2 I_6} X_m Y_n \right) \mathrm{d}x \,\mathrm{d}y \right]^{-1} \tag{2.93}$$

The complex impedance of a rectangular clamped plate with multiple resonances in the low-frequency range ($E = 16\,\mathrm{MPa}$, $\rho_{\mathrm{p}} = 1080\,\mathrm{kg/m^3}$, $\nu = 0.48$, $\eta = 0.1$, $h_{\mathrm{p}} = 0.3\,\mathrm{mm}$, $a = 15\,\mathrm{mm}$, $b = 26\,\mathrm{mm}$) is plotted in Fig. 2.13. The effect of material damping η is displayed by comparing small mechanical damping ($\eta = 0.01$, dashed) with moderate material damping ($\eta = 0.1$, solid). The introduction of mechanical damping reduces the peak strength of the reactance and resistance around the antiresonance region. The maximum resistance peaks are higher for the material with less mechanical damping, whereas the overall resistance increases as expected. Therefore, the acoustic response of a material with sufficient mechanical losses can be expected to be less dominated by small-bandwidth peaks and more overall damping. The resistance and reactance values for the moderate mechanical damping are in the same order of magnitude as in the clamped circular case, depicted in Fig. 2.11. Similar to the clamped circular plate the local minima of the resistance are at frequencies similar to the minima of the second derivative of the reactance, and the negative slopes coincide with the local maxima at the resistance. However, the impedance of the rectangular plate is dominated by one region around 1000 Hz with multiple resonances.

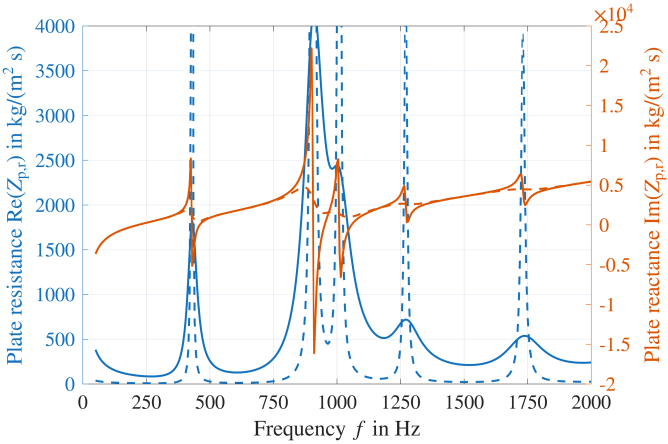

Figure 2.13.: Impedance of two generic rectangular clamped plates with small ($\eta = 0.01$, dashed) and moderate mechanical damping ($\eta = 0.1$, solid)

In summary, the acoustic response of a flexible plate due to a plane pressure difference can be described by a plate transfer impedance that considers higher-order plate modes. The plate transfer impedance was derived in this section for a circular and a rectangular clamped plate. This assumes a thin plate with no pretension, small deflections, and no interaction with a nearby sound pressure field, e.g., due to an attached closed cavity. Clamped plates have higher eigenfrequencies than simply supported plates. The difference is stronger for lower

plate modes. Only uneven plate modes are expected to vibrate significantly because even modes have a mean displacement close to zero. The corresponding eigenmode depictions can help to analyse operating deflection shapes of the flexible wall inside a resonator system. Mechanical losses inside the plate lead to increased broadband damping.

2.5. Plate-Cavity-Interactions

Acoustic–structure interaction refers to the dynamic interplay between acoustic pressure fields and flexible structures.[18] The extensive research field of plate-cavity-interactions, sometimes referred to as acoustoelasticity, is briefly touched here to better understand and interpret the behaviour of the resonator concept. For an in-depth discussion, the interested reader is referred to the relevant literature[102, pp. 63–91, 608–688][225, pp. 95–125][226][153, pp. 114–178][227].

The equations of motion of such a system is usually modelled using the rigid-wall modes of the cavity and the modes of the wall[228],[229]. Fahy and Gardinio[226, pp. 404–408] investigated the fluid structure interaction using a one-dimensional system of a piston coupled to a waveguide. They showed analytically that for low frequencies or short cavities, $k_0 l_{\mathrm{cav}} << 1$, the effect of the cavity is that of a stiffening spring[19], which is sometimes called the Helmholtz stiffening effect. The fluid's effect on the piston is stronger for lighter pistons and shorter cavities. Additionally, they investigated the three-dimensional problem of a flexible plate in a rectangular cavity using finite element methods (FEM)[226, pp. 496–503]. They found flexible mode shapes similar to those of the uncoupled case, except at frequencies where the eigenfrequencies of the flexible plates were similar to the cavities eigenfrequencies, in which the cavity and plate eigenmodes were perturbed so that the pressure distribution and the plate modes conformed. Also using FEM, Gorman et al.[230] studied the acoustic-structural coupling of a circular clamped plate backed by a cylindrical cavity and found that strong coupling exists if the eigenfrequencies of the acoustic and structural subsystems are close and if the appropriate mode shapes are similar. They conclude that the corresponding mode shapes are neither acoustic nor structural in this case, and studying only uncoupled subsystems is insufficient.

A characteristic phenomenon in acoustoelasticity is eigenvalue veering, which involves energetic exchange between eigenmodes and affects the forced response of the system. Leissa[231] coined the term when investigating the natural frequencies of a rectangular clamped membrane. Vidoli and Vestroni[232] investigated veering phenomena in a DDOF and continuous system using perturbation analysis. They found that in an undamped coupled system, a veering region exists in which the inherent eigenvalues approach but never cross and then diverge. A sketch of the behaviour is presented in Fig. 2.14. The eigenvalues remained unchanged outside this veering region compared with the isolated case. However, in this veering region, they found a smooth transition between the eigenvector components, with no 'pure' eigenvectors. The separation between the two system frequency curves at their closest point of approach indicates the coupling strength. A similar effect was found by Fahy and Schofield[233] who theoretically investigated the coupling of a Helmholtz resonator attached to a closed cavity. They noted that when the eigenmode of the uncoupled resonator is tuned to the natural frequency of an isolated room mode,

[18] Rayleigh[152, p. 151] investigated the effect of fluid loading of an infinite space, thus, without a cavity, on a circular piston, which lead to the derivation of the end correction δ in Eq. (2.34).

[19] Similar to the mechanical model of a Helmholtz resonator Eq. (2.22)

two coupled modes are excited with eigenfrequencies on either side of the initial common frequency. This is also sometimes described as frequency splitting, i.e., when an acoustic mode approaches a structural resonance, the coupled system undergoes two distinct modes, with one frequency lower than that of the original structural or acoustic mode and the other frequency higher. Hambric explained these phenomena with mass-controlled and stiffness-controlled boundaries[153, p. 124]. Similar diverging resonance patterns can be found in a plate resonator[234],[235], which is a cavity connected to a duct with a flexible plate.

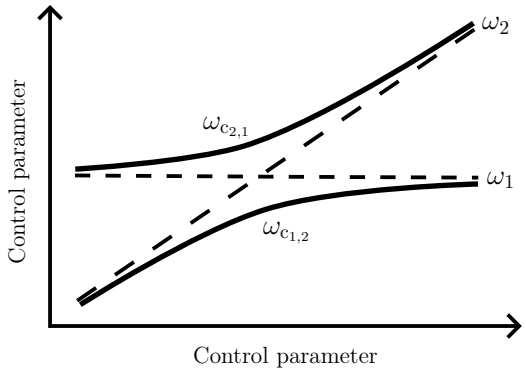

Figure 2.14.: Schematic eigenvalue veering. The system's coupled eigenfrequencies $\omega_{c_{1,2}}$ and $\omega_{c_{2,1}}$ differ from the individual uncoupled eigenfrequencies ω_1 and ω_2 in the intersection region.

Davis[236] investigated the coupling of several flexible structures and acoustic enclosures with non-dimensional quantities. He defined a coupling factor to express the coupling strength between two component modes

$$\eta_{jk} = \left[1 + \left(\frac{\omega_j - \omega_k}{2}\right)^2 \frac{1}{\beta_{jk}}\right]^{-1}, \tag{2.94}$$

which depends on the separation of the component mode frequencies $\omega_j - \omega_k$. η_{jk} varies between zero and one with high values indicating high interactions. β_{jk} is a coupling parameter that determines the extension of the mode interaction and depends on the physical and geometrical properties of the subsystems. For a simply supported plate as one side of a rectangular enclosure he gives

$$\beta_{jk} = \frac{\rho_0 c^2}{\rho_\mathrm{p} h_\mathrm{p} l_\mathrm{cav}} \Psi_{jk} \tag{2.95}$$

with Ψ_{jk} denoting the natural propensity of a structural mode to couple with a given acoustic mode, which can be expressed analytically for a simply supported plate, but not for a clamped plate[236].

Since $\beta_{jk} \propto 1/(h_\mathrm{p}, l_\mathrm{cav})$, stronger coupling is expected for thin plates and shallow cavities. Note that both the structural eigenfrequency in Eq. (2.71), as well as the coupling factor Eq. (2.95) depend on the plate thickness h_p. Consequently, a thinner plate inhibits lower eigenfrequencies and stronger coupling between the plate and the surrounding fluid when the

corresponding eigenfrequencies coincide. A similar effect can be found for the cavity depth l_{cav}, which affects both the coupling strength in Eq. (2.95) and the cavity or Helmholtz resonance Eq. (2.27), respectively.

Briefly summarised, strong coupling between structures and cavities is expected when

- *structural and cavity eigenfrequencies are similar,*
- *with thinner plates,*
- *or shallow cavities.*

In this case, the individual resonances approach each other but do not intersect in a so-called veering region. When both isolated eigenfrequencies agree, one frequency shifts to higher frequencies, whereas the other shifts to lower frequencies. In contrast, the coupled system is expected to behave similarly to a simple sum of the subsystems far from these veering regions.

2.6. Literature review of Helmholtz resonators with flexible elements

The classic Helmholtz resonator model only considers rigid cavity walls. However, compliant walls have been found to alter the Helmholtz resonance. Photiadis[237] investigated the effect of a compliant wall and found that the resonance frequency is lowered due to a reduced stiffness. Zaikin and Rudenko[238] analytically studied a Helmholtz resonator with a movable wall, which they modelled as a rigid piston, and found an additional resonance as well as a lowered Helmholtz resonance. The latter was also found by Griffiths et al.[239], who drilled holes in poro-granular shells to form an elastic Helmholtz resonator to enhance the low-frequency absorption of a porous material. Pishvar and Harne[240] identified that the coupling between the Helmholtz resonator and the compliant wall was strongly affected by the wall thickness and material. Cui and Harne[241],[242] found that compliant walls strongly affect the overall resonance behaviour towards broadband damping due to a coupling among the wall deflection, inner pressure field, and air motion in the opening.

Another type of flexible Helmholtz resonator does not involve structural vibration but seeks adaptivity by changing either the orifice using an iris, 'accordion' structure[243], or an origami folding structure to change the cavity size[244],[245]. This tunability can also be achieved using a pressurised stiff membrane[246]. In a different context, Helmholtz resonators can be combined with plates to attenuate structure-borne sound or sound transmission as Plate-Acoustic-Metamaterials or Membrane-Acoustic-Metamaterials[247],[248],[249],[250],[251].

There exist four types of basic vibration systems: strings, bars, membranes, and plates. Whereas strings and bars are one-dimensional, membranes and plates are their two-dimensional counterparts. Strings and membranes require tension to restore force, whereas bars and plates have flexural rigidity. However, a string cannot effectively radiate sound or be excited by an incoming sound wave due to the small radiation area.[20] Therefore, to the best of the author's knowledge, Helmholtz resonators are not combined with strings in

[20] That is why strings in string instruments are usually attached to a plate, e.g., the top-plate of a violin through a bridge or the soundboard of a piano to transmit the acoustic energy to the latter rather than radiate themselves.

damping systems. However, the other three basic vibrational elements can be combined with a Helmholtz resonator for additional structural resonances. This section provides a brief overview of Helmholtz resonators coupled with these flexible elements.

Helmholtz resonators coupled with bars

Bars can be coupled to Helmholtz resonators in energy harvesters. In this case, the Helmholtz resonator enhances the beam vibration, converting the kinetic energy into electrical power[252]. New manufacturing techniques, such as laser micro-cutting, can be used to cut micro-slits into a face sheet to form a cantilever beam that is fixed on one side and able to move freely on the other three sides[253],[254]. The acoustic effect is a combination of the airflow in the micro-slits and the beam vibration. This can be modelled as a Helmholtz resonator coupled to a beam. The thinner the slits, the stronger the coupling effect[255]. Hoppen et al.[256] showed that the beam adds a damping peak to the system, which can be modelled with Newton's second law of motion and finite element methods. They observed strong coupling when the beam's eigenfrequencies coincide with the Helmholtz resonance frequency. If the uncoupled system has the same resonance frequencies, the coupled system exhibits two distinct resonance frequencies that are close but shifted towards lower and higher frequencies. The coupling strength was also found to be stronger for a large area and small values of the cantilever mass and cavity volume. The coupling is weak when the uncoupled resonance frequencies are far apart. Their simplified analytical model was only valid in the weak coupling regime.

Helmholtz resonators coupled with membranes

Membranes can be combined with a Helmholtz resonator by swapping the rigid back wall with a flexible membrane. Hu et al.[257],[258] considered two analytical lumped element modelling approaches to describe the MDOF system. First, by treating the membrane as an equivalent piston and second as a concentrated mass with both approaches comparing favourably to finite element simulations. Zhang et al.[259] used this model in a piping system with multiple resonators as bandfilters for sound attenuation. They also investigated the sound scattered by the membrane at the back using finite element analysis. Park et al.[260] modelled the system as a lumped element system with a modal description of the membrane similar to a kettledrum with an air-vent. They experienced some difficulties in validation with the vibrometers because the membrane tension rapidly deviated from the initial value. Domingo-Roca et al.[261] investigated an additively manufactured system of multiple Helmholtz resonators with a membrane as the backplate. They compared their modelling based on Hu's work to finite element simulations and experimental results with good agreement. They considered different membrane tensions, which were experimentally determined by fitting the tension to the eigenfrequency determined using a scanning laser vibrometer. Unconventionally, Chen and Park[262] determined the mechanical properties of human skin with a Helmholtz resonator and an elastic membrane by comparing it to the effect of an elastic foundation on a membrane.

The membrane can also be used to subdivide the cavity. Zhu et al.[263] showed that a second resonant peak can be obtained by inserting a membrane with a small rigid mass in the middle. The additional mass alters the vibrational modes and enables high displacements, which is often used in membrane acoustic metamaterials[264]. To make it even more

sophisticated, this platelet may be implemented as a ring with an air-hole in the middle, forming a Helmholtz resonator with a perforated-membrane-face sheet[265],[266],[267]. An overview of these and other types of metamaterials can be found in Ma and Sheng[149]. Svetgoff[268] investigated different membrane configurations inside resonators. He found a strong influence on the position of the membrane inside the resonator and obtained multiple resonances by subdividing the membrane. The stiffness of electroactive polymers changes when a high voltage (kV) is applied. This can be used to adapt the resonant frequency of a membrane, which can be combined with a Helmholtz resonator to form an adaptive liner[269],[270],[271]. An additional damping mechanism is introduced when the rigid backplate is changed to a compliant backplate with a piezoelectric transducer. The proposed system can then be used as an acoustic energy harvester[272],[273],[274].

Researchers have also investigated the effect of membranes as flexible sidewalls to couple different Helmholtz resonators. This approach was pioneered by Griffin et al.[275], who demonstrated that coupling between two resonators can lead to additional transmission loss peaks. They concluded that the membrane provided coupling and alteration of the resonator cavity volume. They developed a mechanical system with lumped elements to predict the transmission loss by modelling the membrane as a piston vibrating only in its first mode. Zhao et al.[276],[277] extended the concept by modelling a similar parallel-coupled system using Green's functions and included higher membrane modes in the process. They found that the additional transmission loss peaks were distinct from the uncoupled resonances and were strongly linked to the membrane stiffness. However, the presence of a grazing flow seemed to negate coupling benefits. Mi and Yu[278] combined two Helmholtz resonators, a circular membrane and a U-shaped duct acting as a Herschel-Quincke tube, to create a sophisticated MDOF resonator. The tensioned membrane was implemented as a flexible backplate for two Helmholtz resonators attached to the same waveguide. They proposed an analytic model based on travelling plane waves and a modal expansion approach of the membrane and compared their transmission loss with that of finite element simulations. Apart from the subsystem resonances (Helmholtz resonance, membrane resonance and Herschel-Quincke resonance), they found an additional low-frequency transmission loss peak, which they attributed to the structural-acoustic coupling. Liu et al.[279] coupled Helmholtz resonators with a piezoelectric composite sheet to construct an acoustic energy harvester. The diaphragm was excited by the phase difference between adjacent Helmholtz resonators with different resonance frequencies.

The performance of resonator systems with membranes is highly sensitive to the tension applied to the membrane. Unfortunately, it is difficult to control and maintain tension over a long period of time; for example, tension could change as time passes or due to temperature or humidity changes. The requirement for accurate and uniform tension also adds complexity to the fabrication process[264]. To overcome these drawbacks, plates can be used instead of membranes.

Helmholtz resonators coupled with plates

Additional damping can be obtained by swapping the rigid backplate with a flexible plate, similar to the membrane case. Horowitz et al.[280],[281] tried to adjust the Helmholtz resonance frequency by substituting a rigid back wall with a piezoelectric composite diaphragm coupled to a passive electrical shunt network. The lumped plate impedance was

modelled based on the static deflection of a clamped plate with radius R

$$Z_{\mathrm{p,H}} = R_{\mathrm{eq}} + \mathrm{i}\omega M_{\mathrm{eq}} + \frac{1}{\mathrm{i}\omega C_{\mathrm{eq}}} \tag{2.96}$$

with $C_{\mathrm{eq}}, M_{\mathrm{eq}}, R_{\mathrm{eq}}$ denoting the equivalent compliance, mass, and resistance and κ an empirically determined constant to account for mechanical losses inside the plate and at non-rigid boundaries. Higher order plate modes are neglected. The mass ratio between the mass of the air in the perforated face sheet and the plate was found to be a good indicator of the coupling strength. The additional resonance can be tuned by adjusting the electrical shunt network connected to the flexible plate. Kim et al.[274] used a similar Helmholtz resonator with an electric backplate as an energy harvester. They expressed the equivalent mechanical mass and stiffness of the rectangular plate with length a, width b, thickness h_{p}, and density ρ_{p} as $M_{\mathrm{eq}} = 0.25\rho_{\mathrm{p}}A_{\mathrm{p}}h_{\mathrm{p}}$ and $C_{\mathrm{eq}} = \frac{4\lambda^4 bD}{\pi^2 a^3}$, where D denotes the flexural rigidity and λ the frequency parameter as introduced in Eq. (2.71). Li et al[282] investigated a similar model with finite element simulations. A Helmholtz resonator with a flexible endplate without electric components was investigated by Nudehi et al.[207],[283],[284],[285]. The plate was modelled with an acoustic receptance H that relates a pressure change with the plate's displaced volume as

$$H = \sum_{n=1}^{\infty} \frac{\kappa_n}{(1+\mathrm{i}\eta)\omega_n^2 - \omega^2} \tag{2.97}$$

with κ_n denoting not disclosed constant coefficients obtained from plate geometry and material properties and ω_n the eigenfrequency for each mode n. They accounted for high sound pressure levels by a cubic nonlinearity in the plate model and a hardening-spring characteristic in the fundamental mode. They later optimised the system for small cavities or high transmission losses with an inhomogeneous plate thickness. Oblak et al.[286] developed a fully coupled analytical model of a Helmholtz resonator with a flexible backplate in a heavy fluid, including evanescent waves and thick plates. They validated their model using finite element simulations.

The perforated face sheet itself can vibrate if the sound excitation is sufficiently high and the perforated plate is sufficiently flexible, e.g. very thin. In this case, the perforated face sheet is the flexible part of the Helmholtz resonator. This can lead to additional structural damping but also to decreased overall absorption because the relative velocity of the air inside the holes is decreased, which leads to less wall friction[287],[288],[289]. In conventional liners, the honeycomb structure underneath limits the vibrating plate size and usually suppresses plate vibrations.[21] Lee et al.[290] neglected the effect of the porosity and modelled a flexible micro-perforated panel based on the modal analysis solution of the classical plate equation coupled with the acoustic wave equation in the cavity. They theoretically and experimentally showed that the flexibility adds a resonance (and antiresonance) to the system, which can be tuned using appropriate material and geometry parameters. For example, flexible resonances that added absorption around 700 Hz were observed for a micro perforated plate with a density of $1000\,\mathrm{kg/m^3}$ (e.g. rubber) of dimensions $10\,\mathrm{cm} \times 10\,\mathrm{cm} \times 3\,\mathrm{mm}$. The acoustic behaviour of the combined movement of the air and the plate can be modelled as a parallel connection between the impedance of the plate and the holes[291]. A special case of a flexible face sheet was presented by Hossain et al.[292] who investigated a plate-valve resonator where the air

[21] The first resonance of a simply supported aluminium plate with dimensions $5\,\mathrm{mm} \times 5\,\mathrm{mm} \times 0.1\,\mathrm{mm}$ is approximately 20 kHz; calculated using Eq. (2.71).

channel size of the perforation was affected by plate vibrations. Additional resonators can be attached to alter the flexible perforated plate structural behaviour[293].

Flexible plates have also been investigated as a mean of coupling multiple resonator chambers. Knobloch et al.[294],[295],[296],[297] replaced the rigid side walls of a liner segment with flexible walls to couple cavities and subsequently enable broadband damping. They found that coupling similar Helmholtz resonators does not excite the flexible wall due to a lack of pressure difference. Therefore, in their studies, active cells with a connection to the duct were coupled with inactive cells by flexible walls. They proved that the concept of integrating flexible walls is beneficial for low-frequency broadband damping both with and without grazing flow. Liu et al.[298] investigated two distinct Helmholtz resonators coupled through a flexible sidewall. They modelled the system using an electromechanical analogy of a Y-type circuit. The impedance of a rectangular clamped plate is calculated using mode superposition theory:

$$Z_\mathrm{p} = \left(\mathrm{i}\omega \sum_{m=1}^{M} \sum_{n=1}^{N} \frac{\left(\int_0^a \int_0^b X_m Y_n \,\mathrm{d}x \,\mathrm{d}z \right)^2}{\rho_\mathrm{p} h_\mathrm{p} ab(\omega_{mn}^2 - \omega) \int_0^a \int_0^b X_m^2 Y_n^2 \,\mathrm{d}x \,\mathrm{d}z} \right)^{-1}, \tag{2.98}$$

which is based on the same derivation as Eq. (2.92).

The flexible plate can be integrated into a Helmholtz resonator to subdivide the cavity. Zhao and Fan[299] placed a flexible plate distanced behind a microperforated plate to obtain low-frequency-damping. The acoustical properties of the plates were not modelled but were entirely educed from vibrometer measurements. Sanada and Tanaka[300] constructed a DDOF resonator comprising a perforated plate and two cavities coupled via a clamped circular plate. They modelled the system by combining lumped elements of the air in the perforated plate, cavities, and the equivalent impedance of the flexible panel. The impedance of the panel was derived from a modal approach and space averaging of the plate velocity, but it was restricted to the first radial plate mode as

$$Z_\mathrm{p} = \frac{\pi R_\mathrm{p}^2}{B} \left(\frac{1}{\mathrm{i}\omega} C_{\mathrm{eq},1} + \mathrm{i}\omega M_{\mathrm{eq},1} \right) \text{ with} \tag{2.99}$$

$$B = \left(2\pi \int_0^{R_\mathrm{p}} \psi(r) r \,\mathrm{d}r \right)^2, \tag{2.100}$$

$$C_{\mathrm{eq},1} = D 2\pi \int_0^{R_\mathrm{p}} \frac{\partial \psi(r)^4}{\partial r^4} \psi(r) r \,\mathrm{d}r, \tag{2.101}$$

$$M_{\mathrm{eq},1} = \rho_\mathrm{p} h_\mathrm{p} 2\pi \int_0^{R_\mathrm{p}} \psi^2(r) r \,\mathrm{d}r. \tag{2.102}$$

ψ denotes the plate eigenfunctions, see Eq. (2.55); D the flexural rigidity, see Eq. (2.48); and h_p the plate thickness. The resonator's fundamental characteristics were investigated using dimensionless parameters. To achieve broadband attenuation, they suggested a lightweight panel with a loss factor as high as possible and a perforated plate with high porosity. However, they did not model the resistance of the resonator in the perforated front plate or in the cavity but determined the resistance experimentally. A similar plate model impedance was used by Kohlenberg et al.[203]. Mizukoshi and Takahashi[301] calculated the

plate impedance as a parallel circuit of radial orthogonal modal impedances as

$$Z_{\mathrm{p}}^{-1} = \sum_{m=1}^{\infty} Z_{\mathrm{p},m}^{-1} \text{ with} \tag{2.103}$$

$$Z_{\mathrm{p},m} = {}^{p}/_{v A_{\mathrm{p}}} = \mathrm{i}\omega\rho_{\mathrm{p}}\tilde{n}_m + \frac{1}{\mathrm{i}\omega}\rho_{\mathrm{p}}\tilde{n}_m\omega_m^2, \tag{2.104}$$

$$\tilde{n}_m = \iint \psi(r)^2 \mathrm{d}A_{\mathrm{p}} / \left(\iint \psi(r) \mathrm{d}A_{\mathrm{p}}\right)^2 \tag{2.105}$$

and checked their results with numerical simulations and experimental data, although no direct comparison between the methods were made. Zhou and Yu[302] investigated a Helmholtz resonator with a flexible intermediate plate with variable thickness to enhance broadband damping using the Wentzel-Kramer-Brillouin method. Liu et al.[303] used two flexible plates inside a Helmholtz resonator – one as a subdividing wall and the other as a flexible backplate. Their modelling was based on a Lagrange formulation of the potential and kinetic energy of the coupled system. This resonator cell was then integrated into a resonator system with multiple resonators to obtain a transmission loss of more than 350 dB. Unfortunately, these values were not verified with experimental data in their study.

In summary, there is a large scientific interest in combining Helmholtz resonators with flexible elements to obtain low-frequency and broadband damping. Helmholtz resonators can be combined with bars, membranes, and plates to change the face sheet, subdivide the cavity, alter the backplate, or couple different resonators. These mechanical elements have been found to add resonances and change the Helmholtz resonance frequency. They are usually modelled using finite element methods, or electroacoustic analogies with an equivalent mechanical mass and stiffness of the flexible element. These models are often restricted to one dominant structural mode or rely on empirical coefficients. Systems with membranes can be tuned easily by altering the membrane tension. However, a drawback is that special care must be taken to ensure that this tension can withstand time and changes in ambient conditions. Plates are more robust in this sense because their elasticity stems from their flexural rigidity. Most research on these novel damping systems has been conducted in a normal-incidence case without considering grazing flow. This has limited many concepts to be put into practice as liners so far.

This thesis aims to bridge that gap by presenting an analytical model that considers all relevant effects based on a combination of published models including higher order plate modes. The literature review suggests that finite element simulations are suitable for this problem; therefore, the concept is also investigated numerically. In agreement with many presented studies, the liner concept is tested in a normal incidence tube to investigate the basic principles. Additionally, its practical acoustic damping potential is measured in a grazing incidence test rig with grazing flow and high sound pressure levels.

3. Analytical Model

This chapter presents an impedance model of a Helmholtz resonator with a flexible wall (FXW). Analytical models have the benefit of explicitly showing dependencies between parameters and the model behaviour and they are usually faster than numerical models without the need for any proprietary software. The proposed impedance model of a Helmholtz resonator with a flexible wall is based on the theory presented in Chapter 2 and consists of two parts:

$$\zeta_{\mathrm{FXW}} = \zeta_{\mathrm{fs}}(\text{face sheet}, p'_{\mathrm{in}}, M_{\mathrm{gf}}) + \zeta_{\mathrm{cav}}(\text{main cavity, plate, back cavity}) \tag{3.1}$$

The face sheet impedance ζ_{fs} is modelled by an equivalent fluid model, which is extended to nonlinear behaviour, as introduced in Section 2.3. The cavity impedance ζ_{cav} including the flexible plate is determined by waveguide theory, which connects the different elements, assuming plane wave propagation inside the resonator. Viscothermal losses near the cavity walls are included by approximations introduced in Section 2.3.6. The impedance of the flexible plate Z_{p} is modelled as an equivalent impedance that considers higher-order plate modes, which was introduced in Section 2.4.
Equation (3.1) assumes that the face sheet and the cavity and flexible plate behave independently. This is reasonable when the flexible plate is far away from the perforate, where any detached vortex due to high sound pressure or grazing flow has decayed. The model does not consider large displacements or pretension during manufacturing or due to static pressure differences between the main and the back cavity due to grazing flow. A schematic resonator with a flexible intermediate wall is depicted in Fig. 3.1.

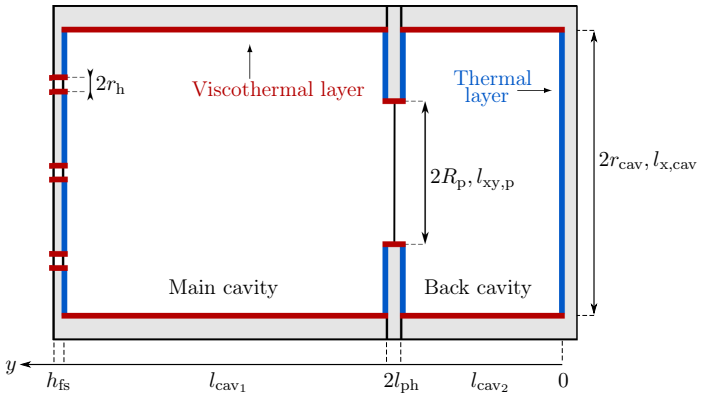

Figure 3.1.: Sketch of a circular Helmholtz resonator with a flexible plate inside a plate holder and a second cavity

3.1. Face sheet impedance

The face sheet is modelled based on the equivalent fluid approach, as introduced in Eq. (2.32) and Eq. (2.33). Laly et al. extended the model of Atalla and Sgard to include the effects of high sound pressure amplitudes[180]. Kubo et al.[187] recently compared different nonlinear impedance models, where the extended equivalent fluid model from Laly et al. was found to be in close agreement with the experimental results under high sound pressure levels. Burgmayer[158] extended the model to incorporate the effect of grazing flow using the empirical end correction of Guess[146]. The face sheet impedance is expressed as

$$\zeta_{\mathrm{fs}} = \mathrm{i}\frac{k_0 h_{\mathrm{fs}}}{\sigma}\frac{\tilde{\rho}_{\mathrm{e}}}{\rho_0}. \tag{3.2}$$

The factor $\frac{1}{\sigma}$ transforms the impedance of one hole into the impedance of the entire face sheet, as discussed in Section 2.3. All viscothermal and nonlinear effects are captured in the effective density $\tilde{\rho}_{\mathrm{e}}$, which for circular holes can be expressed as

$$\tilde{\rho}_{\mathrm{e}} = \alpha_\infty \rho_0 \left(1 + \frac{\sigma\sigma_{\mathrm{t}}}{\mathrm{i}\omega\alpha_\infty\rho_0}\sqrt{1 + \frac{\mathrm{i}4\rho_0\omega\mu\alpha_\infty^2}{\sigma^2\sigma_{\mathrm{t}}^2 r_{\mathrm{h}}^2}}\right). \tag{3.3}$$

Following Burgmayer[158, pp. 102–105], the normalised fluid resistance σ_{t} including high sound pressure and grazing flow effects can be expressed as:

$$\sigma_{\mathrm{t}} = \frac{8\mu}{\sigma r_{\mathrm{h}}^2} + \frac{\rho_0 c}{h_{\mathrm{fs}}}\frac{1-\sigma^2}{\sigma}\cdot\begin{cases} \frac{\beta\left|v'_{\mathrm{h}}\right|}{\pi C_{\mathrm{d}}^2} & \text{if } u_{\mathrm{gf}} = 0 \quad \text{(i.e. no grazing flow)} \\ \left(\frac{\kappa_{\mathrm{SPL}}\left|v'_{\mathrm{h}}\right|}{\pi C_{\mathrm{d}}^2} + \kappa_{\mathrm{gf}} M_{\mathrm{gf}}\right) & \text{if } \left|v'_{\mathrm{h}}\right| > 2u_* \text{ (i.e. transition regime)} \\ \kappa_{\mathrm{gf}} M_{\mathrm{gf}} & \text{if } \left|v'_{\mathrm{h}}\right| \leq 2u_* \text{ (i.e. grazing flow dominates)} \end{cases} \tag{3.4}$$

In Eq. (3.4) a distinction between different flow regimes is made, as explained in Section 2.3.5. High sound pressure levels only lead to an impedance change if the root-mean-square acoustic velocity in the holes v'_{h} exceeds twice the skin friction velocity u_* due to a grazing low. For $\left|v'_{\mathrm{h}}\right| \leq 2u_*$, both the presence of the grazing flow and high sound pressure level add to the face sheet resistance. For $\left|v'_{\mathrm{h}}\right| > 2u_*$ the overflow dominates the resistance and the periodic flow is almost ineffective[158, pp. 102–105].

$\frac{8\mu}{\sigma r_{\mathrm{h}}^2}$ in Eq. (3.4) stems from the resistance of small holes at low frequencies, see Eq. (2.29). The second term represents nonlinear effects of high sound pressure levels and is similar to Eq. (2.41). $\kappa_{\mathrm{SPL}} = 1.6$ is an empirical constant from Laly et al.[180] for high sound pressure level effects. $\kappa_{\mathrm{gf}} = 0.3$ is an empirical constant for grazing flow effects from Rice et al.[183]. The discharge coefficient is assumed to be $C_{\mathrm{d}} = 0.76$ as proposed by Motsinger and Kraft[165, p. 180]. α_∞ denotes the effective tortuosity that is expressed as the effective length of the orifice's fluid volume, normalised by the perforate thickness as

$$\alpha_\infty = 1 + \frac{\delta_{\mathrm{add}}}{h_{\mathrm{fs}}}. \tag{3.5}$$

The reactive end correction is expressed as

$$\delta_{\mathrm{add}} = 2\kappa\frac{8}{3\pi}r_{\mathrm{h}}\psi_{\mathrm{Fock}}\psi_{\mathrm{nl}}. \tag{3.6}$$

$\kappa = 4/3$ is an empirical constant from Maa and Laly et. al[145],[180]. The factor $\frac{8}{3\pi} r_\mathrm{h}$ accounts for the reactive part of the radiation impedance and is based on Eq. (2.34). The hole and wall interactions are accounted for by ψ_Fock, see Eq. (2.37). ψ_nl decreases the correction length with increasing particle velocity in the orifice due to high sound pressure levels and grazing flow and can be expressed as[145],[180]

$$\psi_\mathrm{nl} = \frac{1}{1 + \frac{|v_\mathrm{h}'|}{\sigma c}} \frac{1}{1 + 305 M_\mathrm{gf}^3}. \tag{3.7}$$

The presented face sheet model incorporates viscothermal effects in the face sheet holes as well as resistance and reactance changes due to high sound pressure levels and grazing flow. The individual contributors are similar to existing models from the literature, introduced in Section 2.3. Care has been taken to choose established empirical constants from the literature to ensure a general applicability.

3.2. Cavity impedance including the flexible wall

The proposed model of the cavity impedance is an adaptation and extension of the impedance model of a Helmholtz resonator with a flexible wall developed by Kohlenberg et al.[203]. The inclusion of viscothermal effects at the cavity walls is based on the wide-tube solution presented in Section 2.1.2.

The following workflow is used to calculate the impedance of the cavity, including the flexible plate: The starting point is the rear wall of the cavity ($y = 0$) where the wall is sound-hard and the wall admittance is zero. Hence, the normal incidence impedance only consists of the thermal boundary layer (marked with blue lines in Fig. 3.1)

$$\zeta_\mathrm{bl,th} = (1 - \mathrm{i}) \frac{\sqrt{Pr}}{k_0 \delta_\nu (\gamma - 1)}, \tag{3.8}$$

where γ is the heat capacity ratio, $\delta_\nu = \sqrt{2\nu/\omega}$ is the thickness of the acoustic boundary layer, Pr is the Prandtl number and ν the kinematic viscosity[108]. Note that the effect of the viscous boundary layer at the back wall can be neglected because the wall-parallel component of the particle velocity, which would have to be decelerated by the friction effects, vanishes in front of the hard rear wall of the cavity[106, pp. 181–185].

The lateral boundary layers in the cavity also modify the normalised wave impedance of the cavity sound field, which is defined as the ratio between acoustic pressure and wall-parallel particle velocity, divided by $\rho_0 c$ and averaged over the cavity's cross section[106]

$$w_\mathrm{cav} = \left[\frac{k_\mathrm{cav}}{k_0} \left(1 - \frac{(1 - \mathrm{i})}{2} \frac{U_\mathrm{cav}}{A_\mathrm{cav}} \delta_\nu \right) \right]^{-1}. \tag{3.9}$$

This impedance is transformed spatially inside the cavity. This step considers the one dimensional wave propagation in y-direction in the cavity and the effect of the lateral viscous and thermal boundary layers (marked with red lines in Fig. 3.1). The presence of the viscothermal boundary layers leads to a modified wavenumber for the almost plane waves travelling back and forth in the cavity. The corresponding wavenumber for wide

tubes, see Eq. (2.13), is adapted to the resonator cavity as

$$k_{\mathrm{cav}} = k_0 \left[1 + \frac{1-\mathrm{i}}{4} \left(1 + \frac{\gamma - 1}{\sqrt{Pr}} \right) \frac{U_{\mathrm{cav}}}{A_{\mathrm{cav}}} \delta_\nu \right], \tag{3.10}$$

where A_{cav} is the cross sectional area of the cavity and U_{cav} is the corresponding perimeter.

With the wave number Eq. (3.10) and the wave impedance in the cavity Eq. (3.9), the impedance at the plate holder $y = l_{\mathrm{cav}_2}$ is

$$\zeta_1 = w_{\mathrm{cav}} \frac{1 + r_1 \, \mathrm{e}^{-2\mathrm{i}k_{\mathrm{cav}} l_{\mathrm{cav}_2}}}{1 - r_1 \, \mathrm{e}^{-2\mathrm{i}k_{\mathrm{cav}} l_{\mathrm{cav}_2}}}, \tag{3.11}$$

where the reflection factor of the rigid back wall with a thermal boundary layer is

$$r_1 = \frac{\zeta_{\mathrm{bl,th}} - w_{\mathrm{cav}}}{\zeta_{\mathrm{bl,th}} + w_{\mathrm{cav}}}. \tag{3.12}$$

At the position of the plate holder $y = l_{\mathrm{cav}_2}$, the thermal boundary layer impedance of the back side plate holder and the impedance of the back cavity are connected in parallel since the pressure is constant for both impedances and the acoustic volume flows add up[203]. This leads to

$$\zeta_2 = \left[\frac{1}{\zeta_1} + \frac{1}{\zeta_{\mathrm{bl,th}}} \left(1 - \frac{A_{\mathrm{p}}}{A_{\mathrm{cav}}} \right) \right]^{-1}, \tag{3.13}$$

where A_{p} denotes the plate area, which is ab in the rectangular and πR_{p}^2 for the circular case. The impedance is transformed to the flexible plate as

$$\zeta_3 = \zeta_2 \frac{A_{\mathrm{p}}}{A_{\mathrm{cav}}}, \tag{3.14}$$

in which the factor $A_{\mathrm{p}}/A_{\mathrm{cav}}$ ensures the continuity of the acoustic flux. The influence of the viscothermal boundary layer of the right half of the plate holder, see Fig. 3.1, is accounted for by

$$\zeta_4 = w_{\mathrm{ph}} \frac{1 + r_2 \, \mathrm{e}^{-\mathrm{i}k_{\mathrm{ph}} l_{\mathrm{ph}}}}{1 - r_2 \, \mathrm{e}^{-\mathrm{i}k_{\mathrm{ph}} l_{\mathrm{ph}}}} \quad \text{with} \quad r_2 = \frac{\zeta_3 - w_{\mathrm{ph}}}{\zeta_3 + w_{\mathrm{ph}}}. \tag{3.15}$$

The wavenumber k_{ph} and the wave impedance w_{ph} of the wave propagation within the opening of the plate holder (seen as a one dimensional waveguide) can be adopted from Eq. (3.10) and Eq. (3.9) but with $U_{\mathrm{ph}}/A_{\mathrm{ph}} = 2/R_{\mathrm{p}}$ instead of $U_{\mathrm{cav}}/A_{\mathrm{cav}}$ for a circular plate. For a rectangular plate $U_{\mathrm{ph}}/A_{\mathrm{ph}} = {}^{2(l_x+l_y)}/_{l_x l_y}$. The model can incorporate either the impedance of a clamped circular plate using Eq. (2.66) or a clamped rectangular plate using Eq. (2.92). The flexible plate is connected in series and therefore it yields:

$$\zeta_5 = \zeta_4 + \frac{Z_{\mathrm{p}}}{\rho_0 c} \tag{3.16}$$

The influence of the viscothermal boundary layer of the left half of the plate holder (see Fig. 3.1) is accounted for by

$$\zeta_6 = w_{\mathrm{ph}} \frac{1 + r_3 \, \mathrm{e}^{-\mathrm{i}k_{\mathrm{ph}} l_{\mathrm{ph}}}}{1 - r_3 \, \mathrm{e}^{-\mathrm{i}k_{\mathrm{ph}} l_{\mathrm{ph}}}}, \quad \text{with} \quad r_3 = \frac{\zeta_5 - w_{\mathrm{ph}}}{\zeta_5 + w_{\mathrm{ph}}}. \tag{3.17}$$

The effects of the cross section jump back and the thermal boundary layer of the plate holder towards the perforated plate are described by

$$\zeta_7 = \left[\frac{1}{\frac{A_{\mathrm{cav}}}{A_{\mathrm{p}}}\zeta_6} + \frac{1}{\zeta_{\mathrm{bl,th}}} \left(1 - \frac{A_{\mathrm{p}}}{A_{\mathrm{cav}}} \right) \right]^{-1} . \tag{3.18}$$

Next, the reflection factor at this position is calculated as

$$r_4 = \frac{\zeta_6 - w_{\mathrm{cav}}}{\zeta_6 + w_{\mathrm{cav}}} \tag{3.19}$$

and a spatial transformation along the main cavity is used to the backside of the perforated plate to finally obtain the cavity impedance

$$\zeta_{\mathrm{cav}} = w_{\mathrm{cav}} \frac{1 + r_4 \, \mathrm{e}^{-2\mathrm{i}k_{\mathrm{cav}} l_{\mathrm{cav}_1}}}{1 - r_4 \, \mathrm{e}^{-2\mathrm{i}k_{\mathrm{cav}} l_{\mathrm{cav}_1}}}. \tag{3.20}$$

The cavity impedance is then combined with the face sheet impedance in Eq. (3.1). The impedance must be determined iteratively for each frequency because of the nonlinear face sheet contribution, as the particle velocity is a function of the surface impedance $\left|v'_{\mathrm{h}}\right| = {}^{p'}/_{|\zeta(v'_{\mathrm{h}})|}$.

The corresponding workflow for determining the overall impedance of a Helmholtz resonator with a flexible wall ζ_{FXW} is sketched in Fig. 3.2.

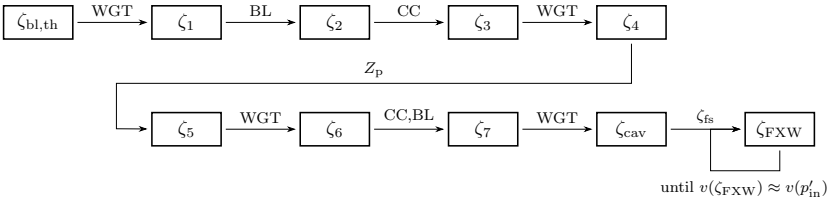

Figure 3.2.: Workflow to determine the overall impedance. 'WGT' refers to wave guide transformation; 'BL' refers to inclusion of the thermal boundary layer, 'CC' refers to a cross section change

4. Experimental Setup

In this chapter, the experimental setups to investigate the Helmholtz resonator with a flexible wall are presented. The resonator system is investigated in three test rigs of the German Aerospace Center (DLR) in Berlin. First, a normal incidence setup is used to measure the normal incidence absorption and impedance over a broad frequency range (D-NIT)[1]. A second normal incidence tube with a vibrometer pointing from the back at the flexible wall is used to link the overall acoustic performance with the plate motion (DUCT-NIT)[2]. Finally, a grazing incidence setup is used to assess the acoustic performance in a more realistic setting under high sound pressure levels and with grazing flow (DUCT-R)[3]. D-NIT was constructed during this thesis work after the measurements at DUCT-NIT for better measurement precision and to extend the frequency range.

4.1. Normal incidence tube (D-NIT)

Fig. 4.1 displays the normal incidence tube D-NIT of the Department of Engine Acoustics as part of the German Aerospace Center, constructed for and used in this work. D-NIT consists of a loudspeaker (BMS-4599-ND) attached to one duct end, a measurement section with flush mounted microphones (G.R.A.S 46BD-FV $^1/_4$") and a sample opposite the loudspeaker.

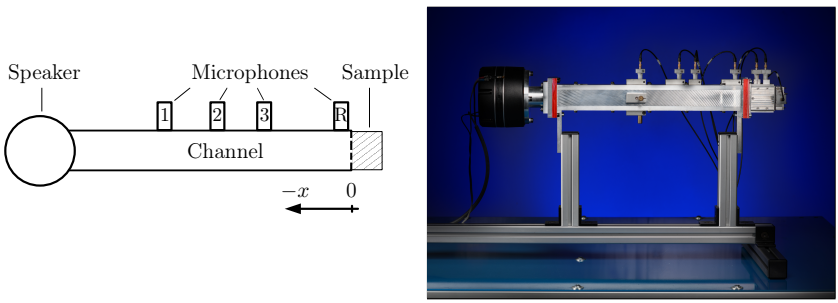

(a) Schematic view (b) Photograph

Figure 4.1.: Normal incidence tube setup to investigate Helmholtz resonators with flexible walls at D-NIT

The square cross section of 35 mm × 35 mm was chosen to match the cross section of the modular resonator system to determine the acoustic properties of a Helmholtz resonator

[1]DLR-AT-TRA – Normal Incidence Tube
[2]DUct aCoustic Test rig – Normal Incidence Tube configuration
[3]DUct aCoustic Test rig – Rectangular cross section

with a flexible wall, which is introduced later in Section 4.4. The main channel has a length of 400 mm. The tube walls are made of four 10 mm thick aluminium plates that are screwed together. During manufacturing, grease has been applied at the connecting surfaces to reduce sound leakage. The wall thickness was chosen to reduce unwanted structural vibrations. For the same reason, the loudspeaker is decoupled from the main structure by a rubber band. The connecting adaptors between the main tube, loudspeaker, and sample were sealed with o-ring seals to reduce airborne sound leakage.

The measurement range of the normal incidence tube setup is restricted to plane waves. The cut-on frequency of the first higher order mode f_c of a rectangular tube is determined by[304]

$$f_c = 0.5 \frac{c}{\max(l_\mathrm{y}, l_\mathrm{z})} \tag{4.1}$$

with c denoting the speed of sound and l_y and l_z the width and height of the channel, respectively. This yields a value of $f_\mathrm{c} = 4900\,\mathrm{Hz}$ at ambient conditions for D-NIT. The lower end of the usable frequency range is bounded by the loudspeaker's excitation range at 200 Hz.

The loudspeaker of type BMS4599 allows for the excitation of high sound pressure amplitudes with relatively low distortion. The input signal is generated by an Agilent 33220 signal generator and amplified by a Dynacord L300 amplifier.

The acoustic properties of perforations and, consequently, Helmholtz resonators are known to be dependent on the incoming sound pressure level, see Section 2.3.4. Therefore, two types of excitation signals are used. A single sine tone with a stationary amplitude is used whenever it is important to know the sound pressure level at the sample, i.e., at high sound pressure levels when nonlinear effects are expected. The sound pressure level of the incoming wave is determined a posteriori and was set to the same value for all frequencies to either 90-110 dB (±1 dB) or 130 dB (±3 dB). For low sound pressure levels in the linear regime, a sine sweep is used, which greatly reduces measurement time. The sweep and measurement time, as well as the amplitude are chosen to yield the same results as the single sine tones at low sound pressure levels.

The measurements are automated using Labview. The ambient pressure is measured by a Comet T7510 sensor, and the ambient temperature is measured using a PT-100 sensor in a four wire configuration with Agilent 34972A. The values are automatically logged during the measurements. The input signals generated by the signal generator to excite the loudspeaker are recorded using an OROS OR36 data acquisition system and the associated NVGate software.

The microphones are suitable for measuring sound fields up to sound pressure levels of 170 dB. All microphones were calibrated in a two-step process before each measurement campaign. First, all microphones were calibrated using a calibrated pistonphone of type BK4228 with a reference signal at 251 Hz with an amplitude of 124 dB to determine the sensitivity of the signal chain, which may change over time and under different ambient conditions. This ensures that all microphones measure the same sound pressure amplitude. Afterwards, all microphones were positioned in a ring at 220 mm, sufficiently far away from any near fields due to impedance changes by either the loudspeaker or a possible sample. These near fields are sufficiently attenuated at a distance of thrice the duct side length with respect to the loudspeaker or twice with respect to the sample[304], i.e. 115 mm or

70 mm, respectively for D-NIT. In this configuration, all microphones measure the same plane wave simultaneously at the same axial position. This configuration ensures that all microphones measure the same phase over the entire frequency range. Correction factors were calculated from the differences in the magnitude and phase of the measured sound pressure of the other microphones compared to one arbitrary chosen reference microphone. These correction factors were included in the measurement evaluation.

The normal incidence tube enables the determination of the sample impedance and normal incidence absorption by plane wave decomposition, which is briefly introduced in the following. A more detailed description of the calibration procedure and analysis of the decomposition method can be found in Lahiri[161, pp. 139–159].

4.1.1. Plane wave decomposition

Using m wall flush mounted microphones, each placed at the discrete axial position x_n respectively, the sound field $p'(x,t)$ in a duct can be discretised by

$$p'(x,t) = \hat{p}^{+}\,\mathrm{e}^{-\mathrm{i}kx_n} + \hat{p}^{-}\,\mathrm{e}^{+\mathrm{i}kx_n}, \qquad n = 1,\ldots,m \in \mathbb{N}\,. \tag{4.2}$$

$\hat{p}^{+}$ and $\hat{p}^{-}$ denote the amplitude of the forward and backward travelling plane sound waves, respectively. A sketch of the plane wave decomposition is depicted in Fig. 4.2.

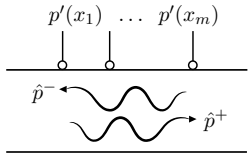

Figure 4.2.: Schematic view of the plane wave decomposition using the multi-microphone method

Each microphone detects the sound waves at a different spatial point and time as $p'(x_\mathrm{n})$. This system of linear equations for determining the unknown amplitudes of the incoming and outgoing plane sound waves can be written in matrix form as:

$$\underbrace{\begin{bmatrix} \mathrm{e}^{-\mathrm{i}kx_1} & \mathrm{e}^{\mathrm{i}kx_1} \\ \vdots & \vdots \\ \mathrm{e}^{-\mathrm{i}kx_3} & \mathrm{e}^{\mathrm{i}kx_3} \end{bmatrix}}_{\boldsymbol{A}} \underbrace{\begin{bmatrix} \hat{p}^{+} \\ \hat{p}^{-} \end{bmatrix}}_{\boldsymbol{x}} = \underbrace{\begin{bmatrix} p'(x_1) \\ \vdots \\ p'(x_m) \end{bmatrix}}_{\boldsymbol{b}}. \tag{4.3}$$

By using just $m = 2$ independent microphones with measured sound pressure level $p'(x_n,t)$, the system matrix $\boldsymbol{A}$ is invertible and thus has one unique solution for $\hat{p}^{+}$ and $\hat{p}^{-}$, known as the two-microphone method[304]. Problems arise when the spacing between two microphones is equal to $n\,\frac{\lambda}{2}$ with λ denoting the acoustic wavelength of the incoming sound wave and $n \in \mathbb{N}$. For these wavelengths, both microphones show the same spatial information at all times; hence, they are linearly dependent. In this case $\boldsymbol{A}$ becomes singular with no unique solution for the frequencies corresponding to these wavelengths. This problem may be overcome by using more than $m = 2$ microphones, in literature referred to as the multi-microphone-method[305], which is used in this work.

Given that at least three microphones are linearly independent, Eq. (4.3) becomes overdetermined and has infinitely many solutions. In other words, there is no unique solution of the system of equations that satisfies all measurement points. In this case, the system matrix $\boldsymbol{A}$ is not invertible, but an optimal solution regarding the Euclidean norm can be found using the Moore-Penrose inverse: $x\,\boldsymbol{A}^{+} = b$ with $\boldsymbol{A}^{+} = (\boldsymbol{A}^{T}\boldsymbol{A})^{-1} \cdot \boldsymbol{A}^{T}$. The viscothermal losses inside the duct walls are considered by a complex wavenumber k as proposed by Dokumaci[114], see Section 2.1.2.

For D-NIT, a multi-microphone method with three microphones flush mounted in the measurement section is employed to decompose the sound field in acoustic waves impinging on and reflected by the liner sample. The sampling frequency is set to 16 384 Hz, which according to the Nyquist–Shannon sampling theorem allows measurements up to 8192 Hz without aliasing. The Welch method[306] is used to transform the measured time signals into the frequency domain. The microphone signals are split into segments with an overlap of 50 % and a weighting with the Hann window function of each segment to reduce leakage during the Fourier transformation of non-periodic signals[161, pp. 140–144]. The microphones are attached at a distance of $x_1 = 110\,\text{mm}$, $x_2 = 145\,\text{mm}$ and $x_3 = 220\,\text{mm}$ to the sample, where the near field of the loudspeakers and sample have sufficiently vanished[304]. A fourth transducer of the same type is installed close to the sample surface to measure a reference sound pressure level; however, it is not used in this work.

Based on the decomposed waves, the complex reflection factor of the sample $r = \hat{p}^{-}/\hat{p}^{+}$ can be calculated. This reflection factor is then used to determine the absorption α and the complex normalised impedance

$$\alpha = 1 - |r|^2 \tag{4.4}$$

$$\zeta = \theta + \mathrm{i}\chi = \frac{1+r}{1-r}, \tag{4.5}$$

where θ is the specific normalised resistance and χ the specific normalised reactance. The calculation of the absorption is based on the idea that all sound energy that is not reflected must have been absorbed by the sample. This is only valid if no sound is transmitted outside, for example, due to sound leakage at the sample.

4.2. Normal incidence tube (DUCT-NIT)

The vibro-acoustic experiments, i.e., simultaneous measurements with a normal incidence tube and a vibrometer to detect the plate motion, are conducted at DUCT-NIT.[4] A schematic view and a photograph of the measurement setup are depicted in Fig. 4.3.

The test rig has a rectangular cross section of $A_{\mathrm{D}} = 60\,\text{mm} \times 80\,\text{mm}$ and therefore, according to Eq. (4.1), a cut-on frequency of the first higher mode of 2142 Hz. The sound source is an upstream loudspeaker (BMS-4599-ND) attached to the side wall of the duct. The end opposite the resonator system has an anechoic termination. In this test rig, the same plane wave decomposition as described in Eq. (4.3) in the measurement section are used to decompose the sound field in incoming and reflecting acoustic waves. However, in this case,

[4] Measurements with a vibrometer are also possible at D-NIT in principle too, but at the time of the experiments, D-NIT had not been constructed yet.

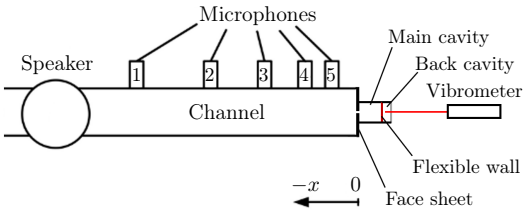

(a) Sketch of the impedance tube DUCT-NIT with the resonator system placed at the upstream end

(b) Photograph of the vibrometer setup

Figure 4.3.: Experimental setup to investigate Helmholtz resonators with flexible walls at DUCT-NIT

five microphones of type 1/4" G.R.A.S. 40BP-S1 with a pre-amplifier of type G.R.A.S. 26AC are used instead of three. The spacing between the microphones increases exponentially to reduce measurement errors. The data acquisition system is an OROS38, whereas the rest of the measurement equipment is of the same type as in D-NIT. Due to the lower cut-on frequency, the sampling frequency is reduced to 8192 Hz.

A laser Doppler vibrometer (Polytec OFV-5000 with an OFV-200 single-point sensor head) is used to determine the local deflection of the flexible wall inside the resonator system. The vibrometer is of a heterodyne-interferometer type in which a helium-neon laser emits a beam with a carrier signal. The sensor head focuses this beam to a small point on the plate. The reflected light of the vibrating object is subject to a Doppler shift proportional to the vibration velocity. This Doppler shift induces a frequency and phase modulation of the carrier signal, which is registered by a light detector inside the vibrometer. The light detector then converts the fluctuation in light intensity into an electric signal. The vibrometer has two decoders. One decoder uses frequency modulation to calculate the vibration velocity, and the other uses phase modulation to calculate the vibration deflection. The largest velocity range ($50\,\mathrm{mm\,s^{-1}\,V^{-1}}$) of the built-in velocity decoder is used to allow a maximum measurement range up to $500\,\mathrm{mm\,s^{-1}}$. With the same idea in mind, the deflection decoder range is set to $5\,\mathrm{mm V^{-1}}$. The acoustic excitation by the loudspeaker in the upstream section is held for five seconds before every measurement to ensure a stationary behaviour of the flexible plate. The experimental setup is similar to that introduced in Knobloch et al.[296], but here the modified channel is terminated with a resonator system instead of a flexible plate.

In preliminary investigations, the motion of the perforated face sheet, plate holder and the transparent back wall was measured. Their vibration amplitudes were found to be at least two orders of magnitude below that of the flexible plate; consequently, they can be assumed rigid (shown in Fig. A.1). This is crucial because the laser beam passes through the transparent back wall onto the flexible plate. A motion of the transparent back wall would corrupt the signal associated with the flexible plate's motion. Furthermore,

investigations were conducted to assess whether the transparent back wall made of acrylic glass (polymethyl methacrylat, PMMA) is suitable for laser vibrometer measurements. The transparency was assessed by measuring the vibration of the flexible plate without the transparent back wall and with the transparent back wall at a sufficient distance from the resonator. Both vibration measurements agreed very well (shown in Fig. A.2) and the transparent back wall can therefore be assumed to be sufficiently transparent.

Laser vibrometer measurements were conducted using a resonator and a flexible circular plate. The flexible plate is assumed to vibrate substantially only in radial modes because higher azimuthal modes have a mean displacement close to zero, see the discussion in Section 2.4.2, and are hardly excited by an incoming plane wave. In this case, the centre point is always a maximum in the deflection and velocity amplitude for a clamped circular plate; hence the centre point was chosen as the focal point of the vibrometer's laser beam. Adding a reflective colour to the centre point does not significantly alter the behaviour of the plate (see Fig. A.3).

4.3. Duct acoustic test rig (DUCT-R)

The experimental investigations with a grazing incidence are conducted at the duct acoustic test rig (DUCT-R) facility. The test rig was introduced in 2012 to assess planar liners[307]. The test facility offers the possibility to measure the effect of grazing flow and nonlinear sound excitation with sound amplitudes of more than 130 dB. The facility is well established and has been extensively used for liner measurements and impedance eductions[115],[307],[296],[106].

The rig is sketched in Fig. 4.4 and consists of two symmetrical parts with a cross section of $A_\mathrm{D} = 60\,\mathrm{mm} \times 80\,\mathrm{mm}$ and according to Eq. (4.1) a cut-on frequency of the first higher mode of 2142 Hz at ambient conditions with no flow. The left half of DUCT-R constitutes DUCT-NIT. Each part is equipped with five flush mounted microphones of type 1/4" G.R.A.S. 40BP-S1 to decompose the sound field into upstream and downstream travelling sound waves in each section, respectively, similar to Eq. (4.3). The signal processing is similar to that at the DUCT-NIT. Additionally, the method of Chung[308] is used with the loudspeaker input signal as a phase reference to reject uncorrelated turbulent flow noise. The sound waves are excited either via upstream speaker A or downstream speaker B (see Fig. 4.4) of type BMS 4599HE with a single tone and an amplitude of the incoming plane wave of either 110 dB or 130 dB(RMS). The propagating direction is downstream, if excited by speaker A, or upstream, if excited by speaker B in the corresponding hard wall section. Anechoic terminations at either end reduce end reflections above 160 Hz down to 15 % or less[106, p. 64].

A radial compressor is attached to the anechoic termination at the upstream section, enabling grazing flow with a centre line Mach number of up to 0.3. The free-flow velocity is measured with a Prandtl tube (KIMO L) in the centre of the duct cross section at the end of the downstream section and a differential capacitance manometer of type Baratron MKS 220D. The temperature in the duct is measured using a PT-100 probe of type GMH 3750. The ambient pressure is determined with a sensor of type Comet T7510. Measured flow velocity profiles in the DUCT-R can be found in Schulz et al.[130]. The grazing flow velocity, averaged over the duct cross section, is estimated using a nonlinear equalisation calculation from the wave numbers in the longitudinal direction $k_x^\pm$. With $k_x^\pm = k_0/(1 \pm M_\mathrm{c})$, there

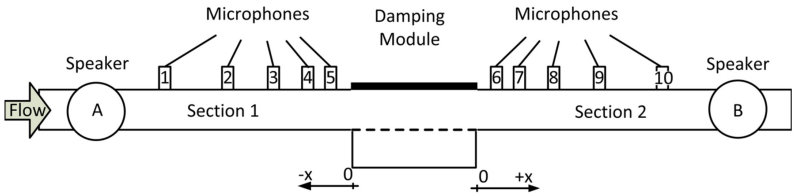

(a) Schematic view

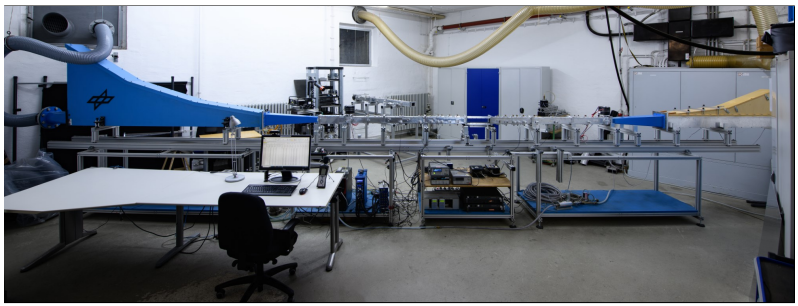

(b) Photograph with visible anechoic terminations

Figure 4.4.: Grazing incidence duct acoustic test rig DUCT-R

is a relationship to the effective, convective flow Mach number M_c for sound propagation, which is a reasonable approximation for the actual Mach number averaged over the duct cross section at low frequencies[106]. The corresponding skin friction velocity near the liner section in DUCT-R is $u_* \approx 0.035 u_{cl}$ with u_{cl} denoting the centre line velocity[158, p. 41].

4.3.1. Determination of scattering coefficients

The acoustic properties of a liner can be described by scattering coefficients. The transition from the sound-reflecting hard wall section to the liner section represents a change in the boundary condition for sound propagation: a certain proportion of the sound is reflected, whereas another proportion is transmitted across the liner. A third proportion that is neither reflected nor transmitted is dissipated by the liner. The scattering coefficients r^+, r^- and t^+, t^- describe the portions of the sound pressure wave reflected or transmitted by the liner at the upstream or downstream end, respectively.

To determine these four independent scattering coefficients, four linearly independent equations are needed. Two equations can be obtained by excitation with one loudspeaker (A) and a plane wave decomposition of the sound field in back $\hat{p}^-$ and forth $\hat{p}^+$ travelling waves in the hard-wall section before (Section 1) and after the liner (Section 2). Two additional equations can be obtained by sound excitation with another loudspeaker (B) at the opposite side of the liner and a plane wave decomposition in both sections. This can be

expressed as[115]

$$\underbrace{\begin{bmatrix} \hat{p}_{1\mathrm{A}}^{-} & \hat{p}_{1\mathrm{B}}^{-} \\ \hat{p}_{2\mathrm{A}}^{+} & \hat{p}_{2\mathrm{B}}^{+} \end{bmatrix}}_{\text{out}} = \underbrace{\begin{bmatrix} r^{+} & t^{-} \\ t^{+} & r^{-} \end{bmatrix}}_{\boldsymbol{S}} \underbrace{\begin{bmatrix} \hat{p}_{1\mathrm{A}}^{+} & \hat{p}_{1\mathrm{B}}^{+} \\ \hat{p}_{2\mathrm{A}}^{-} & \hat{p}_{2\mathrm{B}}^{-} \end{bmatrix}}_{\text{in}}. \tag{4.6}$$

Therefore, the reflection and transmission coefficients of the liner can be determined from the amplitudes of the incoming and outgoing waves obtained from two independent measurements. A sketch with the corresponding variables is depicted in Fig. 4.5.

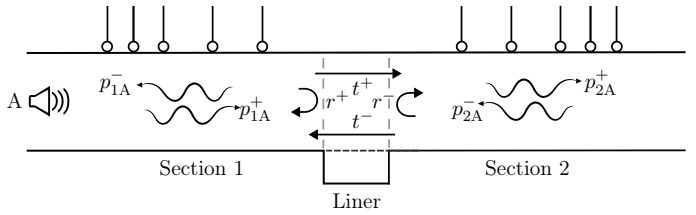

(a) Upstream excitation with loudspeaker A

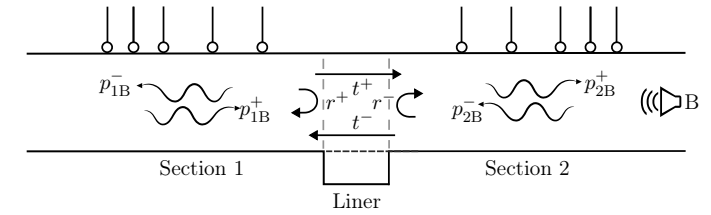

(b) Downstream excitation with loudspeaker B

Figure 4.5.: Schematic sound fields in the duct sections to determine the scattering coefficients of a liner

In the case of a symmetric liner without flow: $r^{+} = r^{-}$ and $t^{+} = t^{-}$ and, hence, only one excitation with two equations is needed to fully determine the system. The energy flux P for plane waves can be expressed as[161, p. 155]

$$P^{\pm} = \frac{A_{\mathrm{D}}}{\rho_0 c}(1 \pm M)^2 \left|\hat{p}^{\pm}\right|^2. \tag{4.7}$$

This way, the pressure reflection and transmission coefficients r, t can be related to the energy reflection and transmission coefficients R, T for plane waves with no cross section or mass flow change before and after the liner via the acoustic energy flux:

$$R^{\pm} = \frac{A_{\mathrm{D}}}{2\rho_0 c}\frac{(1\mp M)^2}{(1 \pm M)^2}\left|r^{\pm}\right|^2 \tag{4.8}$$

$$T^{\pm} = \left|t^{\pm}\right|^2 \tag{4.9}$$

The dissipation coefficient is derived from an energy balance, i.e. everything that is neither

reflected nor transmitted must have been dissipated, given there is no leakage of sound:

$$D^{\pm} = 1 - R^{\pm} - T^{\pm} = 1 - \frac{A_{\mathrm{D}}}{2\rho_0 c}\frac{(1\mp M)^2}{(1\pm M)^2}\left|r^{\pm}\right|^2 - \left|t^{\pm}\right|^2 \tag{4.10}$$

The test rig can also be used to educe the impedance of the liner. With no additional instrumentation, the complex pressure transmission coefficient t can be used to educe the impedance of the liner using the single-mode-method 'LINUS'[309],[307],[106]. Neglecting nearfields and reflections at the discontinuities at the axial liner boundaries with a length L and assuming a homogeneous liner with only one propagating mode, the axial wavenumber k_x over the liner can be determined from the transmission coefficient as

$$t = |t|\,\mathrm{e}^{\mathrm{i}\varphi t} = \mathrm{e}^{-\mathrm{i}k_x L} \qquad \text{with } k_x = \frac{-\varphi}{L} + \mathrm{i}\frac{\ln\left(|t|\right)}{L}. \tag{4.11}$$

In the no-flow case, the wavenumber perpendicular to the liner k_y can be obtained using the dispersion relationship Eq. (2.4) as

$$k_y = \sqrt{k_0^2 - k_x^2}. \tag{4.12}$$

The liner impedance then is simply:

$$\zeta = \frac{\mathrm{i}k_0}{k_y \tan\left(k_y l_y\right)} \tag{4.13}$$

With grazing flow, the solution involves numerical integration of the pressure derivatives along the duct height using the Pridmore-Brown-Equation[307]. 'LINUS' has the advantage of not needing more instrumentation than to determine the scattering coefficients, but is less accurate than measurements with additional microphones on the wall opposite (face-to-face) to the liner.

4.4. Single modular Helmholtz resonator with a flexible wall

In this work, two different types of Helmholtz resonators with flexible walls are investigated: a modular single resonator and three liner samples comprising arrays of resonators with flexible walls. The resonator array samples are used to address the first research question, whether the concept is suitable as a silencer in a grazing incidence setting. However, most research is done on the single modular Helmholtz resonator to investigate the physical mechanisms of the concept as raised by research question two. The single resonator system attached to D-NIT is depicted in Fig. 4.6. Its properties are presented in the following.

This resonator system consists of a face sheet, a main cavity, a plate holder with a flexible wall, a back cavity, and a rigid back wall. The main cavity can be extended on every outer side (each side wall and the back wall). In this case, one of the four rigid side walls is removed and replaced with a flexible clamped plate inside a plate holder and a second cavity. Alternatively, the main cavity can be enlarged to create a Helmholtz resonator with the same overall depth as the configuration with a flexible plate. This modular approach allows the testing of different face sheets, flexible plates, and back cavity sizes[310]. The modular system can also be used to investigate multiple flexible plates on opposite side walls or in series. However, this is beyond the scope of this work. The main cavity has a

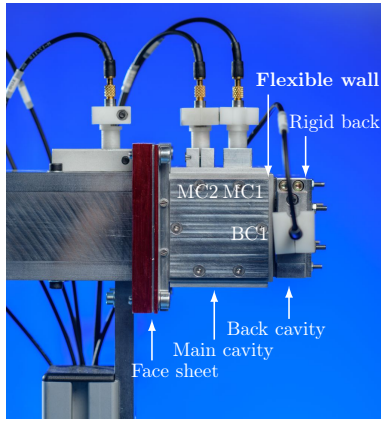

Figure 4.6.: Single modular Helmholtz resonator with a flexible wall mounted at D-NIT

quadratic cross sectional area of $A_{\text{cav}} = 35\,\text{mm} \times 35\,\text{mm}$ and a depth of $l_{\text{cav}_1} = 60\,\text{mm}$. This cross section is the same as D-NIT. For measurements at the DUCT-NIT, the DUCT-NIT's cross section is larger than that of the resonator. Therefore, to comply with the continuity of acoustic flux, the measured overall impedance must be adjusted by the hard wall area around the resonator with the factor $A_{\text{cav}}/A_{\text{D}}$.

The regular cavity walls are made of aluminium with a thickness of 10 mm. The flexible plate is clamped inside a plate holder, followed by a back cavity and rigid back wall. The plate holder consists of two rigid aluminium plates with a thickness of $l_{\text{ph}} = 2\,\text{mm}$ with a variable cut-out, which determines the shape of the flexible plates. The air volume in the cut out of the plate holder slightly increases the volume of the main and back cavities. The depth of the back cavity can be varied; however, in this study, it was fixed to a depth of $l_{\text{cav}_2} = 15\,\text{mm}$. The rigid back wall is made of aluminium, but was exchanged with a 5 mm thick transparent backplate made of acrylic glass for laser vibrometer measurements.

The modular resonator allows the placement of microphones inside the cavities. Two microphones (MC1 and MC2 in Fig. 4.6) are used for a plane wave decomposition inside the main cavity to determine the plate-related absorption $\alpha_{\text{p,cav}}$ and impedance $\zeta_{\text{p,cav}}$, which includes the effect of the flexible plate and the back cavity. The effects of the flexible plate can then be isolated by comparing it to the overall absorption α_{tot} and impedance ζ_{tot} determined by the normal incidence tube microphones outside the resonator. The distinction is sketched in Fig. 4.7.

The back cavity microphone is placed in the middle of the back cavity. The dynamic pressure difference $\Delta_{\text{SPL}} = |p'_{\text{BC1}}| - |p'_{\text{MC1}}|$ between the cavity microphone close to the flexible wall and in the back cavity is used to assess the driving pressure of the flexible plate's motion.

The centre of the main cavity microphones were 22.5 mm (MC1) and 41.5 mm (MC2) away from the face sheet. The decomposed matrix is singular outside the measurement range; however, it cannot be ruled out that nearfield effects from the face sheet and flexible plate

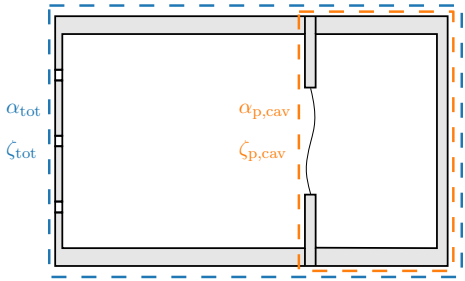

Figure 4.7.: Sketch to distinguish the absorption and impedance of the total resonator and of the plate and back cavity alone

are included in the measured signal, and the data quality is, therefore, expected to be less reliable. This is inevitable because of the space constraints inside the resonator system.

4.4.1. Face sheet

The face sheet serves as the Helmholtz resonator neck and is therefore a crucial component. Four different perforated face sheets are tested in this thesis to investigate their influence on the system's response, i.e., how a face sheet change affects the overall system's response, as well as the individual Helmholtz resonance and flexible wall response. The face sheet's geometric properties are stated in Table 4.1. A photograph of all tested face sheets is presented in Fig. 4.8.

Table 4.1.: Face sheet properties and corresponding Helmholtz resonance frequency

Name	h_{fs} in mm	d_{h} in mm	n_{h}	σ in %	f_{HR} in Hz
FS-I	2	1.5	18	2.6	631
FS-II	2	1	18	1.2	449
FS-III	1	1	64	4.1	1062
FS-IV	2	8.9	1	5.1	527

Additionally, for each face sheet, the corresponding Helmholtz resonance in the case of a cavity depth of $l_{\text{cav}_1} = 60\,\text{mm}$ and no flexible wall is given. Face sheet I is the baseline face sheet used in both the D-NIT and DUCT-NIT.[5] The face sheet has a comparable low porosity and large thickness to obtain a low Helmholtz resonance frequency. Face sheets II and III are only used in D-NIT to investigate the influence of the perforation and Helmholtz resonance. The perforation diameter of face sheet II is decreased to lower the Helmholtz resonance frequency. For face sheet III, the thickness is halved and the number of holes is doubled, resulting in a higher Helmholtz resonance frequency. Face sheet IV is used only in DUCT-NIT with a single large hole. These different face sheets cover a wide range of low Helmholtz resonance frequencies to assess the impact of a Helmholtz resonance lower, close to, or higher than a plate resonance on the overall behaviour.

[5]As the cross section of D-NIT and DUCT-NIT is different, there exist two face sheets labelled 'I', see Fig. 4.8, but they are the same when viewed from the resonator cavity.

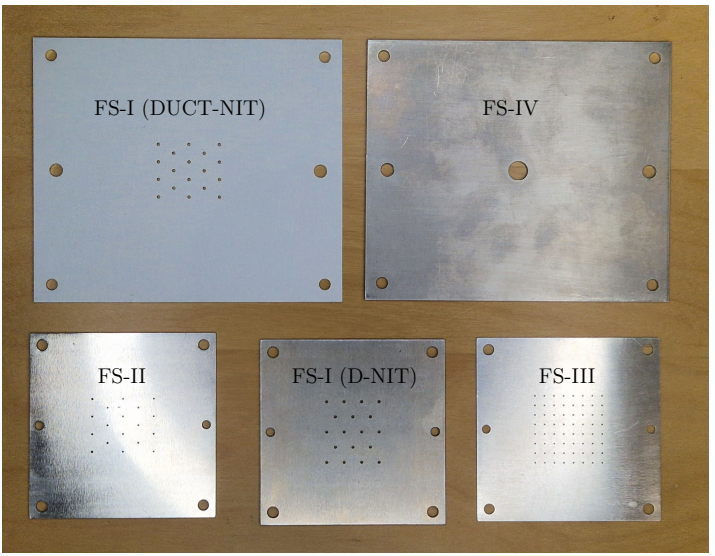

Figure 4.8.: Photograph of tested face sheets

4.4.2. Flexible wall

Another important aspect is the flexible wall material. Since the flexible wall is not prestressed, the restoring forces result from its flexural rigidity. Therefore, the terms 'flexible wall' and 'flexible plate' are used interchangeably in this work. Polymers are suitable candidates for flexible walls for multiple reasons:

1. They can have a very small modulus of elasticity ($E < 100\,\mathrm{MPa}$), which is orders of magnitude lower than e.g. aluminium 70 000 MPa or steel 210 000 MPa. This enables lower plate resonance frequencies, see Eq. (2.58) for a circular or Eq. (2.71) for a rectangular plate.
2. They have a very high deformability, which means that they can be stretched multiple times their original length without plastic deformation. This allows them to sustain high pressure excitations without breaking.
3. They have a high mechanical loss coefficient $\eta > 5\,\%$, which is orders of magnitude higher than for example steel with $\eta \approx 0.01\,\%$[216, pp. 191–197]. This is because the molecule structure of elastomers statistically favours a coiled state in a thermodynamic equilibrium, known as entropy elasticity. When a stress is applied to an elastomer, this coiled up state is untangled, leading to high friction between the polymer chains and subsequently to high energy dissipation[311, pp. 255–275].

The loss coefficient over the Young's modulus for various materials is depicted in Fig. 4.9. Polymers have a relatively low Young's modulus $E < 100\,\mathrm{MPa}$ and a high loss coefficient $\eta > 0.1$, making them a suitable material choice for flexible walls for additional damping. The loss factor of polymers can be approximated by $\eta \approx 0.04E^{-1}$, with E denoted in GPa[312, p. 117]. The trend is depicted as a dashed line in Fig. 4.9. The mechanical losses of

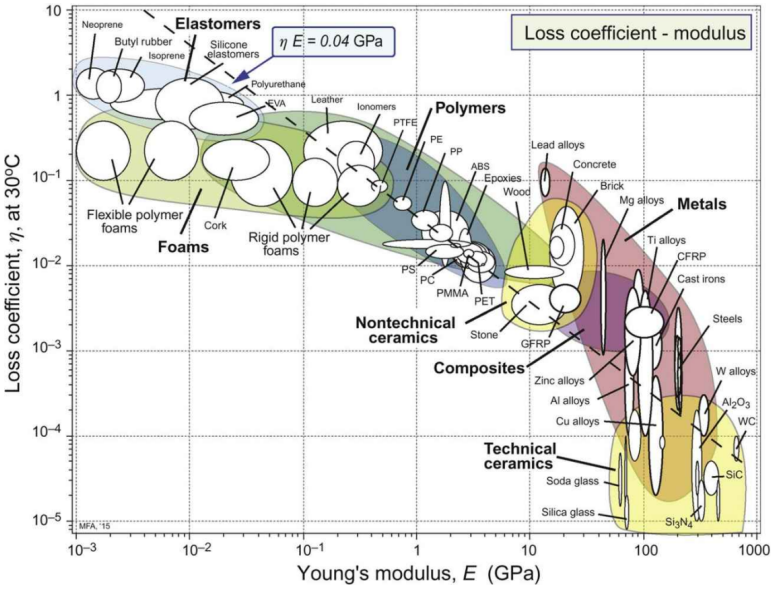

Figure 4.9.: Loss coefficient η versus Young's modulus E for a wide range of materials. This image is protected by copyright; reprinted with permission with permission of Elsevier Ltd. from[312, p. 117]

metals are higher in soft metals like lead and pure aluminium, strongly depend on the alloy, and are mostly frequency-independent[312, pp. 116–119].[6]

Three different materials are tested in this work: Two polymers, thermopolastic polyurethan (TPU) and ethylene butyl acrylate (EBA), and one metal (aluminium). TPU and EBA were selected because of their low stiffness and high mechanical loss coefficient. However, polymers may be susceptible to environmental conditions such as UV radiation, high temperatures, and fluids such as water, fuel, hydraulic oil, and de-icing fluid. Therefore, aluminium has been chosen as an alternative material that is less susceptible to environmental conditions. Since metals have very little mechanical losses, this also helps to determine the importance of inherent mechanical losses.

The mechanical characteristics of the three tested plate materials are presented in Table 4.2. The values for the Young's modulus and mechanical loss factor for the polymers are at ambient conditions in Europe (20 °C) for low frequencies ($<$ 1000 Hz). For the third material, Aluminium, standard textbook values are assumed[312, pp. 794–811]. The density and Poisson's ratio of EBA were estimated from similar polymers.

The Young's modulus E and loss coefficient η for TPU and EBA were determined based on a dynamic mechanical analysis and are both temperature and frequency dependent[313],[314].

[6]Contrary, bells are made out of bronze, which is a Cu alloy, because it has very little mechanical damping to enable more sound radiation.

Table 4.2.: Flexible plate properties

Material	E in MPa	η	h_p in mm	ρ_p in kg/m^3	ν_p
TPU	10-16	0.1	0.3	1080	0.49
EBA	10.5	0.09	0.55	940	0.49
Alu	70 000	0.005	0.05	2700	0.33

The temperature and frequency dependent Young's modulus and loss coefficient for TPU are depicted in Fig. 4.10.

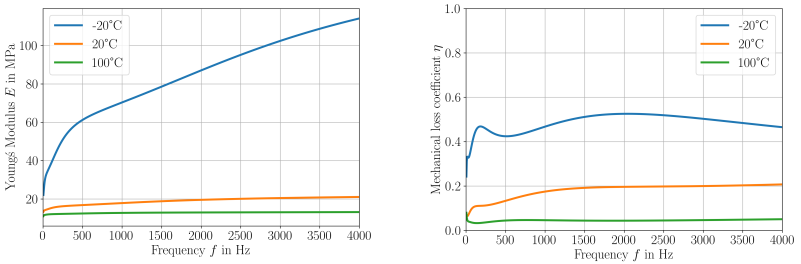

(a) Young's modulus E (b) Mechanical loss coefficient η

Figure 4.10.: Temperature and frequency dependent material properties of TPU

The stiffness and mechanical losses of the TPU samples strongly depend on the temperature. The material has a much higher Young's modulus at lower temperatures, i.e. $> 100\,\mathrm{MPa}$ at $-20\,^\circ\mathrm{C}$ compared to $\approx 10\,\mathrm{MPa}$ at $100\,^\circ\mathrm{C}$. The stiffness increases with frequency, which is more pronounced at lower temperatures, i.e. at $-20\,^\circ\mathrm{C} < 30\,\mathrm{MPa}$ at $50\,\mathrm{Hz}$ and $> 100\,\mathrm{MPa}$ at $3000\,\mathrm{Hz}$, whereas it is nearly constant with respect to frequency at higher temperatures. The mechanical losses are also higher at lower temperatures. Values up to 0.5 are reached at $-20\,^\circ\mathrm{C}$ and $2000\,\mathrm{Hz}$ whereas it is only 0.05 at $100\,^\circ\mathrm{C}$. The frequency dependency is less pronounced for the mechanical losses. It remains nearly constant around 0.05 at $100\,^\circ\mathrm{C}$, whereas it increases up to 0.2 at ambient temperatures. For $-20\,^\circ\mathrm{C}$ the loss factor increases at lower frequencies ($< 1500\,\mathrm{Hz}$), reaches a plateau, and decreases at higher frequencies ($> 2000\,\mathrm{Hz}$). Therefore, considering the frequency dependent material properties of TPU is more important at lower temperatures. This temperature dependency of plastics may become challenging when designing a liner with flexible walls that needs to be effective in different climates.

Sample combinations

The vibroacoustic behaviour of the flexible wall is determined by its material, shape, and boundary condition. The single resonator system was designed such that the flexible wall between both cavities is interchangeable in size, shape, and material. Four different plate geometries are studied: three circular shapes with a diameter of 15 mm, 22.8 mm, and 30 mm and a rectangular cut out of $15\,\mathrm{mm} \times 26\,\mathrm{mm}$. The shapes and sizes, as well as their first three eigenfrequencies are stated in Table 4.3. A photograph is presented in Fig. 4.11.

Table 4.3.: Vibroacoustic properties of the tested flexible wall samples with analytically determined three lowest significant eigenfrequencies

Name	Shape[1]	Material	Length in mm	f_1 in Hz	f_2 in Hz	f_3 in Hz
O-I	◯	TPU	15	349	1358	3044
O-II	◯	TPU	22.8	151	588	1317
O-III	◯	TPU	30	87	340	761
R-I	▯	TPU	15; 26	219	308	462
R-II	▯	EBA5	15; 26	372	523	785
R-III	▯	Alu	15; 26	1412	1985	2982

[1] ◯: Circular, length equals diameter; ▯: Rectangular, length equals side lengths

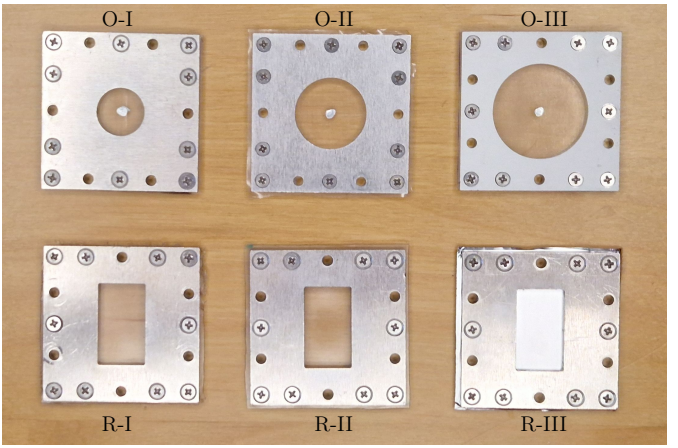

Figure 4.11.: Photograph of all used plate holders with clamped flexible plates. The circular plates have a reflective mark in the centre for vibrometer measurements.

4.5. Resonator array

In addition to the normal incidence case, the single resonator system was also tested as a single-cell-liner in DUCT-R[315],[310]. These investigations have been omitted in this thesis for the sake of brevity. The dissipation of the single resonator system was found to be too low to clearly investigate the influence of grazing flow[203].

Instead, three liner samples were manufactured to investigate the acoustical benefit of adding flexible walls in a grazing incidence setting with and without flow in DUCT-R. One sample is a reference sample (HR), which is a conventional SDOF Helmholtz resonator liner. The second is a resonator array with one flexible side wall per cavity (FXW-1). The third is a resonator array with two flexible side walls per cavity (FXW-2). The geometric properties of the liner samples are stated in Table 4.4, where l_{cav_2} denotes the side cavity

depth and A_p denotes the area of the flexible plate. The flexible plate is made of TPU with a Young's modulus of $E = 16\,\text{MPa}$, a loss coefficient of $\eta = 0.1$, and a thickness of 0.3 mm. The cell and liner sizes were chosen to fit the DUCT-R geometry. The other geometries were selected to allow for a Helmholtz resonance and several plate resonances in the measurable frequency range at DUCT-R. All liner parameters, such as the face sheet porosity, are similar for all liner samples with emphasis on comparing concepts, rather than showing optimal dissipation.

Table 4.4.: Resonator array liner sample geometries

Name	h_{fs} in mm	d_h in mm	σ in %	A_{cav} in mm²	l_{cav_1} in mm	l_{cav_2} in mm	A_p in mm²	Cells
HR	1.5	1.1	6.1	19^2	42	-	-	40
FXW-1	1.5	1.0	6.0	19×15.8	42	2.5	15×26	40
FXW-2	1.5	1.0	6.1	19×15.5	42	2.5	15×26	36

The flexible walls are positioned on the side because the side walls (e.g. $42 \times 19\,\text{mm}^2$ for FXW-1) offer more space for a flexible wall than the back side (e.g. $19 \times 19\,\text{mm}^2$ for FXW-1). In addition, this way the second cavity does not increase the overall liner depth. However, positioning the second cavity at the side leads to an overall reduction of the active liner area, which is defined here as the perforated area of the Helmholtz resonators. A schematic cell and a photograph of each liner sample can be found in Figs. 4.12 to 4.14. The liner samples

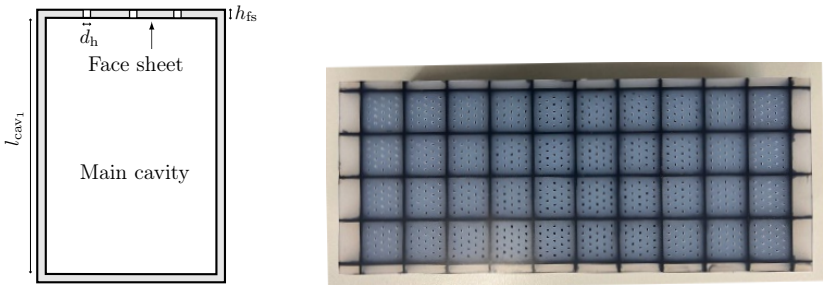

(a) Schematic cell (b) Photograph

Figure 4.12.: Reference liner sample (HR)

were manufactured by the Department of Function-Integrative Lightweight Engineering at the Institute of Lightweight Engineering and Polymer Technology at TU Dresden. They cut polyamide-6 organic sheets with 60 % continuous glass fibre reinforcement (PA6-GF) to size using water jet cutting. After cutting, an adhesive film was applied to the stringers with cut-outs. Subsequently, the TPU plate material was prestressed using a tensioning device, as described in Neubauer et al.[234], to prevent buckling with minimal tension. It was attached to the stringers with light pressure using the adhesive film, see Fig. 4.15s(a, b). Therefore, the flexible wall was prestressed for manufacturing reasons, which may affect the acoustic response. In addition, small holes with a diameter of 0.6 mm were drilled in the stringers to allow for pressure equalisation between the cavities. Without pressure equalisation, a static pressure difference due to grazing flow and the change of static pressure inside the test rig could lead to an unknown static deflection of the flexible plate. Next, the stringers

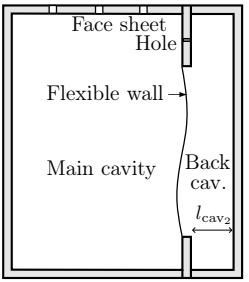

(a) Schematic cell

(b) Photograph

Figure 4.13.: Liner with one flexible wall per cell (FXW-1)

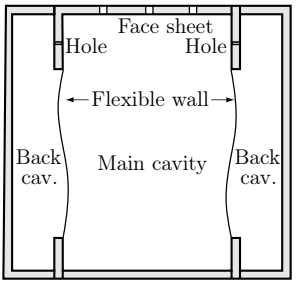

(a) Schematic cell

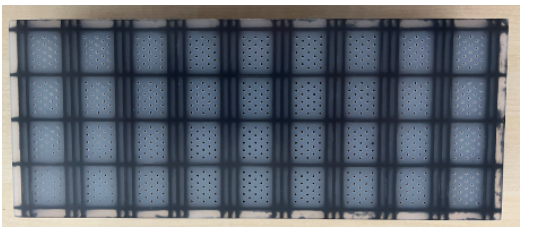

(b) Photograph

Figure 4.14.: Liner with two flexible walls per cell (FXW-2)

were assembled and sealed with a two-component adhesive (DP490, 3M™ Scotch-Weld™) to ensure bonding and prevent the transmission of airborne sound between the cavities, see Fig. 4.15(c). Grooves were milled into the face and base sheet to precisely position the core structure, which were then filled with adhesive to ensure bonding between the sheets and the core structure. Figure 4.15(d) shows sample FXW-2 after the completion of the assembly process. The reference liner and the FXW-1 liner were manufactured by the same process.

Measurement uncertainties

This section provides a brief overview of measurement uncertainties when determining the acoustical properties of the samples.

The accuracy of determining the scattering coefficients at DUCT-R was assessed by measuring the dissipation in an empty tube and an error of approximately 3 % in the no flow case and 4 % with a centre line Mach number of 0.2[317, pp. 40–41]. A similar accuracy can be expected for DUCT-NIT as it comprises one half of DUCT-R. The accuracy of D-NIT was similarly assessed with a sound hard termination, i.e., an empty duct, and is plotted in Fig. 4.16. The absorption, which ideally would be zero if the thermal boundary layer of

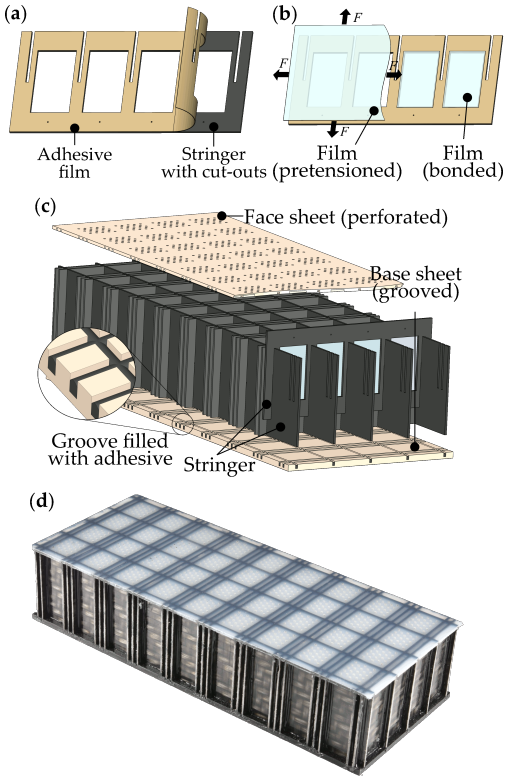

Figure 4.15.: Assembly process of the planar FXW multi-cell resonator array liner[316]

the hard wall is neglected, is around 2-3 % except near 1400 Hz and 3500 Hz where values around 5 % were measured. These increased values are not related to the spacing between the microphones and might be due to unknown side wall vibration.

The restoring forces of ideal plates are only due to their flexural rigidity. The flexible plate in the single modular Helmholtz resonator is clamped into a plate holder tightened by ten screws to a torque of 0.2 Nm to ensure that the plate is clamped on its boundaries. The torque was chosen to be as high as needed to ensure a reproducible clamped boundary condition, while being as low as possible to avoid pretensioning the plate, which would increase the stiffness and consequently its eigenfrequency.
The reproducibility was assessed by removing the back cavity and the flexible plate holder from the modular system and then immediately reattached. The absorption of the flexible plate holder without the main cavity or face sheet for the largest circular plate in Fig. 4.17a shows that the reproducibility is very good for the plate holder with a circular plate. In contrast, the experimentally determined absorption of the resonator with a rectangular plate of TPU showed some variability, as depicted in Fig. 4.17b. The Helmholtz resonance around 700 Hz remains fixed but the exact location of the plate resonances varied up to 100 Hz. This might be due to local tension at the sharp rectangular edges.

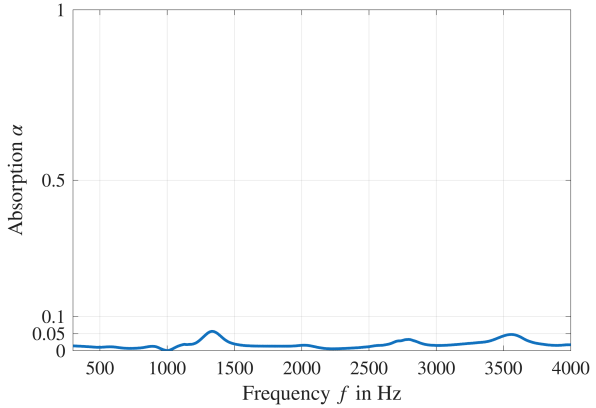

Figure 4.16.: Measured absorption spectrum of empty D-NIT

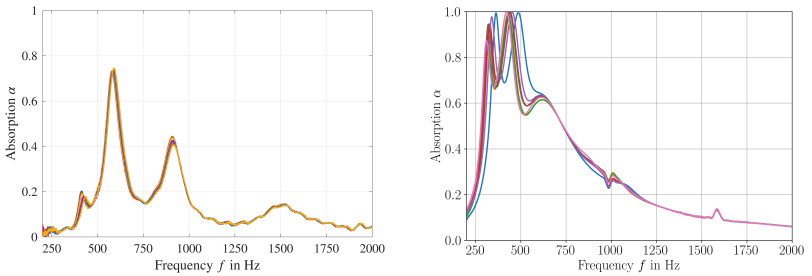

(a) Isolated round plate (O-III) inside plate holder and back cavity

(b) Full resonator with face sheet (FS-I) and rectangular plate (R-I)

Figure 4.17.: Repeatability measurement of the absorption of plate holder component and entire resonator system

The flexible walls in the multi-cell liner were glued under tension with the cavity structure. One additional plate holder with a pretensed flexible plate and one without pretension were manufactured to investigate how a pretension affects the reproducibility. A photograph of the glued plates is presented in Fig. 4.18b.

The repeatability of the tensioned plate in Fig. 4.18c was found to be better than the tension-free version in Fig. 4.18a, which showed a larger variance in the absorption spectra. Additionally, the operating test engineer also makes a difference. The variance of the measured absorption by an instructed but untrained assistant in Fig. 4.18d is even greater than the difference between pretensioned and tension-free. Note that the 'mean' absorption of the tension-free plate is different to the 'mean' absorption of the pretensioned plate. This demonstrates the high sensitivity of the system towards tension effects.

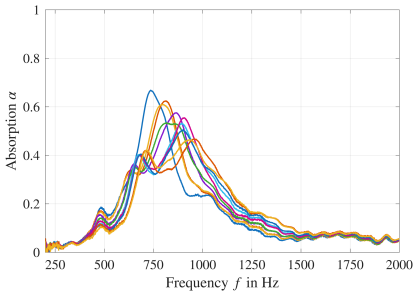

(a) Repeated measurement of absorption of plate holder only with tension-free glued rectangular plate

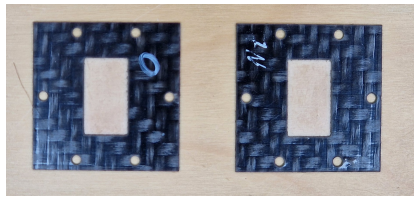

(b) Photograph of glued plate holders for repeatability measurements; left: tension free, right: pretensioned

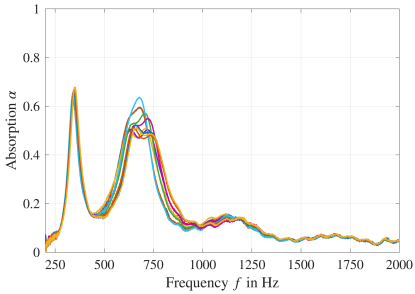

(c) Repeated measurement of absorption of plate holder only with pretensioned glued rectangular plate

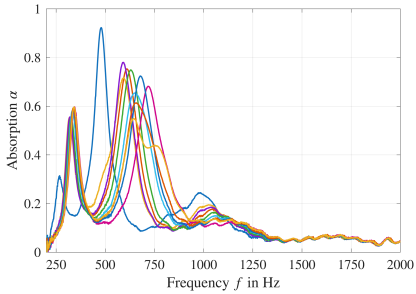

(d) Repeated measurement of absorption of plate holder only with pretensioned glued rectangular plate (untrained assistant)

Figure 4.18.: Repeatability of different flexible plate sample measurements

In summary, the liner concept is investigated with two sample structures in three experimental test rigs. A modular Helmholtz resonator with a flexible intermediate wall was designed to test different face sheet and flexible plate combinations in a normal incidence setup. The acoustic properties are determined based on the reflection coefficient at the resonator surface by a plane wave decomposition in the normal incidence tube. A vibrometer setup is used to resolve the in-situ plate vibration through a transparent back wall. Cavity microphones are installed in the main and the back cavity to resolve the corresponding pressure fields inside the resonator. Polymers show promising mechanical properties for this concept because of their low stiffness and high internal mechanical damping. Liner samples with multiple cells and either none, one, or two flexible walls per cell are investigated with high sound pressure levels and grazing flow. Their acoustic properties are characterised by their scattering coefficients and their impedance, which is determined using flush mounted microphones upstream and downstream of the liner samples.

5. Numerical setup

The analytical and experimental investigations are accompanied by numerical simulations. These simulations allow for a refinement and extension of the parameter space, as well as insights into the spatially resolved pressure distribution and wall movement inside the resonator which are difficult to measure. Furthermore, the numerical model can be used to evaluate geometry or material changes without having to physically build a new sample each time a change is made, which would be necessary for experimental investigations.

The numerical simulations in this work are conducted on a single workstation with an Intel® Core™ i7-12700k Processor (12 Cores, 20 Threads) and 32 GB RAM, using the commercial software Comsol Multiphysics® by Comsol Inc. in version 6.1 with the add-on modules 'Acoustics' and 'Structural Mechanics'. Comsol Multiphysics is based on the finite element method (FEM). FEM is most commonly used in the numerical analysis of vibrations in structures and sound fields in closed or nearly closed volumes[226, pp. 449–455]. Generally speaking, the set of differential equations for the equations of motion and boundary conditions, such as the Helmholtz equation Eq. (2.2) or the plate differential equation Eq. (2.47) state the problem in a 'strong form' since they must be met at every point of the continuum. In FEM, the problem is formulated in a 'weak form', in which the equations of motion and boundary conditions are met only in an average sense by considering an integral expression. This weak form is then solved on a discretised model of the continuum using finite elements[226, pp. 449–455].

Numerical Model

A representation of the numerical models of D-NIT, DUCT-NIT and DUCT-R is displayed in Fig. 5.1.

At the inlet, upstream of the tube geometry a 'port' boundary condition is employed to represent the plane wave excitation p'_{in}, which is the prescribed pressure amplitude. For D-NIT and DUCT-NIT, the inlet port is simultaneously the outlet port, and the outgoing wave is evaluated at the same boundary. The complex reflection coefficient evaluated at the port $r_{\mathrm{port}} = {}^{p'_{\mathrm{in}}}/_{p'_{\mathrm{out}}|_{\mathrm{port}}}$ is transformed to the face sheet using a waveguide transformation $r = r_{\mathrm{port}}\, \mathrm{e}^{\mathrm{i}2k_0 l_x}$, as introduced in Section 3.2. l_x the duct length, i.e., the distance between the port boundary and the face sheet. Subsequently, the resonator impedance and absorption are evaluated as $\zeta = {}^{1+r}/_{1-r}$ and $\alpha = 1 - |r|^2$. The boundaries inside the tube but outside the resonator are modelled as sound hard without thermoviscous losses. This ensures that no losses in the main tube outside the resonator are attributed to the resonator damping. For DUCT-R, the outgoing wave is evaluated at the outlet opposite the inlet. The scattering coefficients are calculated similar to Eq. (4.8) and Eq. (4.10), albeit without flow ($M = 0$).

A simple mesh study to investigate an appropriate mesh size is presented in Section A.3. A

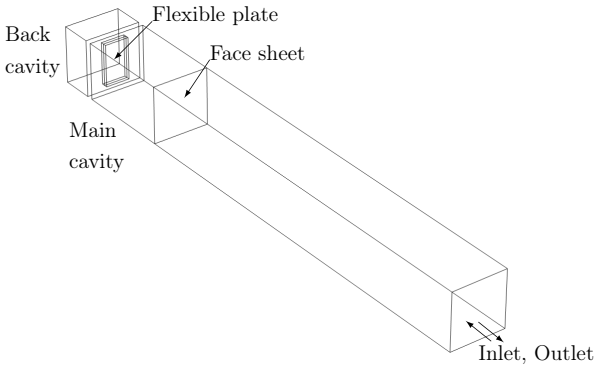

(a) D-NIT

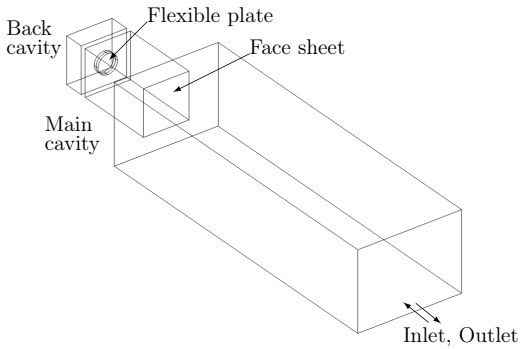

(b) DUCT-NIT

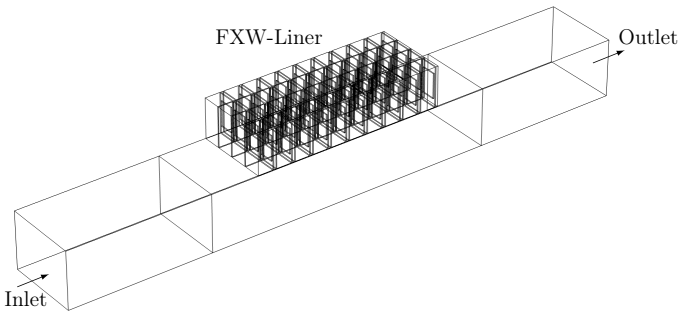

(c) DUCT-R

Figure 5.1.: Geometric model of D-NIT (top), DUCT-NIT (middle) and DUCT-R (bottom)

mesh with six quadratic elements per wavelength in the air domain and a maximum size of ten elements per plate length was found to be a good compromise between accuracy and speed. Double symmetries are exploited in the D-NIT and DUCT-NIT cases, and a single symmetry is exploited in the DUCT-R case to reduce the model size and subsequently reduce computation time. Their equivalency is demonstrated in Section A.3.

5.1. Fluid domain

In the fluid domain the built-in module 'Pressure Acoustics, Frequency Domain' is used that solves the Helmholtz equation[318, pp. 63–154]

$$\Delta p' + k^2 p' = 0, \tag{5.1}$$

which was introduced in Eq. (2.2). Equation (5.1) is converted to an equivalent weak statement formulation and then discretised using finite elements in Comsol Multiphysics.

Wall losses

The wall losses inside the resonator are taken into account using the 'Narrow Region Acoustics Module', which uses an equivalent fluid model to incorporate the effect of the viscothermal boundary layer in the bulk of the fluid[318, p. 321]. The implementation in Comsol Multiphysics is based on the low reduced frequency model[110], as introduced in Section 2.1.2. This is computationally very efficient and has been shown to be accurate for simple geometries, such as tubes and rectangular ducts below the cut-on frequency[111, p. 137].[1] The complex wave number k_c and complex specific impedance Z_c are given by

$$k_c^2 = k_0^2 \left(\frac{\gamma - (\gamma - 1)\Upsilon_{\mathrm{th}}}{\Upsilon_{\mathrm{vis}}} \right) \tag{5.2}$$

$$Z_c^2 = \frac{Z_0^2}{\Upsilon_{\mathrm{vis}}(\gamma - (\gamma - 1)\Upsilon_{\mathrm{th}})} \tag{5.3}$$

with Υ denoting the cross section averaged mean value of the scalar thermal and viscous functions respectively. These are given for a circular duct as

$$\Upsilon_{\square} = -\frac{J_2(k_{\square} R_{\mathrm{D}})}{J_0(k_{\square} R_{\mathrm{D}})}, \tag{5.4}$$

[1] A more rigorous approach would be to fully resolve the viscothermal boundary with a thermoviscous acoustic model. However, this would be too computationally demanding and is not the focus of this work.

and a rectangular duct as

$$\Upsilon_{\square} = k_{\square}^2 \sum_{m=0}^{\infty} \left[(\alpha_m m')^{-2} \left(1 - \frac{\tan(\alpha_m l_y/2)}{\alpha_m l_y/2} \right) + (\beta_m m')^{-2} \left(1 - \frac{\tan(\beta_m l_y/2)}{\beta_m l_y/2} \right) \right], \quad (5.5)$$

$$m' = (m + 1/2)\pi, \quad (5.6)$$

$$\alpha_m = \sqrt{k_{\square}^2 - \left(\frac{2m'}{l_y} \right)} \qquad \beta_m = \sqrt{k_{\square}^2 - \left(\frac{2m'}{l_z} \right)}, \quad (5.7)$$

where $\square$ is a placeholder for either 'vis' (viscous) or 'th' (thermal). R_{D}, l_y, l_z denote the duct radius, width and height, respectively[318, p. 326][111, pp. 58–68].

5.2. Face sheet

Accurately representing the acoustic properties of a perforated face sheet is challenging because it involves thermoviscous effects at the boundaries, higher order mode emergence at the cross-section changes, and nonlinear effects such as flow separation when the sound particle velocity exceeds the face sheet thickness, as explained in Chapter 3. Therefore, a very high spatial and temporal resolution is required for a rigorous numerical solution of the underlying differential equation. Solving this not feasible on a single workstation.

Alternatively, the effects of the perforated face sheet can be represented by an interior boundary with a transfer impedance ζ_{fs}. This approach is used in this work. The boundary impedance for the thin perforated face sheet is modelled in Comsol Multiphysics as[318, pp. 297–321]

$$\begin{aligned} \zeta_{\mathrm{fs}} &= \zeta_{\mathrm{lin}} + \zeta_{\mathrm{nl}} + \zeta_{\mathrm{user}} \\ &= -\mathrm{Re}\left(\frac{\mathrm{i}\omega}{c\sigma} \frac{h_{\mathrm{fs}} + 2\delta_{\mathrm{resist}}}{\Gamma} \psi(\sigma) \right) - \mathrm{iIm}\left(\frac{\mathrm{i}\omega}{c\sigma} \frac{h_{\mathrm{fs}} + 2\delta_{\mathrm{react}}}{\Gamma} \psi(\sigma) \right) \\ &+ \frac{1 - \sigma^2}{(\sigma C_{\mathrm{D}})^2 2c} \left| v_{\mathrm{h}}' \right| + \zeta_{\mathrm{user}}. \end{aligned} \quad (5.8)$$

The formulation of ζ_{lin} is based on Crandall's work[142], see Eq. (2.28), with Γ accounting for viscous wall losses and $\psi(\sigma)$ denoting Fock's function, see Eq. (2.37), accounting for hole interactions. σ denotes the porosity, h_{fs} is the thickness of the face sheet, C_{D} is the discharge coefficient, with δ_{resist} and δ_{react} representing the (unspecified) resistive and reactive end correction, respectively.[2] The nonlinear contribution is the same type as Eq. (2.41). ζ_{user} offers an option for arbitrary impedance corrections by the user. An additional normalised resistance of 0.1 was added to the perforated plate impedance model for the face sheet impedance of the resonator array liner in DUCT-R to account for rig specific contributions not captured in the simulation, such as wall losses outside the resonator in the liner section determined by a reference liner. This formulation is only available in the frequency domain; therefore, time-resolved simulations using the interior boundary impedance representation of a perforated plate are not possible.

[2] Note, that Eq. (5.8) suggests that h_{fs} is also affected by $\psi(\sigma)$, which is most likely a typing error in the manual because $\psi(\sigma)$ is defined as the hole interaction factor for end corrections only.

5.3. Flexible wall

The flexible wall is modelled as a flat two-dimensional shell structure. A shell is a generalised plate that can be curved. This assumes that the in-plane total strains vary linearly through the small thickness and that the stress in the transverse direction is negligible[319, p. 1194]. As the flexible wall is very thin ($h_\mathrm{p}/\min(a,b) < 0.1$), this assumption holds. Otherwise, resolving the three-dimensional structure inside the thin ($< 1\,\mathrm{mm}$) plate would require an unnecessary fine mesh. The flexible wall materials are assumed to be linearly elastic and isotropic with inherent mechanical damping. This means that plastic deformations due to high deflections are not resolved. The mean maximum velocity is calculated as $\hat{v}_\mathrm{p,avg} = A_\mathrm{p}^{-1} \int_{A_\mathrm{p}} |v_\mathrm{p}| \, \mathrm{d}A_\mathrm{p}$. The mechanical losses inside the flexible wall are included in the numerical simulation by a complex Young's modulus $E = (1 + \mathrm{i}\eta)E_\mathrm{real}$. The dissipated energy due to mechanical losses is determined using $D_\mathrm{plate} = Q/P_\mathrm{in}$, where Q is evaluated using the inelastic strain forces in the shell averaged over a period[319, p. 711] and P_in denotes the sound power of the excited incoming wave.

Acoustic-structure interaction

The acoustic pressure causes a fluid load on the solid surface, and the structural acceleration acts as a normal acceleration on the fluid. The coupling between the fluid domain and flexible wall is modelled in the numerical model with the 'Acoustic-Shell Interaction, Frequency Domain' interface, which connects the acoustic pressure variations in the fluid domain with the structural deformation of the shell boundary. Both domains need to be solved simultaneously to capture the effect of the flexible plate on the Helmholtz resonance and vice versa. Mathematically this 'strong' coupling condition[3] on the shell between two fluid domain reads as

$$-\boldsymbol{n} \cdot \left(-\frac{1}{\rho_0} \left(\nabla p' - \boldsymbol{q}_\mathrm{d} \right)_\mathrm{up} \right) = -\boldsymbol{n} \cdot \boldsymbol{u}_\mathrm{tt} \tag{5.9}$$

$$-\boldsymbol{n} \cdot \left(-\frac{1}{\rho_0} \left(\nabla p' - \boldsymbol{q}_\mathrm{d} \right)_\mathrm{down} \right) = -\boldsymbol{n} \cdot \boldsymbol{u}_\mathrm{tt} \tag{5.10}$$

$$\boldsymbol{F}_\mathrm{A} = (p'_\mathrm{t,down} - p'_\mathrm{t,up}), \tag{5.11}$$

where $\boldsymbol{u}_\mathrm{tt}$ is the structural acceleration, $\boldsymbol{n}$ the surface normal, $\boldsymbol{q}_\mathrm{d}$ a dipole domain source and $\boldsymbol{F}_\mathrm{A}$ is the force per unit area experienced by the structure[318, p. 843].

In short, the experimental sample structures introduced in the previous chapter are modelled numerically using the commercial finite element software Comsol Multiphysics. The face sheet is modelled as an impedance boundary condition; the flexible wall is modelled as a two-dimensional shell structure that is strongly coupled to the air domain inside the main and the back cavities. Viscothermal losses inside the cavities are considered using an equivalent fluid model. In addition to the analytical and experimental investigations, the numerical models have the advantage of resolving and visualising the coupled plate vibration and sound pressure fields in the cavities as well as the possibility of exploring arbitrary plate shapes and positions. This helps in gaining a deeper understanding of the concept and assessing the cases in which the assumptions of the analytical model are justified.

[3] In a 'weak' coupling, the differential equations in the respective domains are solved subsequently. This is useful to speed up the simulation e.g. when trying to capture the static pressure onto the plate due to grazing fluid flow; if one assumes that the plate motion does not alter the fluid flow.

6. Results and Discussion

This chapter presents the main results of the analytical, numerical, and experimental studies to answer the two central research questions. The first research question regarding the suitability of the liner concept is investigated through experiments conducted in both the normal incidence setup and the grazing incidence setup, characterised by high sound pressure levels and grazing flow. The benefits and disadvantages of the proposed liner concept with a flexible wall are highlighted by comparing it with a conventional Helmholtz resonator liner.

The second research question, how the concept can be understood and modelled, is addressed with the help of the analytical and numerical models, which were introduced in the previous chapters. These model predictions are compared with the experimental results to demonstrate their applicability and limitations. Further insight into the system is gained using a vibrometer setup to measure the flexible plate response and cavity microphones to determine the pressure field inside the resonator. In addition, numerical simulations are used to resolve the three-dimensional pressure field and two-dimensional plate deflections. The computational speed of the analytical model is exploited to unfold parameter dependencies of the interplay between the Helmholtz resonator and structural resonances of the flexible wall.

The modular Helmholtz resonator with different face sheets, plate geometries, and materials is investigated first in Section 6.1 and Section 6.2 in a normal incidence setting because the determination of the impedance and absorption is easier and more reliable than in a grazing incidence setting. In Section 6.1 the resonator with a circular flexible plate is tested in DUCT-NIT, which has the drawback that the measurement range is limited to approximately 2100 Hz and that its cross section and that of the resonator do not match. To improve the accuracy and increase the measurement range up to 4900 Hz, a new normal incidence tube was developed and used in Section 6.2 with the same cross section as the modular resonator to investigate the resonator with a rectangular flexible plate. However, the quality of the experimental data in DUCT-NIT was found to be sufficiently accurate to investigate the relevant effects; thus, no repetition of the measurements at D-NIT was necessary.
An analytical parameter study of relevant face sheet, cavity geometries, and plate parameters focuses on their individual contribution and the interaction between Helmholtz resonance and plate resonances. The corresponding results are presented in Section 6.3.
Finally, the usage of multiple cells, high sound pressure field and grazing flow effects are investigated in a grazing incidence setting in Section 6.4. The general idea is to use a simpler normal incidence setup to investigate basic interaction effects between Helmholtz and plate resonances first and subsequently use a more sophisticated grazing incidence setup for flow effects.

6.1. Helmholtz resonator with a circular plate and a vibrometer setup

This section[1] shows the results obtained in the DUCT-NIT configuration, as introduced in Section 4.2. In this setup, the normal incidence impedance of the Helmholtz resonator with an intermediate flexible circular plate was measured by plane wave decomposition. Two different face sheets and three different diameters of a flexible clamped circular plate were tested. The specific sample characteristics are stated in Section 4.4. Additionally, the centre plate deflection and velocity were determined using a vibrometer through a transparent backplate. The excitation amplitude of the incoming wave was set to 100 dB (RMS) if not stated otherwise. The plate material was TPU. The experimental results were then compared to predictions from the analytical model introduced in Chapter 3 and the numerical finite element simulations with the setup introduced in Chapter 5 to assess their accuracy.

6.1.1. Experimental results

Figure 6.1a displays the measured normal incidence absorption coefficient α of the FXW resonator as a solid line with face sheet one (FS-I, $h_{\mathrm{fs}} = 2\,\mathrm{mm}$, $d_{\mathrm{h}} = 1.5\,\mathrm{mm}$, $\sigma = 2.6\,\%$) and a flexible plate of diameter $d_{\mathrm{p},1} = 15\,\mathrm{mm}$. The absorption of a simple Helmholtz resonator with the same total depth of $l_{\mathrm{cav,HR}} = l_{\mathrm{cav}_1} + l_{\mathrm{cav}_2} = 75\,\mathrm{mm}$ is plotted as a reference (HR, dashed). The frequency range is restricted up to 1000 Hz to focus on the relevant low-frequency effects. The measured frequency points are marked with circles for the absorption, boxes for the resistance and diamonds for the reactance for better distinction.

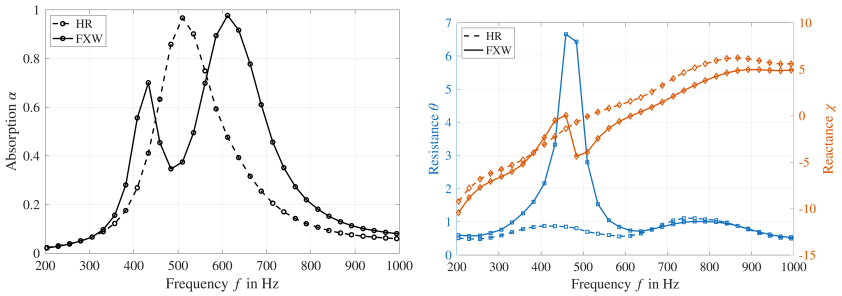

(a) Absorption α (b) Normalised impedance $\zeta = \theta + \mathrm{i}\chi$

Figure 6.1.: Measured normal incidence absorption α and normalised impedance $\zeta = \theta + \mathrm{i}\chi$ for a resonator with a flexible plate (solid), FS-I, $d_{\mathrm{p},1} = 15\,\mathrm{mm}$ and for a simple Helmholtz resonator (dashed) and with the same face sheet and same total depth . The legend entries for the impedance plot are black as the line-style applies to both the resistance (blue squares) and reactance (red diamonds).

Two absorption maxima around 430 Hz and 610 Hz are visible for the resonator with a flexible plate (solid) compared to just one for the simple Helmholtz resonator (dashed)

[1] Parts of this section were published in Kohlenberg et al.[320].

around 510 Hz. The introduction of the flexible plate successfully extends the damping of the Helmholtz resonator to lower frequencies in this configuration. However, at the same time, the Helmholtz resonance is shifted from 510 Hz to 610 Hz. These local absorption maxima correspond to local minima in the absolute values of the reactance (red, diamonds) in Fig. 6.1b and can, therefore, be interpreted as the system's resonances. The introduction of a flexible plate adds a low-frequency resonance and the Helmholtz resonance is shifted to higher frequencies. The additional low-frequency resonance has a smaller bandwidth and a lower peak value than the Helmholtz resonance. In between, the antiresonance is visible around 480 Hz as a maximum in the normalised resistance (blue, square, solid) and a negative slope of the reactance for the resonator with a flexible plate. This corresponds to a local minimum in the absorption. However, because the antiresonance is close to both resonances, the distinction is less clear in the reactance. In contrast, the simple Helmholtz resonator (blue, square, dashed) shows no antiresonance in this frequency range.

The additional absorption maximum around 430 Hz roughly corresponds to the first radial eigenfrequency of the flexible plate 350 Hz, stated in Table 4.3. The frequencies are not expected to fully agree because the flexible plate is embedded in the resonator system. For example, the air in the back cavity stiffens the plate, which raises the corresponding plate related resonance frequency. Consequently, in this configuration, the resonator acts as a double-degree of freedom resonator with the air mass in the perforated plate as one degree of freedom and the first mode of vibration of the flexible plate as the other. The compressible air volumes in the main and the back cavities can be thought of as springs connecting the masses.

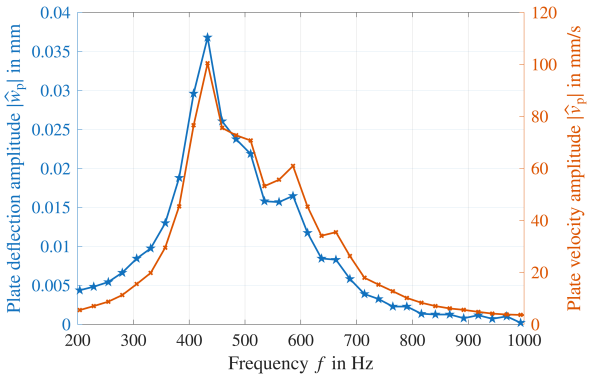

Figure 6.2.: Measured centre point plate deflection amplitude $|\hat{w}_\mathrm{p}|$ (blue) and plate velocity amplitude $|\hat{v}_\mathrm{p}|$ (red) for FS-I, $d_{\mathrm{p},1} = 15\,\mathrm{mm}$

The corresponding deflection and velocity spectra at the centre point of the flexible plate, as measured by the vibrometer, are presented in Fig. 6.2. The highest amplitudes were measured around 480 Hz. Therefore, the first resonance can be attributed to the flexible plate, whereas the second resonance is the Helmholtz resonance. Note that the deflection amplitude near the plate resonance $|w_\mathrm{p}| = 0.038\,\mathrm{mm}$ already exceeded 10 % of the plate thickness $h_\mathrm{p} = 0.3\,\mathrm{mm}$. Although these deflection amplitudes are still small compared to the plate thickness, excitation amplitudes of just 120 dB suggest plate deflections in the same range as the plate thickness, assuming that the plate deflection increases proportionally to

the incoming acoustic pressure wave amplitude. This may pose problems when attempting to model the flexible plate using linear plate theory, which assumes small deflections.

Additionally, the vibrometer measurements revealed that the plate was strongly excited around the Helmholtz resonance near 610 Hz as well. This is plausible because the flexible plate is driven by a pressure difference between the main and the back cavity, which is increased near the Helmholtz resonance. This also means that far from the Helmholtz resonance (excluding higher cavity modes), there is not enough pressure difference to excite the flexible plate. The antiresonance did not appear to affect the plate vibration. At frequencies higher than the Helmholtz resonance, no additional maxima are visible in the vibration spectra, and it can be concluded that no higher plate modes were excited in this configuration, as they are too far away from the Helmholtz resonance with little pressure difference between the cavities.

Influence of plate size

Based on this reasoning, if multiple plate eigenfrequencies are near the Helmholtz resonance, the resonator system should exhibit multiple absorption peaks. This was investigated using larger flexible plates with lower eigenfrequencies. Figure 6.3a displays the absorption spectra of the resonator system with three different circular clamped plates with diameters of $d_{\mathrm{p},1} = 15\,\mathrm{mm}$, $d_{\mathrm{p},2} = 22.8\,\mathrm{mm}$ and $d_{\mathrm{p},3} = 30\,\mathrm{mm}$, respectively.

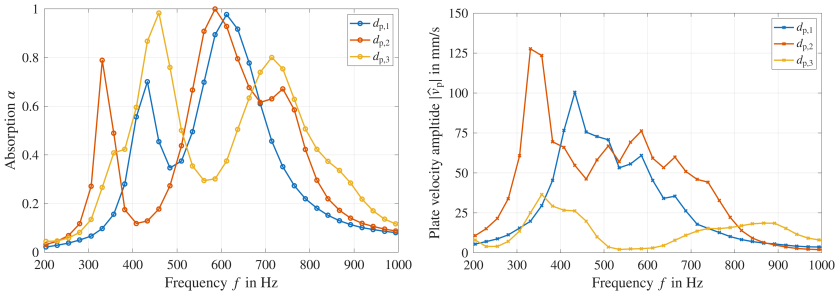

(a) Absorption α (b) Centre plate velocity amplitude $|v_{\mathrm{p}}|$

Figure 6.3.: Absorption α and plate velocity amplitude at the centre point $|v_{\mathrm{p}}|$ for different flexible plate diameters, FS-I

The absorption spectrum of the resonator with a plate with $d_{\mathrm{p},2}$ (red) consists of three local maxima around 330 Hz, 590 Hz and 740 Hz. Therefore, plates with a larger diameter indeed show a multimodal behaviour in this configuration. Assuming that the Helmholtz resonance did not change significantly, the second peak around 590 Hz can be interpreted as the Helmholtz resonance. Therefore, the intermediate plate provides a lower resonance below and above the Helmholtz resonance and a weaker shift of the Helmholtz resonance to higher frequencies than the small flexible plate.

The absorption spectrum of the resonator system with the largest plate $d_{\mathrm{p},3}$ (yellow) consists of even more characteristic points, which, however, are not as distinct. The two larger maxima around 460 Hz and 710 Hz are accompanied by slope changes around 350 Hz and 870 Hz. Note that these resonance frequencies and slope changes are similar but do not

match the isolated eigenfrequencies, listed in Table 4.3 because of the presence of the Helmholtz resonator and the back cavity. Therefore, a priori determined eigenfrequencies provide an estimate of the expected number of significant plate modes in the resonator system but are not sufficient to predict the complete resonance behaviour. The first slope change around 350 Hz may be a weakly excited first radial plate mode, even though one would expect its resonance frequency to be below that of $d_{\mathrm{p},2}$. A possible explanation is that the flexible plate with the largest diameter $d_{\mathrm{p},3}$ was slightly prestressed during application because a tensed plate is stiffened, and consequently, its resonance frequency is shifted towards higher frequencies. The second slope change around 870 Hz is most likely due to a weakly excited higher radial plate mode. The absorption maximum around 460 Hz is considered the Helmholtz resonance, following the downshift from $d_{\mathrm{p},1}$ (blue) to $d_{\mathrm{p},2}$ (red) with a similar distinct absorption amplitude. Therefore, the introduction of a large flexible plate has shifted the Helmholtz resonance towards lower frequencies by more than 150 Hz when comparing the resonator system with the largest and smallest flexible plate. Therefore, the flexible plate can either shift the Helmholtz resonance to higher or lower frequencies. The plate diameter is, consequently, a crucial parameter for tuning both the broadband, i.e., multimodal, and the system's low-frequency absorption.[2] The downshift of the Helmholtz resonance is due to the interaction between plate resonances and Helmholtz resonance.

The measured plate velocity for the same configurations is depicted in Fig. 6.3b. The highest velocity was measured for the configuration with a circular plate with a diameter of $d_{\mathrm{p},2} = 22.8\,\mathrm{mm}$ (red) near the first resonance around 330 Hz. The second highest plate velocity is near the Helmholtz resonance 590 Hz, whereas the velocity at the second plate resonance at 740 Hz is smaller. The plate velocity amplitude of the largest plate $d_{\mathrm{p},3} = 30\,\mathrm{mm}$ (yellow) was the lowest among all plate configurations. The highest values are around 350 Hz near the first slope change, which gives further reason to expect the first plate mode in this frequency region. Additionally, a substantial vibration can be detected at higher frequencies around 900 Hz, near the second slope change, which hints at a higher radial eigenmode nearby. Nevertheless, the vibration velocity of the largest plate diameter was only roughly one quarter of the values of the other plate diameters. Note that only the centre point velocity was measured using the vibrometer setup. Therefore, an explanation might be that excitation and consequently the acoustic velocity is more concentrated in the centre point for a smaller plate and more spread out for a larger plate. However, this does not explain why $d_{\mathrm{p},2}$ showed larger amplitudes than $d_{\mathrm{p},1}$. Another contributing factor might be that a larger plate is relatively less constraint by the clamped boundary than a smaller plate. Thus, no clear trend was observed between the vibration amplitude and plate size.

The changes in the normalised impedance are depicted in Fig. 6.4. The resistance in Fig. 6.4a is dominated by resistance peaks that differ for each plate diameter. They are not due to nonlinear face sheet losses because the amplitude of the incoming acoustic wave is too low. Additionally, nonlinear effects predominantly appear near the Helmholtz resonance, and the resistance peaks do not appear at the Helmholtz resonance frequency. In contrast, they can be attributed to the antiresonances between the system's resonances. The resonator with $d_{\mathrm{p},1}$ (blue) exhibits only one resistance peak around 480 Hz, that is between the plate resonance and the Helmholtz resonance. The resonator with $d_{\mathrm{p},2}$ (red)

[2] Technically, the volume of the main cavity is increased slightly by approximately 1.5 % because the plate holder is thicker than the flexible plate and blocks more volume for smaller plates, see Fig. 4.11. This minimal increase in volume is insufficient to explain the downshift of the Helmholtz resonance.

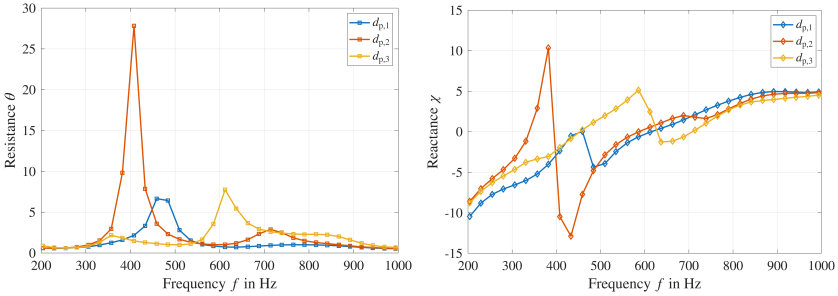

(a) Normalised resistance θ (b) Normalised reactance χ

Figure 6.4.: Normalised impedance $\zeta = \theta + \mathrm{i}\chi$ for different flexible plate diameters

exhibits one strong resistance maximum around 400 Hz and one weak maximum around 700 Hz above and below the Helmholtz resonance frequency around 600 Hz. The resonator system with the largest plate diameter $d_{\mathrm{p},3}$ (yellow) has three weak resistance maxima because the number of significant flexible plate modes increases with larger plate diameters.

The reactance of all resonators are similar in the low and high frequency limit where the reactance of the main cavity or the face sheet dominate.[3] The different flexible plates mainly alter the resonance behaviour between 300 Hz and 800 Hz. The intermediate plate $d_{\mathrm{p},2}$ (red) with the highest velocity amplitudes and the strongest antiresonance peak also showed the largest drop in the reactance around 400 Hz. This suggests that a higher plate velocity strongly affects the resonance as well as the antiresonance behaviour. However, the antiresonance resistance peaks of $d_{\mathrm{p},1}$ and $d_{\mathrm{p},2}$ have a similar magnitude, even though the centre plate velocity was much higher for $d_{\mathrm{p},1}$. Therefore, no clear trend between plate velocity and antiresonance behaviour, i.e., frequencies between resonances where little absorption is observed, can be found in the experimental data.

Influence of face sheet

The flexible plate is embedded into a resonator system comprising a face sheet, a main cavity, the flexible plate itself, and a back cavity. Therefore, the perforated face sheet is a crucial component for the acoustic performance. The absorption and plate velocity spectra under face sheet variation are depicted in Fig. 6.5a. The face sheet properties are stated in Table 4.1. Note that the scale of the plate velocity amplitude has been changed compared to Fig. 6.3 to better distinguish the individual lines.

The global maximum of the absorption (blue) is shifted towards lower frequencies in the resonator with FS-IV (FS-IV dashed). FS-IV ($h_{\mathrm{fs}} = 2\,\mathrm{mm}$, $d_{\mathrm{h}} = 8.9\,\mathrm{mm}$, $\sigma = 5.1\,\%$) has a higher porosity than FS-I (solid). In contrast, the flexible plate resonance around 430 Hz is not significantly altered by the Helmholtz resonance shift from 610 Hz to 560 Hz. However, the absolute value increases as the Helmholtz resonance is closer to the plate resonance. These trends can also be observed in the plate velocity spectrum, depicted in red in Fig. 6.5a. The plate velocity follows the Helmholtz resonance downshift and increases around the

[3] See the discussion for Fig. 2.3.

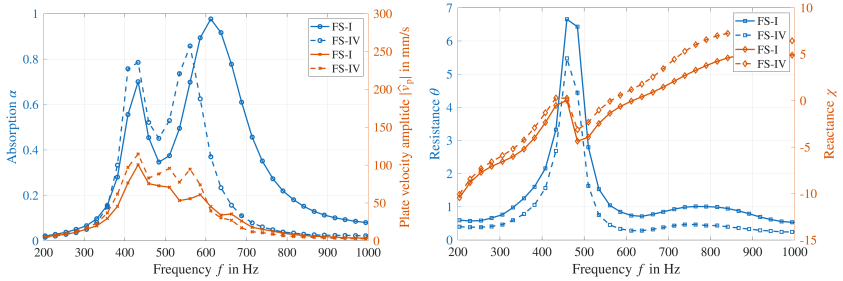

(a) Absorption α (blue) and plate vibration amplitude $|v_\mathrm{p}|$ (red) for face sheets I (solid) and IV (dashed).

(b) Normalised resistance (blue) and reactance (red) for face sheets I (solid) and IV (dashed).

Figure 6.5.: Effect of different face sheets on the resonator with the smallest flexible plate diameter $d_{\mathrm{p},1} = 15\,\mathrm{mm}$

lower resonance, whereas it is slightly decreased above 600 Hz. Overall, the plate velocity is higher when the plate mode and Helmholtz resonance are closer. Fig. 6.5b shows a comparison of the resonator impedance with variable face sheets, revealing that FS-I has a higher resistance than FS-IV due to more viscothermal losses in the face sheet holes. On the contrary, the reactance is higher for FS-IV, which leads to lower resonance frequencies. The reactance difference increases with frequency.

Similar trends can be observed in the absorption and plate velocity spectra under variations in the face sheet of the resonator with larger plates, as depicted in Fig. 6.6.

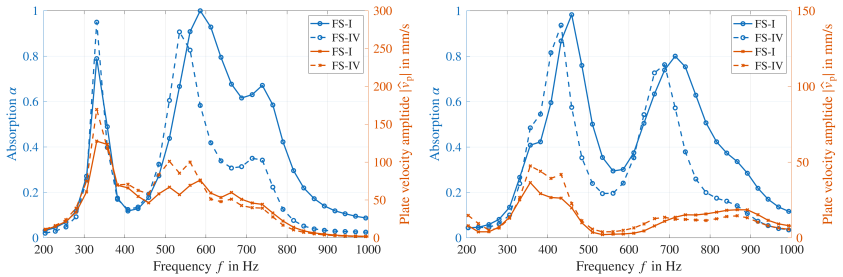

(a) Intermediate flexible plate diameter $d_{\mathrm{p},2}$

(b) Largest flexible plate diameter $d_{\mathrm{p},3}$

Figure 6.6.: Absorption α (blue) and centre point plate vibration amplitude $|v_\mathrm{p}|$ (red) for FS-I (solid) and FS-IV (dashed) of the resonator with a flexible plate of diameter $d_{\mathrm{p},2}$ (left) and $d_{\mathrm{p},3}$ (right)

Regarding the resonator with the intermediate flexible plate in Fig. 6.6a, the downshift of the Helmholtz resonance using FS-IV leads to increased absorption (blue) at the lower plate resonance near 350 Hz and to less absorption at the higher plate resonance near 750 Hz. This trend is also visible in the centre point plate velocity (red), indicating that the flexible plate is more effective for additional absorption when the Helmholtz resonance is closer. Similar trends can be observed for the resonator with the largest plate in Fig. 6.6b. Note

that the global maximum velocity is increased for both plates using FS-IV, which has a larger porosity. This suggests that higher porosities allow for stronger plate excitation as more acoustic energy is transmitted through the face sheet. This is investigated using cavity microphones in Section 6.2.

In short, the introduction of a flexible circular plate into a Helmholtz resonator extends the absorption spectrum to additional lower and higher resonance frequencies. The different resonances can be separated using a vibrometer setup. Both, the plate size and the face sheet, can be tuned in such a way, that the Helmholtz resonance frequency lies between multiple radial plate modes to obtain a broad absorption spectrum with multiple absorption peaks. The closer the Helmholtz resonance is, the more absorptive are the nearby plate resonances.

6.1.2. Comparison with analytical and numerical predictions

These experimental results are compared with the analytical and numerical predictions in this subsection. A comparison of the resonator with FS-I and the smallest circular plate is presented in Fig. 6.7. The analytical (red) and numerical models (yellow) largely agree with the experimental results (blue) in their predicted absorption of the resonator.

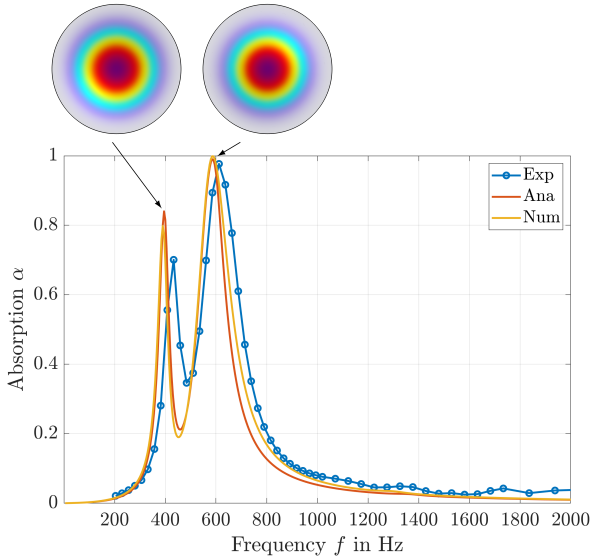

Figure 6.7.: Comparison between experimentally (blue), analytically (red) and numerically (yellow) determined absorption α and corresponding numerically determined plate deflection shapes for resonator with FS-I, $d_{\mathrm{p},1}$

However, the analytical model predicts a slightly higher absorption near the plate resonance and the numerical model predicts a slightly higher absorption above the Helmholtz resonance, respectively. Both models predict a lower plate resonance and Helmholtz resonance than the experimental data (blue). A possible explanation for this is that the flexible plate was slightly prestressed in the experiment, which increases the effective stiffness, as discussed in

Section 4.5. The numerically determined deflection shape of the flexible plate at 400 Hz in Fig. 6.7 strongly resembles the first radial eigenmode in Fig. 2.10. Red indicates a high deflection, green-blue a moderate deflection and grey no deflection. The plate deflection shape at the Helmholtz resonance at 610 Hz is very similar to the aforementioned deflection shape because the eigenfrequency of the second radial eigenmode (1358 Hz, see Table 4.3) is too high to contribute significantly.

Similar trends can be found for the absorption spectra with FS-IV in Fig. 6.8. Both the analytical and numerical models largely agree and correctly predict the downshift of the Helmholtz resonance from 610 Hz to 550 Hz. However, they differ from the experimental data in so far as that they predict a stronger plate resonance at lower frequencies (390 Hz instead of 410 Hz). It seems plausible that the plate resonance in the experiment was between the two measurement frequencies and that the peak absorption in the experiment was higher. Another source of error is the clamped boundary condition in the analytical and numerical model, whereas in reality the boundary condition might be somewhere between clamped and simply supported. However, a simply supported plate has lower eigenfrequencies than a clamped plate, see Table 2.1.

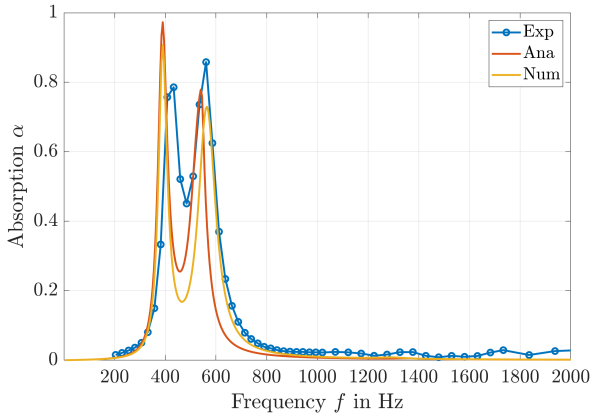

Figure 6.8.: Comparison between experimentally (blue), analytically (red) and numerically (yellow) determined absorption α for the resonator with FS-IV, $d_{\mathrm{p},1}$

The analytical (red) and numerical (yellow) models align in their absorption prediction for the resonator with an intermediate sized flexible plate in Fig. 6.9, although the numerical model predicts slightly higher absorption for the higher resonance peak near 700 Hz. The models generally agree with the experimental data (blue) as three absorption peaks are predicted and measured. Additionally, the predicted lower plate resonance frequency almost perfectly agrees with the measurement result. However, the resonance frequency of the Helmholtz resonance and the higher plate resonance was measured higher than predicted. The absorption of the higher plate resonance is overestimated as well. The reason for the discrepancy is unclear, as a possible pretension of the flexible plate would affect both additional plate resonances. Note that the predictions agree with the measurement results for higher frequencies, i.e. no additional absorption due to even higher plate resonances. The numerically determined deflection shapes in Fig. 6.9 at the lower resonance peak are very similar to that of the first radial plate eigenmode, whereas the plate deflection shape

of the third resonance peak resembles the second radial plate eigenmode in Fig. 2.10. The deflection shape at the Helmholtz resonance around 600 Hz in between is a blend of both eigenmodes. Higher azimuthal modes in the same frequency range were not excited and did not contribute to the overall absorption as their mean displacement is zero, which is in agreement with the discussion in Section 2.4.2.

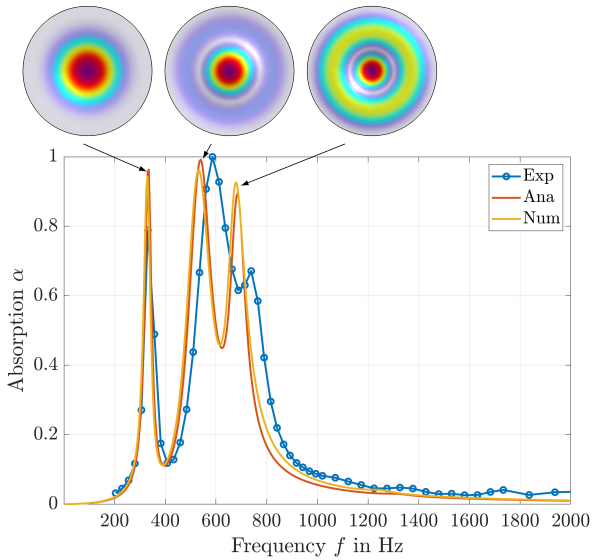

Figure 6.9.: Comparison between experimentally (blue), analytically (red) and numerically (yellow) determined absorption α and corresponding numerically determined plate deflection shapes for the resonator with FS-I, $d_{\mathrm{p},2}$

Similar results can be found for the absorption of the resonator with the largest plate, as depicted in Fig. 6.10. The analytical (red) and numerical (yellow) models mostly align in their prediction, although they differ near a higher plate resonance around 800 Hz, where the numerical model predicts a higher absorption at slightly lower frequencies. Both predictions agree reasonably well with the measurement data (blue), but the differences are larger than those for the small plates. The first small absorption peak in the predictions around 300 Hz is barely visible as a slope change around 350 Hz in the measurement results. The corresponding deflection shape resembles the first radial eigenmode, but a faint second ring is also visible. Predictions and experimental results agree very well for the Helmholtz resonance around 500 Hz. Thus, the downshift of the Helmholtz resonance is correctly predicted. The frequencies of the third and fourth absorption peaks around 700 Hz and 900 Hz is lower in the predictions. This gives further reason to assume that the plate was slightly prestressed in the experiment, as all plate resonance predictions are lower than the measured values. The plate deflection shapes of the higher absorption peaks resemble each other. They differ from the eigenmodes, indicating a stronger interaction between Helmholtz resonator and flexible plate for larger diameters.

The absorption spectrum for high incoming sound pressure levels of 130 dB of the resonator

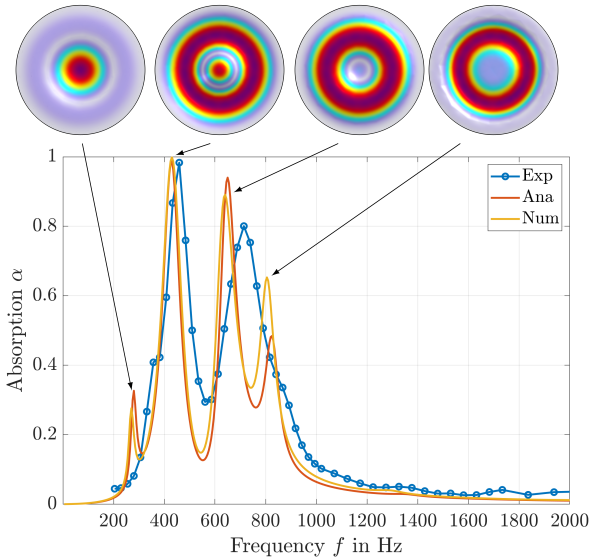

Figure 6.10.: Comparison between experimentally (blue), analytically (red) and numerically (yellow) determined absorption α and corresponding numerically determined plate deflection shapes for the resonator with FS-I, $d_{\mathrm{p},3}$

with FS-I and $d_{\mathrm{p},1}$ is depicted in Fig. 6.11a. In comparison with the absorption at 100 dB (purple), the peak absorption of the Helmholtz resonance is reduced but the bandwidth is increased. The plate resonance is shifted to higher frequencies, and the bandwidth is also increased. This might be due to a stiffening effect of high deflection amplitudes. The analytical model prediction agrees very well with the experimental data for the Helmholtz resonance. Note that the analytical and numerical models only consider the effect of higher sound pressure levels in the face sheet. Therefore, they cannot predict the plate resonance shift to higher frequencies because both models are restricted to small plate deflections. Additionally, the numerical model predicts the absorption near the Helmholtz resonance less accurately in this case. The plate vibration velocities exceeded the measurement range of the vibrometer, and no usable vibrometer data were acquired for these high incoming sound pressure levels.

The general absorptive behaviour – the peak absorption at the Helmholtz resonance is reduced but the bandwidth is increased – is similar for the resonator with $d_{\mathrm{p},2}$ in Fig. 6.11b. The lower and higher plate resonances are shifted to higher frequencies because of the high sound pressure level, which is not accurately represented by the analytical and numerical models.

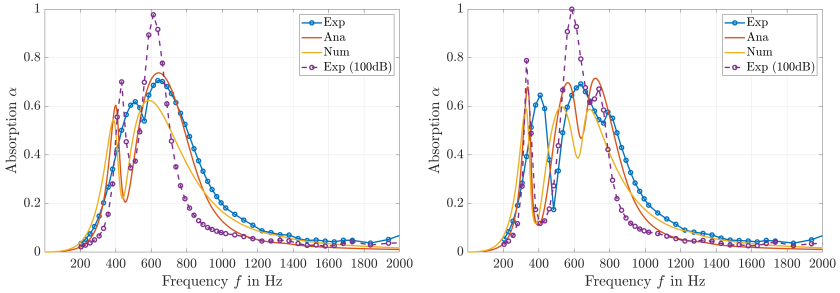

(a) FS-I, $d_{\mathrm{p},1}$ (b) FS-I, $d_{\mathrm{p},2}$

Figure 6.11.: Comparison between experimental (blue), analytically (red) and numerically (yellow) determined absorption at high sound pressure level $p_{\mathrm{in}} = 130\,\mathrm{dB}$. The linear case (purple) is given as a reference.

Summed up, the analytical and numerical models align for most configurations with different plate sizes and face sheets. They agree with the experimental data for different face sheets and small and intermediate plates, which gives confidence that the relevant physical effects are captured in the models. However, larger differences were observed for a resonator with a larger plate or excited with high sound pressure levels. The latter is expected because the analytical and numerical models consider the nonlinear effects of the face sheet but not those of the flexible plate.

6.2. Helmholtz resonator with a rectangular plate and cavity microphones

This section presents the results of the modular resonator with a rectangular flexible plate obtained at D-NIT.[4] In contrast to DUCT-NIT, D-NIT has the same cross section area as the modular resonator system and allows the measurement of a larger frequency range. Additional microphones are placed inside the main and back cavities to separate plate-related contributions from the overall characteristics. Three different face sheets and three different material samples with a rectangular shape were tested and the results are presented in the following.

6.2.1. Experimental results

Figure 6.12 displays the experimental results of the baseline configuration of the resonator system with face sheet I (FS-I, $h_{\mathrm{fs}} = 2\,\mathrm{mm}$, $d_{\mathrm{h}} = 1.5\,\mathrm{mm}$, $\sigma = 2.6\,\%$) and a rectangular ($15\,\mathrm{mm} \times 26\,\mathrm{mm}$) flexible wall made of TPU. The blue line represents the measured overall absorption coefficient α_{tot} as determined by the plane wave decomposition using the three channel microphones in D-NIT. The dashed orange line represents the measured absorption coefficient $\alpha_{\mathrm{p,cav}}$ that includes the isolated effect of the back cavity and the plate holder with the flexible plate. $\alpha_{\mathrm{p,cav}}$ is determined using the microphones MC1 and MC2 installed inside the main cavity, see Figs. 4.6 and 4.7.

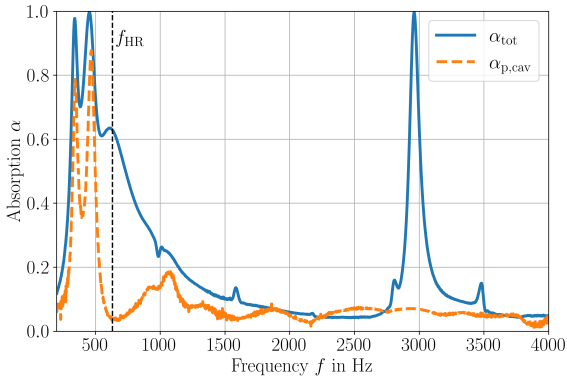

Figure 6.12.: Overall absorption (solid, blue) and isolated absorption of the flexible plate and back cavity inside the same resonator system (dashed, orange) with FSI and rectangular TPU plate

The overall absorption spectrum (blue) shows high absorption around 360 Hz, 470 Hz and to a minor degree around 630 Hz, and 1100 Hz. Therefore, the resonator with a rectangular plate inhibits stronger low-frequency resonances than the circular plate. The absorption spectrum of the plate and back cavity (orange) displays only plate-related resonance

[4] Parts of this section were published in Kohlenberg and Knobloch[321].

absorption peaks around 360 Hz, 470 Hz and 1100 Hz. The theoretical Helmholtz resonance frequency calculated using Eq. (2.27) is marked with a dashed black vertical line. The Helmholtz resonance is only visible in the overall absorption but not in the plate-related absorption. Therefore, both contributions can be successfully separated using additional cavity microphones. At the Helmholtz resonance, the main cavity compresses uniformly, meeting the resonance condition for a maximum pressure at the rear and a maximum particle velocity at the face sheet. This resonance condition is also fulfilled when the main cavity is not compressed uniformly but with a pressure node located in the middle of the cavity, specifically at a frequency of approximately 3000 Hz.[5] This manifests as a sharp absorption peak within the overall absorption spectrum.

The corresponding normalised impedance $\zeta = \theta + \mathrm{i}\chi$, focused on frequencies below 1500 Hz, is displayed in Fig. 6.13.

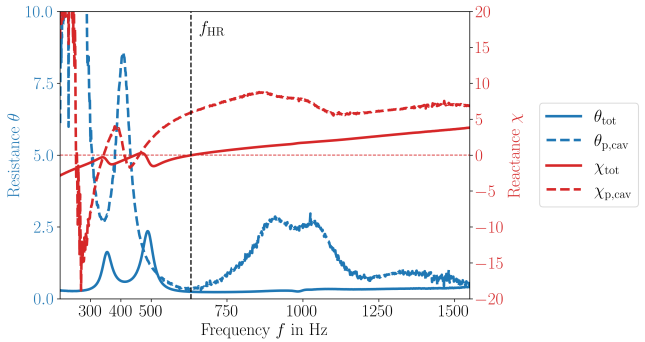

Figure 6.13.: Overall impedance (solid) and isolated impedance of the flexible plate and back cavity inside the same resonator system (dashed) with FSI and rectangular TPU plate

The overall impedance θ_{tot} and χ_{tot} is plotted as solid lines. The overall impedance reflects the multi-resonant behaviour with three resonance points below 800 Hz, i.e. around around 360 Hz, 470 Hz and 630 Hz, corresponding to nearly zero-crossings of the reactance (red, solid) with a positive slope indicating high absorption. The overall reactance is rather smooth with less pronounced resonances below 700 Hz. A zero-crossing of the reactance with a negative slope corresponds to an antiresonance with a sharp increase in the resistance, resulting in a reduced absorption. The overall resistance (blue, solid) shows local maxima at the antiresonances between the plate resonances and the Helmholtz resonances around 350 Hz and 500 Hz. Note that in the normal incidence case, maximum absorption is achieved at a purely real valued impedance of $\zeta = 1 + \mathrm{i}\,0$.

The complex behaviour of the isolated plate and back cavity $\theta_{\mathrm{p,cav}}$ and $\chi_{\mathrm{p,cav}}$ is measured at the same time as the overall impedance. It is dominated by spikes below 500 Hz. The

[5] This is similar to a quarter wave resonator, which also has higher resonances for example when $^3/_4{}^{\mathrm{th}}$ of the acoustic wavelength matches the cavity depth. However, the resonance frequency at 3000 Hz is not a harmonic of the Helmholtz resonance frequency $f_{\mathrm{HR}} = 630$ Hz because it is not merely a standing wave of the cavity, but a resonant system of the cavity combined with the face sheet, see Fig. 2.3. The surface pressure in the resonator cavities for this frequency is shown at the end of this section in Fig. 6.22e.

reactance (red, dashed) is very high for very low frequencies below 300 Hz that indicates that the flexible plate is sound-hard for low frequencies. However, the data quality appears to be poor due to the position of the microphones inside the resonator, rendering the results highly susceptible to phase inaccuracies at very low frequencies with long wavelengths. Between 300 Hz and 600 Hz the reactance exhibits multi-resonance behaviour as there are multiple zero-crossings and slope changes due to flexible wall resonances. The reactance above 600 Hz rises with a soft slope change around 1000 Hz and seems to reach a plateau for higher frequencies.

The corresponding resistance of the flexible plate and back cavity (blue, dashed) has peaks near the antiresonances, i.e., reactance with a negative slope at 250 Hz, 450 Hz and near 1000 Hz. The resistance has one pronounced antiresonance peak around 450 Hz between the plate resonances but lacks the antiresonance peak due to the Helmholtz resonance. Therefore, the comparison of the overall and plate-cavity impedances further helps to separate the contributions and analyse plate characteristics that are covered by the face sheet.

To further investigate the interaction between Helmholtz and plate resonances, the Helmholtz resonance, i.e., the face sheet was changed. The results for the system with the same flexible plate but face sheet II are presented in Fig. 6.14.

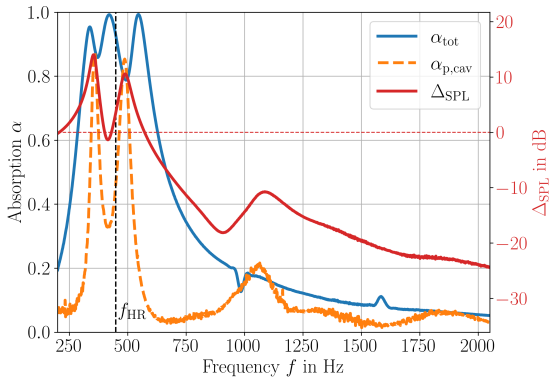

Figure 6.14.: Overall absorption (solid, blue), isolated absorption of the flexible plate and back cavity inside the same resonator system (dashed, orange), and sound pressure difference between the main and the back cavity (solid, red) of the resonator with FS-II and rectangular TPU plate

Face sheet II (FS-II, $h_{\mathrm{fs}} = 2\,\mathrm{mm}$, $d_{\mathrm{h}} = 1\,\mathrm{mm}$, $\sigma = 1.2\,\%$) has a lower porosity and accordingly a lower Helmholtz resonance. The effect of the lower porosity can be observed in Fig. 6.14, as the theoretical Helmholtz resonance frequency (dashed) has shifted down to around 450 Hz. All low-frequency absorption peaks of the entire resonator system (blue) have been changed to lower frequencies. However, the absorption spectrum of the back cavity and flexible plate, shown in orange, indicates that the flexible plate's response remains unchanged with different face sheets. Note that the orange plate-cavity isolated absorption peaks occur at higher frequencies than the blue overall absorption peaks, but at the same

frequencies as in the configuration with FS-I in Fig. 6.12. Consequently, altering the face sheet leads to a change in the overall response, resulting in additional absorption peaks that diverge from the plate resonances, yet the underlying plate behaviour remains unaltered. Viewed from the outside, the Helmholtz resonance shifted the lower plate resonance towards lower frequencies, i.e. 360 Hz to 335 Hz and the higher plate resonance to higher frequencies, i.e. 490 Hz to 550 Hz.[6] The dynamic pressure difference $\Delta_{\mathrm{SPL}} = |p'_{\mathrm{BC1}}| - |p'_{\mathrm{MC1}}|$ (red) as measured by the microphones in the main and the back cavities (MC1 and BC1) strongly correlates with $\alpha_{\mathrm{p,cav}}$. The pressure in the back cavity increased near the plate resonances at 350 Hz, 500 Hz and 1000 Hz. The incoming acoustic wave excites the flexible plate, which subsequently radiates sound into the back cavity, which is then reflected back by the rigid termination. This creates a dynamic pressure difference between the main and the back cavity in the steady state, which can be identified as the driving force for the plate vibration and used to identify plate resonances. If the flexible plate is excited far away from a resonance, no dynamic pressure difference is observed, and the acoustic wave is reflected back to the main cavity. In addition, the pressure is higher in the back cavity than in the main cavity below 600 Hz and vice versa above. This can be explained with the help of the impedance of the baseline configuration in Fig. 6.13. The resistance and the reactance of the plate-back-cavity subsystem increase with higher frequencies, showing that the flexible plate reflects more acoustic energy back, resulting in a higher dynamic pressure in the main cavity and a lower dynamic pressure in the back cavity.

A similar behaviour can be found in Fig. 6.15 with face sheet III (FS-III, $h_{\mathrm{fs}} = 1\,\mathrm{mm}$, $d_{\mathrm{h}} = 1\,\mathrm{mm}$, $\sigma = 4.1\,\%$) and a higher Helmholtz resonance. In this case, the Helmholtz resonance near 1000 Hz is distinct from the first plate resonances, and the overall absorption at these peaks is very similar to the plate and back cavity resonances alone. In this case, the resonances act independently of each other. The pressure difference is very similar to Fig. 6.14, which means that it is largely independent of the face sheet and, consequently, of the Helmholtz resonance. As the pressure difference is thought to be the driving force of the plate oscillations, this means that a higher porosity does not necessarily lead to a stronger plate excitation.

The absorption and pressure difference for a resonator with a flexible plate made of EBA with the same plate geometry ($15\,\mathrm{mm} \times 26\,\mathrm{mm}$) is depicted in Fig. 6.16. EBA has a slightly lower Young's modulus ($E = 10.5\,\mathrm{MPa}$) but is thicker ($h_{\mathrm{p}} = 0.55\,\mathrm{mm}$). The overall absorption is expected to be slightly shifted towards higher frequencies because the plate eigenfrequencies are higher than for TPU, see Table 4.3.

The resonator system displays two plate resonances around 500 Hz and 800 Hz and the Helmholtz resonance in between around 600 Hz. The local maxima of $\alpha_{\mathrm{p,cav}}$ coincide with the ones in α_{tot} without a significant shift. An additional plate resonance around 1750 Hz is only visible in $\alpha_{\mathrm{p,cav}}$ and Δ_{SPL} but not in the overall absorption α_{tot}. $\alpha_{\mathrm{p,cav}}$ appears to be slightly negative around 1100 Hz. It is theoretically possible that the flexible plate acted like a loudspeaker and generated sound. Since there is no other energy reservoir, e.g. grazing flow, the generated sound would need to stem from other frequencies. However, for

[6] Without any prior knowledge, one could also think that the Helmholtz resonance is shifted towards higher frequencies, i.e., the highest frequency absorption peak is actually the Helmholtz resonance and the plate resonances are both shifted to lower frequencies. This can be dismissed with the help of the parameter study presented later in Fig. 6.25c, where the gradual change of the Helmholtz resonance with a porosity change was evaluated.

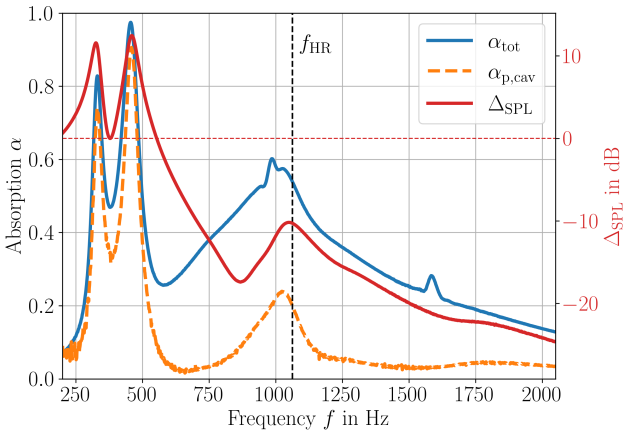

Figure 6.15.: Overall absorption (solid, blue), isolated absorption of the flexible plate and back cavity inside the same resonator system (dashed, orange), and sound pressure difference between the main and the back cavity (solid, red) of the resonator with FS-III and rectangular TPU plate

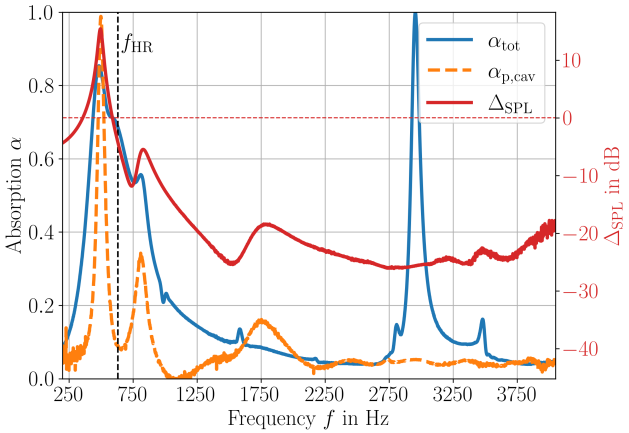

Figure 6.16.: Overall absorption (solid, blue), isolated absorption of the flexible plate and back cavity inside the same resonator system (dashed, orange), and sound pressure difference between the main and the back cavity (solid, red) of the resonator with FS-I and rectangular EBA plate

$\alpha_{\mathrm{p,cav}} < 0.1$ and $f < 1500\,\mathrm{Hz}$ significant variation can be observed in the absorption. A more convincing explanation is that the signal-to-noise ratio was too low, and near-field

effects distorted the measured data, with absorption values near zero being slightly negative because of random error. The second Helmholtz resonance around 3000 Hz is the same as that of the TPU plate and is therefore largely independent of the flexible plate material. In addition, the flexible plate behaviour is not affected by the second Helmholtz resonance, because $\alpha_{\mathrm{p,cav}}$ and Δ_{SPL} remain unchanged near 3000 Hz.

The resonator with a flexible metal plate of aluminium only showed significant overall absorption α_{tot} near the Helmholtz resonance around 630 Hz, as depicted in Fig. 6.17. In contrast, $\alpha_{\mathrm{p,cav}}$ has multiple absorption peaks at 1900 Hz, 2200 Hz, 3300 Hz and 3800 Hz. Again, they also appear as increased back cavity pressure in Δ_{SPL}, but the net pressure difference is always negative. Consequently, the aluminium plate appears to be too reflective to significantly contribute to the overall absorption. As a result, aluminium plates are not suitable in this configuration for achieving further absorption.[7]

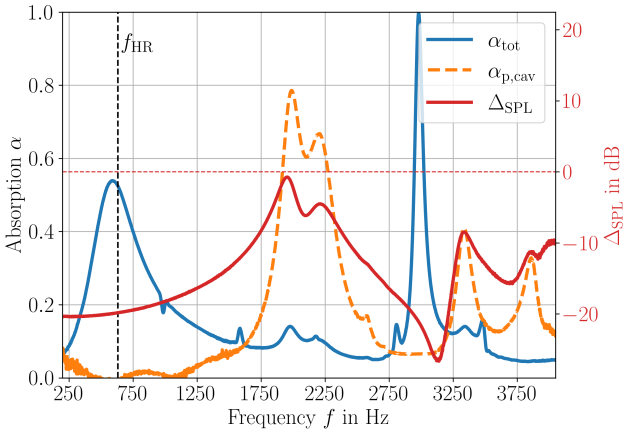

Figure 6.17.: Overall absorption (solid, blue), isolated absorption of the flexible plate and back cavity inside the same resonator system (dashed, orange), and sound pressure difference between the main and the back cavity (solid, red) of the resonator with FS-I and rectangular aluminium plate

6.2.2. Comparison with analytical and numerical predictions

A comparison between measurements and predictions of the baseline configuration is presented in Fig. 6.18. Excellent agreement between the absorption spectra determined experimentally (blue), analytically (red), and numerically (yellow) can be found for both the plate-related resonances and the Helmholtz resonance. Thus, the analytical and numerical model are able to capture the relevant phenomena. The models slightly underestimate the absorption near the Helmholtz resonance at approximately 600 Hz. The numerical

[7] However, this result suggests that a plate resonator ($\alpha_{\mathrm{p,cav}}$, i.e., flexible plate and back cavity without a face sheet) with a metal plate may absorb more sound than combined with a face sheet, albeit at higher frequencies.

model predicts slightly higher absorption near the higher plate modes around 1000 Hz than the analytical model. The experimentally determined spectrum is between the two predicted spectra. Both models accurately capture the frequency and amplitude of the second Helmholtz resonance.

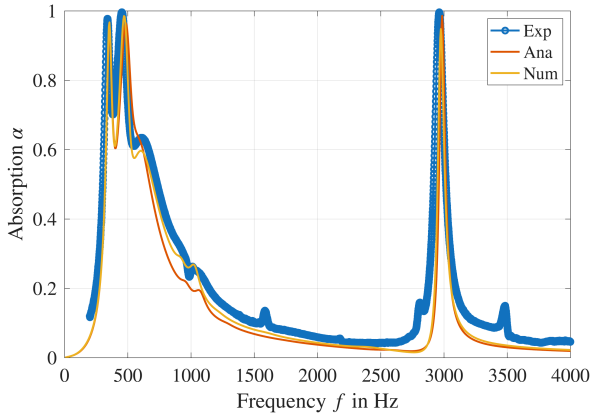

Figure 6.18.: Comparison between experimentally, analytically and numerically determined absorption of FS-I with TPU plate

A closer look at the corresponding impedance in Fig. 6.19, focusing on the low-frequency region, also shows an excellent agreement. Therefore, both the resonance as well as the anti-resonance behaviour is modelled precisely. Minor discrepancies near the first resonance at 360 Hz in both reactance (red) and resistance (blue) are apparent and may be attributed to experimental uncertainties such as material properties or uncontrolled flexible wall tension.

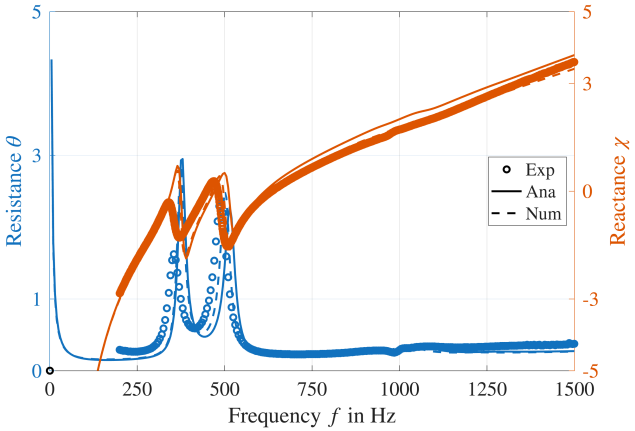

Figure 6.19.: Comparison between experimentally, analytically and numerically determined impedance of FS-I with TPU plate

The absorption spectra for the resonators with different face sheets, determined both experimentally and numerically, are shown in Fig. 6.20. The effect of changing the face sheet is captured very well in the numerical setup too, as the lines agree very well. However, the models forecast a more pronounced decrease in absorption at the anti-resonance than what was observed. The absorption of the higher plate mode around 1000 Hz is slightly better captured in the numerical model, especially when the Helmholtz resonance is near in Fig. 6.20b.

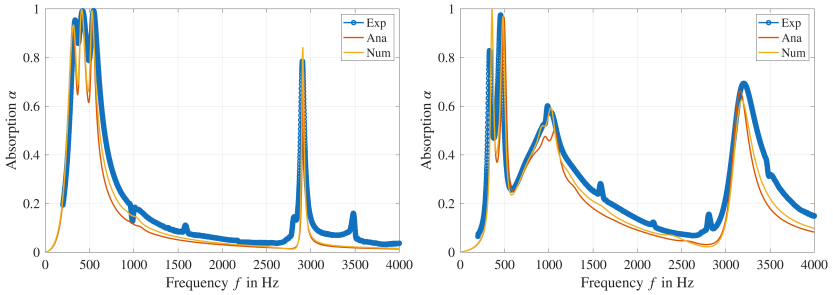

(a) FS II (b) FS III

Figure 6.20.: Comparison between numerical and experimental results with variable face sheets and rectangular TPU plate

A less clear result is found when the plate material is changed, as depicted in Fig. 6.21. The main absorption trends for a resonator system with a flexible plate of EBA, as shown in Fig. 6.21a generally agree, as three local maxima can be observed in all absorption spectra below 1000 Hz. The first and third are associated with plate resonances. However, a discrepancy exists between the experimentally (blue), analytically (red), and numerically (yellow) calculated absorption values, as the analytical and numerical predictions are shifted slightly towards lower frequencies than the experimental results. A possible explanation is that the stiffness of the material sample in the experiment was higher than that in the simulation. However, they mainly differ from the experimental results near the Helmholtz resonance around 600 Hz.

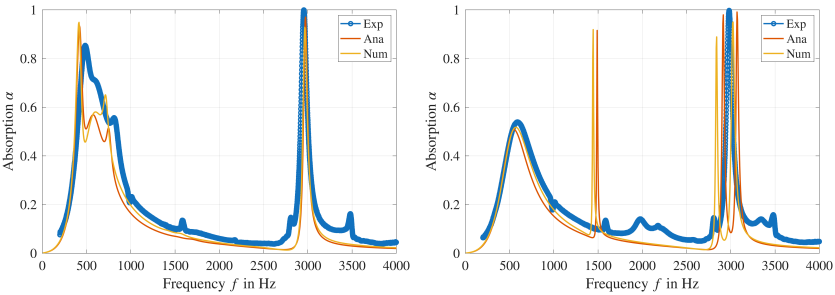

(a) EBA (b) Aluminium

Figure 6.21.: Comparison between numerical and experimental results with FS-I and variable plate material

Two key findings can be derived from the resonator with a metal plate, as shown in figure Fig. 6.21b: The predicted Helmholtz resonance-associated absorption maxima are in good agreement with the experimentally determined spectrum (blue). In contrast, the plate resonance-associated absorption peaks were not observed in the experimentally determined absorption. However, additional small absorption peaks are visible around 2000 Hz and 3500 Hz, which might indicate that the plate appeared stiffer in the experiment and was stronger damped due to boundary effects than simulated. The analytical and numerical models indicate a Helmholtz resonance occurring at approximately 600 Hz, accompanied by sharp absorption peaks near 1450 Hz, 2800 Hz and another resonance near 3000 Hz. The plate-associated absorption peaks are very narrow because of the low mechanical losses inside the aluminium plate. The discrepancy between predicted and not observed plate-related peaks may result from friction losses at the plate's edges, which may reduce the peak absorption amplitudes but are neglected in the models, as the analytical and numerical models only account for internal friction losses inside the material with a complex Young's modulus. Because the loss coefficient is very low for aluminium, considering other friction sources may be more important for aluminium than for plates with high internal damping such as TPU or EBA.

The surface pressure in the resonator cavities and the resulting plate deflection of the reference configuration are illustrated in Fig. 6.22. The numerical simulations are consistent with the experimental data in predicting a greater dynamic pressure in the back cavity for the two lowest absorption peaks at 330 Hz and 460 Hz, as well as predicting a lower dynamic pressure at higher frequencies. The plate deflection shapes for 330 Hz and 460 Hz closely resemble the first and third eigenmodes in Fig. 2.12.

For the circular plate, the plate deflection shape at the Helmholtz resonance in Fig. 6.9 was a blend between two adjacent eigenmodes, which is not the case for the rectangular plate in Fig. 6.22c. On first glance, the plate deflection shape at the Helmholtz resonance at 605 Hz resembles the second eigenmode. However, both deflection peaks point in the same direction towards the back cavity, whereas the two maxima of the second eigenmode point in different directions, see Fig. 2.12. The deflection shape at the minor absorption peak at 1015 Hz loosely resembles the third eigenmode in the lateral direction. The pressure node inside the cavity is visible for the second Helmholtz resonance at 2975 Hz with minimal plate excitation. Similar results can be obtained for the other configurations.

Briefly summed up: The introduction of a rectangular plate added strong additional low-frequency absorption to the Helmholtz resonator for plates made of TPU and EBA. In contrast, aluminium was not found to be a good alternative to polymers due to its low damping properties. The addition of cavity microphones enabled further insight into the system's behaviour. With a plane wave decomposition inside the resonator the contribution of the plate and the Helmholtz resonator can be separated. It was shown that in certain configurations, the overall resonance behaviour is different from the individual resonances. The data from the microphones in the main and the back cavities showed that the pressure difference between the cavities invokes plate oscillations. In conclusion, both the analytical and the numerical model capture the absorption behaviour of the resonator system reasonably well. However, face sheet effects are captured more reliably than plate material effects. This might be due to varying manufacturing material parameters, such as thickness, complex stiffness, or imperfect mounting conditions in the experiments. The analytical model allows for fast impedance and absorption prediction of the resonator system, whereas the numerical model enables additional analysis of the spatial pressure and plate deflection distributions.

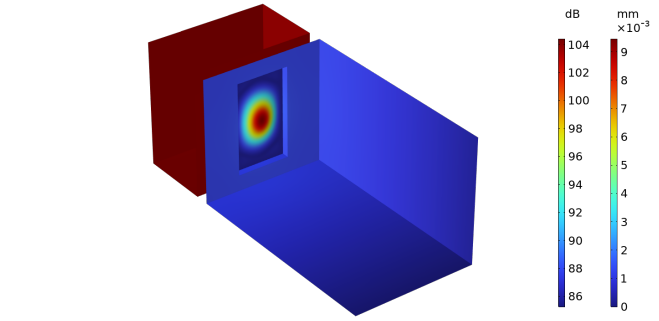

(a) 330 Hz

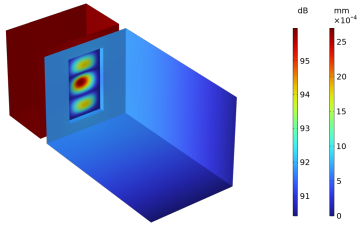

(b) 460 Hz

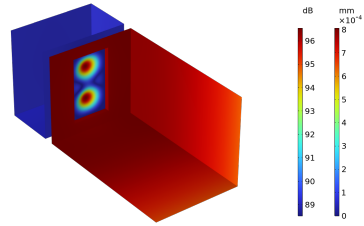

(c) 605 Hz

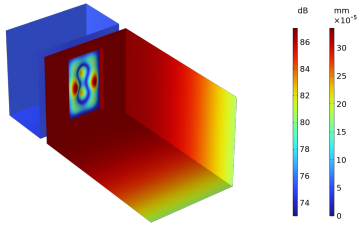

(d) 1015 Hz

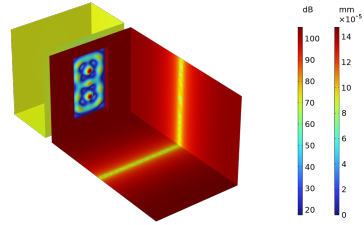

(e) 2975 Hz

Figure 6.22.: Surface pressure and plate deflection for FS-I with TPU plate for different characteristic frequencies

6.3. Analytical parameter study

The favourable comparison between the model predictions and the experimental results enable a parameter and sensitivity study of the relevant parameters which is presented in the following. The analytical and numerical models were used to investigate the influence of the parameters of the face sheet, cavities, and plate properties to evaluate their relative contribution towards the overall damping characteristics. The goal of this parameter study is to investigate whether these parameters affect the Helmholtz resonance, plate resonances and the interaction between both resonances. This addresses the second research question, i.e. how the resonator can be modelled and in which configurations the analytical or the numerical model is more appropriate. A strong interaction is expected when the resonance frequencies coincide, see Section 2.5, for which a fine resolution of the parameter is needed, which is not feasible with experimental investigations. Additionally, this parameter study helps to identify parameters to tune the system towards either broadband or low-frequency damping. Results from the analytical model are compared to the numerical predictions to show the applicability and limits of the analytical model with a special focus on the interactions between Helmholtz resonance and plate resonances.

The baseline values and the corresponding value range of the varied parameters are listed in Table 6.1.

Table 6.1.: Parameter list

Parameter	Baseline	Value range	Unit
	Face sheet		
Thickness h_{fs}	2	0.5 – 2.5	mm
Hole diameter d_{h}	1.5	0.7 – 2	mm
Porosity σ	2.6	1 – 20	%
	Cavities		
Main cavity depth l_{cav_1}	60	5 – 70	mm
Back cavity depth l_{cav_2}	15	1 – 20	mm
Cavity ratio $l_{\mathrm{cav}_2}/(l_{\mathrm{cav}_1} + l_{\mathrm{cav}_2})$	0.2	0.01 – 0.99	-
	Plate material		
Density ρ_{p}	1080	700 – 1200	kg m^{-3}
Loss coefficient η	0.1	0 – 0.5	-
Young's modulus E	16	1 – 1000	MPa
	Plate geometry		
Thickness h_{p}	0.3	0.1 – 1	mm
Square side length $l_{\mathrm{xy,p}}$	(15; 26)	10 – 35	mm
Diameter d_{p}	15	10 – 35	mm
	Other		
Incident SPL p'_{in}	90	90 – 130	dB
Temperature T	20	−20 – 100	°C

Only one parameter was changed per variation because the goal was to highlight the influence of individual parameters rather than global optimisation. The remaining parameters correspond to the baseline case. The only exceptions are the variation of both the main and the back cavity sizes with a fixed total depth, as well as the variation of the temperature which affects the speed of sound, the Young's modulus and the loss factor. The baseline values were derived from the experimental baseline resonator, as investigated in the previous section. The face sheet parameter limits were chosen to be in agreement with reasonable liner geometry limits from literature[39]. The plate sizes are bounded by the cavity cross section, which remains unchanged at $35\,\mathrm{mm} \times 35\,\mathrm{mm}$. The baseline plate size $15\,\mathrm{mm} \times 26\,\mathrm{mm}$ is the same as the rectangular one from the experimental investigations from the previous section. The plate material parameter limits are reasonable estimates for elastomers and polymers, see Fig. 4.9. The densities of metals are higher, e.g. aluminium: $2700\,\mathrm{kg/m^3}$ or steel $7850\,\mathrm{kg/m^3}$. They are outside the investigated parameter range because they also have a much higher Young's modulus and aluminium was not found to be a good plate material in the experimental investigations presented in the previous section. The temperature was varied to investigate its simultaneous effect on the temperature dependent material properties of TPU and the Helmholtz resonance.

These parameters were varied using both the analytical and the numerical models. Calculating all numerical variations of Table 6.1 with a resolution of approximately 50 steps per parameter range took about 10 h for the Helmholtz resonator with the circular plate and 28 h for the Helmholtz resonator with the rectangular plate, despite exploiting double symmetries, i.e., quarter models, which were used to speed up the numerical calculations, which are presented in Section A.3. The numerical results were interpolated in a post-processing step to reduce the effect of the low parameter step size.

On the other hand, the analytical solutions have a five-fold higher resolution of 250 steps per parameter while still being 10-20 times faster to calculate than the numerical solutions. Calculating all analytical variations of Table 6.1 with a resolution of 250 steps per parameter took about 3 min for the Helmholtz resonator with the circular plate and 110 min for the Helmholtz resonator with the rectangular plate. The rectangular case takes longer because the determination of the plate impedance involves numerical integration. The derivatives of the deflection like $\frac{\partial^4 X_m}{\partial x^4}$ in Eq. (2.83) were determined analytically once and then implemented in the code to speed up the calculations.

The influence of the face sheet and cavities were very similar for the resonator with a circular or rectangular plate. Hence, for the sake of brevity, only the results of the analytical method of the resonator with a rectangular flexible plate are presented here. Naturally, the exception is the variation of the plate diameter, which was calculated using the circular plate model. A comparison between the prediction results of the analytical and numerical model for selected parameters is shown at the end of the next section.

6.3.1. Face sheet parameters

The normal incidence absorption and impedance of the resonator with a variable *face sheet hole diameter* are depicted in Fig. 6.23. The absorption spectra of the parameters with the highest, lowest, and mean variations are displayed. All resistance (solid) and reactance (dashed) solutions were plotted to display the spread of variation.

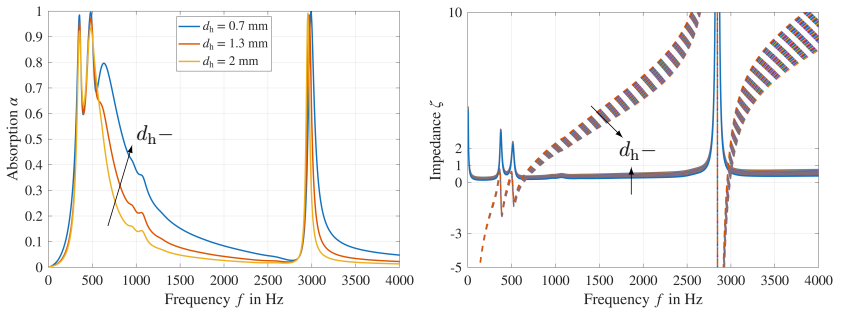

(a) Absorption, $f_{\mathrm{HR}} \approx 700\,\mathrm{Hz}$ (b) Impedance; solid: θ, dashed: χ

Figure 6.23.: Variation of face sheet hole diameter d_h

Changing the hole diameters while maintaining a constant porosity mainly alters the third absorption peak, which is associated with the Helmholtz resonance. The first two absorption maxima originate from the flexible plate. Their resonance frequencies remain largely unaffected by the change in orifice diameter, but their absorption amplitudes increase for smaller orifices. This can be explained by the fact that a face sheet with a small orifice diameter has a higher resistance, see Eq. (2.28), because the viscothermal boundary layer covers a relatively larger portion of the cross section. The resistance trend is visible in Fig. 6.23b. The increased resistance leads to increased absorption because the resistance is below the optimal value of $\theta = 1$ for most frequencies, except near the antiresonance frequencies, where it is too high. Additionally, the reactance decreases for smaller orifices because $\delta_\mathrm{tot} \propto d_\mathrm{h}$, see Eq. (3.6), which leads to a higher Helmholtz resonance around 700 Hz. The reactance is reduced more at higher frequencies.

The effect of increasing the *face sheet thickness* is presented in Fig. 6.24. Again, the main changes occur in the third peak associated with the Helmholtz resonance and the second Helmholtz resonance near 3000 Hz. The absorptive effect of a plate resonance is enhanced when the Helmholtz resonance is nearby, which is visible around 1000 Hz or near the decreased valley around 420 Hz. Increasing the face sheet thickness mainly leads to more air mass in the orifice, which translates into a higher reactance as $\zeta_\mathrm{fs} \propto h_\mathrm{fs}$, see Eq. (3.2), which is visible in Fig. 6.24b. An increased reactance slope results in a lower Helmholtz resonance frequency with a lower resonance bandwidth. The resistance also increases for thicker face sheets because of the longer viscothermal boundary layer near the orifice walls.[8]

The *face sheet porosity* has a strong effect on the overall damping characteristics, which is visible in Fig. 6.25. The porosity is a crucial face sheet parameter because it affects the transformation of the impedance from one orifice to the whole face sheet, see Eq. (3.2), the effective density, see Eq. (3.3), and the hole interaction, see Eq. (2.37).[9] Therefore, both the reactance and resistance are very sensitive to porosity changes, as visible in Fig. 6.25b. The porosity mainly affects the Helmholtz resonance. Decreasing the porosity shifts the Helmholtz resonance to lower frequencies with a smaller bandwidth as the slope of the reactance increases. In contrast, the plate resonance is largely unaffected by the

[8]The face sheet thickness also takes part in the nonlinear contributions; however, these are irrelevant in the baseline case and this parameter variation because the incoming sound pressure level is too low.

[9]The face sheet porosity also takes part in the nonlinear contributions.

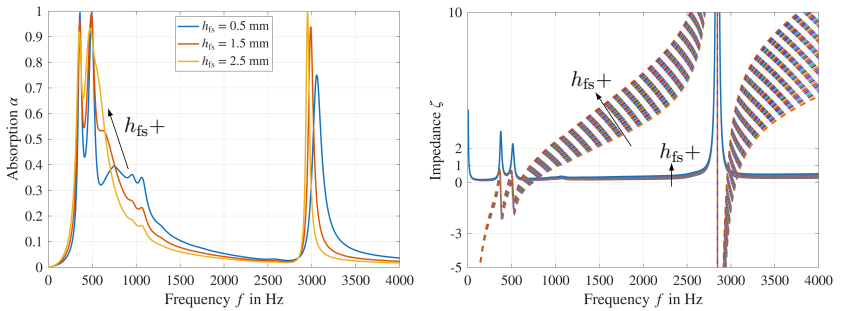

(a) Absorption, $f_{HR} \approx 600 - 800\,\text{Hz}$ (b) Impedance; solid: θ, dashed: χ

Figure 6.24.: Variation of face sheet thickness h_{fs}

face sheet porosity, except when the Helmholtz resonance frequency is in the vicinity of a plate resonance. In the case of $\sigma = 5\,\%$ the Helmholtz resonance frequency is higher, and subsequently, the higher plate resonance is better excited. The Helmholtz resonance lies between the two dominant plate resonances for very small porosities ($\sigma < 2.5\,\%$), which is better visible in Fig. 6.25c. Note that the frequency range of the colour map is only presented up to 2000 Hz for better visibility of the relevant effects. If the Helmholtz resonance is between two dominant plate resonances, the lower plate resonance gets pushed to lower frequencies, and the higher plate resonance gets pushed to higher frequencies.[10] A transition zone is visible around $\sigma \approx 2\,\%$ where the Helmholtz resonance and the second plate absorption peak intersect. The Helmholtz resonance becomes more broadband with a lower peak absorption at higher frequencies for higher porosities, whereas both lower plate resonances remain largely unaffected.

[10]This effect was also found in the experimental data in Fig. 6.14.

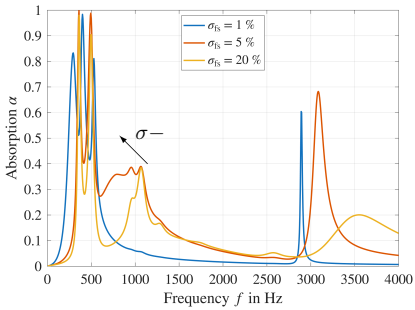

(a) Absorption, $f_{HR} \approx 400$ Hz (blue), 800 Hz (red), 3500 Hz (yellow)

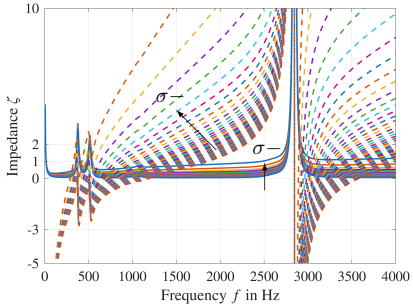

(b) Impedance; solid: θ, dashed: χ

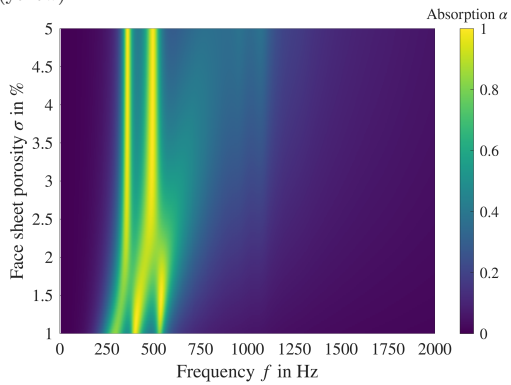

(c) Absorption map

Figure 6.25.: Variation of face sheet porosity σ

6.3.2. Cavity parameters

The influence of the *main cavity depth* is depicted in Fig. 6.26. The main cavity depth drastically affects the overall acoustic behaviour of the resonator system.

A very shallow cavity (blue) has a high Helmholtz resonance frequency around 2000 Hz, as depicted in Fig. 6.26a. In this case, the lower plate resonances are distant and remain largely unaffected. The intermediate cavity depth (red) slightly amplifies the peak absorption values of the plate resonances around 800 Hz as the Helmholtz resonance is nearby. For a very deep cavity (yellow), the Helmholtz resonance blends with the second plate resonance as the bandwidth increases. Additionally, the second Helmholtz resonance around 2600 Hz is visible. The depiction of the impedances in Fig. 6.26b appears to be chaotic and only reveals that the mean cavity has a great impact and shifts the Helmholtz and second Helmholtz resonance. The colourmap in Fig. 6.26c paints a clearer picture of this effect. For small cavities, the Helmholtz resonance is around 2000 Hz that decreases for larger cavity depths. The absorption bandwidth is small for shallow cavities but more broadband in the vicinity of the plate resonances, e.g., for cavity depths larger than 15 mm. Plate resonances are enhanced if they have a resonance frequency similar to the Helmholtz resonance frequency,

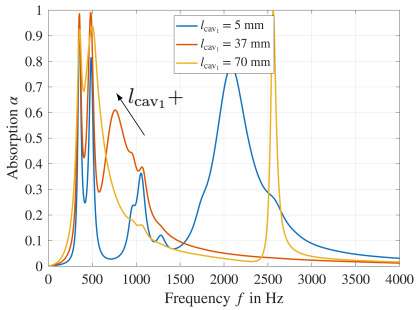

(a) Absorption, $f_{\mathrm{HR}} \approx 2100\,\mathrm{Hz}$ (blue), 800 Hz (red), 500 Hz (yellow)

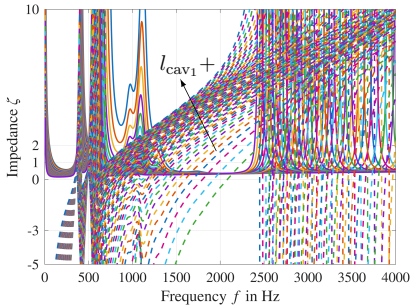

(b) Impedance; solid: θ, dashed: χ

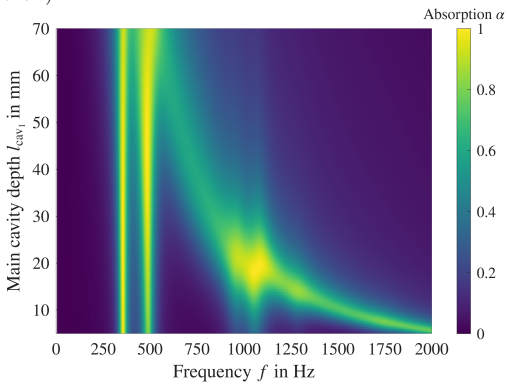

(c) Absorption map

Figure 6.26.: Variation of main cavity depth l_{cav_1}

which is the case for a main cavity depth around 20 mm and 70 mm in this configuration.

In contrast, the *back cavity depth* primarily affects the plate resonances, as depicted in Fig. 6.27. In the case of a very shallow back cavity (blue), only one absorption maximum around 600 Hz with additional small local maxima around 800 Hz and 1400 Hz is visible. In this case, the air in the shallow cavity is too stiff and plate vibrations are suppressed. For a back cavity depth of 10 mm (red), both low-plate resonances around 400 Hz and 500 Hz are visible. The second one has a larger absorption bandwidth because the Helmholtz resonance is nearby. For a large back cavity (yellow), the plate resonances have a lower resonance frequency as the stiffness of the back cavity is further reduced.

The depiction of the corresponding impedances in Fig. 6.27b highlights that the main changes occur in the vicinity of the plate resonances below 1000 Hz. The second Helmholtz resonance around 3000 Hz is unaffected by changes in the back cavity depth. The colourmap in Fig. 6.27c reveals that the frequency and amplitude of the absorption peaks change more for small back cavities < 7 mm. In this case, the second plate resonance, starting around 800 Hz is particularly absorptive, whereas the first plate resonance, starting around 400 Hz for very shallow cavities, is barely visible. This relative contribution is flipped for larger

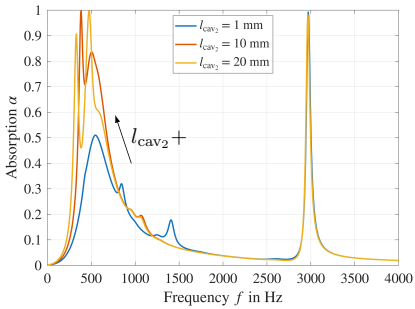

(a) Absorption, $f_{\mathrm{HR}} \approx 600\,\mathrm{Hz}$

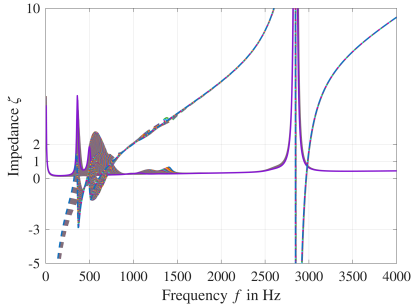

(b) Impedance; solid: θ, dashed: χ

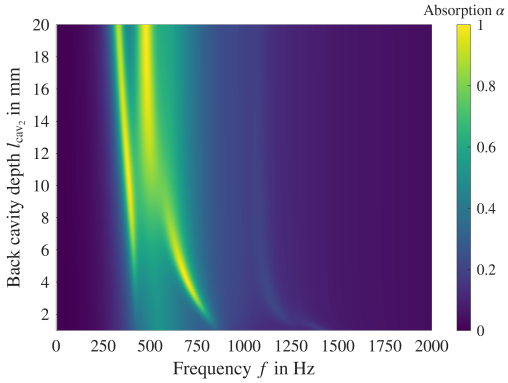

(c) Absorption map

Figure 6.27.: Variation of back cavity depth l_{cav_2}

back cavities, and the first plate resonance contributes more to the absorption. Additionally, a transition zone around $l_{\mathrm{cav}_2} \approx 10\,\mathrm{mm}$ is visible, where the Helmholtz resonance and second plate resonance seem to blend into a single, more broadband peak. This suggests that although the frequency of the Helmholtz resonance and the second plate resonance agree, they do not appear to be strongly coupled.

A common requirement of liners is that they must not exceed a certain total depth. In this case, the *cavity ratio* $^{l_{\mathrm{cav}_2}}/_{(l_{\mathrm{cav}_1}+l_{\mathrm{cav}_2})}$ with a fixed total cavity depth can be used to find a suitable main cavity depth and back cavity depth to achieve better overall absorption. The corresponding colourmap is depicted in Fig. 6.28. For ratios below 0.3, i.e., a shallow back cavity and deep main cavity, the overall absorption changes mainly due to the depth of the back cavity. The lowest plate resonances are suppressed by a stiff back cavity. The second lowest plate resonance, which starts around 800 Hz, decreases more rapidly than the lowest plate resonance, with an increasing ratio of up to approximately 0.2. In this region, the Helmholtz resonance frequency is in the same frequency region and rises with increasing ratio because the main cavity depth decreases. For higher ratios, i.e., a deeper back cavity and shallower main cavity, the Helmholtz resonance shifts to higher frequencies,

and the first plate resonance shifts to lower frequencies. The former can be attributed to the main cavity, see Fig. 6.26c, and the latter to the back cavity, see Fig. 6.27c. This ratio constitutes a design parameter for tailored absorption. Naturally, the optimal ratio depends on the noise spectrum to be damped.

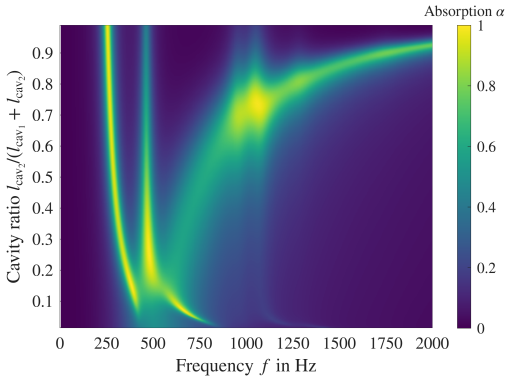

Figure 6.28.: Influence of back cavity depth to total depth ratio, given a constant total depth. Smaller values mean a large main cavity and a small back cavity.

6.3.3. Plate parameters

Variations of plate parameters predominantly affect the low-frequency plate resonances and only to a minor degree the Helmholtz resonance, which is the highest of the three low-frequency resonances around 600 Hz. Increasing the *plate density* leads to lower plate resonance frequencies, as depicted in Fig. 6.29. Increasing the density from 700 kg/m^3 to 1200 kg/m^3 decreases the first resonance frequencies by approximately 100 Hz. This trend agrees with the formula of the eigenfrequencies Eq. (2.71), i.e. $f_{m,n} \propto 1/\sqrt{\rho_{\mathrm{P}}}$.

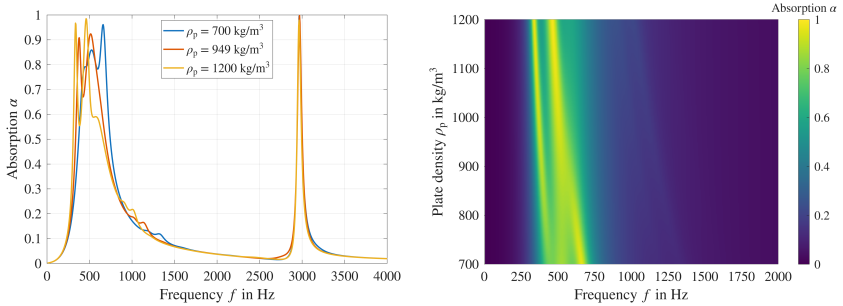

(a) Absorption, $f_{\mathrm{HR}} \approx 600$ Hz

(b) Absorption map

Figure 6.29.: Variation of plate density ρ_{p}

The *mechanical loss factor* affects the amplitude and bandwidth of the plate-related resonances, as depicted in Fig. 6.30. A higher mechanical loss factor results in broader

absorption with reduced amplitude. Higher plate resonances are visible as spikes in the reactance above 800 Hz for very low mechanical loss factors. This behaviour is relevant for metals with low mechanical losses. These spikes, e.g. around 1000 Hz or 2600 Hz, are not shifted but are widened and their peak values are reduced for higher mechanical losses and do not significantly contribute to the overall absorption in either case. However, mechanical losses lead to greatly increased low-frequency absorption expressed as increased resistance in the vicinity of the Helmholtz resonance when comparing the absorption spectrum for a loss coefficient of $\eta = 0$ (blue) and $\eta = 0.1$ (red). Therefore, the plate damping expressed in the loss coefficient is highly beneficial for this resonator concept. However, for real materials, the loss coefficient is material-specific and not tunable independently of the Young's modulus. Additionally, loss factors greater than 0.1 may only be obtainable near the glass–liquid transition zone of polymers, which is both frequency- and temperature-dependent, as shown in Section 4.4.2.

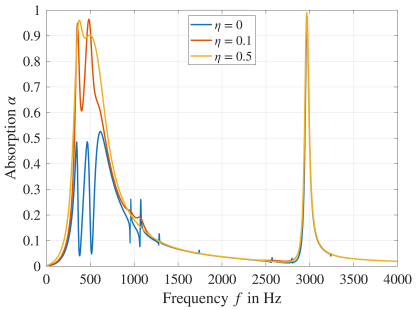

(a) Absorption, $f_{\mathrm{HR}} \approx 600\,\mathrm{Hz}$

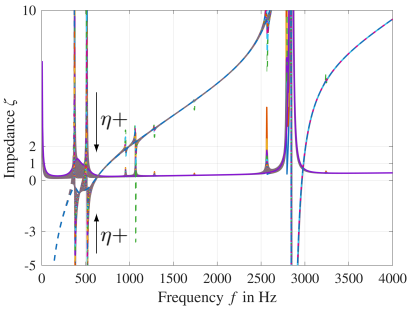

(b) Impedance; solid: θ, dashed: χ

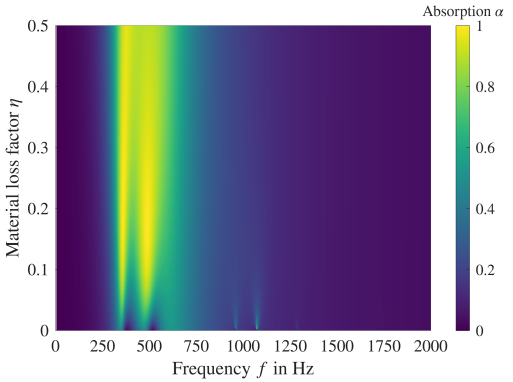

(c) Absorption map

Figure 6.30.: Variation of mechanical loss factor η

Polymers differ greatly in their *stiffness*, which is commonly expressed as the Young's modulus. Accordingly, the varied parameter range contains three orders of magnitude that significantly impact the overall absorption of the resonator system. The corresponding absorption spectra are depicted in Fig. 6.31. Higher low-frequency absorption can be

achieved with the lowest Young's modulus (blue) as all isolated plate eigenfrequencies $f_{m,n} \propto \sqrt{E}$, see Eq. (2.71). These resonance frequencies are shifted to higher frequencies as the Young's modulus increases. For very stiff plates (yellow), only the Helmholtz resonance and a very small plate resonance around 1800 Hz is visible. Fig. 6.31b reveals that the plate resonances seem to follow an 's-shape', which is best visible at the lower plate resonances. For example, the second plate resonance frequency starts around 250 Hz for $E = 1$ MPa and only changes to around 400 Hz up to $E = 20$ MPa. In contrast, the resonance frequency changes to 700 Hz for $E = 40$ MPa in the vicinity of the Helmholtz resonance. The first plate resonance only contributes to the overall damping for $E > 5$ MPa and has less peak absorption near the Helmholtz resonance, whereas the peak absorption of the higher plate resonances seem to be unaffected by the presence of the Helmholtz resonance. This suggests a stronger interaction between the first plate resonance and the Helmholtz resonance than between the higher plate resonances and the Helmholtz resonance. Plate resonances have a significant impact on the overall absorption only below or near the Helmholtz resonance frequency, with no notable contribution from plate resonances above 1300 Hz. Multiple plate modes contribute to the overall absorption for a material with a low stiffness, i.e., four for $E = 5$ MPa, in contrast to only one for $E > 100$ MPa. Therefore, as a rule of thumb, materials with low Young's modulus should be favoured for the resonator concept to obtain both low-frequency and broadband damping.

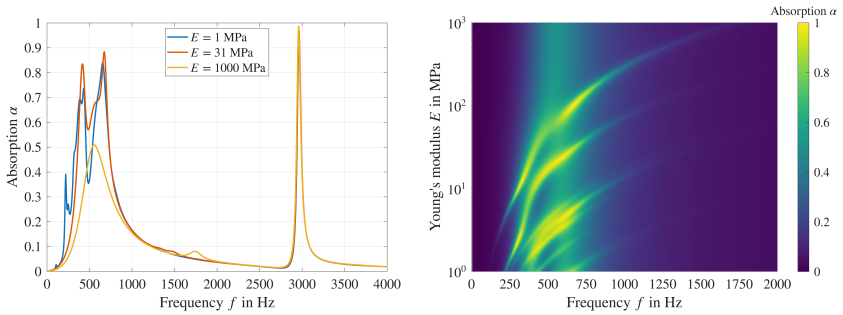

(a) Absorption, $f_{\mathrm{HR}} \approx 600$ Hz (b) Absorption map

Figure 6.31.: Variation of Young's modulus E

Similar trends were observed for the *plate thickness*, as presented in Fig. 6.32. The general trends roughly agree with the isolated plate eigenfrequencies that linearly increase with the plate thickness $f_{m,n} \propto h_{\mathrm{p}}$, see Eq. (2.71). The overall absorption is highly sensitive to thickness variations for plates that are very thin, namely those less than 0.2 mm in thickness, where multiple plate modes contribute to the overall absorption. The lowest plate resonance is significant only above 0.2 mm and has an s-shape similar to that in the variation of the Young's modulus. However, the shape appears to be stretched, which might be due to the fact that the y-axis is linear for the plate thickness, whereas the scale was logarithmic for the variation of the Young's modulus. For thicker plates > 0.5 mm only the Helmholtz resonance and the first plate resonance are visible. Therefore, thinner plates should be favoured for low-frequency and broadband damping. However, the sensitivity to external factors, such as unwanted pretension, is very high for very thin plates because the flexural rigidity and, consequently, the restoring forces are very small. Therefore, resonators with these predicted absorption spectra might be difficult to manufacture reproducibly.

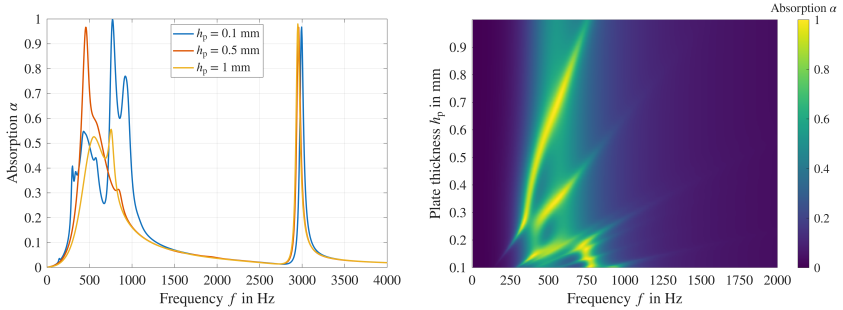

(a) Absorption, $f_{\mathrm{HR}} \approx 600\,\mathrm{Hz}$ (b) Absorption map

Figure 6.32.: Variation of plate thickness h_p

The absorption spectra of a variable *plate side length* for a square flexible plate are presented in Fig. 6.33. Both side lengths are simultaneously increased, leading to a larger plate area. The side length affects the frequency and number of relevant plate modes, i.e., the larger the plate, the lower the eigenfrequencies.[11] For plate lengths $l_{\mathrm{xy,p}} < 15\,\mathrm{mm}$ only one additional resonance is observed. The corresponding resonance frequency decreases with larger plates; for $15\,\mathrm{mm} < l_{\mathrm{xy,p}} < 23\,\mathrm{mm}$ two, for $23\,\mathrm{mm} < l_{\mathrm{xy,p}} < 27\,\mathrm{mm}$ three and above, even four plate-related additional resonances are visible. The first resonance fades for very large plates, implying that the number of relevant modes does not continue to grow indefinitely. Larger plates typically exhibit greater broadband absorption; nevertheless, for very low-frequency absorption, smaller plates, for instance, $l_{\mathrm{xy,p}} = 25\,\mathrm{mm}$, may be more suitable.

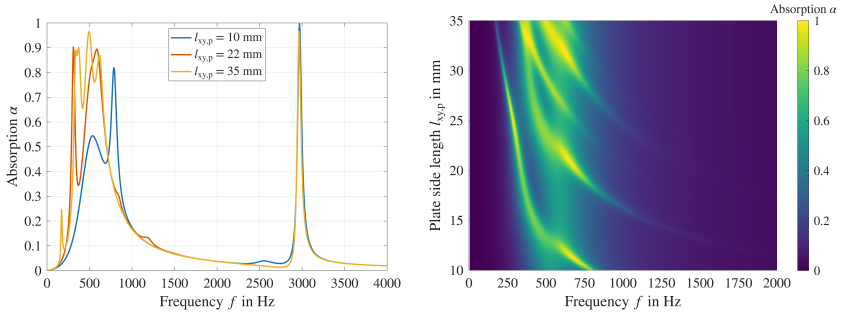

(a) Absorption, $f_{\mathrm{HR}} \approx 600\,\mathrm{Hz}$ (b) Absorption map

Figure 6.33.: Variation of the square plate side length $l_{\mathrm{xy,p}}$

The variation of the *plate diameter* in the case of a resonator system with a circular flexible plate is depicted in Fig. 6.34. The general trends resemble those of the square plate; however, the additional resonances are more pronounced. The plate resonances decrease with larger

[11] The plate area alone is a fair indicator but is insufficient to describe the plate resonance behaviour. A circular, rectangular, or square plate may have the same plate area but different eigenfrequencies. This can be seen by comparing the spectra for $l_{\mathrm{xy,p}} = 30\,\mathrm{mm}$ in Fig. 6.33 and $d_\mathrm{p} = 34\,\mathrm{mm}$ in Fig. 6.34, which have the same plate area but distinct absorption characteristics.

plate diameters, which agrees with the isolated eigenfrequencies Eq. (2.58). Depending on the chosen diameter, only the first radial mode ($d_\mathrm{p} < 18\,\mathrm{mm}$), first and second radial modes ($18\,\mathrm{mm} < d_\mathrm{p} < 28\,\mathrm{mm}$) or first three radial modes for ($d_\mathrm{p} > 28\,\mathrm{mm}$) plate resonances significantly contribute to the overall absorption. The corresponding plate deflection shapes are presented in Section 6.1.2.

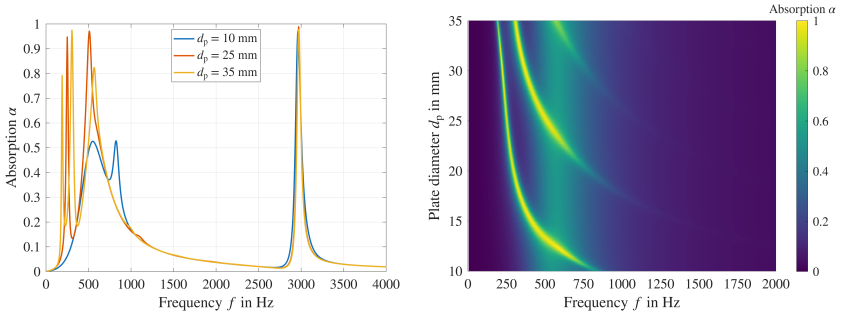

(a) Absorption, $f_\mathrm{HR} \approx 600\,\mathrm{Hz}$ (b) Absorption map

Figure 6.34.: Variation of plate diameter d_p

The analytical model is also used to assess the influence of the *ambient temperature*. The results are depicted in Fig. 6.35. The temperature affects both the Helmholtz resonance frequency $f_\mathrm{HR} \propto c(\sqrt{T})$, see Eq. (2.27), as well as the mechanical properties of the flexible TPU plate, see Fig. 4.10. TPU was found to be stiffer with a higher mechanical loss factor for lower temperatures in the investigated frequency range. Below $-20\,^\circ\mathrm{C}$ only one absorption peak is visible, which is a blend of the Helmholtz resonance and the first plate mode. At $20\,^\circ\mathrm{C}$ two absorption peaks are visible, where the Helmholtz resonance is close to the second plate mode around 550 Hz. For high temperatures, i.e. $100\,^\circ\mathrm{C}$ multiple resonances are visible because the stiffness is significantly reduced. However, because the mechanical loss factor is also lower, the resonances have a smaller bandwidth. The Helmholtz frequency is increased from 500 Hz to 700 Hz in the investigated temperature range. This dependency is better visible in the second Helmholtz resonance, which is shifted from 2500 Hz to 3500 Hz due to the increased temperature.

The effects of *high sound pressure levels* are shown in Fig. 6.36. These results are highly uncertain because the linear plate theory does not consider the effect of large deflections, and only the face sheet impedance is affected. Nevertheless, the absorption near the Helmholtz resonance increases significantly at high incoming sound pressure levels in this configuration because of the increased resistance in the face sheet.

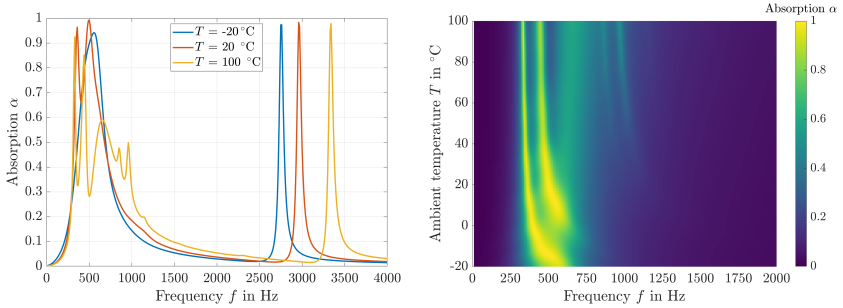

(a) Absorption, $f_{\mathrm{HR}} \approx 500$ - 700 Hz (b) Absorption map

Figure 6.35.: Variation of ambient temperature T

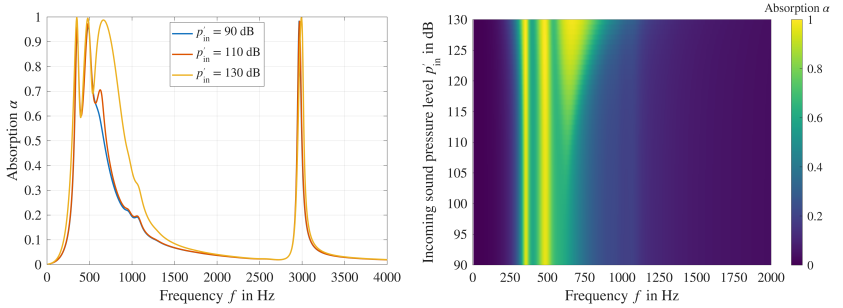

(a) Absorption, $f_{\mathrm{HR}} \approx 600$ Hz (b) Absorption map

Figure 6.36.: Variation of incoming sound pressure level p'_{in}

6.3.4. Comparison with numerical results

In the analytical model, the acoustical characteristics of the plate are represented by an equivalent plate transfer impedance, which is determined separately from the fluid domain in the cavity and is connected via waveguide transformation. However, the numerical model exhibits a higher degree of fidelity because the plate deflection is spatially resolved and fully coupled to the fluid domain in the cavities. This subsection compares selected representative results from the parameter study to determine where both are in agreement, indicating that the analytical model is sufficient, and in which configurations they diverge, indicating that the proposed analytical approach is inadequate. Comparisons for the other parameters not shown here can be found in Section A.4.

A comparison of the absorption for a variation of the main cavity depth l_{cav_1} and back cavity depth l_{cav_2} as calculated by the analytical and numerical models is presented in Fig. 6.37. Both results largely agree, and only minor differences in the absorption amplitude e.g. for the higher plate resonance above 1200 Hz, marked with a dashed white rectangle, are visible. Similar results can be found regarding a variation of face sheet parameters, in Section A.4. The numerical model does not resolve the fluid inside the face sheet; instead, an equivalent transfer impedance is used. Therefore, a comparison of the analytical and

numerical face sheet variation predictions of the absorption is essentially just a comparison between two face sheet impedance models. Both representations agree in their predictions of the face sheet and cavity parameters.

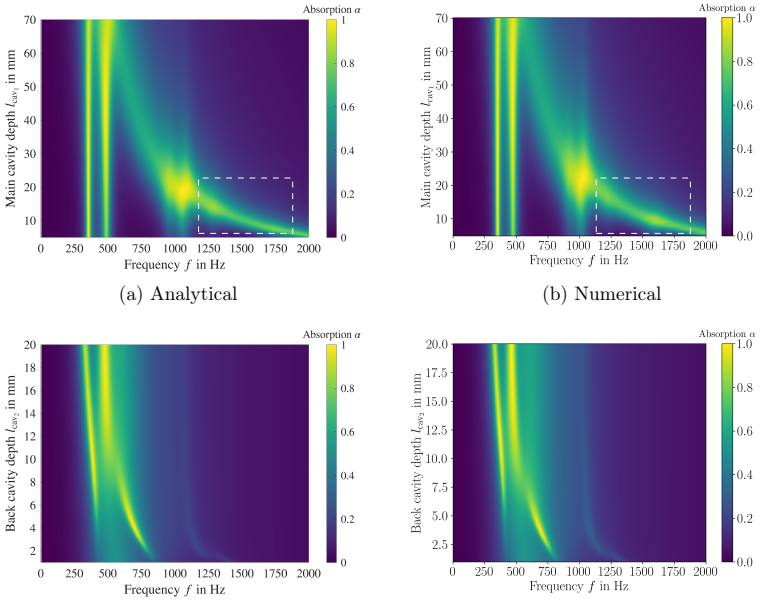

(a) Analytical

(b) Numerical

(c) Analytical

(d) Numerical

Figure 6.37.: Comparison between analytical (left) and numerical (right) absorption maps. First row: Variation of main cavity depth l_{cav_1}, second row: Variation of back cavity depth l_{cav_2}. White dashed boxes indicate regions with differences between both models

A comparison between analytical and numerical results regarding plate stiffness and plate thickness are depicted in Fig. 6.38. Again, both predictions largely agree. However, marginal differences can be seen for very flexible plates, e.g. near 350 Hz at $E \approx 10\,\mathrm{MPa}$ or very thin $h_\mathrm{p} < 0.2\,\mathrm{mm}$ plates, e.g. near 600 Hz at $h_\mathrm{p} \approx 0.1\,\mathrm{mm}$. The analytical model predicts slightly more broadband absorption whereas the resonance peaks are more pronounced in the numerical model.

Larger discrepancies between the analytical and numerical models appear when variable plate sizes are considered, as depicted in Fig. 6.39. Although the general trends agree, the individual resonances deviate, especially for larger plate sizes, i.e., $l_{\mathrm{xy,p}}$ or $d_\mathrm{p} > 20\,\mathrm{mm}$. Therefore, predictions from the analytical model for larger plates are less accurate. The analytical model predicts more pronounced plate-related absorption peaks that decrease in frequency with increasing plate size. These analytically predicted trends are largely independent of the Helmholtz resonance. In contrast, the resonance patterns in the numerical model appear to be more complex with more cross-resonance interactions, indicating eigenvalue veering, as explained in Section 2.5. There is a stronger coupling

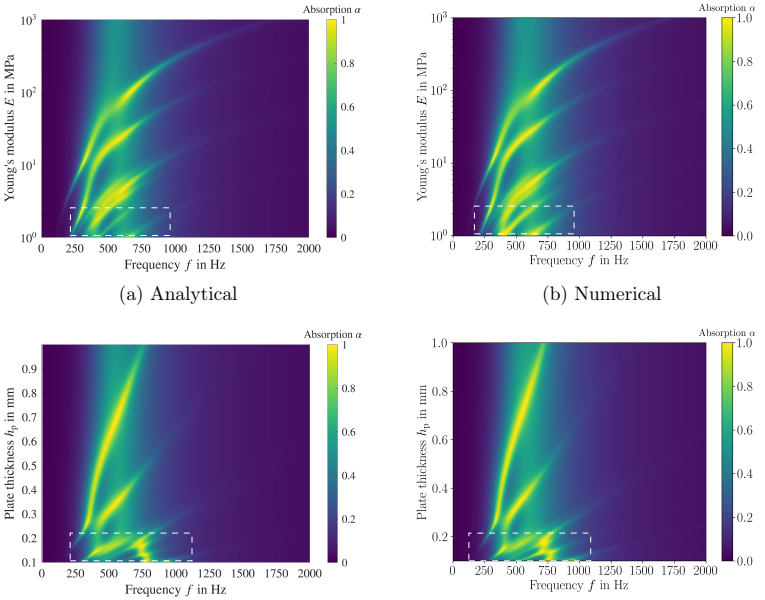

(a) Analytical

(b) Numerical

(c) Analytical

(d) Numerical

Figure 6.38.: Comparison between analytical (left) and numerical (right) absorption maps. First row: Young's modulus E, second row: plate thickness h_p. White dashed boxes indicate regions with differences between both models

for larger plates between the flexible plate and the back cavity as well as the Helmholtz resonator, which is only accounted for in the numerical model. This may be related to the particle velocity in the vicinity of the flexible plate. The analytical model assumes a plane wave excitation that might not hold for larger flexible plates inside the resonator system with higher plate order and, consequently, more complex deflection shapes.

The surface sound pressure level inside the resonator with a circular plate with $d_\mathrm{p} = 30\,\mathrm{mm}$ is depicted in Fig. 6.40. There is a large acoustic pressure difference between the main and the back cavities at the resonance frequencies 270 Hz and 800 Hz that drives the plate oscillations, denoted as red crosses in Fig. 6.39. For 270 Hz the surface pressure at the plate is almost constant whereas it shows a radial dependency at 800 Hz. The analytical model assumes a constant pressure over the plate area, which may explain the differences in the predicted absorption for higher order plate modes in Fig. 6.39.

Briefly summed up, the analytical and numerical models have been proven to be valuable tools for investigating the damping mechanisms of the novel liner concept. The analytical parameter study revealed that the face sheet parameters and the main cavity depth mainly affect the Helmholtz resonance, whereas the plate size and material as well as the back cavity depth mainly affect the plate resonances. In the case of a flexible TPU plate, the temperature affects both resonance types. Plate resonances are more absorptive when the Helmholtz

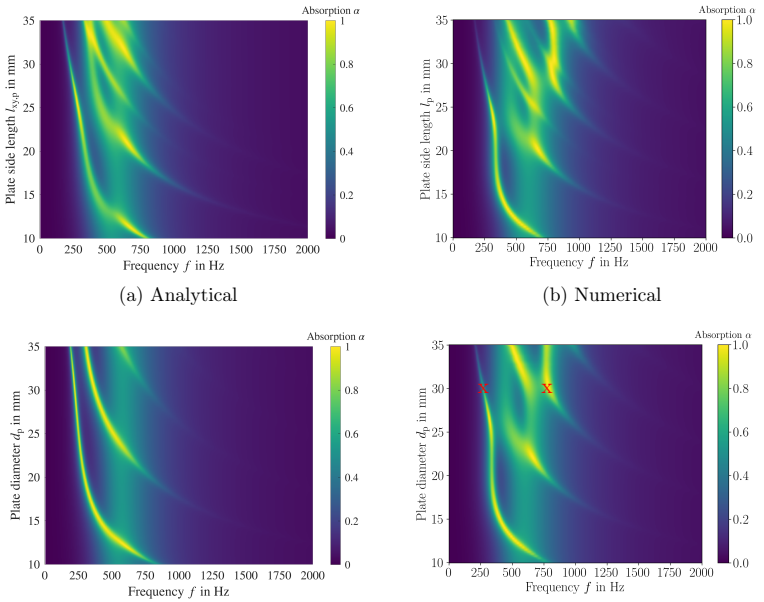

(a) Analytical

(b) Numerical

(c) Analytical

(d) Numerical

Figure 6.39.: Comparison between analytical (left) and numerical (right) absorption maps. First row: Square plate side length $l_{\mathrm{xy,p}}$, second row: plate diameter. d_{p}. Red crosses denote the configurations in Fig. 6.40

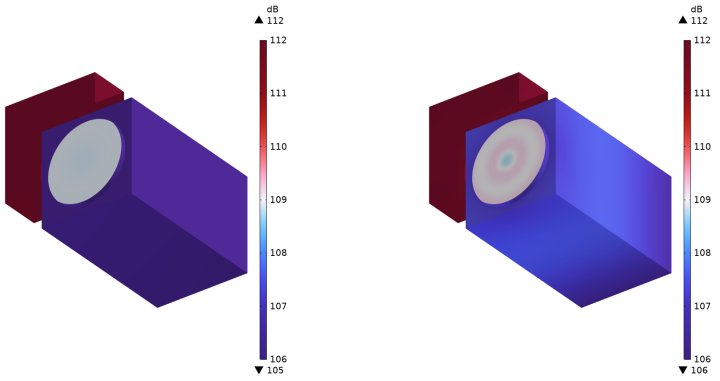

(a) 270 Hz

(b) 800 Hz

Figure 6.40.: Surface sound pressure level inside the resonator and on the flexible plate ($d_{\mathrm{p}} = 30\,\mathrm{mm}$) for a low frequency (left) and high frequency resonance (right)

resonance is nearby. If a Helmholtz resonance coincides with a plate resonance, both resonances are shifted away from each other. Both models largely agree in their predictions, which gives further confidence to the analytical model. Differences arise for very thin and very large plates, where the assumption of an impinging acoustic plane wave may no longer hold. In these cases, more confidence should be put into the numerical predictions.

The Helmholtz resonance and plate resonances must be tuned accordingly to obtain resonator system with low-frequency absorption. A low Helmholtz resonance can be obtained by combining a thick face sheet with a low porosity and a deep main cavity. A deeper back cavity also leads to low-frequency plate absorption. A good compromise was found to be a back cavity size of one-tenth to one-fifth of the total depth. Thin, larger plates with a low Young's modulus and high material damping are preferred to obtain a high plate-related absorption. Based on Fig. 4.9, elastomers are a good choice. However, their durability inside aircraft liners must be ensured. If the flexible plates are too thin, i.e. smaller than 0.2 mm, the absorption is more broadband and less low-frequency dominated. In addition, very thin plates with a low Young's modulus have a low flexural rigidity with small restoring forces that makes their response more receptive to pretension, because the restoring forces due to pretension would dominate in this case. This may lead to a stronger mismatch between prediction and experiment in the case of unknown pretension. Exploring these parameter ranges helps in gaining a deeper understanding of the concept and can be used for future optimisation to design a liner with a flexible wall that excels in damping a specific noise signature.

6.4. Resonator array with flexible side walls under grazing flow

This section presents the results of the liner samples with multiple resonator cells in a grazing incidence setting as introduced in Section 4.5.[12] The samples were investigated experimentally at DUCT-R, introduced in Section 4.3, to address the first research question and evaluate their effectiveness in a more realistic setting with and without flow. This was evaluated by comparing the damping of the liner samples with and without flexible walls. The experimental results also serve as a reference case for the numerical model, as presented in Chapter 5. The numerical model was used to gain more insight into the sound field inside and above the liner and the vibration of the flexible plates.

6.4.1. Experimental results

The measured dissipation of the reference sample (HR) and with one (FXW-1) and two (FXW-2) flexible intermediate walls (TPU, 15 mm × 26 mm) with a single-tone excitation at an incoming sound pressure wave of 110 dB and no grazing flow are displayed in Fig. 6.41. The step-size was chosen as 25 Hz below 1000 Hz to detect low-frequency resonances with small bandwidth and 50 Hz above to reduce measurement time. The reference sample is

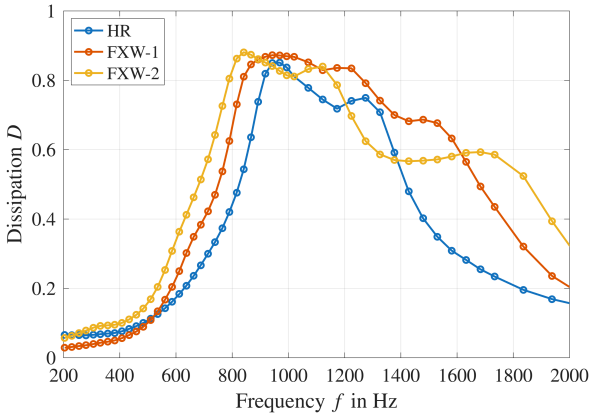

Figure 6.41.: Dissipation of HR liner (blue), FXW-1 liner (red) and FXW-2 liner (yellow), 110 dB without grazing flow

a simple Helmholtz resonator. The corresponding dissipation Δ is depicted in blue, with one dominant damping peak around 1000 Hz (Helmholtz resonance) and a second damping peak around 1300 Hz, which depends on the liner length. The FXW-1 liner allows for much stronger and wider damping, depicted in red with the same available space. The FXW liners have multiple damping mechanisms: the Helmholtz resonance, which is similar to that of the reference sample's and additional damping due to the flexible walls. The damping is extended towards lower and higher frequencies due to multiple structural resonances around 800 Hz, 1100 Hz for both FXW liners and 1500 Hz for FXW-1 and 1700 Hz for FXW-2. In the case of only one dominant structural resonance, the damping would be extended either

[12] Parts of this section were published in Kohlenberg et al.[316].

towards lower or higher frequencies, but not both. However, the additional dissipation due to the flexible walls is less pronounced and more broadband compared to the single modular resonator in the normal incidence setting from the previous section. One explanation for this is that the multiple flexible plates in the resonator array are slightly different due to manufacturing reasons with altered plate resonances. This would lead to a more broadband acoustic behaviour. No strong additional damping below 600 Hz is observed, although the same plate material (TPU) with the same plate area as the baseline configuration in Section 6.2 was used. This may be because the flexible plate is mounted as a sidewall and the second cavity is smaller (5 mm instead of 15 mm). The parameter study in Fig. 6.27 revealed that a small back cavity can suppress low plate resonances due to its increased stiffness.
Doubling the number of flexible walls in each cavity (FXW-2) increases the flexible walls' acoustic effect. The main dissipation peak of the FXW-2 liner, depicted in yellow, is shifted towards lower frequencies even further and additional higher-frequency damping is visible around 1700 Hz. However, dissipation is also decreased around 1400 Hz.

The spectra of all scattering coefficients for the HR and FXW-1 liner are shown in Fig. 6.42. Note that the measurement point marks are dropped for better visibility. The introduction

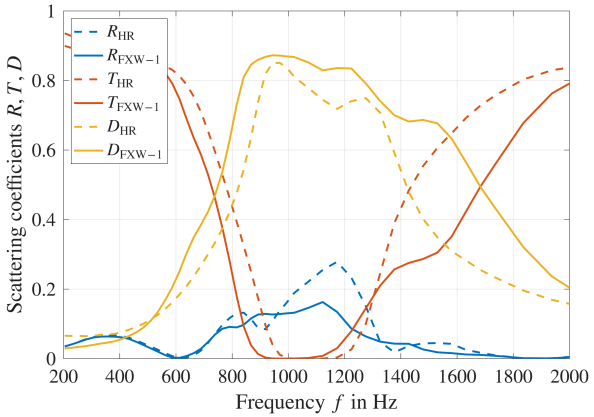

Figure 6.42.: Scattering coefficients of HR liner (dashed) and FXW-1 liner (solid) without grazing flow

of the flexible walls shifts the transmission (T, red) towards lower frequencies and reduces the reflection (R, blue) near the main resonance around 1100 Hz. Therefore, the combined reduction of reflected acoustic energy and increased dissipation leads to a reduced sound transmission of the novel liner concept.[13]

The corresponding normalised impedance of the three liner samples is depicted in Fig. 6.43. The reference liner has the lowest resistance and reactance. The resistance is relatively low at approximately 0.3, except at low frequencies. Near the Helmholtz resonance at 1000 Hz the reactance has a zero crossing and the resistance is slightly serrated, which might be

[13] Alternatively, from a measurement point of view, the combined reduction of reflected and transmitted sound leads to an amplified dissipation because the dissipation is calculated from the energetic reflection and transmission coefficient, see Eq. (4.10).

due to the impedance eduction method. In comparison, FXW-1 has a higher reactance and, consequently, a slightly lower Helmholtz resonance. The resistance increases across the entire frequency range to approximately 0.4 with a local maximum around 1500 Hz. This flexible wall effect is amplified in the FXW-2 sample, where resistance values of up to 1.2 are reached around 1650 Hz. These frequencies coincide with the measured additional dissipation of the FXW liner in Fig. 6.42. In contrast to the modular resonator described in the previous section in the normal incidence setting, the influence of plate resonances and antiresonances are less pronounced.

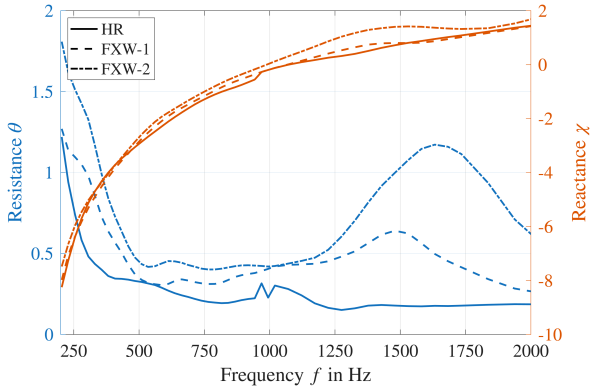

Figure 6.43.: Normalised impedance of HR liner (solid), FXW-1 liner (dashed) and FXW-2 liner (dot-dashed), 110 dB without grazing flow

The effect of a high sound pressure level and grazing flow on the reference sample is displayed in Fig. 6.44.

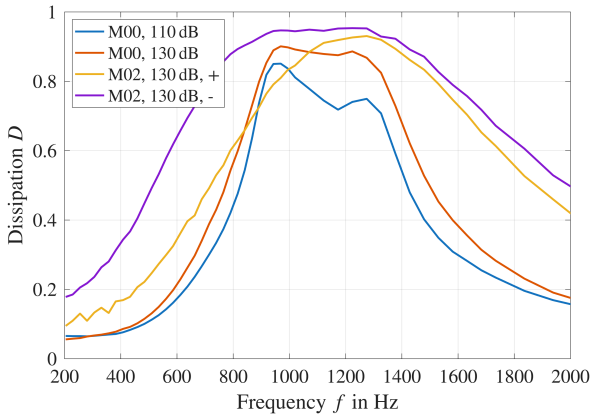

Figure 6.44.: Dissipation of HR liner under high sound pressure level excitation and with grazing flow

The HR liner shows higher damping at an incoming sound pressure level of 130 dB (red)

compared to 110 dB (blue). This can be explained by the fact that increasing the sound pressure level leads to additional losses, as acoustic energy is converted into turbulent energy due to jet formation near the Helmholtz resonance, where the sound particle velocity is at its maximum, as explained in Section 2.3.4.

The introduction of a grazing flow with a centre-line Mach number of $M = 0.2$ alters the sound field in the duct and demonstrates two aspects. First, the damping is increased again due to the mean flow and turbulent effects, resulting in additional dissipation for this particular liner set. Second, the damping is different in flow direction (downstream, +, yellow) and against flow direction (upstream, -, violet). The liner dissipation against flow is more broadband in a lower frequency range, whereas peak dissipation shifts to higher frequencies in flow direction. This is due to convective and refractive effects. Convection increases attenuation against the flow direction because the sound waves travel slower over the lined section. Refraction is due to the boundary layer profile near the duct walls, which directs the sound wave towards the liner downstream[106, p. 126]. Note, that the optimal impedance also depends on the flow direction, see Fig. 2.1.

The grazing flow also changes the liner impedance. The corresponding normalised impedances of the reference liner are depicted in Fig. 6.45.

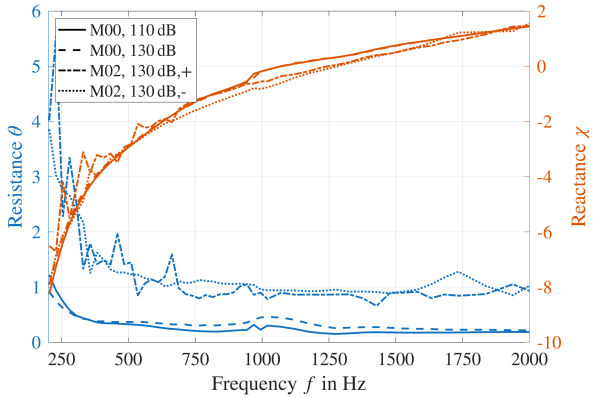

Figure 6.45.: Normalised impedance of HR liner under high sound pressure level excitation and with grazing flow

Increasing the amplitude of the incident sound pressure wave to 130 dB leads to a higher resistance near the Helmholtz resonance around 1000 Hz, but does not affect the reactance substantially. The grazing flow results in an overall higher resistance around 1 and a reduced reactance near the Helmholtz resonance. In contrast, the resistance is only $0.2 - 0.5$ above 400 Hz. Therefore, the contribution of grazing flow resistance is much higher than the viscous and nonlinear contributions. The educed impedance in flow direction is more serrated for frequencies below 750 Hz.[14]

Similar relationships can be found for the FXW-1 liner in Fig. 6.46. The higher sound

[14]Whether a liner impedance of the same sample that differs with flow direction is meaningful or not is not touched here and out of the scope of this thesis, e.g. see the discussion by Jones et al.[125] or Schulz et al.[124].

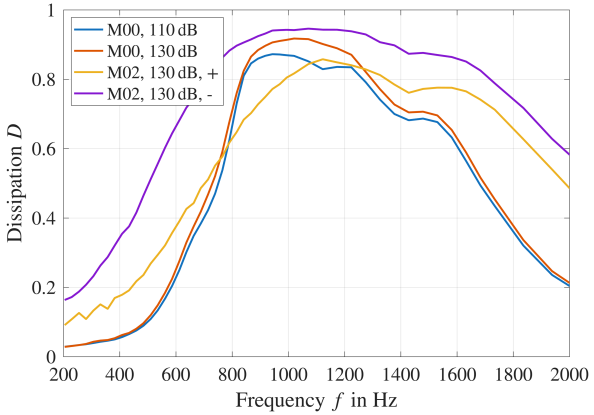

Figure 6.46.: Dissipation of FXW-1 liner under high sound pressure level excitation and with grazing flow

pressure level mainly alters the dissipation near the Helmholtz resonance at 1000 Hz but only minor near the additional damping due to the flexible plates around 700 Hz and 1500 Hz. These results suggest that high sound pressure levels predominantly affect the acoustic properties of the face sheet but not the flexible plates in the liner samples. However, in the vicinity of the Helmholtz resonance, both the face sheet and possibly the flexible plate can behave nonlinearly, i.e., amplitude-dependently. Therefore, a clear separation of the effects is not possible. However, far away from the Helmholtz resonance, nonlinear effects should only affect the flexible plate because no high sound particle velocities in the face sheet are involved. Since the dissipation changes far away from the Helmholtz resonance are smaller, this suggests that high sound pressure levels mainly affect the face sheet. Similar to the HR liner, the dissipation of the FXW-1 liner with grazing flow is higher upstream than downstream. The additional damping due the flexible walls around 1700 Hz is visible in both directions.

The corresponding impedances for the FXW-1 liner are depicted in Fig. 6.47. Increasing the sound pressure level of the incoming wave from 110 dB to 130 dB (dashed) results in a slight additional resistance between 600 Hz and 1200 Hz, whereas the reactance is almost identical. Compared with the baseline liner, the resistance is generally higher and more serrated with grazing flow (dash-dotted in flow direction, dotted against flow direction), which is linked to the used impedance eduction method. The altered reactance slope around 1500 Hz is still visible with grazing flow in both directions. This gives further reason that the grazing flow mainly affects the face sheet characteristics.

Figure 6.48 displays a comparison between all liner samples under high sound pressure level and with grazing flow. In flow direction (dashed), the reference performs better between 1000 Hz and 1600 Hz. This may be due to the reduced active liner area from the side-mounted second cavities and consequently weaker dissipation near the Helmholtz resonance. The advantages of the flexible walls only appear above 1700 Hz and below 1000 Hz, but are more pronounced against flow direction (solid). The FXW-1 liner adds substantial dissipation above 1400 Hz, whereas the FXW-2 liner adds low- and high-frequency dissipation.

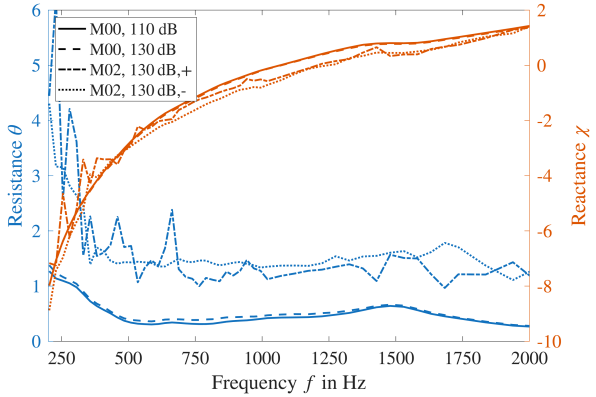

Figure 6.47.: Normalised impedance of FXW-1 liner under high sound pressure level excitation and with grazing flow

Therefore, the experimental investigations showed that the liner concept with flexible walls inside the cavities adds additional dissipation with and without grazing flow below and above the Helmholtz resonance. Note that neither liner has been optimised but adapted for a better comparison in the existing environment. Consequently, their geometries were chosen to allow a fair comparison between the concepts rather than showing optimal dissipation.

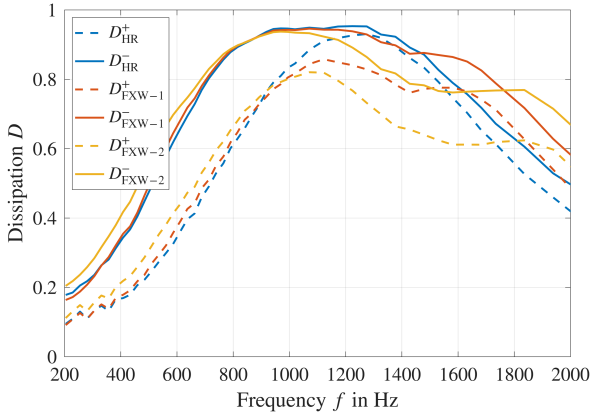

Figure 6.48.: Dissipation of HR liner (blue), FXW-1 liner (red) and FXW-2 liner (yellow) at $M = 0.2$, downstream (solid) and upstream (dashed)

6.4.2. Comparison with numerical predictions

The reference liner (HR) and the liner with one flexible wall (FXW-1) were modelled using the numerical setup introduced in Chapter 5 to assess the damping contributions of the

novel liner concept. The analytical model is not applicable to the liner with a flexible side wall because it assumes a plane wave impinging on the flexible plate with normal incidence. The numerical model enables the prediction of the scattering coefficients and analysis of the pressure field inside the resonator and the plate vibrations that are difficult to determine experimentally.

A comparison between the simulated and experimentally determined scattering coefficients at an incoming wave amplitude of 110 dB and no flow for the reference sample is shown in Fig. 6.49. An excellent agreement was found for all scattering coefficients, with slight differences away from the Helmholtz resonance. Therefore, the model can correctly predict the reference liner's acoustic properties.

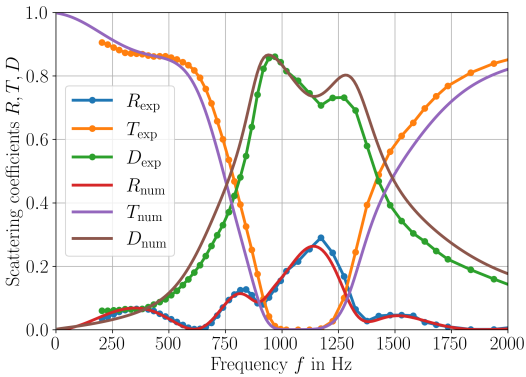

Figure 6.49.: Simulated and experimentally determined scattering coefficients for HR liner at 110 dB incoming wave amplitude and no flow

The comparison between the prediction and test results of the FXW-1 liner sample is depicted in Fig. 6.50. Again, a good agreement was found, as the numerical model correctly predicted a higher dissipation at higher frequencies (> 1000 Hz) due to the presence of the flexible walls. A comparison between Fig. 6.49 and Fig. 6.50 reveals that the reduced transmission around 900 Hz and 1600 Hz is mainly due to increased dissipation, whereas the energetic reflection coefficient remains relatively unchanged. The numerical model predicts a stronger reflection around 1200 Hz than measured. Some differences between the experimental and prediction results might be due to the neglection of the static pressure difference ('hole' in Fig. 4.13). Another source of uncertainty is the boundary condition at the plate edge. The plates were glued to the structure which is neither clamped nor simply supported. The gluing process also involved slight pretension to prevent buckling. The pretension is neglected in the simulation. Additional repeatability measurements of the glued plates revealed a larger uncertainty with respect to the plate absorption compared to the clamped plate, see Fig. 4.18. In addition, the Young's modulus and loss coefficient of thermoplastics are temperature- and frequency-dependent, which were not considered in the numerical model.

The numerical simulations allow for a simultaneous analysis of the sound pressure field and the plate vibration. Both are depicted in Fig. 6.51 with the incoming sound wave

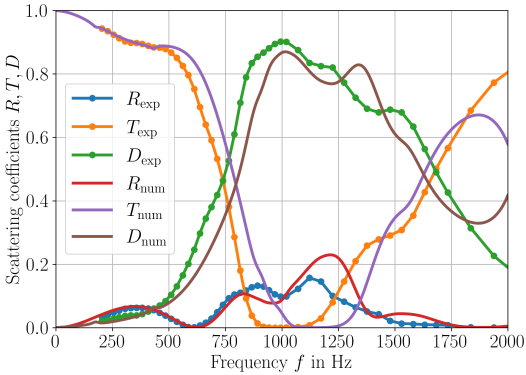

Figure 6.50.: Simulated and experimentally determined scattering coefficients for FXW-1 liner sample at 110 dB incoming wave amplitude without flow

coming from the left at 1000 Hz where strong dissipation occurs. Note that the plane wave assumption breaks down above the liner. The pressure in the resonator cavities is amplified, and the plate velocity pattern shows a combination of higher-order structural modes. Notably, the instantaneous plate velocity fields differ between the cells, i.e., they change depending on the phase of the incoming sound wave.

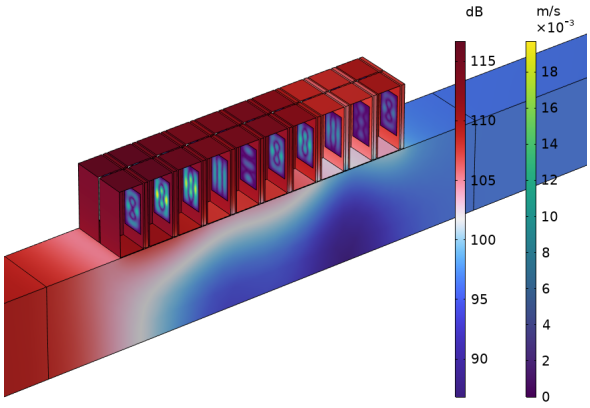

Figure 6.51.: Cut-view of sound pressure level field and plate velocities for FXW-1 liner sample at 1000 Hz

Furthermore, the overall dissipation can be compared to the flexible plate's vibration, averaged over all flexible plates, as depicted in Fig. 6.52. The strongest vibrations of the flexible plates are observed near the Helmholtz resonance due to the increased pressure inside the cavities, visible in Fig. 6.51. For better comparison, the first six uneven in-vacuo

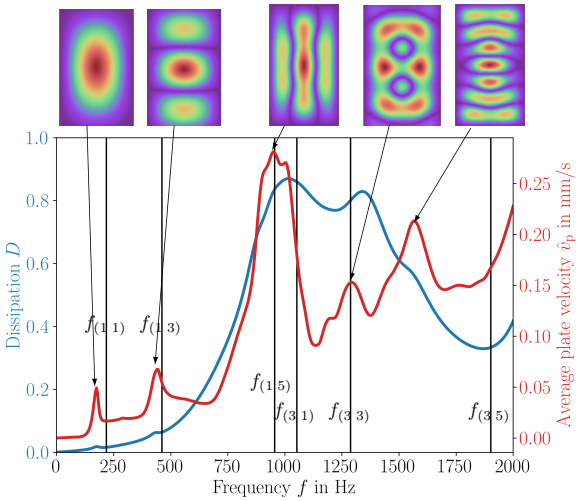

Figure 6.52.: Comparison between overall dissipation, average plate velocity and corresponding velocity fields of FXW-1 liner

eigenfrequencies of the flexible plate are depicted with vertical lines. The operating velocity shapes near 200 Hz and 450 Hz are close to the corresponding eigenfrequency and resemble the first and third eigenmode of the flexible wall. They show large velocities but are too far away from the Helmholtz resonance frequency to significantly contribute to the overall dissipation. Thus, to obtain strong additional damping, the lower eigenfrequencies of the flexible walls must be tuned to be near the Helmholtz frequency. However, higher operating velocity shapes also allow for additional high-frequency damping. The velocity fields near the Helmholtz resonance do not correspond to 'pure' eigenmodes, even though the eigenfrequency of the (1,5) mode is very close. These 'mixed' operating velocity shapes appear to be a blend of different eigenmodes because they are not the same as in-vacuo eigenmode shapes of a rectangular plate, as displayed in Fig. 2.12. This again suggests that the resonance behaviour of the flexible plate is altered by the Helmholtz resonance and second cavity. Another contributing factor is that the velocity of the flexible plate depends on the pressure difference inside the cavity, which is higher near the Helmholtz resonance, regardless of nearby eigenmodes. The depiction of the plate velocity fields in Fig. 6.52 is captured at the highest mean velocity. However, the instantaneous velocity field depends on the phase of the incoming acoustic excitation. This is visible in Fig. 6.51, as the plate velocity fields differ for each cell, even though they are all excited at the same frequency at 1000 Hz.

The damping contributions of the flexible plates and the viscothermal boundaries inside the cavities are depicted in Fig. 6.53. The cavity losses of all the main and second cavities are calculated as the difference in the total dissipation between one simulation including core losses and one simulation excluding core losses, i.e., a simulation without considering the viscothermal losses at the cavity walls. The energy dissipated due to mechanical losses in the plates is evaluated using the stress and strain tensor, as introduced in Section 5.3. The flexible plates add substantial dissipation around 900 Hz and 1600 Hz whereas the influence of the viscothermal boundaries at the rigid walls inside the core is negligible.

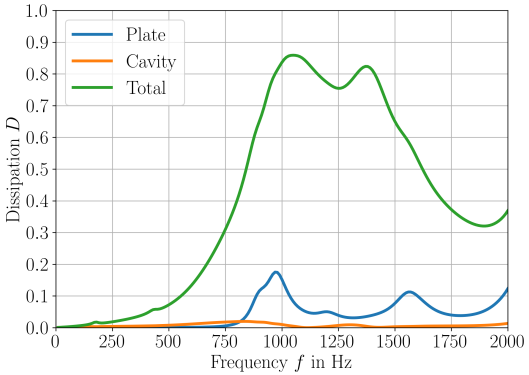

Figure 6.53.: Damping contributions of the flexible plates and viscothermal boundaries inside the cavities to the total FXW-1 liner dissipation

Summed up, the liner sample investigations showed that the flexible walls provide additional dissipation compared to a reference Helmholtz resonator liner with and without grazing flow. It was shown that this liner concept is a suitable silencer, because it is acoustically beneficial, can be manufactured and can be predicted using numerical methods. The numerical methods revealed that the flexible side walls add significant dissipation lower and higher than the Helmholtz resonance when placed inside the liner. Their operating velocity shapes were found to be different to the plate eigenmodes and their shape depends on the phase of the incoming wave. Future optimisation is possible using the presented numerical model to assess the full noise attenuation capabilities.

7. Conclusion and Outlook

This thesis investigated a novel liner concept to dampen the low-frequency and broadband noise of future aircraft engines. The concept combines airborne and structural resonances by subdividing the cavity of a Helmholtz resonator using a flexible wall. The system was investigated analytically, numerically, and experimentally. Each approach contributed to a deeper understanding of the underlying physical principles and highlighted the benefits of the novel liner concept.

Experimental results

A modular resonator cell was designed and manufactured to test different face sheets and flexible plates. The impedance and absorption were measured in a normal incidence setting. It was successfully demonstrated that a flexible plate extends the absorption spectrum of a Helmholtz resonator with additional low and high frequency resonances. These resonances were separated by simultaneously measuring the acoustic absorption by microphones with a normal incidence tube and the plate velocity through a transparent back wall with a vibrometer setup. Additionally, it was shown that the plate contribution could also be distinguished by a plane wave decomposition with microphones inside the resonator. It was shown that the overall resonance behaviour of the Helmholtz resonator coupled to a flexible plate is different from the individual resonances. Additional data from the microphone in the back cavity showed that the dynamic pressure difference is the driving force of the plate oscillations in the steady state. The modular sample design enabled the testing of different face sheets, plate geometries, and plate materials. The face sheet should be chosen such that the Helmholtz resonance frequency is in the vicinity of plate resonances. Polymers, such as TPU and EBA, are suitable choices as plate materials because of their low Young's modulus and high mechanical losses. Aluminium was not found to be a good alternative because of its high stiffness and low mechanical losses.

To test the benefits of the novel liner concept under more realistic conditions with high sound pressure levels and grazing flow, two multi-cell liner comprising multiple Helmholtz resonators with one or two flexible side walls were designed and manufactured. The measurement results showed that the liner concept with flexible walls inside the cavities adds additional dissipation with and without grazing flow below and above the Helmholtz resonance. The acoustic benefits of the flexible walls were highlighted in a favourable comparison with a reference single-degree-of-freedom Helmholtz resonator liner. Therefore, it can be concluded that the liner concept of Helmholtz resonators with flexible walls is a suitable silencer.

Analytical model

An analytical model of the system was derived based on existing models from the literature to understand the relevant effects and predict the system's behaviour. The proposed

analytical model combines the effects of the face sheet, the main and the back cavities and the flexible intermediate plate between both cavities, which can be either circular or rectangular. The model assumes an acoustic plane wave inside the cavities and in the vicinity of the flexible plate and small plate deflections. Possible modal interactions between cavity air modes and structural plate modes are neglected.

The analytical model's prediction quality was assessed by comparing it with the experimental results of the modular resonator system. A good agreement was found with the experimental data for different face sheets and circular and rectangular plates made of TPU. Therefore, the analytical model can be used to successfully predict the system's acoustic behaviour. Some differences were found for a resonator with large plates, other materials, and high sound pressure level. The latter is expected because the analytical model only considers the nonlinear effects of the face sheet but not due to large deflections of the flexible plate.

Parameter study

The computational speed of the analytical model was exploited in a parameter study. Tuning individual parameters helped to gain a better understanding of the system's sensitivity. The analytical model revealed that face sheet parameters and main cavity depth primarily influence the Helmholtz resonance, whereas plate size and material, along with back cavity depth, primarily affect the plate resonances. In the case of a flexible polymer plate, the temperature affects both resonance types because the speed of sound as well as the complex stiffness are temperature-dependent. The main finding of the parameter study is that absorption due to plate resonances is enhanced if the Helmholtz resonance is nearby. This means that tuning the Helmholtz resonance also affects the flexible plate's absorptive capabilities. Therefore, looking at the individual elements alone is insufficient. The eigenfrequencies of the flexible plate give a first estimate of the number and frequency of the expected additional absorption peaks. However, they differ because the vibration of the plate is affected by the air in the back cavity and the Helmholtz resonance. If the Helmholtz resonance coincides with a plate resonance, the resonances split up, a phenomenon known as eigenvalue veering.

The plate size and the face sheet can be tuned such that the Helmholtz resonance frequency lies between multiple radial plate modes to obtain a broad absorption spectrum with multiple absorption peaks. The closer the Helmholtz resonance, the more absorptive the nearby plate resonances.

Numerical model

A numerical finite element model of the same system was created using a commercial software that spatially resolves the acoustic sound pressure inside the cavity and the deflection of the flexible plate. Numerical and analytical models concur in their predictions for most configurations. This gives further confidence in the analytical model that the assumptions of the analytical model generally hold. Differences between the two approaches were observed for very thin and very large plates. This can be explained by visualising the sound pressure field in the vicinity of the flexible plate using the finite element model. The sound field in the vicinity of the flexible plate is no longer a plane wave for very large plates with complex mode shapes, which is an assumption of the analytical model. Numerical simulations of the multi-cell liner revealed that the flexible side walls add substantial dissipation lower and higher than the Helmholtz resonance when placed inside the liner.

Their operating velocity shapes were found to be different to plate eigenforms, and their shape depends on the phase of the incoming wave.

It was shown that the damping mechanisms of the novel liner concept can be modelled accurately with both approaches. Both models have proven to be valuable tools with specific advantages. The computational speed of the analytical model can be exploited for future optimisation of the geometries and materials. The numerical model can be used for flexible side walls, complex geometries, and if greater precision or spatial pressure and plate deflection distribution analysis is required.

Outlook and future work

Great progress has been achieved to mature the concept but still some open questions remain. This work focused on the general applicability and understanding of the physical mechanism of the liner concept. In the analytical model, the cavity is represented as a one-dimensional waveguide with a plane wave impinging on the flexible plate as one element. When the flexible wall is mounted as a side wall, the plane wave propagation direction is parallel to the wall, and the current analytical model is not applicable but needs to be adapted. This can be overcome in the future by resolving the air in the cavity as a modal field and coupling these modes to the flexible plates mode similar to plate silencer models.

Conventional liner structures have a honeycomb structure because of their high stiffness-to-weight ratio. The presented results showed that covering a large portion of the cross section with a flexible plate is acoustically beneficial. This means that ideally, the flexible plate should match the hexagonal shape of the cavity. Therefore, the analytical and numerical model should be extended to hexagonal shapes to match the cavity cross section. Finally, the potential of adding a concentrated mass at the plate centre for resonance tuning or the effect of a variable thickness as a 'acoustic black hole' may be explored.

The investigated flexible walls subdivide the cavity with the back cavity not connected to the duct. To save space, one can use a shared flexible side wall between two Helmholtz resonators. Previous research has shown that a direct coupling of two similar Helmholtz resonators with a shared flexible side wall is not beneficial because of the lack of dynamic pressure difference to excite the flexible wall. However, this may be overcome using a flexible side wall of two neighbouring, but distinct Helmholtz resonators without a second cavity. In this case, a dynamic pressure difference is expected at both distinct Helmholtz resonance frequencies. Since plate resonances were found to be more effective near a Helmholtz resonance, having two Helmholtz resonances may lead to even more broadband damping.

The resonator array samples demonstrate that a prototype liner with embedded flexible walls can be manufactured. However, the acoustic measurements of single, slightly prestressed glued plates displayed some variation in the measured absorption. Therefore, great care should be taken to ensure repeatable manufacturing to prevent unforeseen mismatches between prediction and experiment. Exploring the potential of alternative manufacturing techniques, including the sonic welding of flexible plates onto cavity structures or additive manufacturing, is recommended for the industrial-scale production of liners with flexible walls. The models presented in this thesis can be used to determine the optimal mechanical properties of flexible plates. These optimal materials must then be checked to determine whether they can withstand the harsh conditions during flight operation. Finally, other non-acoustical requirements, such as reliability or costs, must be addressed for a successful

future application in a real aeroplane engine. However, the concept is not limited to aircraft liners and can also be applied to other applications, such as heating, ventilation, and air conditioning systems or room acoustics, that require low-frequency broadband noise reduction with limited space.

Even the finite element models investigated in this work include strong simplifications. Certain plate effects, such as pretension, large deformations, or mechanical losses at the edges, are neglected. However, determining a possible pretension and quantifying edge losses as input parameters for numerical simulations is challenging. Large deformations are resolvable but require a different numerical plate model, and resolving the full stress-strain tensor within the plate may be more appropriate than employing a shell approximation. This was not possible with the available computational power during this study but may be feasible for future investigations.

The face sheet was modelled as a transfer impedance and therefore does not resolve the fluid flow in the vicinity of the face sheet. A more sophisticated numerical model would resolve the boundary layer and turbulent flow effects. The interaction between high-sound-pressure levels, grazing flow, and acoustic waves is challenging in itself, and the introduction of a flexible wall complicates it even further. For example, jets are formed if the sound particle velocity amplitude exceeds the facesheet thickness. These jets may interact with the flexible plate for thin cavities, which must be addressed accordingly. Grazing flow may also lead to a difference in static pressure between the main and the back cavities if no pressure equilibrium hole is introduced. On the one hand, if the hole is too small, the flexible plate may be prestressed due to a difference in static pressure, leading to unknown differences with predictions. On the other hand, if the hole is too large, the dynamic pressure difference between the cavities is bridged, which reduces plate vibrations. Therefore, the optimal hole size should be investigated either experimentally (i.e., by drilling different-sized holes into the plate holder) or numerically. This aspect is similar to the drainage holes in conventional liners to ensure that unwanted environmental fluids do not agglomerate inside the liner cavities.

This work serves as a foundation for such more advanced research studies to explore the full potential of Helmholtz resonators with flexible walls in a multi-objective optimisation. Hopefully, this enables a practical application of the concept in aero engines or other environments where low-frequency and broadband noise damping with little available space is needed.

A. Appendix

A.1. Volume displacement of a clamped circular plate

This brief section presents the calculation of the volume displacement of a clamped circular plate during the derivation of the equivalent impedance in Section 2.4.2. For ease of notation the argument of the Bessel functions is dropped if the argument is a scalar: e.g. $J_0(k_\mathrm{b}R_\mathrm{p}) = J_0$. Additionally, for the same reason, in this section $k_\mathrm{b} = k$ and $R_\mathrm{p} = R$. Arguments of functions are denoted with round brackets, whereas square brackets imply multiplication. With these prerequisites, the mean displacement of a clamped circular plate due to a plane wave excitation $\hat{w}_\mathrm{avg}$ in Eq. (2.64) can be expressed as follows:

$$\hat{w}_\mathrm{avg} = 2\pi \int_0^R \xi r \mathrm{d}r \tag{A.1}$$

$$= 2\pi \int_0^R \frac{\Delta p}{k^4 D} \left[\frac{I_1}{J_0 I_1 + J_1 I_0} J_0(kr) + \frac{J_1}{J_0 I_1 + J_1 I_0} I_0(kr) - 1 \right] r \mathrm{d}r \tag{A.2}$$

$$= \frac{2\pi\Delta p}{k^4 D} \left[\frac{I_1}{J_0 I_1 + J_1 I_0} \int_0^R J_0(kr) r \mathrm{d}r + \frac{J_1}{J_0 I_1 + J_1 I_0} \int_0^R I_0(kr) r \mathrm{d}r - \int_0^R r \mathrm{d}r \right] \tag{A.3}$$

$$= \frac{2\pi\Delta p}{k^4 D} \left[\frac{I_1}{J_0 I_1 + J_1 I_0} \left. \frac{r J_1(kr)}{k} \right|_0^R + \frac{J_1}{J_0 I_1 + J_1 I_0} \left. \frac{r I_1(kr)}{k} \right|_0^R - \left. \frac{r^2}{2} \right|_0^R \right] \tag{A.4}$$

$$= \frac{2\pi\Delta p}{k^4 D} \left[\frac{I_1}{J_0 I_1 + J_1 I_0} \frac{R J_1(kR)}{k} + \frac{J_1}{J_0 I_1 + J_1 I_0} \frac{R I_1(kR)}{k} - \frac{R^2}{2} \right] \tag{A.5}$$

$$= \frac{\pi R^2 \Delta p}{k^4 D} \left[\frac{2}{kR} \left[\frac{I_1 J_1}{J_0 I_1 + J_1 I_0} + \frac{J_1 I_1}{J_0 I_1 + J_1 I_0} \right] - 1 \right] \tag{A.6}$$

$$= \frac{\pi R^2 \Delta p}{k^4 D} \left[\frac{2}{kR} \left[\frac{2 J_1 I_1}{J_0 I_1 + J_1 I_0} \right] - 1 \right] \tag{A.7}$$

$$= \frac{\pi R^2 \Delta p}{k^4 D} \left[\frac{2 J_1 I_1 + 2 J_1 I_1 - kR[J_0 I_1 + J_1 I_0]}{kR[J_0 I_1 + J_1 I_0]} \right] \tag{A.8}$$

$$= \frac{\pi R^2 \Delta p}{k^4 D} \left[\frac{I_1[2J_1 - kRJ_0] + J_1[2I_1 - kRI_0]}{kR[J_0 I_1 + J_1 I_0]} \right] \tag{A.9}$$

$$= \frac{\pi R^2 \Delta p}{k^4 D} \left[\frac{I_1[kRJ_2] - J_1[kRI_2]}{kR[J_0 I_1 + J_1 I_0]} \right] \tag{A.10}$$

$$= \frac{\pi R^2 \Delta p}{k^4 D} \left[\frac{I_1(kR) J_2(kR) - J_1(kR) I_2(kR)}{J_0(kR) I_1(kR) + J_1(kR) I_0(kR)} \right], \tag{A.11}$$

in which the following identities have been used:

$$\int J_0(ax)x\mathrm{d}x = \frac{xJ_1(ax)}{a} + c \qquad \int I_0(ax)x\mathrm{d}x = \frac{xI_1(ax)}{a} + c \tag{A.12}$$

$$2J_1(x) - xJ_0 = xJ_2(x) \qquad 2I_1(x) - xI_0 = -xI_2(x). \tag{A.13}$$

A.2. Additional vibrometer setup information

This brief section provides additional information about the vibrometer setup.

The laser beam of the vibrometer must pass through the transparent back wall. If the transparent back wall vibrates, then the vibration of the transparent wall corrupts the measured plate vibration. The flexible plate is mounted inside a plate holder. If the plate holder vibrates, then the measured plate vibration is corrupted by the plate holder motion. Therefore, the vibrometer was focused on the back plate and plate holder to measure their in-situ vibration. Photographs of the vibrometer setup and the measured velocity of the flexible plate, the plate holder and the back plate are presented in Fig. A.1. Because the vibration amplitude of the flexible plate is orders of magnitude higher than those of the other parts, their influence was found to be negligible.

The transparency of the back wall was assessed by measuring the vibration of the flexible plate with and without the transparent back wall at a sufficient distance from the resonator. Photographs of the different setups are presented in Fig. A.2. These setups isolate the effect of the transparent back wall, thereby avoiding the change of vibration behaviour between open and closed back cavities. The plate vibration velocity and the absorption between a distanced and removed transparent back plate agreed very well in Fig. A.2. Therefore, the transparent back wall can be assumed to be sufficiently transparent.

Because TPU is transparent, a reflective colour had to be added to the centre point to measure the vibration. The spectra with and without reflective colour agree in Fig. A.3. Therefore, adding a reflective colour to the centre point did not significantly alter the behaviour of the plate.

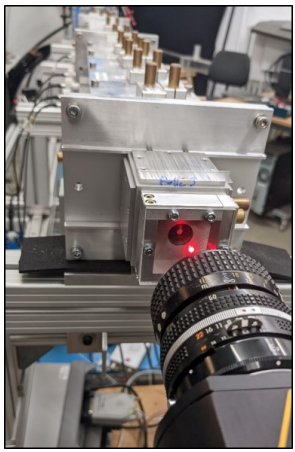

(a) Vibrometer setup to determine plate holder vibration

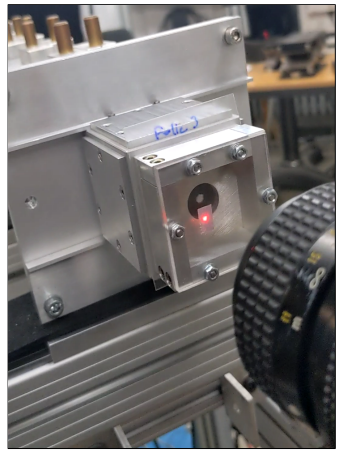

(b) Vibrometer setup to determine back plate vibration

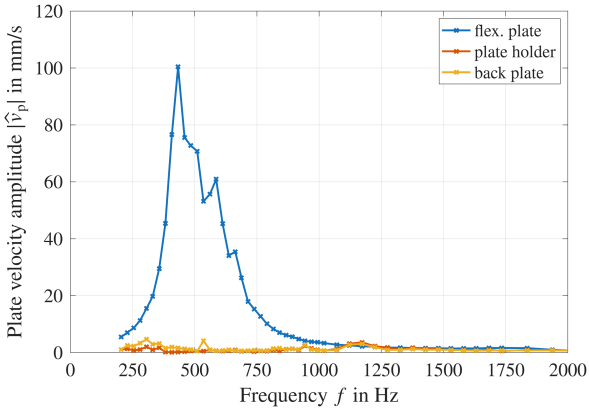

(c) Vibration velocity

Figure A.1.: Setup and comparison to show that the plate holder and back plate show no significant vibration. The sound pressure level excitation was 110 dB for all cases.

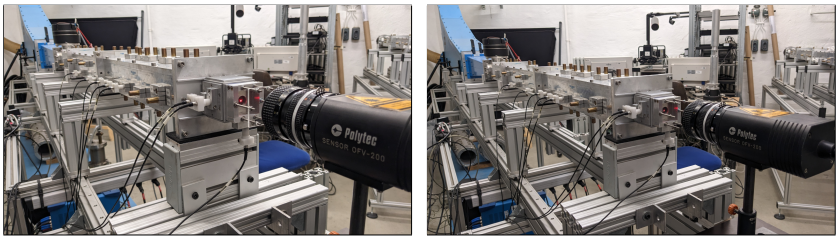

(a) Vibrometer setup with distanced back wall

(b) Vibrometer setup with no back wall

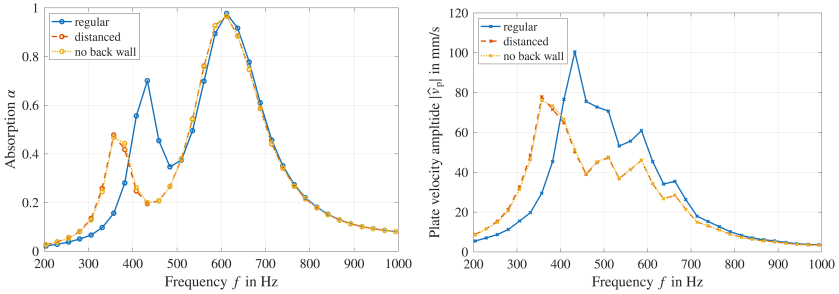

(c) Absorption

(d) Plate vibration velocity

Figure A.2.: Setup and comparison to show that the transparent back wall does not affect the measured plate vibration. The sound pressure level excitation was 100 dB for all cases. Removing the back wall shifts the plate related absorption peak towards lower frequencies.

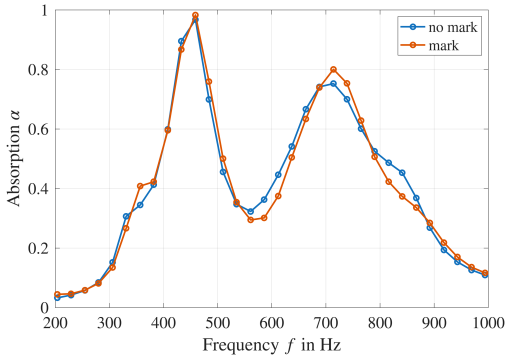

Figure A.3.: Absorption of the resonator at DUCT-NIT with a flexible plate with a diameter of 30 mm without (solid) and with reflective marking in the centre (dashed) to enable vibrometer measurements. A slight difference is visible, which also might be random.

A.3. Numerical mesh study

A mesh refinement study of the numerical models was conducted to evaluate the necessary resolution for simulating the acoustic effects with sufficient accuracy and minimal computational expense. The normal incidence absorption and the average plate velocity were chosen as the outcome parameters to evaluate the simulation accuracy in this mesh refinement study. For meshes used in finite element methods for acoustic problems, a general guideline is that six quadratic elements per wavelength in the air domain are usually sufficient to accurately model the acoustic field. However, no such well-recognised rule exists for the resolution of plate vibrations.

Four different meshes with different resolutions were tested. Their properties are stated in Table A.1.

Table A.1.: Mesh properties, normal incidence case

Mesh type	Coarse (Fig. A.4a)	Baseline (Fig. A.4b)	Fine (Fig. A.4c)	Very Fine (Fig. A.4d)	Quarter (Fig. A.7)
Max. plate element size	$d_\mathrm{p}/5$	$d_\mathrm{p}/10$	$d_\mathrm{p}/20$	$d_\mathrm{p}/40$	$d_\mathrm{p}/10$
Number of elements	3378	7402	28870	112524	2014
Computation time in min	2.3	5	24.5	154	1.7

A depiction of the meshes can be found in Fig. A.4. The channel is a structured mesh with six quadratic elements per wavelength. The mesh inside the resonator was a free tetrahedral mesh with a maximum element size of six quadratic elements per wavelength and a maximum growth factor of 1.2. For the baseline mesh Fig. A.4b, the maximum element size at the plate surface was set to $d_\mathrm{p}/10$. The latter value was changed to $d_\mathrm{p}/5$ for the coarse mesh (Fig. A.4a) and $d_\mathrm{p}/20$ or $d_\mathrm{p}/40$ for the fine (Fig. A.4c) and very fine mesh (Fig. A.4d), respectively. The plate diameter is 30 mm. Changes in plate resolution also affect the mesh in the resonator volume linked by the growth factor. The frequency resolution was set to 5 Hz between 5 Hz and 4000 Hz.

The corresponding absorption spectra are depicted in Fig. A.5. The results largely overlap. The only marginal differences in the absorption can be observed near higher plate resonances around 1400 Hz. The largest difference was observed between the coarse mesh (blue) and the baseline mesh (orange). Using a finer mesh than the baseline mesh does not result in significantly different results. The same conclusion can be drawn from the mean absolute plate velocity spectra for the different meshes in Fig. A.6.

Thus, a maximum element size of $d_\mathrm{p}/10$ at the plate was sufficient to resolve both the overall acoustic performance (absorption) and the plate behaviour (mean absolute plate velocity). Similar results were achieved for the resonator with a rectangular flexible plate, with the maximum element size being $l_\mathrm{p}/10$, where l_p refers to the shortest side of the plate.

Symmetric boundary conditions of the model were used to further increase the computation speed. The normal incidence model is double-symmetric, and the mesh size can be reduced

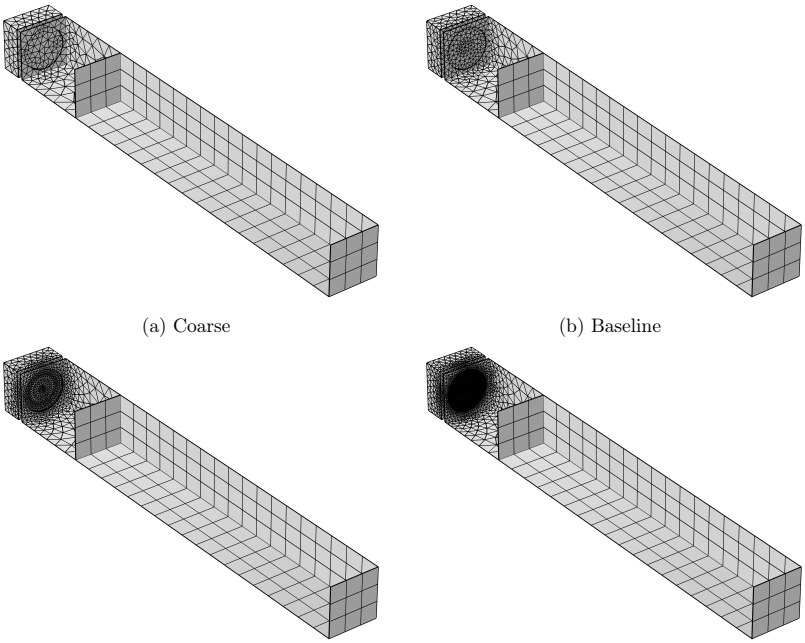

(a) Coarse (b) Baseline

(c) Fine (d) Very fine

Figure A.4.: Different mesh resolutions

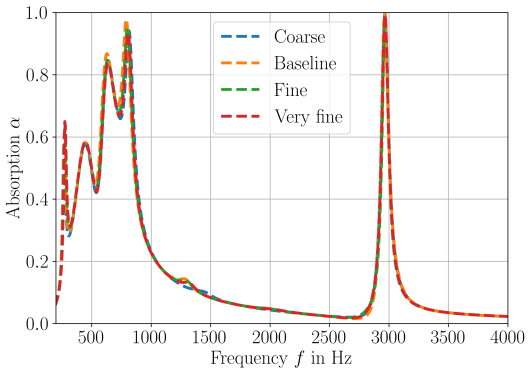

Figure A.5.: Absorption for different mesh resolutions

to a quarter of its initial size. The quarter model with the mesh resolution of the baseline case is depicted in Fig. A.7; the symmetry conditions are applied at the top and right plane or edge, respectively.

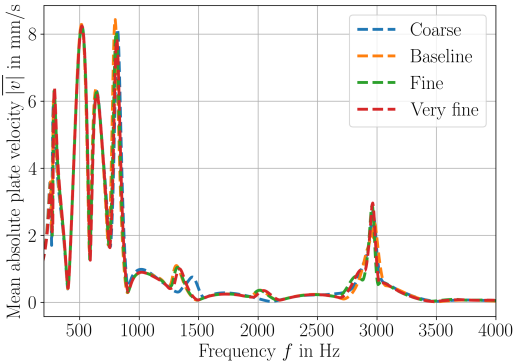

Figure A.6.: Mean absolute plate velocity for different mesh resolutions

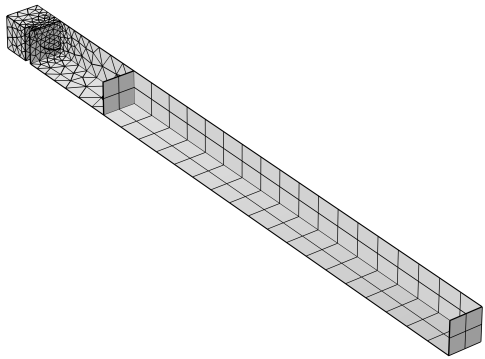

Figure A.7.: Quarter mesh with double symmetric (top and right side) boundary conditions

The predicted absorption spectra are presented in Fig. A.8. As the predictions align nearly perfectly, the quarter wave model is able to achieve the same accuracy as the full model in a fraction of the computation time.

A similar study was conducted for the grazing incidence configuration, i.e., the liner sample with one flexible wall (FXW-1) in the DUCT-R setting, to evaluate exploiting the symmetry. The mesh properties are stated in Table A.2.

Notably, the computation time of the full model is more than double than that of the half model. This might be because the temporary data exceeded the single workstation's random-access memory and had to be stored in the solid-state drive, which slowed down computation. The corresponding full and half models with a symmetry condition are depicted in Fig. A.9; additional information can be found in Table A.2. The predicted

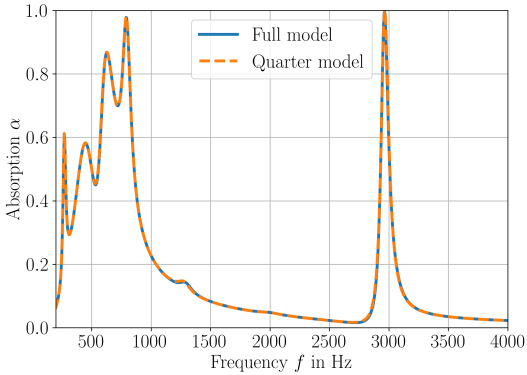

Figure A.8.: Absorption as predicted by the full model and the quarter model

Table A.2.: Mesh properties, grazing incidence case

Mesh type	Full (Fig. A.9a)	Half (Fig. A.9b)
Number of elements	186100	93205
Computation time in min	119	33

scattering coefficients are plotted in Fig. A.10, with perfect alignment between the full and half models for all parameter predictions.

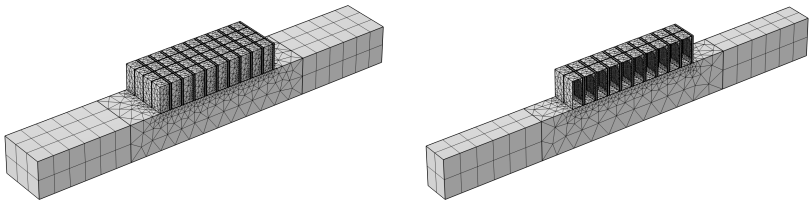

(a) Full mesh (b) Half mesh

Figure A.9.: Grazing incidence meshes of FXW-1 model

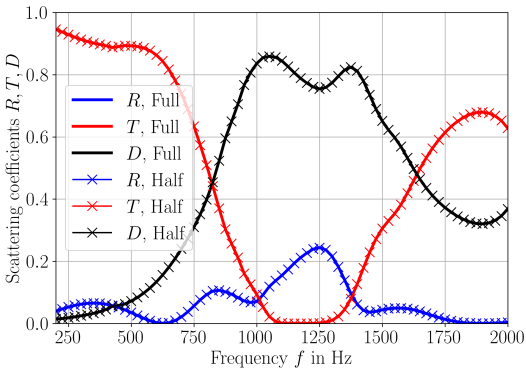

Figure A.10.: Scattering coefficients for full model and half model (FXW-1) with symmetry conditions

A.4. Additional comparisons between analytical and numerical models

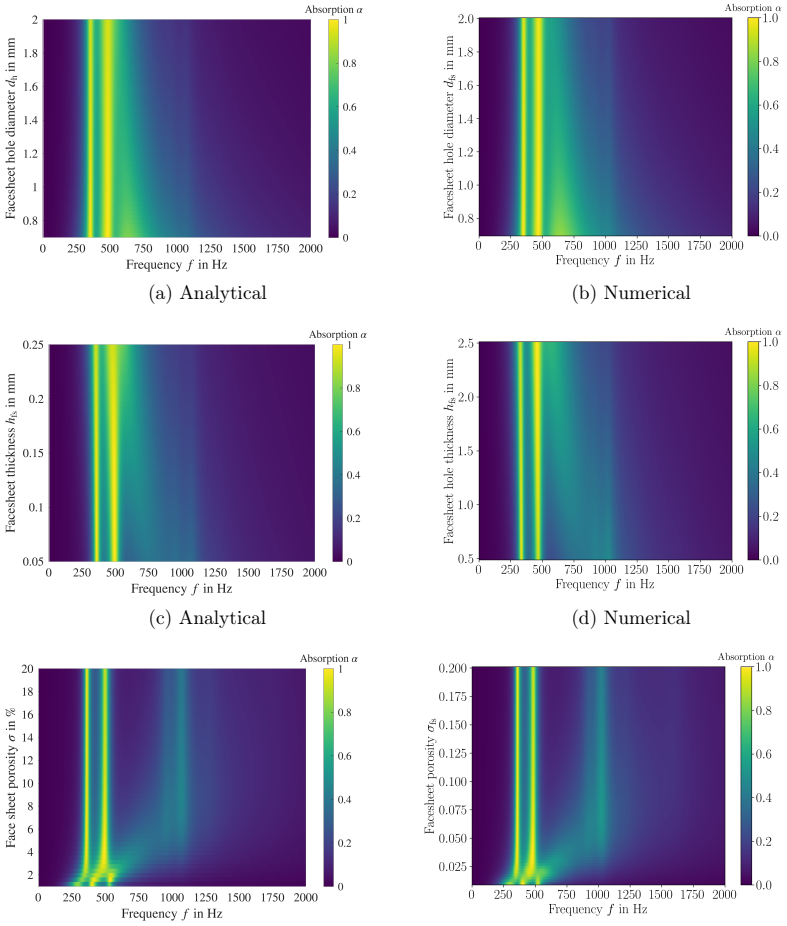

Figure A.11.: Comparison between analytical (left) and numerical (right) absorption maps. First row: Variation of face sheet hole diameter d_{h}, second row: Variation of face sheet thickness h_{fs}, third row: Variation of face sheet porosity σ

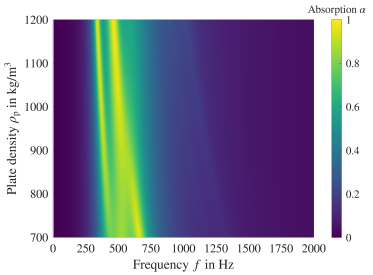

(a) Analytical

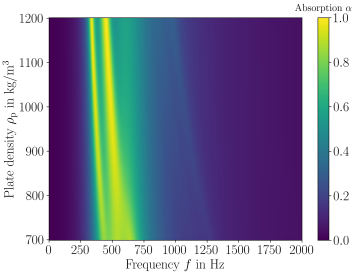

(b) Numerical

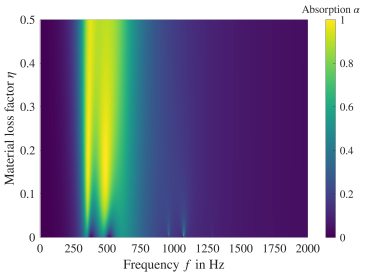

(c) Analytical

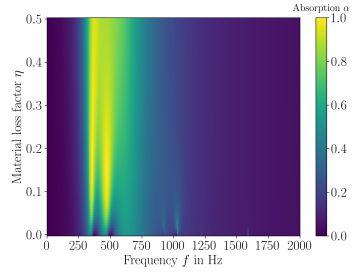

(d) Numerical

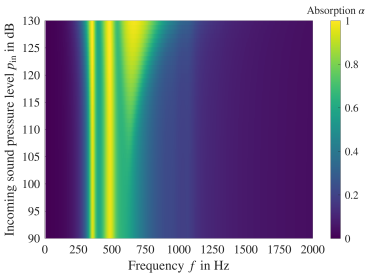

(e) Analytical

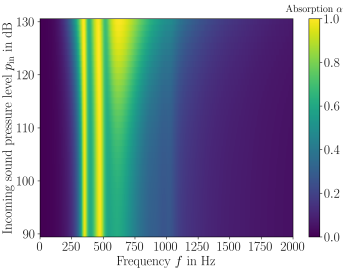

(f) Numerical

Figure A.12.: Comparison between analytical (left) and numerical (right) absorption maps. First row: Variation of plate density ρ_p, second row: Variation of material loss factor η, third row: Variation of incoming sound pressure level p'_{in}

Bibliography

[1] C. Bergero, G. Gosnell, D. Gielen, S. Kang, M. Bazilian, and S. J. Davis. 'Pathways to net-zero emissions from aviation'. In: *Nature Sustainability* 6.4 (2023), pp. 404–414. DOI: 10.1038/s41893-022-01046-9 (cit. on p. 1).

[2] B. Berglund, T. Lindvall, and D. H. Schwela. *Guidelines for community noise*. 1999 (cit. on p. 1).

[3] 'WHO Environmental Noise Guidelines for the European Region: A Systematic Review on Environmental Noise and Cardiovascular and Metabolic Effects: A Summary'. In: *International Journal of Environmental Research and Public Health* 15.2 (2018). DOI: 10.3390/ijerph15020379 (cit. on p. 1).

[4] European Environment Agency. *European Aviation environmental report*. 2022. DOI: 10.2822/129746 (cit. on p. 1).

[5] E. Commission, D.-G. for Research, and Innovation. *Fly the Green Deal – Europe's vision for sustainable aviation*. Publications Office of the European Union, 2022. DOI: 10.2777/732726 (cit. on p. 1).

[6] M. J. T. Smith. *Aircraft noise*. 2nd ed. Vol. 3. Cambridge aerospace series. Cambridge: Cambridge University Press, 2004. DOI: 10.1017/CBO9780511584527 (cit. on pp. 1 sqq.).

[7] M. Jones, B. Howerton, and E. Ayle. 'Evaluation of Parallel-Element, Variable-Impedance, Broadband Acoustic Liner Concepts'. In: *18th AIAA/CEAS Aeroacoustics Conference (33rd AIAA Aeroacoustics Conference)*. Colorado Springs, Colorado, 2012. DOI: 10.2514/6.2012-2194 (cit. on pp. 1, 7).

[8] D. P. Lockard and M. L. Geoffrey. *The airframe noise reduction challenge*. Tech. rep. NASA/TM–2004–213013. National Aeronautics and Space Administration, 2004 (cit. on p. 1).

[9] L. Leylekian, A. Covrig, and A. Maximova. *Aviation Noise Impact Management: Technologies, Regulations, and Societal Well-Being in Europe*. Springer Cham, 2022. DOI: 10.1007/978-3-030-91194-2 (cit. on pp. 1 sq.).

[10] E. Benini, C. Mistry, and A. R. Wadia. 'Historical Developments in Fan Technologies for Aeroengines'. In: *Proceedings of ASME Turbo Expo 2023*. GT2023-101639. 2023 (cit. on pp. 1 sq.).

[11] CFM International. *LEAP Overview Brochure*. 2017 (cit. on p. 2).

[12] Pratt & Whitney. *Commercial engines PW1100G-JM: Advantage, Powering the Airbus 320neo Family*. 2024 (cit. on p. 2).

[13] Vetters et al. 'Ultra High Bypass Ratio Turbofan Engine'. US 2014/0363276 A1. 2014 (cit. on p. 2).

[14] R. K. Bhargava. 'Evolution of Gas Turbine Technologies for Air, Land and Sea: 80+ Years of Historical Overview'. In: *Proceedings of ASME Turbo Expo 2023*. GT2023-101627. 2023 (cit. on p. 2).

[15] E. Nesbitt. 'Current engine noise and reduction technology'. In: *CEAS Aeronautical Journal* 10.1 (2019), pp. 93–100. DOI: 10.1007/s13272-019-00381-6 (cit. on pp. 2 sq.).

[16] C. E. Hughes. *NASA Collaborative research on the ultra high bypass engine cycle and potential benefits for noise, performance and emissions*. Tech. rep. NASA/TM—2013-216345. National Aeronautics and Space Administration, 2013 (cit. on p. 2).

[17] S. Moreau. 'Turbomachinery Noise Predictions: Present and Future'. In: *Acoustics* 1.1 (2019), pp. 92–116. DOI: 10.3390/acoustics1010008 (cit. on p. 2).

[18] E. A. S. A. (EASA). *Type-certificate data sheet No.IM.E.093 for PW1100G-JM Series Engines; Issue: 06*. 2019 (cit. on p. 2).

[19] J. F. Groeneweg, T. G. Sofrin, E. J. Rice, and P. R. G. Gliebe. *Turbomachinery Noise*. Tech. rep. NASA Reference Publication 1258, Vol. 1 WRDC Technical Report 90-3052. National Aeronautics and Space Administration, 1991 (cit. on pp. 3 sq.).

[20] S. Moreau and M. Roger. 'Turbomachinery Noise Review'. In: *International Journal of Turbomachinery, Propulsion and Power* 9.1 (2024), p. 11. DOI: 10.3390/ijtpp9010011 (cit. on p. 2).

[21] M. H. Robinson, D. G. MacManus, K. Richards, and C. Sheaf. 'Short and slim nacelle design for ultra-high BPR engines'. In: *55th AIAA Aerospace Sciences Meeting*. Grapevine, Texas, 2017. DOI: 10.2514/6.2017-0707 (cit. on p. 3).

[22] E. Envia. *Fan Noise Reduction: An Overview*. Tech. rep. NASA/TM—2001-210699. National Aeronautics and Space Administration, 2001 (cit. on p. 3).

[23] X. Liu, D. Zhao, Di Guan, S. Becker, D. Sun, and X. Sun. 'Development and progress in aeroacoustic noise reduction on turbofan aeroengines'. In: *Progress in Aerospace Sciences* 130 (2022), p. 100796. DOI: 10.1016/j.paerosci.2021.100796 (cit. on p. 3).

[24] R. E. Owens. *Energy efficient engine propulsion system - aircraft integration evaluation*. Tech. rep. NASA-CR-159488. National Aeronautics and Space Administration, 1978 (cit. on p. 4).

[25] M. G. Jones, F. Simon, and R. Roncen. 'Broadband and Low-Frequency Acoustic Liner Investigations at NASA and ONERA'. In: *AIAA Journal* (2022), pp. 1–20. DOI: 10.2514/1.J060862 (cit. on pp. 4, 6 sqq.).

[26] H. Shahzad, S. Hickel, and D. Modesti. 'Turbulence and added drag over acoustic liners'. In: *Journal of Fluid Mechanics* 965 (2023). DOI: 10.1017/jfm.2023.397 (cit. on p. 4).

[27] B. M. Howerton. 'Acoustic Liner Drag: Measurement Uncertainty Reduction and Application to Novel Perforate Geometries'. In: *30th AIAA/CEAS Aeroacoustics Conference (2024)*. Rome, Italy, 2024. DOI: 10.2514/6.2024-3247 (cit. on p. 5).

[28] H. Shahzad, S. Hickel, and D. Modesti. 'Physics-Informed Acoustic Liner Optimization: Balancing Drag and Noise'. In: *AIAA Journal* (2024), pp. 1–9. DOI: 10.2514/1.J063677 (cit. on p. 5).

[29] Alan S. Hersh and Bruce Walker. *Effect of Grazing Flow on the Acoustic Impedance of Helmholtz Resonators Consisting of Single and Clustered Orifices*. Tech. rep. NASA-CR-3177. National Aeronautics and Space Administration, 1979 (cit. on pp. 5, 27).

[30] D. Rockwell and E. Naudascher. 'Review—Self-Sustaining Oscillations of Flow Past Cavities'. In: *Journal of Fluids Engineering* 100.2 (1978), pp. 152–165. DOI: 10.1115/1.3448624 (cit. on p. 5).

[31] F. Ghanadi, M. Arjomandi, B. Cazzolato, and A. Zander. 'Interaction of a flow-excited Helmholtz resonator with a grazing turbulent boundary layer'. In: *Experimental Thermal and Fluid Science* 58 (2014), pp. 80–92. DOI: 10.1016/j.expthermflusci.2014.06.016 (cit. on p. 5).

[32] S. Palani, P. Murray, A. McAlpine, K. Knepper, and C. Richter. 'Experimental and numerical assessment of novel acoustic liners for aero-engine applications'. In: *28th AIAA/CEAS Aeroacoustics 2022 Conference*. Southampton, UK, 2022. DOI: 10.2514/6.2022-2900 (cit. on pp. 5, 7).

[33] D. M. Nark and M. G. Jones. 'Design of an Advanced Inlet Liner for the Quiet Technology Demonstrator 3'. In: *25th AIAA/CEAS Aeroacoustics Conference*. Delft, The Netherlands: American Institute of Aeronautics and Astronautics, 2019. DOI: 10.2514/6.2019-2764 (cit. on p. 5).

[34] André Spillere. 'Boundary layer effects on acoustic liners for turbofan engines: from experimental methods to optimization techniques'. PhD thesis. Florianópolis: Universidade Federal de Santa Catarina, 2022. DOI: 10.13140/RG.2.2.21486.89927 (cit. on pp. 5, 17).

[35] J. W. S. Rayleigh. 'V. On the theory of resonance'. In: *Philosophical Transactions of the Royal Society of London* 161 (1871), pp. 77–118. DOI: 10.1098/rstl.1871.0006 (cit. on pp. 5, 19).

[36] L. F. Kinsler, A. R. Frey, A. B. Coppens, and J. V. Sanders. *Fundamentals of Acoustics*. 4th ed. New York: John Wiley & Sons, Inc., 2000, pp. 284–288 (cit. on pp. 5, 12, 16, 20).

[37] M. G. Jones, W. R. Watson, D. M. Nark, B. M. Howerton, and M. Brown. *A Review of Acoustic Liner Experimental Characterization at NASA Langley*. Tech.

rep. NASA/TP–2020–220583. National Aeronautics and Space Administration, 2020 (cit. on pp. 5, 8, 17).

[38] R. E. Kraft, J. Yu, and H.-W. Kwan. *Acoustic Treatment Design Scaling Methods: Volume 2: Advanced Treatment Impedance Models for High Frequency Ranges*. Tech. rep. NASA / CR-1999-209120/VOL2. National Aeronautics and Space Administration, 1999 (cit. on p. 5).

[39] M. Jones, M. Tracy, W. Watson, and T. Parrott. 'Effects of Liner Geometry on Acoustic Impedance'. In: *8th AIAA/CEAS Aeroacoustics Conference and Exhibit*. Breckenridge, Colorado, 2002. DOI: 10.2514/6.2002-2446 (cit. on pp. 5, 108).

[40] Y. Murata, T. Ishii, S. Enomoto, H. Oinuma, K. Nagai, J. Oki, and H. Daiguji. 'Acoustic Liners Combined with Fine Perforated Film'. In: *AIAA Journal* 62.6 (2024), pp. 2200–2213. DOI: 10.2514/1.J063239 (cit. on p. 6).

[41] G. W. Bielak, J. W. Premo, and A. S. Hersh. *Advanced Turbofan Duct Liner Concepts*. Tech. rep. NASA/DR-1999-209002. NASA Langley, 1999 (cit. on p. 6).

[42] G. Bielak, J. Gallman, R. Kunze, J. P. P. Mziway, M. Kosanchick, A. Hersh, J. Celano, and B. Walker. *Advanced Nacelle Acoustic Lining Concepts Development*. Tech. rep. NASA/CR-2002-211672. National Aeronautics and Space Administration, 2002 (cit. on p. 6).

[43] P. G. Ferrante, D. Copiello, and M. Beutke. 'Design and Experimental Verification of "True Zero-Splice" Acoustic Liners in the Universal Fan Facility Adaptation (UFFA) Modular Rig'. In: *17th AIAA/CEAS Aeroacoustics Conference (32nd AIAA Aeroacoustics Conference)*. Portland, Oregon, 2011. DOI: 10.2514/6.2011-2728 (cit. on p. 6).

[44] D. L. Lansing and W. E. Zorumski. 'Effects of wall admittance changes on duct transmission and radiation of sound'. In: *Journal of Sound and Vibration* 27.1 (1973), pp. 85–100. DOI: 10.1016/0022-460X(73)90037-0 (cit. on p. 7).

[45] T. L. Parrott and M. G. Jones. 'Parallel-element liner impedances for improved absorption of broadband sound in ducts'. In: *Noise Control Engineering Journal* 43.6 (1995), p. 183. DOI: 10.3397/1.2828379 (cit. on pp. 7, 32).

[46] L. D. Koch, M. G. Jones, P. J. Bonacuse, C. J. Miller, J. C. Johnston, and M. A. Kuczmarski. 'An introduction to NASA's broadband acoustic absorbers that resemble natural reeds'. In: *International Journal of Aeroacoustics* 20.5-7 (2021), pp. 662–679. DOI: 10.1177/1475472X211033492 (cit. on p. 7).

[47] A. Gautam, A. Celik, and M. Azarpeyvand. 'Double Degree of Freedom Helmholtz Resonator Based Acoustic Liners'. In: *AIAA AVIATION 2021 FORUM*. Virtual Event, 2021. DOI: 10.2514/6.2021-2205 (cit. on p. 7).

[48] F. Bake, R. Burgmayer, A. Schulz, K. Knobloch, L. Enghardt, and M. G. Jones. 'IFAR liner benchmark challenge #1 – DLR impedance eduction of uniform and axially segmented liners and comparison with NASA results'. In: *International Journal*

of Aeroacoustics 20.5-7 (2021), pp. 478–496. DOI: 10.1177/1475472X211023844 (cit. on pp. 7, 17).

[49] G. Catapane, L. M. Cardone, G. Petrone, O. Robin, T. Humbert, and K. Verdiére. 'Labyrinth-Coiling Quarter Wavelength Tubes Embedded in Honeycomb Cells for Advanced Acoustic Liner Designs'. In: *30th AIAA/CEAS Aeroacoustics Conference (2024)*. Rome, Italy, 2024. DOI: 10.2514/6.2024-3251 (cit. on p. 7).

[50] M. C. Brown and M. G. Jones. 'Evaluation of Variable Facesheet Liner Configurations for Broadband Noise Reduction'. In: *AIAA AVIATION 2020 FORUM*. Reno, Nevada, 2020. DOI: 10.2514/6.2020-2616 (cit. on p. 7).

[51] S. Xie, Da Wang, Z. Feng, and S. Yang. 'Sound absorption performance of microperforated honeycomb metasurface panels with a combination of multiple orifice diameters'. In: *Applied Acoustics* 158 (2020), p. 107046. DOI: 10.1016/j.apacoust.2019.107046 (cit. on p. 7).

[52] Y. Sun, C. Liu, X. Song, X. Xu, J. Zhou, and F. Ma. 'An ultrathin high-order micro-perforated meta-liner for broadband sound attenuation under grazing flow'. In: *International Journal of Mechanical Sciences* 294 (2025), p. 110228. DOI: 10.1016/j.ijmecsci.2025.110228 (cit. on p. 7).

[53] D. L. Sutliff, D. M. Nark, and M. G. Jones. 'Multi-degree-of-freedom liner development: Concept to flight test'. In: *International Journal of Aeroacoustics* 20.5-7 (2021), pp. 792–825. DOI: 10.1177/1475472X211023860 (cit. on p. 7).

[54] M. G. Jones, D. M. Nark, A. Baca, and C. R. Smith. 'Applications of Parallel-Element, Embedded Mesh-Cap Acoustic Liner Concepts'. In: *2018 AIAA/CEAS Aeroacoustics Conference*. Atlanta, Georgia, 2018. DOI: 10.2514/6.2018-3445 (cit. on p. 7).

[55] J. R. Kreitzman and M. G. Jones. 'Toward Fully 3D-Printed Two Degree of Freedom Acoustic Liners'. In: *AIAA SCITECH 2024 Forum*. Orlando, Florida, 2024. DOI: 10.2514/6.2024-2801 (cit. on p. 7).

[56] Y. Wang, X. Qiu, L. Du, X. Jing, and X. Sun. 'Investigation of broadband performance of periodic parallel-element liners with multi-layer acoustic septa'. In: *30th AIAA/CEAS Aeroacoustics Conference (2024)*. Rome, Italy, 2024. DOI: 10.2514/6.2024-3300 (cit. on p. 7).

[57] B. M. Howerton, J. R. Kreitzman, and C. Solano. 'Extending Acoustic Liner Bandwidth with Simple Embedded Septa'. In: *30th AIAA/CEAS Aeroacoustics Conference (2024)*. Rome, Italy, 2024. DOI: 10.2514/6.2024-3302 (cit. on p. 7).

[58] S. Palani, P. Murray, A. McAlpine, D. Sasaki, and C. Richter. 'Slanted septum and multiple folded cavity liners for broadband sound absorption'. In: *International Journal of Aeroacoustics* 20.5-7 (2021), pp. 633–661. DOI: 10.1177/1475472X211023835 (cit. on p. 7).

[59] J. Yu and E. Chien. 'Folding Cavity Acoustic Liner For Combustion Noise Reduction'. In: *12th AIAA/CEAS Aeroacoustics Conference (27th AIAA Aeroacoustics*

Conference). Cambridge, Massachusetts, 2006. DOI: 10.2514/6.2006-2681 (cit. on p. 7).

[60] R. Sugimoto, P. Murray, and R. J. Astley. 'Folded Cavity Liners for Turbofan Engine Intakes'. In: *18th AIAA/CEAS Aeroacoustics Conference (33rd AIAA Aeroacoustics Conference)*. Colorado Springs, Colorado, 2012. DOI: 10.2514/6.2012-2291 (cit. on p. 7).

[61] M. G. Jones, D. M. Nark, and N. H. Schiller. 'Evaluation of Variable-Depth Liners with Slotted Cores'. In: *28th AIAA/CEAS Aeroacoustics 2022 Conference*. Southampton, UK, 2022. DOI: 10.2514/6.2022-2823 (cit. on p. 7).

[62] E. P. Ross, K. M. Figueroa-Ibrahim, S. C. Morris, D. L. Sutliff, and G. J. Bennett. 'Evaluating an Additive Manufactured Acoustic Metamaterial Using the Advanced Noise Control Fan'. In: *AIAA Journal* (2024), pp. 1–17. DOI: 10.2514/1.J063384 (cit. on p. 7).

[63] P. B. Murray, G. Dilillo, and N. Gravagnone. 'Design and Test of Novel Aero Engine Inlet Liners at the AneCom AeroTest Facility – Part II, Measurements'. In: *30th AIAA/CEAS Aeroacoustics Conference (2024)*. Rome, Italy, 2024. DOI: 10.2514/6.2024-3370 (cit. on p. 7).

[64] J. R. Kreitzman. *Conceptual Design and Validation of a Bent-Perforation-Path Acoustic Liner*. Tech. rep. NASA/TM–20230018517. National Aeronautics and Space Administration, 2024 (cit. on p. 8).

[65] F. Simon. 'Long Elastic Open Neck Acoustic Resonator for low frequency absorption'. In: *Journal of Sound and Vibration* 421 (2018), pp. 1–16. DOI: 10.1016/j.jsv.2018.01.044 (cit. on p. 8).

[66] K. Mahesh, S. K. Ranjith, and R. S. Mini. 'Recent Advancements in Helmholtz Resonator Based Low-Frequency Acoustic Absorbers: A Critical Review'. In: *Archives of Computational Methods in Engineering* (2024). DOI: 10.1007/s11831-023-10038-7 (cit. on p. 8).

[67] X. Cai, Q. Guo, G. Hu, and J. Yang. 'Ultrathin low-frequency sound absorbing panels based on coplanar spiral tubes or coplanar Helmholtz resonators'. In: *Applied Physics Letters* 105.12 (2014), p. 121901. DOI: 10.1063/1.4895617 (cit. on p. 8).

[68] C. Yang, P. Zhang, S. Jacob, E. Trigell, and M. Åbom. 'Investigation of Extended-Tube Liners for Control of Low-Frequency Duct Noise'. In: *AIAA Journal* 59.10 (2021), pp. 4179–4194. DOI: 10.2514/1.J059988 (cit. on p. 8).

[69] Z. Mei, Y. Lyu, X. Li, X. Cheng, and J. Yang. 'Parallel-coupled hierarchical and reconfigurable structure for broadband sound absorption'. In: *Applied Acoustics* 221 (2024), p. 109990. DOI: 10.1016/j.apacoust.2024.109990 (cit. on p. 8).

[70] S. Busse-Gerstengarbe, S. Nitsch, F. Bake, and L. Enghardt. 'Study on a Generic Nonlocally Reacting Liner'. In: *AIAA Journal* 53.1 (2015), pp. 123–131. DOI: 10.2514/1.J053021 (cit. on p. 8).

[71] M. Jones and T. Parrott. 'Assessment of Bulk Absorber Properties for Multi-Layer Perforates in Porous Honeycomb Liners'. In: *12th AIAA/CEAS Aeroacoustics Conference (27th AIAA Aeroacoustics Conference)*. Cambridge, Massachusetts, 2006. DOI: 10.2514/6.2006-2403 (cit. on p. 8).

[72] Y. Sun, X. Wang, L. Du, and X. Sun. 'On the flow-acoustic coupling of fan blades with over-the-rotor liner'. In: *Journal of Fluid Mechanics* 941 (2022). DOI: 10.1017/jfm.2022.323 (cit. on p. 8).

[73] D. L. Sutliff, R. F. Bozak, M. G. Jones, and D. M. Nark. 'Investigations of three over-the-rotor liner concepts at various technology readiness levels'. In: *International Journal of Aeroacoustics* 20.5-7 (2021), pp. 826–866. DOI: 10.1177/1475472X211025803 (cit. on p. 8).

[74] S. Palleja-Cabre, I. Saraceno, and P. Chaitanya. 'On the modification of tip leakage noise sources by over-tip liners'. In: *Physics of Fluids* 36.2 (2024). DOI: 10.1063/5.0187951 (cit. on p. 8).

[75] J. F. Herschel. 'LXIII. On the absorption of light by coloured media, viewed in connexion with the undulatory theory'. In: *The London, Edinburgh, and Dublin Philosophical Magazine and Journal of Science* 3.18 (1833), pp. 401–412. DOI: 10.1080/14786443308648217 (cit. on p. 8).

[76] G. Quincke. 'Über Interferenzapparate für Schallwellen'. In: *Annalen der Physik und Chemie* 204.6 (1866), pp. 177–192. DOI: 10.1002/andp.18662040602 (cit. on p. 8).

[77] G. W. Stewart. 'The Theory of the Herschel-Quincke Tube'. In: *Physical Review* 31.4 (1928), pp. 696–698. DOI: 10.1103/PhysRev.31.696 (cit. on p. 8).

[78] R. F. Hallez and R. A. Burdisso. 'The Herschel-Quincke Tube Concept as a Noise Control Device for Turbofan Engines'. In: *39th Aerospace Sciences Meeting and Exhibit*. Reno, Nevada, 2001. DOI: 10.2514/6.2001-816 (cit. on p. 8).

[79] R. A. Burdisso and W. F. Ng. *Fan Noise Control Using Herschel-Quincke Resonators*. Tech. rep. NASA/CR—2003-212097. National Aeronautics and Space Administration, 2003 (cit. on p. 8).

[80] B. Poirier, C. Maury, and J.-M. Ville. 'The use of Herschel–Quincke tubes to improve the efficiency of lined ducts'. In: *Applied Acoustics* 72.2-3 (2011), pp. 78–88. DOI: 10.1016/j.apacoust.2010.09.010 (cit. on p. 8).

[81] Z. B. Wang, Y. K. Chiang, Y. S. Choy, C. Q. Wang, and Q. Xi. 'Noise control for a dipole sound source using micro-perforated panel housing integrated with a Herschel–Quincke tube'. In: *Applied Acoustics* 148 (2019), pp. 202–211. DOI: 10.1016/j.apacoust.2018.12.016 (cit. on p. 8).

[82] P. Sijtsma and H. van der Wal. 'Modelling a Spiralling Type of Non-Locally Reacting Liner'. In: *9th AIAA/CEAS Aeroacoustics Conference and Exhibit*. Hilton Head, South Carolina, 2003. DOI: 10.2514/6.2003-3308 (cit. on p. 8).

[83] H. Matsushisa, B. Ren, and S. Sato. 'Semiactive Control of Duct Noise by a Volume-Variable Resonator'. In: *JSME International Journal* 35.2 (1991), pp. 223–228 (cit. on p. 9).

[84] J. M. de Bedout, M. A. Franchek, R. J. Bernhard, and L. Mongeau. 'Adaptive-Passive Noise Control with Self-Tuning Helmholtz Resonators'. In: *Journal of Sound and Vibration* 202.1 (1997), pp. 109–123. DOI: 10.1006/jsvi.1996.0796 (cit. on p. 9).

[85] Kostek, Theodore M.: Franchek, M. A. 'Hybrid Noise Control in Ducts'. In: *Journal of Sound and Vibration* 237.1 (2000), pp. 81–100. DOI: 10.1006/jsvi.2000.3056 (cit. on p. 9).

[86] D. Zhao and A. S. Morgans. 'Tuned passive control of combustion instabilities using multiple Helmholtz resonators'. In: *Journal of Sound and Vibration* 320.4-5 (2009), pp. 744–757. DOI: 10.1016/j.jsv.2008.09.006 (cit. on p. 9).

[87] J. Gaeta and K. Ahuja. 'A tunable 2DOF liner'. In: *5th AIAA/CEAS Aeroacoustics Conference and Exhibit*. Bellevue, Washington, 1999. DOI: 10.2514/6.1999-1852 (cit. on p. 9).

[88] K. Nagaya, Y. Hano, and A. Suda. 'Silencer consisting of two-stage Helmholtz resonator with auto-tuning control'. In: *The Journal of the Acoustical Society of America* 110.1 (2001), pp. 289–295. DOI: 10.1121/1.1370524 (cit. on p. 9).

[89] O. Cherrier, V. Pommier-Budinger, and F. Simon. 'Panel of resonators with variable resonance frequency for noise control'. In: *Applied Acoustics* 73.8 (2012), pp. 781–790 (cit. on p. 9).

[90] V. Pommier-Budinger and O. Cherrier. 'Baffle silencer with tunable resonators for adaptive control of variable tonal noise'. In: *Journal of Vibration and Control* 21.9 (2015), pp. 1801–1809. DOI: 10.1177/1077546313499928 (cit. on p. 9).

[91] R. J. Gaeta and K. K. Ahuja. 'Effect of orifice shape on acoustic impedance'. In: *International Journal of Aeroacoustics* 15.4-5 (2016), pp. 474–495. DOI: 10.1177/1475472X16642133 (cit. on pp. 9, 26).

[92] J. R. Kreitzman, F. Calkins, D. Nicholson, A. Lafranchi, L. Cattafesta, and C. Dodge. 'Active Acoustic Liners enabled by Shape Memory Alloy Technology'. In: *AIAA AVIATION 2020 FORUM*. Virtual Event, 2020. DOI: 10.2514/6.2020-2617 (cit. on p. 9).

[93] C. Solano, B. M. Howerton, and M. G. Jones. 'An Acoustic Liner with a Multi-layered Active Facesheet'. In: *28th AIAA/CEAS Aeroacoustics 2022 Conference*. Southampton, UK, 2022. DOI: 10.2514/6.2022-2902 (cit. on p. 9).

[94] R. Burgmayer, F. Bake, and L. Enghardt. 'Design and Evaluation of a Zero Mass Flow Liner'. In: *28th AIAA/CEAS Aeroacoustics 2022 Conference*. Southampton, UK, 2022. DOI: 10.2514/6.2022-2820 (cit. on p. 9).

[95] D. Zhao, A. S. Morgans, and A. P. Dowling. 'Tuned Passive Control of Acoustic Damping of Perforated Liners'. In: *AIAA Journal* 49.4 (2011), pp. 725–734. DOI: 10.2514/1.J050613 (cit. on p. 9).

[96] K. Billon, M. Gillet, E. Salze, M. Volery, E. de Bono, M. Ouisse, H. Lissek, M. Collet, and J. Mardjono. 'Smart acoustic lining for UHBR technologies engine: from the design of an electroacoustic metasurface to experimental characterization under flow'. In: *Active and Passive Smart Structures and Integrated Systems XVII*. Ed. by S. Tol, M. A. Nouh, S. Shahab, J. Yang, and G. Huang. SPIE, 2023, p. 72. DOI: 10.1117/12.2658519 (cit. on p. 9).

[97] M. Yang and P. Sheng. 'Sound Absorption Structures: From Porous Media to Acoustic Metamaterials'. In: *Annual Review of Materials Research* 47.1 (2017), pp. 83–114. DOI: 10.1146/annurev-matsci-070616-124032 (cit. on p. 9).

[98] G. Palma and U. Iemma. 'A metacontinuum model for phase gradient metasurfaces'. In: *Scientific reports* 13.1 (2023), p. 13038. DOI: 10.1038/s41598-023-39956-z (cit. on p. 9).

[99] D. Broszat, R. Maier, and R. Pongratz. 'The Virtual Scarf Inlet'. In: *13th AIAA/CEAS Aeroacoustics Conference (28th AIAA Aeroacoustics Conference)*. Rome, Italy, 2007. DOI: 10.2514/6.2007-3553 (cit. on p. 9).

[100] G. Palma, H. Mao, L. Burghignoli, P. Göransson, and U. Iemma. 'Acoustic Metamaterials in Aeronautics'. In: *Applied Sciences* 8.6 (2018), p. 971. DOI: 10.3390/app8060971 (cit. on p. 9).

[101] G. Palma, L. Burghignoli, F. Centracchio, and U. Iemma. 'Innovative Acoustic Treatments of Nacelle Intakes Based on Optimised Metamaterials'. In: *Aerospace* 8.10 (2021), p. 296. DOI: 10.3390/aerospace8100296 (cit. on p. 9).

[102] P. M. Morse and K. U. Ingård. *Theoretical acoustics*. Princeton, NJ: Princeton University Press, 1986 (cit. on pp. 12, 25, 47).

[103] A. D. Pierce. *Acoustics: An Introduction to Its Physical Principles and Applications*. 3rd ed. 2019. Cham: Springer International Publishing and Imprint: Springer, 2019 (cit. on pp. 12 sq.).

[104] S. W. Rienstra and A. Hirschberg. *An Introduction to Acoustics*. Eindhoven, 2021 (cit. on p. 12).

[105] B. S. Finn. 'Laplace and the Speed of Sound'. In: *Isis* 55.1 (1964), pp. 7–19. DOI: 10.1086/349791 (cit. on p. 13).

[106] A. Schulz. 'Die akustischen Randbedingungen perforierter Wandauskleidungen in Strömungskanälen: Physikalische Modelle und Eduktion"'. PhD thesis. Berlin: Technische Universität Berlin, 2019. DOI: 10.14279/depositonce-7943 (cit. on pp. 13 sqq., 17, 57, 65 sq., 68, 127).

[107] K. Ehrenfried. *Strömungsakustik: Skript zur Vorlesung*. Vol. 1. Berliner Hochschulskripte. Berlin: Mensch-und-Buch-Verl., 2004 (cit. on p. 14).

[108] L. Cremer. 'About the acoustic boundary layer in front of rigid walls [Original in German: Über die akustische Grenzschicht vor starren Wänden]'. In: *Archiv der elektrischen Übertragung* 2 (1948), pp. 136–139 (cit. on pp. 14, 57).

[109] D. T. Blackstock. *Fundamentals of physical acoustics*. New York: Wiley, 2000 (cit. on pp. 14 sq., 20).

[110] H. Tijdeman. 'On the propagation of sound waves in cylindrical tubes'. In: *Journal of Sound and Vibration* 39.1 (1975), pp. 1–33. DOI: 10.1016/S0022-460X(75)80206-9 (cit. on pp. 15, 82).

[111] Ronald Kampinga. 'Viscothermal acoustics using finite elements - analysis tools for engineers'. PhD thesis. Twente: Universiteit Twente, 2010 (cit. on pp. 15, 82 sq.).

[112] G. Kirchhoff. 'Über den Einfluss der Wärmeleitung in einem Gase auf die Schallbewegung'. In: *Annalen der Physik und Chemie* 210.6 (1868), pp. 177–193. DOI: 10.1002/andp.18682100602 (cit. on p. 15).

[113] C. Zwikker and C. W. Kosten. *Sound Absorbing Materials*. Elsevier Publishing Company, Inc, 1949 (cit. on pp. 15, 22).

[114] E. Dokumacı. 'A note on transmission of sound in a wide pipe with mean flow and viscothermal attenuation'. In: *Journal of Sound and Vibration* 208.4 (1997), pp. 653–655. DOI: 10.1006/jsvi.1997.1043 (cit. on pp. 16, 63).

[115] C. Lahiri, L. Enghardt, F. Bake, S. Sadig, and M. Gerendás. 'Establishment of a High Quality Database for the Acoustic Modeling of Perforated Liners'. In: *Journal of Engineering for Gas Turbines and Power* 133.9 (2011). DOI: 10.1115/1.4002891 (cit. on pp. 16, 29, 65, 67).

[116] T. Cox and P. D'Antonio. *Acoustic Absorbers and Diffusers, Third Edition: Theory, Design and Application*. 3rd ed., revised. Boca Raton and Florence: CRC Press LLC and Taylor & Francis Group, 2016, p. 27. DOI: 10.1201/9781315369211 (cit. on pp. 16, 19, 35).

[117] C. L. Morfey. *Dictionary of Acoustics*. San Diego, Calif.: Academic Press, 2001 (cit. on pp. 16, 18).

[118] F. P. Mechel, M. L. Munjal, M. Vorländer, P. Költzsch, M. Ochmann, A. Cummings, W. Maysenhölder, and W. Arnold, eds. *Formulas of acoustics*. 2. ed. Berlin: Springer, 2008 (cit. on p. 17).

[119] International Organization for Standardization. *ISO 10534-2:1998 Acoustics — Determination of sound absorption coefficient and impedance in impedance tubes — Part 2: Transfer-function method*. Norm. Geneva, 1998 (cit. on p. 17).

[120] P. D. Dean. 'An in situ method of wall acoustic impedance measurement in flow ducts'. In: *Journal of Sound and Vibration* 34.1 (1974), 97–IN6. DOI: 10.1016/S0022-460X(74)80357-3 (cit. on p. 17).

[121] V. Lafont, F. Méry, R. Roncen, F. Simon, and E. Piot. 'Liner Impedance Eduction Under Shear Grazing Flow at a High Sound Pressure Level'. In: *AIAA Journal* 58.3 (2020), pp. 1107–1117. DOI: 10.2514/1.J058756 (cit. on p. 17).

[122] A. Schulz, F. Bake, L. Enghardt, and D. Ronneberger. 'Impedance Eduction of Acoustic Liners Based on Four Different Levels of Physical Modeling'. In: *AIAA-2016-2726*. Lyon, France: 22nd AIAA/CEAS Aeroacoustics Conference, 2016. DOI: 10.2514/6.2016-2726 (cit. on p. 17).

[123] L. A. Bonomo, N. T. Quintino, A. M. N. Spillere, P. B. Murray, and J. A. Cordioli. 'A comparison of in situ and impedance eduction experimental techniques for acoustic liners with grazing flow and high sound pressure level'. In: *International Journal of Aeroacoustics* 23.1-2 (2024), pp. 60–83. DOI: 10.1177/1475472X231225629 (cit. on p. 17).

[124] A. Schulz, D. Ronneberger, C. Weng, and F. Bake. 'The effect of the convective momentum transfer on the acoustic boundary condition of perforated liners with grazing mean flow'. In: *International Journal of Aeroacoustics* 20.5-7 (2021), pp. 737–772. DOI: 10.1177/1475472X211023842 (cit. on pp. 17, 32, 127).

[125] M. G. Jones, D. M. Nark, and B. M. Howerton. 'NASA Investigation of Flow Direction Effects on Impedance Eduction for Acoustic Liners'. In: *30th AIAA/CEAS Aeroacoustics Conference (2024)*. Rome, Italy, 2024. DOI: 10.2514/6.2024-3297 (cit. on pp. 17, 30, 127).

[126] J. F. Unruh. 'Finite length tuning for low frequency lining design'. In: *Journal of Sound and Vibration* 45.1 (1976), pp. 5–14. DOI: 10.1016/0022-460X(76)90663-5 (cit. on p. 17).

[127] L. Cremer. 'Theorie der Luftschall-Dämpfung im Rechteckkanal mit schluckender Wand und das sich dabei ergebende höchste Dämpfungsmass'. In: *Acustica* 1958.3 (1953) (cit. on p. 17).

[128] B. J. Tester. 'The optimization of modal sound attenuation in ducts, in the absence of mean flow'. In: *Journal of Sound and Vibration* 27.4 (1973), pp. 477–513. DOI: 10.1016/S0022-460X(73)80358-X (cit. on p. 17).

[129] B. J. Tester. 'The propagation and attenuation of sound in lined ducts containing uniform or "plug" flow'. In: *Journal of Sound and Vibration* 28.2 (1973), pp. 151–203. DOI: 10.1016/S0022-460X(73)80102-6 (cit. on p. 17).

[130] A. Schulz, C. Weng, F. Bake, L. Enghardt, and D. Ronneberger. 'Modeling of liner impedance with grazing shear flow using a new momentum transfer boundary condition'. In: *23rd AIAA/CEAS Aeroacoustics Conference*. Denver, Colorado, 2017. DOI: 10.2514/6.2017-3377 (cit. on pp. 17, 65).

[131] H. von Helmholtz. 'Theorie der Luftschwingungen in Röhren mit offenen Enden'. In: *Journal für reine und angewandte Mathematik* Bd. LVII (1860), pp. 1–72 (cit. on p. 19).

[132] H. von Helmholtz. *Die Lehre von den Tonempfindungen als physiologische Grundlage für die Theorie der Musik*. 4th ed. Braunschweig: Friedrich Vieweg und Sohn, 1877 (cit. on p. 19).

[133] U. Ingård. 'On the Theory and Design of Acoustic Resonators'. In: *The Journal of the Acoustical Society of America* 25.6 (1953), pp. 1037–1061. DOI: 10.1121/1.1907235 (cit. on pp. 19, 22, 25 sq., 28 sq.).

[134] M. L. Munjal. *Acoustics of Ducts and Mufflers*. 1st ed. John Wiley & Sons, Inc., 1987 (cit. on p. 19).

[135] L. Cremer and H. A. Müller. *Die wissenschaftlichen Grundlagen der Raumakustik*. 2. Stuttgart: Hirzel, 1976 (cit. on p. 19).

[136] S. Polychronopoulos, D. Kougias, P. Polykarpou, and D. Skarlatos. 'The Use of Resonators in Ancient Greek Theatres'. In: *Acta Acustica united with Acustica* 99.1 (2013), pp. 64–69. DOI: 10.3813/AAA.918589 (cit. on p. 19).

[137] N. H. Fletcher and T. D. Rossing. *The Physics of Musical Instruments*. Second Edition. New York: Springer, 1998. DOI: 10.1007/978-0-387-21603-4 (cit. on p. 19).

[138] F. Hergert and P. Hale. 'A Review of Technical Inventions to include deep Bass Tones into Pipe Organs despite Space Constraints'. In: *Fourth Vienna Talk on Music Acoustics*. Proceedings of Meetings on Acoustics. ASA, 2023, p. 035011. DOI: 10.1121/2.0001672 (cit. on p. 19).

[139] T. D. Rossing, F. R. Moore, and P. Wheeler. *The science of sound*. 3. ed. Harlow: Pearson Education, 2014 (cit. on p. 19).

[140] Y. Fu, A. Kiyama, G. Liu, L. Zhang, and S. Jung. 'Revealing the sound, flow excitation, and collision dynamics of human handclaps'. In: *Physical Review Research* 7.1 (2025). DOI: 10.1103/PhysRevResearch.7.013259 (cit. on p. 19).

[141] S. Rienstra. 'Impedance Models in Time Domain, Including the Extended Helmholtz Resonator Model'. In: *12th AIAA/CEAS Aeroacoustics Conference (27th AIAA Aeroacoustics Conference)*. Cambridge, Massachusetts, 2006. DOI: 10.2514/6.2006-2686 (cit. on p. 20).

[142] I. B. Crandall. *Theory of Vibrating Systems and Sound*. New York: D. Van Nostrand Company, 1926, pp. 229–241 (cit. on pp. 22, 83).

[143] M. G. Jones, J. R. Kreitzman, and D. M. Nark. *Examination of Perforate Facesheet Impedance Prediction Models*. Tech. rep. NASA/TP-20240006417. National Aeronautics and Space Administration, 2024 (cit. on pp. 22, 31).

[144] T. H. Melling. 'The acoustic impendance [*sic!*] of perforates at medium and high sound pressure levels'. In: *Journal of Sound and Vibration* 29.1 (1973), pp. 1–65. DOI: 10.1016/S0022-460X(73)80125-7 (cit. on pp. 22, 25 sq., 29).

[145] Dah-You Maa. 'Potential of microperforated panel absorber'. In: *The Journal of the Acoustical Society of America* 104.5 (1998), pp. 2861–2865 (cit. on pp. 22, 57).

[146] A. W. Guess. 'Calculation of perforated plate liner parameters from specified acoustic resistance and reactance'. In: *Journal of Sound and Vibration* 40.1 (1975), pp. 119–137. DOI: 10.1016/S0022-460X(75)80234-3 (cit. on pp. 22, 26 sq., 29, 31 sq., 56).

[147] N. Atalla and F. Sgard. 'Modeling of perforated plates and screens using rigid frame porous models'. In: *Journal of Sound and Vibration* 303.1-2 (2007), pp. 195–208. DOI: 10.1016/j.jsv.2007.01.012 (cit. on pp. 23, 27).

[148] J. F. Allard and N. Atalla. *Propagation of sound in porous media: Modelling sound absorbing materials*. 2. ed. Chichester: Wiley, 2009 (cit. on p. 23).

[149] G. Ma and P. Sheng. 'Acoustic metamaterials: From local resonances to broad horizons'. In: *Science advances* 2.2 (2016), e1501595. DOI: 10.1126/sciadv.1501595 (cit. on pp. 23, 51).

[150] D. L. Johnson, J. Koplik, and R. Dashen. 'Theory of dynamic permeability and tortuosity in fluid-saturated porous media'. In: *Journal of Fluid Mechanics* 176.-1 (1987), p. 379. DOI: 10.1017/S0022112087000727 (cit. on p. 23).

[151] Y. Champoux and J.-F. Allard. 'Dynamic tortuosity and bulk modulus in air-saturated porous media'. In: *Journal of Applied Physics* 70.4 (1991), pp. 1975–1979. DOI: 10.1063/1.349482 (cit. on p. 23).

[152] J. W. S. Rayleigh. *The Theory of Sound*. Vol. 2. Dover Books on Physics. Newburyport: Dover Publications, 1878, pp. 319–326 (cit. on pp. 25, 47).

[153] S. A. Hambric, S. H. Sung, and D. J. Nefske. *Engineering Vibroacoustic Analysis*. Wiley, 2016. DOI: 10.1002/9781118693988 (cit. on pp. 25, 47 sq.).

[154] F. P. Mechel. *Schallabsorber: Äußere Schallfelder - Wechselwirkungen*. Stuttgart: Hirzel, 1989 (cit. on p. 25).

[155] N. S. Dickey, A. Selamet, and J. M. Novak. 'The effect of high-amplitude sound on the attenuation of perforated tube silencers'. In: *The Journal of the Acoustical Society of America* 108.3 Pt 1 (2000), pp. 1068–1081. DOI: 10.1121/1.1287707 (cit. on p. 25).

[156] H. T. Nia, A. D. Jain, Y. Liu, M.-R. Alam, R. Barnas, and N. C. Makris. 'The evolution of air resonance power efficiency in the violin and its ancestors'. In: *Proceedings. Mathematical, physical, and engineering sciences* 471.2175 (2015). DOI: 10.1098/rspa.2014.0905 (cit. on p. 26).

[157] L. J. Sivian. 'Acoustic Impedance of Small Orifices'. In: *The Journal of the Acoustical Society of America* 7.2 (1935), pp. 94–101. DOI: 10.1121/1.1915795 (cit. on pp. 26, 29).

[158] R. Burgmayer. 'Untersuchung und Auslegung periodisch durchströmter Schalldämpfer'. PhD thesis. Berlin: Technische Universität Berlin, 2024. DOI: 10.14279/depositonce-20682 (cit. on pp. 26, 32, 56, 66).

[159] K. U. Ingård. 'Scattering and Absorption by Acoustic Resonators'. PhD thesis. Massachusetts Institute of Technology, 1950 (cit. on p. 26).

[160] V. A. Fock. 'A Theoretical Investigation of the Acoustical Conductivity of a Circular Aperture in a Wall put across a tube'. In: *Comptes Rendus (Doklady) de l'Académie des Sciences de l'URSS* Volume XXXI, No 9 (1941), pp. 875–878 (cit. on p. 27).

[161] C. Lahiri. 'Acoustic Performance of Bias Flow Liners in Gas Turbine Combustors'. PhD thesis. Berlin: Technische Universität Berlin, 2014. DOI: 10.14279/depositonce-4270 (cit. on pp. 27, 33, 62 sq., 67).

[162] V. S. Nesterov. 'An experimental study of the acoustical conductivity of a circular orifice in a partition placed across a tube'. In: *Comptes Rendus (Doklady) de l'Académie des Sciences de l'URSS* Volume XXXI, No 9 (1941), pp. 879–882 (cit. on p. 27).

[163] I. L. Vér and L. L. Beranek, eds. *Noise and vibration control engineering: Principles and applications*. 2nd ed. Hoboken, N.J: Wiley, 2005. DOI: 10.1002/9780470172568 (cit. on p. 27).

[164] Tamer Elnady. 'Modelling and Characterization of Perforates in Lined Ducts and Mufflers'. PhD thesis. Stockholm: KTH, 2004 (cit. on pp. 27, 29).

[165] R. E. Motsinger and R. E. Kraft. *Design and Performance of Duct Acoustic Treatment*. Tech. rep. NASA Reference Publication 1258, Vol. 2 WRDC Technical Report 90-3052. National Aeronautics and Space Administration, 1991 (cit. on pp. 27, 29, 56).

[166] J. Yu, M. Ruiz, and H.-W. Kwan. 'Validation of Goodrich Perforate Liner Impedance Model Using NASA Langley Test Data'. In: *14th AIAA/CEAS Aeroacoustics Conference (29th AIAA Aeroacoustics Conference)*. Vancouver, British Columbia, Canada, 2008. DOI: 10.2514/6.2008-2930 (cit. on pp. 27, 31).

[167] J. W. Kooi and S. L. Sarin. 'An experimental study of the acoustic impedance of Helmholtz resonator arrays under a turbulent boundary layer'. In: *7th Aeroacoustics Conference*. Palo Alto, California, 1981. DOI: 10.2514/6.1981-1998 (cit. on pp. 27, 31 sq.).

[168] P. Murray and M. Di Giulio. 'Development and validation of a single degree of freedom perforate impedance model under high SPL and grazing flow'. In: *28th AIAA/CEAS Aeroacoustics 2022 Conference*. Southampton, UK, 2022. DOI: 10.2514/6.2022-2929 (cit. on pp. 27, 29).

[169] R. Tayong. 'On the holes interaction and heterogeneity distribution effects on the acoustic properties of air-cavity backed perforated plates'. In: *Applied Acoustics* 74.12 (2013), pp. 1492–1498. DOI: 10.1016/j.apacoust.2013.05.016 (cit. on p. 28).

[170] N. H. Schiller and M. G. Jones. 'Smeared Impedance Model for Variable Depth Liners'. In: *2018 AIAA/CEAS Aeroacoustics Conference*. Atlanta, Georgia, 2018. DOI: 10.2514/6.2018-3774 (cit. on p. 28).

[171] A. Javareshkian, A. Dancelme, H. Chen, and T. Sattelmayer. 'Influence of Hole-to-Hole Interaction on the Acoustic Behavior of Multi-Orifice Perforated Plates'. In: *Journal of Engineering for Gas Turbines and Power* 144.3 (2022). DOI: 10.1115/1.4052647 (cit. on p. 28).

[172] G. Müller and M. Möser, eds. *Taschenbuch der technischen Akustik: Mit 119 Tabellen*. 3.ed. Berlin and Heidelberg: Springer, 2004 (cit. on p. 28).

[173] A. Javareshkian. 'Modeling and Characterization of Acoustically Absorbing Liners'. PhD thesis. München: TUM School of Engineering and Design, 2022 (cit. on p. 28).

[174] L. Jaouen and F.-X. Bécot. 'Acoustical characterization of perforated facings'. In: *The Journal of the Acoustical Society of America* 129.3 (2011), pp. 1400–1406. DOI: 10.1121/1.3552887 (cit. on p. 28).

[175] U. Ingård. 'Absorption Characteristics of Nonlinear Acoustic Resonators'. In: *The Journal of the Acoustical Society of America* 44.4 (1968), pp. 1155–1156. DOI: 10.1121/1.1911215 (cit. on pp. 29 sq.).

[176] U. Ingård and S. Labate. 'Acoustic Circulation Effects and the Nonlinear Impedance of Orifices'. In: *The Journal of the Acoustical Society of America* 22.2 (1950), pp. 211–218. DOI: 10.1121/1.1906591 (cit. on p. 29).

[177] C. K. Tam, H. Ju, M. G. Jones, W. R. Watson, and T. L. Parrott. 'A computational and experimental study of resonators in three dimensions'. In: *Journal of Sound and Vibration* 329.24 (2010), pp. 5164–5193. DOI: 10.1016/j.jsv.2010.06.005 (cit. on p. 29).

[178] U. Ingård and H. Ising. 'Acoustic Nonlinearity of an Orifice'. In: *The Journal of the Acoustical Society of America* 42.1 (1967), pp. 6–17. DOI: 10.1121/1.1910576 (cit. on p. 29).

[179] B. T. Zinn. 'A theoretical study of non-linear damping by Helmholtz resonators'. In: *Ultrasonics* 9.2 (1971), p. 124. DOI: 10.1016/0041-624X(71)90165-X (cit. on p. 29).

[180] Z. Laly, N. Atalla, and S.-A. Meslioui. 'Acoustical modeling of micro-perforated panel at high sound pressure levels using equivalent fluid approach'. In: *Journal of Sound and Vibration* 427 (2018), pp. 134–158. DOI: 10.1016/j.jsv.2017.09.011 (cit. on pp. 29, 56 sq.).

[181] S.-H. Park. 'A design method of micro-perforated panel absorber at high sound pressure environment in launcher fairings'. In: *Journal of Sound and Vibration* 332.3 (2013), pp. 521–535. DOI: 10.1016/j.jsv.2012.09.015 (cit. on p. 29).

[182] M. A. Temiz, J. Tournadre, I. L. Arteaga, and A. Hirschberg. 'Non-linear acoustic transfer impedance of micro-perforated plates with circular orifices'. In: *Journal of Sound and Vibration* 366 (2016), pp. 418–428. DOI: 10.1016/j.jsv.2015.12.022 (cit. on p. 30).

[183] E. J. Rice. *A model for the acoustic impedance of a perforated plate liner with multiple frequency excitation*. Tech. rep. NASA TM X-67950. National Aeronautics and Space Administration, 1971 (cit. on pp. 30 sq., 56).

[184] H. Boden and J. Fritzell. 'A study of high level tonal and broadband random excitation for acoustic liners'. In: *23rd AIAA/CEAS Aeroacoustics Conference*. Reston, Virginia: American Institute of Aeronautics and Astronautics, 2017. DOI: 10.2514/6.2017-4192 (cit. on p. 30).

[185] J. R. Kreitzman and M. G. Jones. 'Influence of Source Type on Acoustic Liner Impedance in No Flow'. In: *30th AIAA/CEAS Aeroacoustics Conference (2024)*. Rome, Italy: American Institute of Aeronautics and Astronautics, 2024. DOI: 10.2514/6.2024-3249 (cit. on p. 30).

[186] R. Roncen. 'Revisiting nonlinear impedance in acoustic liners'. In: *Journal of Sound and Vibration* 608 (2025), p. 119058. DOI: 10.1016/j.jsv.2025.119058 (cit. on p. 30).

[187] G. Kubo, T. Ishii, K. Nagai, H. Oinuma, S. Enomoto, Y. Murata, and J. Oki. 'Evaluation of Nonlinear Impedance Models for Acoustic Liners Under the Normal Incident Sound Wave'. In: *30th AIAA/CEAS Aeroacoustics Conference (2024)*. Rome, Italy, 2024. DOI: 10.2514/6.2024-3367 (cit. on pp. 30, 56).

[188] R. Burgmayer, H.-F. Kohlenberg, and K. Knobloch. 'IFAR Benchmark Challenge #4'. In: *30th AIAA/CEAS Aeroacoustics Conference (2024)*. Rome, Italy: American Institute of Aeronautics and Astronautics, 2024. DOI: 10.2514/6.2024-3301 (cit. on p. 30).

[189] E. Feder and L. W. Dean. *Analytical and experimental studies for predicting noise attenuation in acoustically treated ducts for turbofan engines*. Tech. rep. NASA-CR-1373. National Aeronautics and Space Administration, 1969 (cit. on p. 30).

[190] D. Ronneberger. 'The acoustical impedance of holes in the wall of flow ducts'. In: *Journal of Sound and Vibration* 24.1 (1972), pp. 133–150. DOI: 10.1016/0022-460X(72)90129-0 (cit. on p. 30).

[191] A. L. Goldman and Ronald L. Panton. 'Measurement of the acoustic impedance of an orifice under a turbulent boundary layer'. In: *The Journal of the Acoustical Society of America* 60.6 (1976), pp. 1397–1405. DOI: 10.1121/1.381233 (cit. on pp. 30, 32).

[192] A. S. Hersh and C. K. Tam. *Numerical and Physical Modeling of the Response of Resonator Liners to Intense Sound and Grazing Flow*. Tech. rep. NNX09CF01. National Aeronautics and Space Administration, 2009 (cit. on p. 30).

[193] T. Rogers and A. S. Hersh. *Effect of grazing flow on steady-state resistance of isolated square-edged orifices*. Tech. rep. NASA-CR-2681. National Aeronautics and Space Administration, 1976 (cit. on p. 30).

[194] R. Kabral, H. Boden, and T. Elnady. 'Determination of Liner Impedance under High Temperature and Grazing Flow Conditions'. In: *20th AIAA/CEAS Aeroacoustics Conference*. Atlanta, Georgia, 2014. DOI: 10.2514/6.2014-2956 (cit. on pp. 31 sq.).

[195] L. J. Heidelberg, E. J. Rice, and L. Homyak. *Experimental evaluation of a spinning-mode acoustic-treatment design concept for aircraft inlets*. Tech. rep. NASA-TP-1613. National Aeronautics and Space Administration, 1980 (cit. on p. 31).

[196] P. Murray and R. J. Astley. 'Development of a single degree of freedom perforate impedance model under grazing flow and high SPL'. In: *18th AIAA/CEAS Aeroacoustics Conference (33rd AIAA Aeroacoustics Conference)*. Colorado Springs, Colorado, 2012. DOI: 10.2514/6.2012-2294 (cit. on p. 31).

[197] W. Eversman and M. Drouin. 'Refinement of Impedance Models for Single and Two Degree of Freedom Linings Based on Grazing Flow Duct Predictions and Measurements'. In: *28th AIAA/CEAS Aeroacoustics 2022 Conference*. Southampton, UK, 2022. DOI: 10.2514/6.2022-2966 (cit. on p. 31).

[198] Q. Zhang and D. J. Bodony. 'Numerical investigation of a honeycomb liner grazed by laminar and turbulent boundary layers'. In: *Journal of Fluid Mechanics* 792 (2016), pp. 936–980. DOI: 10.1017/jfm.2016.79 (cit. on p. 31).

[199] E. J. Rice, C. E. Feiler, and Acker, Loren W,. *Acoustic and aerodynamic performance of a 6-foot-diameter fan for turbofan engines. 3 - Performance with noise suppressors*. Tech. rep. NASA-TN-D-6178. National Aeronautics and Space Administration, 1971 (cit. on p. 32).

[200] M. G. Jones and D. M. Nark. 'Comparisons of Impedance Prediction Models for Perforate-over-Honeycomb Liners'. In: *AIAA AVIATION 2023 Forum*. San Diego, California, 2023. DOI: 10.2514/6.2023-3637 (cit. on p. 32).

[201] Y. Renou and Y. Aurégan. 'Failure of the Ingard-Myers boundary condition for a lined duct: an experimental investigation'. In: *The Journal of the Acoustical Society of America* 130.1 (2011), pp. 52–60. DOI: 10.1121/1.3586789 (cit. on p. 32).

[202] Y. Aurégan. 'On the use of a stress-impedance model to describe sound propagation in a lined duct with grazing flow'. In: *The Journal of the Acoustical Society of America* 143.5 (2018), p. 2975. DOI: 10.1121/1.5037585 (cit. on p. 32).

[203] F. Kohlenberg, A. Schulz, L. Enghardt, and K. Knobloch. 'Modeling of Advanced Helmholtz Resonator Liners with a Flexible Wall'. In: *AIAA Journal* 61.7 (2023), pp. 3108–3118. DOI: 10.2514/1.J062227 (cit. on pp. 33, 53, 57 sq., 74).

[204] R. D. Blevins. *Formulas for dynamics, acoustics and vibration*. Wiley series in acoustics noise and vibration. Chichester (UK): Wiley, 2016. DOI: 10.1002/9781119038122 (cit. on pp. 35, 37, 41 sq.).

[205] W. Frommhold, H. V. Fuchs, and S. Sheng. 'Acoustic Performance of Membrane Absorbers'. In: *Journal of Sound and Vibration* 170.5 (1994), pp. 621–636. DOI: 10.1006/jsvi.1994.1091 (cit. on p. 35).

[206] J. Kang and H. V. Fuchs. 'Predicting the Absorption of Open Weave Textiles and Microperforated Membranes Backed by an Air Space'. In: *Journal of Sound and Vibration* 220.5 (1999), pp. 905–920. DOI: 10.1006/jsvi.1998.1977 (cit. on p. 35).

[207] Umar Farooq, Shahin S. Nudehi. 'A Nonlinear Acoustic Resonator'. In: *Proceedings of the ASME 2007 International Design Engineering Technical Conferences and Computers and Information in Engineering Conference* (2007). DOI: 10.1115/DETC2007-34700 (cit. on pp. 35, 52).

[208] F. Bucciarelli and M. Meo. 'Broadening sound absorption coefficient with hybrid resonances'. In: *Applied Acoustics* 160 (2020), p. 107136. DOI: 10.1016/j.apacoust.2019.107136 (cit. on p. 35).

[209] Q. Xu, J. Qiao, G. Zhang, and L. Li. 'Low-frequency sound-absorbing metasurface constructed by a membrane-covered and coiled Helmholtz resonator'. In: *Journal of Applied Physics* 133.7 (2023). DOI: 10.1063/5.0138834 (cit. on p. 35).

[210] F. P. Mechel. 'Schallabsorber: Vol. 2 Innere Schallfelder - Strukturen'. In: Stuttgart: Hirzel, 1995, pp. 767–771 (cit. on p. 35).

[211] Y. Yang, B. Li, Z. Chen, N. Sui, Z. Chen, M.-U. Saeed, Y. Li, R. Fu, C. Wu, and Y. Jing. 'Acoustic properties of glass fiber assembly-filled honeycomb sandwich panels'. In: *Composites Part B: Engineering* 96 (2016), pp. 281–286. DOI: 10.1016/j.compositesb.2016.04.046 (cit. on p. 36).

[212] J. N. Reddy. *Theory and Analysis of Elastic Plates and Shells, Second Edition*. 2nd ed. Series in Systems and Control. Hoboken: CRC Press, 2015 (cit. on pp. 35 sq.).

[213] C. Y. Wang. *Structural Vibration: Exact Solutions for Strings, Membranes, Beams, and Plates*. Hoboken: CRC Press, 2014 (cit. on p. 35).

[214] S. Timoshenko and S. Woinowsky-Krieger. *Theory of plates and shells*. McGraw-Hill Inc., 1959 (cit. on p. 36).

[215] R. Szilard. *Theories and applications of plate analysis: Classical, numerical, and engineering methods*. Hoboken NJ: John Wiley, 2004 (cit. on p. 36).

[216] L. Cremer, M. Heckl, and B. A. T. Petersson. *Structure-borne sound: Structural vibrations and sound radiation at audio frequencies*. 3. ed. Berlin: Springer, 2005. DOI: 10.1007/b137728 (cit. on pp. 36, 71).

[217] A.W. Leissa. *Vibration of Plates*. Tech. rep. NASA SP-160. National Aeronautics and Space Administration, 1969 (cit. on pp. 38, 41 sq.).

[218] Z. Škvor. *Vibrating Systems and their Equivalent Circuits*. 1st ed. Studies in electrical and electronic engineering 40. Elsevier Science Publishing Company, Inc, 1991 (cit. on p. 38).

[219] F. Bongard, H. Lissek, and J. R. Mosig. 'Acoustic transmission line metamaterial with negative/zero/positive refractive index'. In: *Physical Review B* 82.9 (2010). DOI: 10.1103/PhysRevB.82.094306 (cit. on p. 38).

[220] N. Jiménez, O. Umnova, and J.-P. Groby. *Acoustic Waves in Periodic Structures, Metamaterials, and Porous Media*. Vol. 143. Cham: Springer International Publishing, 2021. DOI: 10.1007/978-3-030-84300-7 (cit. on p. 38).

[221] Y. Xing and B. Liu. 'New exact solutions for free vibrations of rectangular thin plates by symplectic dual method'. In: *Acta Mechanica Sinica* 25.2 (2009), pp. 265–270. DOI: 10.1007/s10409-008-0208-4 (cit. on p. 41).

[222] G. B. Warburton. 'The Vibration of Rectangular Plates'. In: *Proceedings of the Institution of Mechanical Engineers* 168.1 (1954), pp. 371–384. DOI: 10.1243/PIME_PROC_1954_168_040_02 (cit. on pp. 41 sq.).

[223] C.-C. Sung and J. T. Jan. 'The Response of and Sound Power Radiated by a Clamped Rectangular Plate'. In: *Journal of Sound and Vibration* 207.3 (1997), pp. 301–317. DOI: 10.1006/jsvi.1997.1125 (cit. on pp. 42, 44 sq.).

[224] T.-Y. Huang, C. Shen, and Y. Jing. 'On the evaluation of effective density for plate- and membrane-type acoustic metamaterials without mass attached'. In: *The Journal of the Acoustical Society of America* 140.2 (2016), p. 908. DOI: 10.1121/1.4960590 (cit. on p. 45).

[225] T. D. Rossing and N. H. Fletcher. *Principles of Vibration and Sound*. Second Edition. New York, NY: Springer, 2004. DOI: 10.1007/978-1-4757-3822-3 (cit. on p. 47).

[226] F. Fahy and P. Gardonio. *Sound and structural vibration: Radiation, transmission and response*. 2nd ed. Amsterdam: Academic Press, 2007 (cit. on pp. 47, 80).

[227] M. Gzal, A. F. Vakakis, and O. V. Gendelman. 'Vibroacoustics of a membrane-finite cavity resonator: Traditional and alternative approaches for analysis'. In: *Journal of Sound and Vibration* 573 (2024), p. 118214. DOI: 10.1016/j.jsv.2023.118214 (cit. on p. 47).

[228] A. J. Pretlove. 'Free vibrations of a rectangular panel backed by a closed rectangular cavity by a closed rectangular cavity'. In: *Journal of Sound and Vibration* 2.3 (1965), pp. 197–209. DOI: 10.1016/0022-460X(65)90108-2 (cit. on p. 47).

[229] E. H. Dowell, G. F. Gorman, and D. A. Smith. 'Acoustoelasticity: General theory, acoustic natural modes and forced response to sinusoidal excitation, including comparisons with experiment'. In: *Journal of Sound and Vibration* 52.4 (1977), pp. 519–542. DOI: 10.1016/0022-460X(77)90368-6 (cit. on p. 47).

[230] D. G. Gorman, J. M. Reese, J. Horácek, and K. Dedouch. 'Vibration analysis of a circular disc backed by a cylindrical cavity'. In: *Proceedings of the Institution of Mechanical Engineers, Part C: Journal of Mechanical Engineering Science* 215.11 (2001), pp. 1303–1311. DOI: 10.1243/0954406011524685 (cit. on p. 47).

[231] A. W. Leissa. 'On a curve veering aberration'. In: *ZAMP Zeitschrift für angewandte Mathematik und Physik* 25.1 (1974), pp. 99–111. DOI: 10.1007/BF01602113 (cit. on p. 47).

[232] S. Vidoli and F. Vestroni. 'Veering Phenomena in Systems With Gyroscopic Coupling'. In: *Journal of Applied Mechanics* 72.5 (2005), pp. 641–647. DOI: 10.1115/1.1940666 (cit. on p. 47).

[233] F. J. Fahy and C. Schofield. 'A note on the interaction between a Helmholtz resonator and an acoustic mode of an enclosure'. In: *Journal of Sound and Vibration* 72.3 (1980), pp. 365–378. DOI: 10.1016/0022-460X(80)90383-1 (cit. on p. 47).

[234] M. Neubauer, J. Genßler, V. Radmann, F. Kohlenberg, M. Pohl, K. Böhme, K. Knobloch, E. Sarradj, K. Höschler, N. Modler, and L. Enghardt. 'Experimental and Numerical Investigation of Novel Acoustic Liners and Their Design for Aero-Engine Applications'. In: *Aerospace* 10.1 (2023), p. 5. DOI: 10.3390/aerospace10010005 (cit. on pp. 48, 75).

[235] V. Radmann, F. Kohlenberg, and E. Sarradj. 'Modeling of a 3D Plate Resonator Liner and Comparison to Numerical and Experimental Investigations'. In: *AIAA AVIATION 2023 Forum*. San Diego, California, 2023. DOI: 10.2514/6.2023-3639 (cit. on p. 48).

[236] R. B. Davis. 'A simplified approach for predicting interaction between flexible structures and acoustic enclosures'. In: *Journal of Fluids and Structures* 70 (2017), pp. 276–294. DOI: 10.1016/j.jfluidstructs.2017.02.003 (cit. on p. 48).

[237] D. M. Photiadis. 'The effect of wall elasticity on the properties of a Helmholtz resonator'. In: *The Journal of the Acoustical Society of America* 88 (1990), p. 20. DOI: 10.1121/1.2028905 (cit. on p. 49).

[238] A. A. Zaikin and Rudenko O.V. 'A Nonlinear Model of the Helmholtz Resonator with a Movable Wall'. In: *Acoustical Physics* 42.3 (1995), pp. 329–333 (cit. on p. 49).

[239] S. Griffiths, B. Nennig, and S. Job. 'Porogranular materials composed of elastic Helmholtz resonators for acoustic wave absorption'. In: *The Journal of the Acoustical Society of America* 141.1 (2017), p. 254. DOI: 10.1121/1.4973691 (cit. on p. 49).

[240] M. Pishvar and R. L. Harne. 'Nonlinear Behavior of Helmholtz Resonator With a Compliant Wall for Low-Frequency, Broadband Noise Control'. In: *Journal of Vibration and Acoustics* 144.3 (2022). DOI: 10.1115/1.4052870 (cit. on p. 49).

[241] S. Cui and R. L. Harne. 'Soft Materials with Broadband and Near-Total Absorption of Sound'. In: *Physical Review Applied* 12.6 (2019). DOI: 10.1103/PhysRevApplied.12.064059 (cit. on p. 49).

[242] S. Cui and R. L. Harne. 'Acoustic-Structure Interaction in an Adaptive Helmholtz Resonator by Compliance and Constraint'. In: *Journal of Vibration and Acoustics* 142.2 (2020). DOI: 10.1115/1.4045456 (cit. on p. 49).

[243] S. J. Estève and M. E. Johnson. 'Adaptive Helmholtz resonators and passive vibration absorbers for cylinder interior noise control'. In: *Journal of Sound and Vibration* 288.4-5 (2005), pp. 1105–1130. DOI: 10.1016/j.jsv.2005.01.017 (cit. on p. 49).

[244] A. Benouhiba, P. Rougeot, N. Andreff, M. Ouisse, and K. Rabenorosoa. 'Transforming acoustic control: the first tunable broadband origami-based Helmholtz resonator'.

In: *Smart Materials and Structures* 33.10 (2024), p. 105042. DOI: 10.1088/1361-665X/ad7c0b (cit. on p. 49).

[245] G. Wen, S. Zhang, H. Wang, Z.-P. Wang, J. He, Z. Chen, J. Liu, and Y. M. Xie. 'Origami-based acoustic metamaterial for tunable and broadband sound attenuation'. In: *International Journal of Mechanical Sciences* 239 (2023), p. 107872. DOI: 10.1016/j.ijmecsci.2022.107872 (cit. on p. 49).

[246] F. Mizukoshi and H. Takahashi. 'A Tunable Open Planar Acoustic Notch Filter Utilizing a Pneumatically Modulated Helmholtz Resonator Array'. In: *IEEE Access* 10 (2022), pp. 118213–118221. DOI: 10.1109/ACCESS.2022.3220366 (cit. on p. 49).

[247] T. Yamamoto. 'Acoustic metamaterial plate embedded with Helmholtz resonators for extraordinary sound transmission loss'. In: *Journal of Applied Physics* 123.21 (2018). DOI: 10.1063/1.5025570 (cit. on p. 49).

[248] F. Langfeldt. 'Membrane-type acoustic metamaterials for aircraft noise shields'. PhD thesis. Hamburg, Germany: Hamburg University of Technology, 2018. DOI: 10.15480/882.1780 (cit. on p. 49).

[249] F. Langfeldt, A. J. Khatokar, and W. Gleine. 'Plate-type acoustic metamaterials with integrated Helmholtz resonators'. In: *Applied Acoustics* 199 (2022), p. 109019. DOI: 10.1016/j.apacoust.2022.109019 (cit. on p. 49).

[250] Z. Laly, R. Panneton, and N. Atalla. 'Characterization and development of periodic acoustic metamaterials using a transfer matrix approach'. In: *Applied Acoustics* 185 (2022), p. 108381. DOI: 10.1016/j.apacoust.2021.108381 (cit. on p. 49).

[251] R.-S. Li, X.-W. Sun, X.-L. Gao, G.-G. Xu, T. Song, and J.-H. Tian. 'Sound transmission loss overlay mechanism of plate-type acoustic metamaterials with Helmholtz resonators'. In: *Physics Letters A* 538 (2025), p. 130358. DOI: 10.1016/j.physleta.2025.130358 (cit. on p. 49).

[252] S. Noh, H. Lee, and B. Choi. 'A study on the acoustic energy harvesting with Helmholtz resonator and piezoelectric cantilevers'. In: *International Journal of Precision Engineering and Manufacturing* 14.9 (2013), pp. 1629–1635. DOI: 10.1007/s12541-013-0220-x (cit. on p. 50).

[253] Y. Aurégan and M. Farooqui. 'In-parallel resonators to increase the absorption of subwavelength acoustic absorbers in the mid-frequency range'. In: *Scientific Reports* 9.1 (2019), p. 11140. DOI: 10.1038/s41598-019-47516-7 (cit. on p. 50).

[254] M. E. D'Elia, T. Humbert, and Y. Aurégan. 'On articulated plates with micro-slits to tackle low-frequency noise'. In: *Acta Acustica* 5 (2021), p. 31. DOI: 10.1051/aacus/2021024 (cit. on p. 50).

[255] T. Abily, J. Regnard, G. Gabard, and S. Durand. 'Non-linear effects in thin slits for low frequency sound absorption'. In: *Journal of Sound and Vibration* 546 (2023), p. 117432. DOI: 10.1016/j.jsv.2022.117432 (cit. on p. 50).

[256] H. Hoppen, F. Langfeldt, W. Gleine, and O. von Estorff. 'Helmholtz resonator with two resonance frequencies by coupling with a mechanical resonator'. In: *Journal*

of Sound and Vibration 559 (2023), p. 117747. DOI: 10.1016/j.jsv.2023.117747 (cit. on p. 50).

[257] G. Hu, L. Tang, and X. Cui. 'On the modelling of membrane-coupled Helmholtz resonator and its application in acoustic metamaterial system'. In: *Mechanical Systems and Signal Processing* 132 (2019), pp. 595–608. DOI: 10.1016/j.ymssp.2019.07.017 (cit. on p. 50).

[258] G. Hu, L. Tang, and Y. Yang. 'Acoustic metamaterial containing an array of Helmholtz resonators coupled with mass-loaded membranes'. In: *Health Monitoring of Structural and Biological Systems IX*. 2020, p. 48. DOI: 10.1117/12.2554870 (cit. on p. 50).

[259] Z. Zhang, D. Yu, J. Liu, B. Hu, and J. Wen. 'Transmission and bandgap characteristics of a duct mounted with multiple hybrid Helmholtz resonators'. In: *Applied Acoustics* 183 (2021), p. 108266. DOI: 10.1016/j.apacoust.2021.108266 (cit. on p. 50).

[260] M. Park, K. Toboonchuay, and P. Rattanangkul. 'Helmholtz resonator coupled with circular membrane'. In: *Applied Acoustics* 221 (2024), p. 110003. DOI: 10.1016/j.apacoust.2024.110003 (cit. on p. 50).

[261] R. Domingo-Roca, A. Feeney, J. F. C. Windmill, and J. C. Jackson-Camargo. 'On the directionality of membrane coupled Helmholtz resonators under open air conditions'. In: *Scientific reports* 14.1 (2024), p. 27771. DOI: 10.1038/s41598-024-79568-9 (cit. on p. 50).

[262] Y. Chen and Y.-H. Park. 'A Helmholtz resonator on elastic foundation for measurement of the elastic coefficient of human skin'. In: *Journal of the mechanical behavior of biomedical materials* 101 (2020), p. 103417. DOI: 10.1016/j.jmbbm.2019.103417 (cit. on p. 50).

[263] X. Zhu, Z. Chen, Y. Jiao, and Y. Wang. 'Broadening of the Sound Absorption Bandwidth of the Perforated Panel Using a Membrane-Type Resonator'. In: *Journal of Vibration and Acoustics* 140.3 (2018). DOI: 10.1115/1.4038942 (cit. on p. 50).

[264] T.-Y. Huang, C. Shen, and Y. Jing. 'Membrane- and plate-type acoustic metamaterials'. In: *The Journal of the Acoustical Society of America* 139.6 (2016), pp. 3240–3250. DOI: 10.1121/1.4950751 (cit. on pp. 50 sq.).

[265] F. Langfeldt, H. Kemsies, W. Gleine, and O. von Estorff. 'Perforated membrane-type acoustic metamaterials'. In: *Physics Letters A* 381.16 (2017), pp. 1457–1462. DOI: 10.1016/j.physleta.2017.02.036 (cit. on p. 51).

[266] Y. Xu, J. H. Wu, Y. Cai, and F. Ma. 'Investigation on dynamic effective parameters of perforated thin-plate acoustic metamaterials'. In: *Journal of Physics D: Applied Physics* 52.40 (2019), p. 405301. DOI: 10.1088/1361-6463/ab3011 (cit. on p. 51).

[267] J.-S. Chen, Y.-B. Chen, H.-J. Tsai, K.-Y. Chen, and L.-C. Chou. 'Membrane-ring acoustic metamaterials with an orifice'. In: *Materials Research Express* 6.9 (2019), p. 095802. DOI: 10.1088/2053-1591/ab3088 (cit. on p. 51).

[268] Alexander A. Svetgoff. 'An investigation of lightweight concepts for low-frequency performance enhancement in acoustic liners'. Master Thesis. Stillwater: Oklahoma State University, 2018 (cit. on p. 51).

[269] A. Abbad, K. Rabenorosoa, M. Ouisse, and N. Atalla. 'Adaptive Helmholtz resonator based on electroactive polymers: modeling, characterization, and control'. In: *Smart Materials and Structures* 27.10 (2018), p. 105029. DOI: 10.1088/1361-665X/aad939 (cit. on p. 51).

[270] C. Solano and L. Cattafesta. 'Modeling, design, and optimization of a dielectric elastomer acoustic liner'. In: *International Journal of Aeroacoustics* 22.5-6 (2023), pp. 599–620. DOI: 10.1177/1475472X231199187 (cit. on p. 51).

[271] C. Dodge. 'A Study of a Dielectric Elastomer Acoustic Liner'. PhD thesis. Tallahassee: Florida State University, 2023 (cit. on p. 51).

[272] F. Liu, A. Phipps, S. Horowitz, K. Ngo, L. Cattafesta, T. Nishida, and M. Sheplak. 'Acoustic energy harvesting using an electromechanical Helmholtz resonator'. In: *The Journal of the Acoustical Society of America* 123.4 (2008), pp. 1983–1990. DOI: 10.1121/1.2839000 (cit. on p. 51).

[273] J. Liu, T. Su, Z. Yan, S. Duan, F. Zhang, and H. Lv. 'Design of Tunable Acoustic Liner and Adaptive Control System'. In: *Acoustics Australia* 49.1 (2021), pp. 83–91. DOI: 10.1007/s40857-020-00210-5 (cit. on p. 51).

[274] S. Kim, J. Choi, H. M. Seung, I. Jung, K. H. Ryu, H.-C. Song, C.-Y. Kang, and M. Kim. 'Gradient-index phononic crystal and Helmholtz resonator coupled structure for high-performance acoustic energy harvesting'. In: *Nano Energy* 101 (2022), p. 107544. DOI: 10.1016/j.nanoen.2022.107544 (cit. on pp. 51 sq.).

[275] S. Griffin, S. A. Lane, and S. Huybrechts. 'Coupled Helmholtz Resonators for Acoustic Attenuation'. In: *Journal of Vibration and Acoustics* 123.1 (2001), pp. 11–17. DOI: 10.1115/1.1320812 (cit. on p. 51).

[276] D. Zhao. 'Transmission Loss Analysis of a Parallel-Coupled Helmholtz Resonator Network'. In: *AIAA Journal* 50.6 (2012), pp. 1339–1346. DOI: 10.2514/1.J051453 (cit. on p. 51).

[277] D. Zhao, C. Ji, and M. Yin. In: *Aerospace Science and Technology* 128 (2022), p. 107799. DOI: 10.1016/j.ast.2022.107799 (cit. on p. 51).

[278] Y. Mi and X. Yu. 'Attenuation of low-frequency sound in U-shaped duct with membrane coupled acoustic resonator: Modeling and analysis'. In: *Journal of Sound and Vibration* 489 (2020), p. 115679. DOI: 10.1016/j.jsv.2020.115679 (cit. on p. 51).

[279] G.-S. Liu, Y.-Y. Peng, M.-H. Liu, X.-Y. Zou, and J.-C. Cheng. 'Broadband acoustic energy harvesting metasurface with coupled Helmholtz resonators'. In: *Applied Physics Letters* 113.15 (2018), p. 153503. DOI: 10.1063/1.5041731 (cit. on p. 51).

[280] S. B. Horowitz, T. Nishida, L. N. Cattafesta, and M. Sheplak. 'Characterization of a Compliant-Backplate Helmholtz Resonator for an Electromechanical Acoustic

Liner'. In: *International Journal of Aeroacoustics* 1.2 (2002), pp. 183–205. DOI: 10.1260/147547202760236969 (cit. on p. 51).

[281] F. Liu. 'A Tunable Electromechanical Helmholtz Resonator'. PhD thesis. Tallahassee: University of Florida, 2007 (cit. on p. 51).

[282] D. Li, M. Hu, F. Wu, K. Liu, M. Gao, Z. Ju, J. Zhao, and A. Bao. 'Design of tunable low-frequency acoustic energy harvesting barrier for subway tunnel based on an optimized Helmholtz resonator and a PZT circular plate'. In: *Energy Reports* 8 (2022), pp. 8108–8123. DOI: 10.1016/j.egyr.2022.06.042 (cit. on p. 52).

[283] S. S. Nudehi, G. S. Duncan, and U. Farooq. 'Modeling and Experimental Investigation of a Helmholtz Resonator with a Flexible Plate'. In: *Journal of Vibration and Acoustics* 135.4 (2013). DOI: 10.1115/1.4023810 (cit. on p. 52).

[284] M. H. Kurdi, G. Scott Duncan, and S. S. Nudehi. 'Optimal Design of a Helmholtz Resonator With a Flexible End Plate'. In: *Journal of Vibration and Acoustics* 136.3 (2014). DOI: 10.1115/1.4026849 (cit. on p. 52).

[285] M. Kurdi, S. Nudehi, and G. S. Duncan. 'Tailoring Plate Thickness of a Helmholtz Resonator for Improved Sound Attenuation'. In: *Journal of Vibration and Acoustics* 141.3 (2019). DOI: 10.1115/1.4042519 (cit. on p. 52).

[286] M. Oblak, M. Pirnat, and M. Boltežar. 'Modal-interaction approach to the strong structural–acoustic coupling of an elastic Helmholtz resonator and an acoustic cavity containing a heavy fluid'. In: *Journal of Sound and Vibration* 535 (2022), p. 117120. DOI: 10.1016/j.jsv.2022.117120 (cit. on p. 52).

[287] W. Zheng, Q. Huang, S. Li, and Z. Guo. 'Sound Absorption of Hybrid Passive-Active System Using Finite Flexible Micro-Perforated Panels'. In: *Journal of Low Frequency Noise, Vibration and Active Control* 30.4 (2011), pp. 313–328. DOI: 10.1260/0263-0923.30.4.313 (cit. on p. 52).

[288] T. Bravo, C. Maury, and C. Pinhède. 'Vibroacoustic properties of thin micro-perforated panel absorbers'. In: *The Journal of the Acoustical Society of America* 132.2 (2012), pp. 789–798. DOI: 10.1121/1.4733555 (cit. on p. 52).

[289] S. Palani, R. R. Subramanyam, C. Paruchuri, and P. Joseph. 'Flexible Membrane Type Non-Linear Liner'. In: *29th International Congress of Sound and Vibration*. Prague, Czech Republic, 2023 (cit. on p. 52).

[290] Y. Y. Lee, E. Lee, and C. F. Ng. 'Sound absorption of a finite flexible micro-perforated panel backed by an air cavity'. In: *Journal of Sound and Vibration* 287.1-2 (2005), pp. 227–243. DOI: 10.1016/j.jsv.2004.11.024 (cit. on p. 52).

[291] Y. Y. Lee and E. Lee. 'Widening the sound absorption bandwidths of flexible micro-perforated curved absorbers using structural and acoustic resonances'. In: *International Journal of Mechanical Sciences* 49.8 (2007), pp. 925–934. DOI: 10.1016/j.ijmecsci.2007.01.008 (cit. on p. 52).

[292] M. R. Hossain, E. P. Ross, and G. J. Bennett. 'Acoustic plate-valve resonator for low-frequency sound absorption'. In: *AIP Advances* 13.6 (2023). DOI: 10.1063/5.0142908 (cit. on p. 52).

[293] W. Y. Yeang, D. Halim, X. Yi, and H. Chen. 'On improving low-frequency sound absorption using a compound microperforated panel backed by a panel-type resonator with tuned multi-frequency resonators'. In: *Journal of Sound and Vibration* 570 (2024), p. 118134. DOI: 10.1016/j.jsv.2023.118134 (cit. on p. 53).

[294] M. Dannemann, M. Kucher, E. Kunze, N. Modler, K. Knobloch, L. Enghardt, E. Sarradj, and K. Höschler. 'Experimental Study of Advanced Helmholtz Resonator Liners with Increased Acoustic Performance by Utilising Material Damping Effects'. In: *Applied Sciences* 8.10 (2018), p. 1923. DOI: 10.3390/app8101923 (cit. on p. 53).

[295] K. Knobloch, L. Enghardt, and F. Bake. 'Helmholtz Resonator Liner with Flexible Walls'. In: *2018 AIAA/CEAS Aeroacoustics Conference*. Atlanta, Georgia, 2018. DOI: 10.2514/6.2018-4102 (cit. on p. 53).

[296] K. Knobloch, L. Enghardt, and F. Bake. 'Investigation of Flexible Walls for Acoustic Liners'. In: *25th AIAA/CEAS Aeroacoustics Conference*. Delft, The Netherlands, 2019. DOI: 10.2514/6.2019-2565 (cit. on pp. 53, 64 sq.).

[297] K. Knobloch, L. Enghardt, E. Sarradj, K. Höschler, and O. Kahle. 'Helmholtz-Resonator-Liner'. DE 10 2017 205 515 B4 2021.09.02 (cit. on p. 53).

[298] X. Liu, J. H. Wu, J. Niu, W. Li, and C. Liu. 'Vibro-acoustic Helmholtz absorber with soft wall for broadband sound absorption'. In: *International Journal of Mechanical Sciences* 289 (2025), p. 110083. DOI: 10.1016/j.ijmecsci.2025.110083 (cit. on p. 53).

[299] X. Zhao and X. Fan. 'Enhancing low frequency sound absorption of micro-perforated panel absorbers by using mechanical impedance plates'. In: *Applied Acoustics* 88 (2015), pp. 123–128. DOI: 10.1016/j.apacoust.2014.08.015 (cit. on p. 53).

[300] A. Sanada and N. Tanaka. 'Extension of the frequency range of resonant sound absorbers using two-degree-of-freedom Helmholtz-based resonators with a flexible panel'. In: *Applied Acoustics* 74.4 (2013), pp. 509–516. DOI: 10.1016/j.apacoust.2012.09.012 (cit. on p. 53).

[301] F. Mizukoshi and H. Takahashi. 'Open planar acoustic notch filter using a film-integrated Helmholtz resonator array'. In: *Japanese Journal of Applied Physics* 62.3 (2023), p. 034002. DOI: 10.35848/1347-4065/acc0b7 (cit. on p. 53).

[302] X. Q. Zhou and D. Y. Yu. 'Acoustic energy absorption and dissipation characteristic of Helmholtz resonator enhanced and broadened by acoustic black hole'. In: *Aerospace Science and Technology* 81 (2018), pp. 237–248. DOI: 10.1016/j.ast.2018.08.009 (cit. on p. 54).

[303] J. Liu, W. Dong, T. Wang, M. Chen, and Y. Lu. 'Acoustic propagation through a duct metamaterial attached with periodic multi-resonant cavities'. In: *Journal of Vibration*

and Control 30.5-6 (2024), pp. 1368–1377. DOI: 10.1177/10775463231162649 (cit. on p. 54).

[304] *DIN EN ISO 10534-2:2001 Akustik_ - Bestimmung des Schallabsorptionsgrades und der Impedanz in Impedanzrohren - Teil 2: Verfahren mit Übertragungsfunktion*. Berlin. DOI: 10.31030/9139179 (cit. on pp. 61 sqq.).

[305] S.-H. Jang and J.-G. Ih. 'On the multiple microphone method for measuring in-duct acoustic properties in the presence of mean flow'. In: *The Journal of the Acoustical Society of America* 103.3 (1998), pp. 1520–1526. DOI: 10.1121/1.421289 (cit. on p. 62).

[306] P. Welch. 'The use of fast Fourier transform for the estimation of power spectra: A method based on time averaging over short, modified periodograms'. In: *IEEE Transactions on Audio and Electroacoustics* 15.2 (1967), pp. 70–73. DOI: 10.1109/TAU.1967.1161901 (cit. on p. 63).

[307] S. Busse-Gerstengarbe, F. Bake, L. Enghardt, and M. G. Jones. 'Comparative Study of Impedance Eduction Methods, Part 1: DLR Tests and Methodology'. In: *AIAA-2013-2124*. Berlin, Germany: 19th AIAA/CEAS Aeroacoustics Conference, 2013. DOI: 10.2514/6.2013-2124 (cit. on pp. 65, 68).

[308] J. Y. Chung. 'Rejection of flow noise using a coherence function method'. In: *The Journal of the Acoustical Society of America* 62.2 (1977), pp. 388–395. DOI: 10.1121/1.381537 (cit. on p. 65).

[309] L. Enghardt, A. Schulz, A. Fischer, and S. Busse. 'Determination of the impedance for lined ducts with grazing flow'. In: *18th AIAA/CEAS Aeroacoustics Conference (33rd AIAA Aeroacoustics Conference)*. Colorado Springs, Colorado: American Institute of Aeronautics and Astronautics, 2012. DOI: 10.2514/6.2012-2243 (cit. on p. 68).

[310] J. Genßler, F. Kohlenberg, K. Knobloch, and L. Enghardt. 'Experimental Investigations of Flexible Wall Effects in Helmholtz Resonators for Aircraft Engine Acoustic Liners'. In: *AIAA AVIATION 2023 Forum*. San Diego, California, 2023. DOI: 10.2514/6.2023-3347 (cit. on pp. 68, 74).

[311] V. L. Popov. *Contact Mechanics and Friction*. Berlin, Heidelberg: Springer Berlin Heidelberg, 2017. DOI: 10.1007/978-3-662-53081-8 (cit. on p. 71).

[312] M. F. Ashby. *Materials selection in mechanical design*. Fifth edition. Oxford, United Kingdom: Cambridge, MA : Butterworth-Heinemann, an imprint of Elsevier, 2017 (cit. on pp. 71 sq.).

[313] M. Neubauer, M. Pohl, M. Kucher, R. Böhm, K. Höschler, and N. Modler. 'DMA of TPU Films and the Modelling of Their Viscoelastic Properties for Noise Reduction in Jet Engines'. In: *Polymers* 14.23 (2022). DOI: 10.3390/polym14235285 (cit. on p. 72).

[314] O. Kahle and D. M. C. Uhlig. *Abschlussbericht: Entwicklungsbegleitende Beratungen und Untersuchungen zu Materialeigenschaften von polymerbasierten Werkstoffen*

,

(Folien) im Hinblick auf luftfahrtspezifische Anforderungen mit besonderem Bezug auf Dämpfungseigenschaften. Tech. rep. Fraunhofer PYCO, 2024 (cit. on p. 72).

[315] F. Kohlenberg, A. Schulz, L. Enghardt, and K. Knobloch. 'Modelling of Acoustic Liners Consisting of Helmholtz Resonators Coupled with a Second Cavity by Flexible Walls'. In: *28th AIAA/CEAS Aeroacoustics 2022 Conference*. Southampton, UK, 2022. DOI: 10.2514/6.2022-2824 (cit. on p. 74).

[316] F. Kohlenberg, M. Neubauer, J. Genßler, V. Radmann, and K. Knobloch. 'Manufacturing, modelling and testing of acoustic liners extended with flexible walls'. In: *CEAS Aeronautical Journal* (2025). DOI: 10.1007/s13272-025-00853-y (cit. on pp. 77, 124).

[317] S. Busse-Gerstengarbe. 'Untersuchung von lokal und nichtlokal reagierenden akustischen Dämpfern (Linern) für Triebwerke'. PhD thesis. Berlin: Technische Universität Berlin, 2014. DOI: 10.14279/depositonce-4488 (cit. on p. 76).

[318] Comsol Multiphysics. *Acoustics Module User's Guide (Comsol 6.1)*. 2022 (cit. on pp. 82 sqq.).

[319] Comsol Multiphysics. *Structural Mechanics Module User's Guide (Comsol 6.1)*. 2022 (cit. on p. 84).

[320] F. Kohlenberg, V. Radmann, J. Genßler, L. Enghardt, and K. Knobloch. 'Experimental and Numerical Analysis of the Vibro-Acoustic Behavior of a Helmholtz Resonator with a Flexible Wall'. In: *AIAA AVIATION 2023 Forum*. San Diego, California, 2023. DOI: 10.2514/6.2023-3348 (cit. on p. 86).

[321] F. Kohlenberg and K. Knobloch. 'Experimental and Numerical Parameter Study of a Helmholtz Resonator with a Flexible Wall'. In: *30th AIAA/CEAS Aeroacoustics Conference (2024)*. Rome, Italy: American Institute of Aeronautics and Astronautics, 2024. DOI: 10.2514/6.2024-3077 (cit. on p. 97).